THE UNIVERSITY OF
WARWICK

AUTHOR: **David Andrew Duncan** DEGREE: **Ph.D.**

TITLE: **Adsorbate structure determination using energy scanned photoelectron diffraction**

DATE OF DEPOSIT: .....

I agree that this thesis shall be available in accordance with the regulations governing the University of Warwick theses.

I agree that the summary of this thesis may be submitted for publication.

I **agree** that the thesis may be photocopied (single copies for study purposes only).

Theses with no restriction on photocopying will also be made available to the British Library for microfilming. The British Library may supply copies to individuals or libraries. subject to a statement from them that the copy is supplied for non-publishing purposes. All copies supplied by the British Library will carry the following statement:

> "Attention is drawn to the fact that the copyright of this thesis rests with its author. This copy of the thesis has been supplied on the condition that anyone who consults it is understood to recognise that its copyright rests with its author and that no quotation from the thesis and no information derived from it may be published without the author's written consent."

AUTHOR'S SIGNATURE: .....

USER'S DECLARATION

1. I undertake not to quote or make use of any information from this thesis without making acknowledgement to the author.
2. I further undertake to allow no-one else to use this thesis while it is in my care.

DATE SIGNATURE ADDRESS

.....

.....

.....

.....

.....

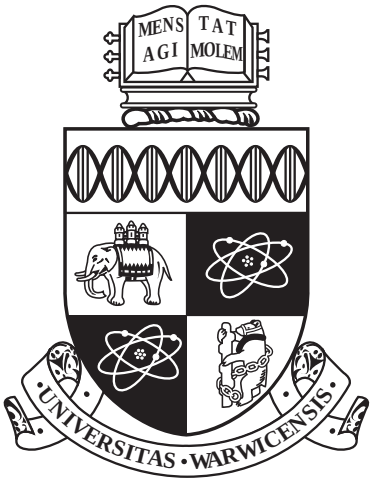

Adsorbate structure determination using energy scanned photoelectron diffraction

by

David Andrew Duncan

Thesis

Submitted to the University of Warwick

for the degree of Doctor of Philosophy

Doctor of Philosophy

Department of Physics

March 2012

THE UNIVERSITY OF
WARWICK

Contents

List of Tables

List of Figures

Acknowledgments

I would like to dedicate this thesis to my grandfather (Andrew Rankin) who is probably the kindest and most helpful person I know. Not only has he always been there for me, but also many others. I can only hope to be half the man he is. I would also like to thank my parents (Alistair Duncan and Hazel Roy), who through hard work, love and care have made my life easier than it has any right to be. I also am deeply indebted to my supervisor Phil Woodruff who has been a brilliant inspiration into what it means to be a scientist, I hope he finds as much joy in retirement as he found in his career.

I would also like to acknowledge my former supervisors (Niko Ernsting of the Humboldt-Universität, Berlin and Donald MacLaren of the University of Glasgow) whose brilliant work ethic inspired me to do better. The post-docs who gently educated me in the ways of vacuum science; Tsenolo Lerotholi and Werner Unterberger - between them they made the my PhD run smoothly. I would also like to acknowledge Dagmar Kreikemeyer Lorenzo – who has done the same PhD as me, but started 2 months earlier in Berlin (and always seemed to get the interesting systems!!); she always made beam times worth looking forward to. I would also like to thank my resident DFT monkey, Matt Bradley. Not only did he twist the crank of that black box of adsorbate structures that is DFT, but he was also a constant companion in the less salubrious adventures.

I am loud, inconsiderate and demanding, as such I must thank my various house mates for putting up with me; Steve Parsons, Matt Butchers, Matt Bradley, Joao Bento, Callum Lister, Shi-Ying Kam and Chris Hussey. Similarly I would like to thank my various office mates; Agenor Hentz (who solved all of my unix issues), Dan Sheppard (who solved all my unix issues after Age left), Tsenolo Lerotholi (three leaving dos, doesn't invite me to one!!), Anidita Chaundhori (who did her best to

teach us all Bengali), Matt Bradley (who was in the office in spirit, at least), Amanda Window, Daryl Jackson (who gave me so many of my systems), Matt Butchers (who graced us on his tour of every office in the department, before finally settling in a corridor), Jake Choi, Dae-Sung and Liam Fishwick (who solved all my unix issues after Age and Dan left). Further I would like to thank the rest of my group members (current and past) of various seniority; Chris McConville, Gavin Bell, Tim Veal, Rob Johnston, Jim Aldous, Louise Bailey, Chris Burrows, Marc Walker, Sepehr Farahani, Wojciech Linhart, Nessa Fereshteh Saniee, Dan Higgins, Ian Maskery, Andrzej Stacel and James Mudd. Specifically I would like to thank Jim Robinson for always keeping the group computing up and running – a thankless job.

I would also like to thank Manuel Dos Santos Dias, Euan Cowie, Chris Brady, Francis Casson and Frank Filsinger who provided suggestions and aid that lead to so much success within my PhD. I would also like to thank my close friends Steph Watson and Greig Davidson for being, well, good friends.

Finally I would like to thank you for taking the time to read this,

David A. Duncan.

Declarations

This thesis is submitted to the University of Warwick in partial fulfillment of the requirements for admission to the degree of Doctor of Philosophy. The work presented here is my own, except where specifically stated otherwise, and was performed in the Department of Physics at the University of Warwick under the supervision of Professor D.P. Woodruff FRS during the period October 2008 to April 2012. The measurements were performed at the Berliner Elektronenspeicherring-Gesellschaft für Synchrotronstrahlung mbH (BESSY II) in Berlin in collaboration with the Fritz-Haber Institute, Berlin. All DFT (density functional theory) results referenced here were performed by M.K. Bradley unless otherwise stated. The measurements of tartaric acid on Cu(110) (§4.4) were performed before the beginning of this PhD by W. Unterberger, D.C. Jackson, M.K. Knight, E.A. Kröger, K.A. Hogan and T.J. Lerotholi, partial results of which form part of the thesis of D.C. Jackson. The measurements of Cytosine on Cu(110) (§4.2) were also performed before the beginning of the PhD by D.C Jackson, W. Unterberger, T.J. Lerotholi and D. Kreikemyer Lorenzo, partial results of which form part of the thesis of D.C. Jackson. The measurements of vanadyl phthalocyanine on Au(111) (§8 were performed before the beginning of the PhD by W. Unterberger and T.J. Lerotholi and preliminary analysis was done by K.A. Hogan. The measurements of methanol on Ru(0001) (§6), uracil on Cu(110) (§4.3) and glycine on Cu(111) (§4.5) were measured in collaboration with D. Kreikemeyer Lorenzo and W. Unterberger of the Fritz Haber Institute, Berlin and T.J. Lerotholi of the University of Warwick / University of Witwatersrand. The dataset for water decomposition on TiO_2(110) has been previously published by Allegretti et al. [37] and the reduction of the data used within this study was also performed by F. Allegretti of the Technische Universät München.

Details of the work presented here are / will be published in the following

articles:

- D.A. Duncan, W. Unterberger, K.A. Hogan, T.J. Lerotholi, C.L.A Lamont and D.P. Woodruff, "A photoelectron diffraction investigation of vanadyl phthalocyanine on Au(111)", Surface Science, 604 (2010) 47-53

- D.C. Jackson, D.A. Duncan, W. Unterberger, T.J. Lerotholi, D. Kreikemeyer Lorenzo, M.K. Bradley and D.P. Woodruff, "Structure of Cytosine on Cu(110): a Scanned-Energy Mode Photoelectron Diffraction Study", Journal of Physical Chemistry C, 114 (2010) 15454-15463

- M.K. Bradley, D.A. Duncan, J. Robinson and D.P. Woodruff, "The structure of furan reaction products on Pd(111)", Physical Chemistry Chemical Physics, 13 (2011) 7975-7984

- D.A. Duncan, W. Unterberger, D. Kreikemeyer Lorenzo and D.P. Woodruff, "Uracil on Cu(110): A quantitative structure determination by energy-scanned photoelectron diffraction", Journal of Chemical Physics, 135 (2011) 014704

- D.A. Duncan, J.L. Choi and D.P. Woodruff, "Global search algorithms in photoelectron diffraction structure determination", Surface Science, 606 (2012) 278-284

- D.A. Duncan, M.K. Bradley, T.J. Lerotholi, D. Kreikemeyer Lorenzo, W. Unterberger and D.P. Woodruff, "Glycine on Cu(111): A quantitative structure determination by energy scanned photoelectron diffraction", submitted to the Journal of Physics Chemistry C

- D.A. Duncan, W. Unterberger, D. Kreikemeyer Lorenzo and D.P. Woodruff, "Does methanol produce a stable methoxy species on Ru(0001)?", submitted to Surface Science

- D.A. Duncan, F. Allegretti and D.P. Woodruff, "Water does dissociate on the perfect TiO_2 surface: a quantitative structure determination", submitted to Physical Review Letters

- D.A. Duncan, W. Unterberger, D.C. Jackson, M.K. Knight, E.A. Kröger, K.A. Hogan, C.L.A. Lamont, T.J. Lerotholi and D.P. Woodruff, "Quantitative structure determination of R,R-tartaric acid on Cu(110): Monotartrate and Bitartrate phases", to be published

A full publication list is shown in Appendix A.

David A Duncan March 2012

Abstract

Energy-scanned photoelectron diffraction was used to determine the local adsorption site of several molecular species on well defined single crystal surfaces.

Cytosine and uracil on Cu(110) were found to adsorb with their molecular planes perpendicular to the surface and mostly aligned along the close packed $[1\bar{1}0]$ direction. Both molecules were found to adsorb through their constituent oxygen atom(s) and a deprotonated nitrogen atom. The associated Cu-O and Cu-N bond lengths were found to be 1.94 (+0.06/-0.04) Å and 1.94 (+0.07 / -0.03) Å, respectively, for cytosine and 1.96 ± 0.04 / 1.93 ± 0.04 Å and 1.96 ± 0.04 Å, respectively, for uracil.

The mono- and bi- tartrate phases of tartaric acid on Cu(110) were found to adsorb via deprotonated carboxylic acid groups with the oxygen atoms in different near-atop sites. The associated Cu-O bond lengths were found to be 1.92 ± 0.08 Å / 1.93 ± 0.06 Å and 1.93 – 1.97 ± 0.06 – 0.09 Å respectively.

Glycine on Cu(111) was found to adsorb via both its nitrogen and oxygen constituent atoms, though three competing models were found for the local adsorption site of the oxygen atoms. The nitrogen atom was found to adsorb in a near-atop site with an associated Cu-N bond length of 2.02 ± 0.03 Å. The oxygen adsorption site was found to at least have some near-atop characteristics, with the near-atop site having an associated Cu-O bond length of 2.00 – 2.02 ± 0.04 – 0.07 Å.

Reanalysis of the C 1s PhD data of the hydrocarbon remnant from the decomposition of furan on Pd(111) found that the lowest energy model predicted by DFT does not occur, at least in large quantities, on the surface. The most likely structure was found to be CH–C–CH_2.

On the Ru(0001) surface, dehydrogenation of methanol was not observed in the temperature range around 150 K, with no evidence for the strong modulations in the O 1s PhD spectra predicted for a methoxy species.

A reexamination of water adsorption of the rutile TiO_2(110) surface found that water does, at least partially, dissociate on the perfect surface as well as at defect sites – in contrast to previously published experimental results. The associated Ti-O bond lengths for the resulting atop and bridging hydroxyl species were found to be 1.85 ± 0.08 Å and 1.94 ±0.07 Å respectively.

Finally vanadyl phthalocyanine was found to adsorb upright (with the oxygen atom further from the surface than the vanadium atom) on the Au(111) surface. The V=O bond length was found to be 1.60 ± 0.04 Å.

Abbreviations

- **ARUPS**: angle resolved ultraviolet photoemission spectroscopy
- **AFM**: atomic force microscopy
- **BESSY**: Berlin Elektronenspeicherring-Gesellschaft für Synchrotronstrahlung
- **DFT**: density functional theory
- **EDC**: energy distribution curve
- **eV**: electron volts
- **EXAFS**: extended X-ray absorption fine structure
- **FCC**: face centred cubic
- **FT-RAIRS**: fourier transform-RAIRS
- **HCP**: hexagonal close packed
- **HREELS**: high resolution electron energy loss spectroscopy
- **LEED**: low energy electron diffraction
- **ML**: monolayer
- **NE**: normal emission
- **NEXAFS**: near edge X-ray absorption fine structure
- **NI**: normal incidence
- **NIXSW**: normal incidence X-ray standing waves
- **PhD**: energy scanned photoelectron diffraction

- **PSO**: particle swarm optimisation
- **RAIRS**: Reflection absorption infrared spectroscopy
- **RAME**: reduced angular momentum expansion
- **STM**: scanning tunnelling microscopy
- **UHV**: ultra-high vacuum
- **UPS**: ultraviolet photoemission spectroscopy
- **VOPc**: vanadyl phthalocyanine
- **x**: cartesian coordinate, close-packed direction
- **XPS**: X-ray photoemission spectroscopy

Chapter 1

Introduction

1.1 General Introduction

Surface science has been an important field in the material sciences for over 40 years - with a large amount of cross disciplinary work between physics and chemistry[1–4] . Specific objectives of surface science would be a greater understanding of how heterogeneous catalytic reactions proceed (which could reduce industrial waste and the cost of products), and understanding the mechanisms of the inorganic/organic interface (which could lead to better design of medical equipment and implants). Being able to determine the structure (geometry) of these adsorbate / substrate systems in real world circumstances would allow a more rigorous approach to catalysis and pharmaceutical engineering, however, quantitative determination of these structures is beyond our (humanity's) current capabilities. Perhaps by understanding how these adsorbate / substrate systems work in model systems (in ultra-high vacuum (UHV) on near perfect single crystals) we can make some inferences on more realistic conditions and perhaps also explore the basic physical and chemical interactions between metals and non-metals.

Even within these ideal conditions there are few techniques that provide quantitative structural information of these adsorbate / substrate systems. One of the requirements in attempting to characterise a surface is to develop a probe that is surface sensitive. Typically electrons, which have small elastic and inelastic mean free paths, are used to provide surface specificity. As the electron has a small elastic mean free path it will interact on the scale (typically Ångströms) of the surface, however, as the inelastic mean free path is also short, electrons will not be able to penetrate through the bulk of a sample. Therefore surface sensitivity can be gained via injecting electrons into a sample (electrons in), via detecting electrons emitted from a sample (electrons out) or a mixture of both (electrons in / electrons out). However, as the electron-atom scattering cross-section is so large, electrons will only

travel a short distance in air ($\sim$ a μm) therefore most (though not all) electron based experiments must performed in UHV, in which the mean free path is much longer ($\sim$ a km). However the requirement of performing these calculations in UHV means that the calculation will not be performed in real life conditions. Further, these structural techniques that provide quantitative information typically require well ordered single crystals. Therefore it not clear that work performed in these ideal conditions will be representative of what happens in a catalytic environment. However, by studying the structure of these adsorbate systems and, specifically, by gaining quantitative information, we gain significant insight into how organic molecules interacts with inorganic matter. One specific area that quantitative structural determination can illuminate is what are the important forces in how and where molecules adsorb on a surface - for example it has shown that the adsorption site is not determined simply by element that interacts with surface but that elements of the same kind in different functional groups interact differently (e.g. Refs. [5, 6]), that the adsorbate-surface bondlength is only weakly affected by the strength of the interaction, but that (similar to metal-complexes) it is the bond order that is impotant (e.g. Ref. [7]), and that, even though the iteractions seems to be largely dominated by similar forces to that in metal-complexes, the termination of the surface still has a measurable affect (e.g. Ref. [5]). Further, by providing quantitative structural information these techniques provide an important test of the predictions made by density functional theory (DFT). With this in mind the sections of the work presented in this thesis will explore the effects of steric hinderance and increased complexity on the adsorption site and the adsorbate-substrate bond length, as well as looking at systems whose lowest energy geometric structure has been predicted by DFT. Perhaps by understanding what is and is not important to how

The benchmark technique, and the one that has the most solved structures to date, is quantitative low energy electron diffraction (LEED)[8–10]. In LEED (§3.2.1) a beam of low energy electrons is incident on a sample, and the backscattered component of the electron wave is detected in different directions. If there is some lateral ordering of the surface, diffraction peaks will appear in the backscattered signal and, as the energy (and therefore the wavelength) of the incident electron beam is varied, the intensity of the diffracted beams will also vary. It is this variation that can provide structural information. However, LEED requires that the adsorbate / substrate system has long range order which can, in many cases, be difficult or even impossible to achieve.

Similar in concept to LEED is the technique of energy-scanned photoelectron diffraction (PhD)[11, 12]. In PhD (§2) a core level electron is emitted from its bound state by light in the X-ray spectrum. A component of the electron wave will be directly emitted towards the detector, however, other components of the electron

wave will be elastically backscattered off the substrate (and adsorbate) atoms and will coherently interfere with the directly emitted component (see Fig. 1.1). As the energy of the incident light is varied, the kinetic energy (and therefore the wavelength) of the photoemitted electrons will vary - causing the different paths of the scattered electron waves to come into and out of phase with the directly emitted component.

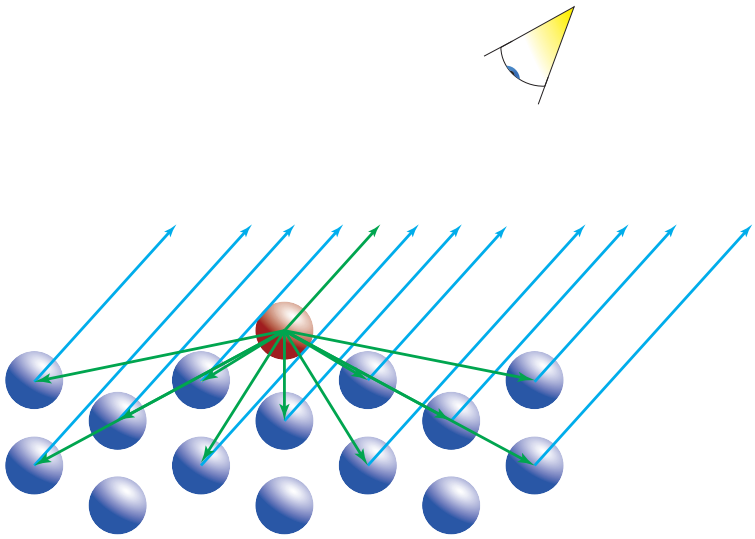

Figure 1.1: Schematic showing a simplified single scattering case with emission from the red atom and backscattering off the blue atoms.

The advantage of PhD is that whereas LEED has both the experimental source and detector at (effective) infinity, the source of electrons in PhD is local. As such, PhD does not require long-range ordering, only a well defined local adsorption site. As core level electron energy levels (which display significant binding energy shifts due to the chemical environment of the species) are utilised, the technique is not only elementally sensitive, but also chemically sensitive - allowing the structure of atoms of the same element in different chemical environments to be determined separately.

However, there are several limitations of PhD. Specifically, as with all quantitative structural techniques in surface science, theoretical modelling is necessary to gain quantitative information (§2) and the measurements must be performed in UHV. Additionally PhD requires a tunable light source (such as a synchrotron, §3.3.1) in the necessary energy range ($\sim$ 100-1000 eV).

In this work applications of the PhD technique to determine the local adsorption geometry of four different organic molecules adsorbed onto a low index Cu surface, and three unrelated systems are presented. Specifically, studies of the nucleobases uracil (§4.3) and cytosine on Cu(110) (§4.2), tartaric acid on Cu(110) (§4.4), and the amino acid glycine on Cu(111) (§4.5) will be explored in depth. The other systems – the hydrocarbon remnant of furan decomposition on Pd(111) (§5), Methanol on Ru(0001) (§6), hydroxyl decomposition product from water adsorption

on TiO_2(110) (§7) and vanadyl phthalocyanine (VOPc) on Au(111) (§8) – shall also be briefly described.

1.2 Organisation of the Thesis

The following chapter (§2) provides an in-depth discussion of the PhD technique, including the experimental method, data reduction, multiple scattering theory and global search algorithms. In the subsequent chapter (§3) an outline of the supporting surface science techniques which were employed in this work is described, as well as a general overview of synchrotron radiation and the UHV experimental chamber. Chapters 4 – 8 are concerned with the results for the systems presented within this thesis. Each chapter discusses the motivation for the work, details the work previously performed on these systems, provides specific experimental information, and presents the analysis interpretation of the results. Each of these chapters also contains a short conclusion. Finally chapter 9 contains an overall summary of the work presented within this thesis.

Chapter 2

Energy Scanned Photoelectron Diffraction

2.1 Introduction

This thesis is concerned with the quantitative determination of surface adsorbate structure. While multiple techniques are used to characterise the adsorbate systems (eg. X-ray photoemission spectroscopy (XPS) [§3.2.2], low energy electron diffraction (LEED) [§3.2.1]), provide qualitative structural information (eg. near edge X-ray absorption fine structure (NEXAFS) [§3.2.3]) or theoretically predict possible adsorbate structures (DFT [§3.2.4]), the single technique that provides the primary source of experimental quantitative structural information in this thesis is energy-scanned photoelectron diffraction, PhD[11][12]. This chapter provides an overview of the PhD technique, including the basic physics through which the technique arises, data acquisition and treatment procedures, a description of the multiple scattering calculations that are performed in order to gain structural information, and discussion of the search algorithms employed in the structure determinations.

2.2 Basic Background Theory

As mentioned in section 1.1 the photoelectron diffraction technique exploits the coherent interference of the directly-emitted component of a photoelectron wave-field from a core level of a surface atom, with the components of the same wave-field that are elastically backscattered by the nearby substrate atoms as shown in Fig 1.1. If the detection angle or the energy of the incident photons (and hence the kinetic energy / wavelength of the photo-emitted electrons) is varied, then the different components of the wave-field will come into and out of phase with respect to the directly emitted component, resulting in a modulation of the total electron yield at the detector.

Therefore, in a simplistic approach, the photoelectron diffraction can be seen as creating a photoelectron hologram of the local environment of the emitter atom, with the directly emitted component acting as the reference beam, and the scattered components acting as the object beam[11]. This implies that a simple Fourier transform of the photoelectron diffraction modulations would provide direct structural information. However, the electrons not only experience a scattering phase shift that has an angle and energy dependence, but also have a significant probability of having been scattered by multiple atoms before being detected, making such direct analysis impossible. In order to gain quantitative structural information it is, instead, necessary to adopt a trial and error method comparing the results of multiple scattering calculations to the experimental spectra. The multiple scattering theory and the assumed approximations for the calculations within this thesis are described in more depth later in this chapter (§2.4).

2.3 Data acquisition and reduction

In essence, the data acquisition of PhD consists of measuring multiple XP spectra (§3.2.2), referred to as energy distribution curve (EDC)s, at different photon energies. A typical raw PhD spectral data set is shown in Fig 2.1 as a function of of kinetic energy. Note that XP spectra are usually displayed using a binding energy ordinal, however, if PhD spectra were displayed in this manner all of the EDC's would be superimposed. To reduce the data each EDC is then fitted with a sum of a Gaussian distribution, a Gauss error function (a broadened step function) and a tilted template background. A Gaussian distribution is used to represent the line shape of the photoemission peak as the instrumental effects in the experimental equipment are considered outweigh the intrinsic lifetime broadening (which is a Lorentzian distribution) of the electron energy states, and the background is modelled by smooth template which span the whole kinetic energy range of the PhD measurement [13]. The intensities (specifically the product of the peak height and the peak width) of the Gaussian distributions are then plotted as a function of kinetic energy, $I(E)$, and are also used to define a stiff spline, $I_0(E)$, as shown in Fig 2.2. This spline represents the non-diffractive contributions to the photoemission intensity. The experimental photoelectron diffraction modulations, $\chi(E)_{exp}$, are then calculated by,

$$\chi(E)_{exp} = \frac{I(E) - I_0(E)}{I_0(E)}. \tag{2.1}$$

Note that, unlike the absolute electron yield detected in XPS, the values of $\chi(E)_{exp}$ are not arbitrary, but instead represent the fractional contribution of the diffractive effects to the photoemission spectrum.

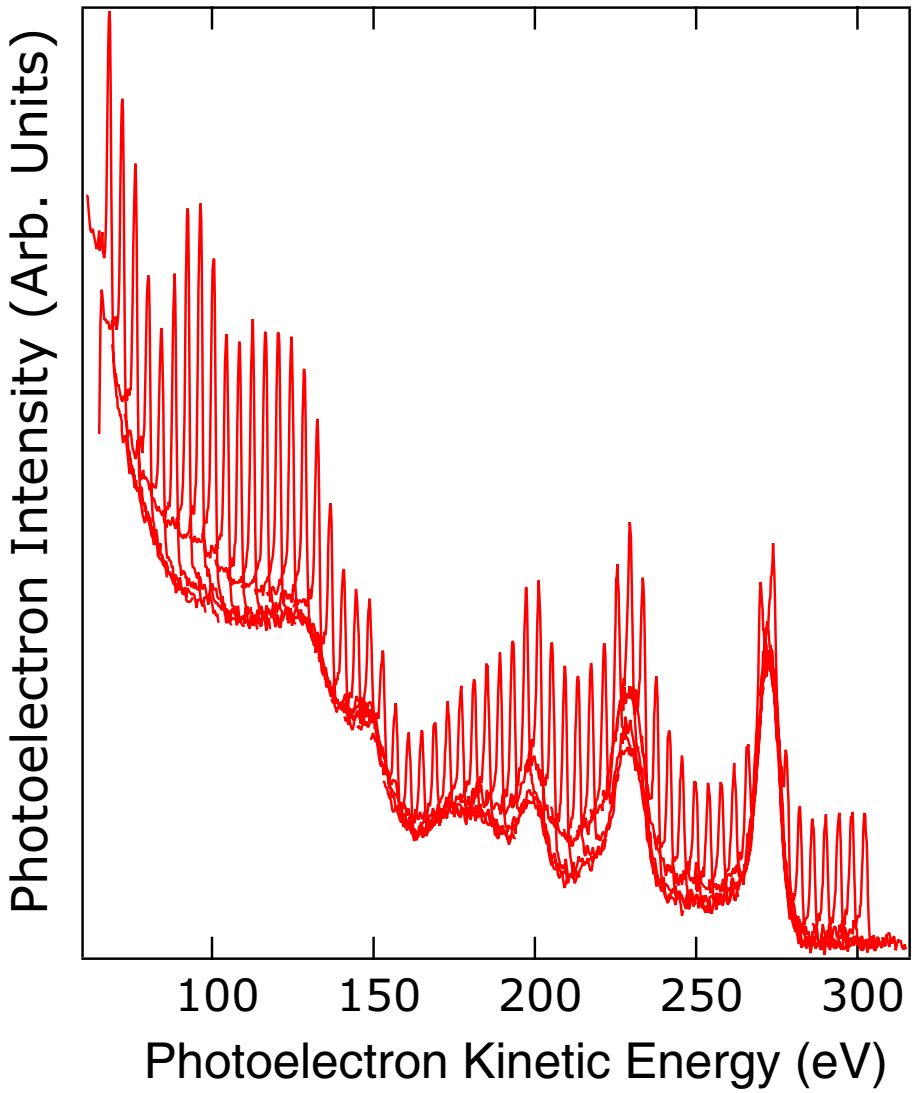

Figure 2.1: Sample raw O 1s PhD spectrum, measured in the normal emission direction for oxygen on Ru(0001). Note that the peaks present in the background intensity are due to Ru Auger emission.

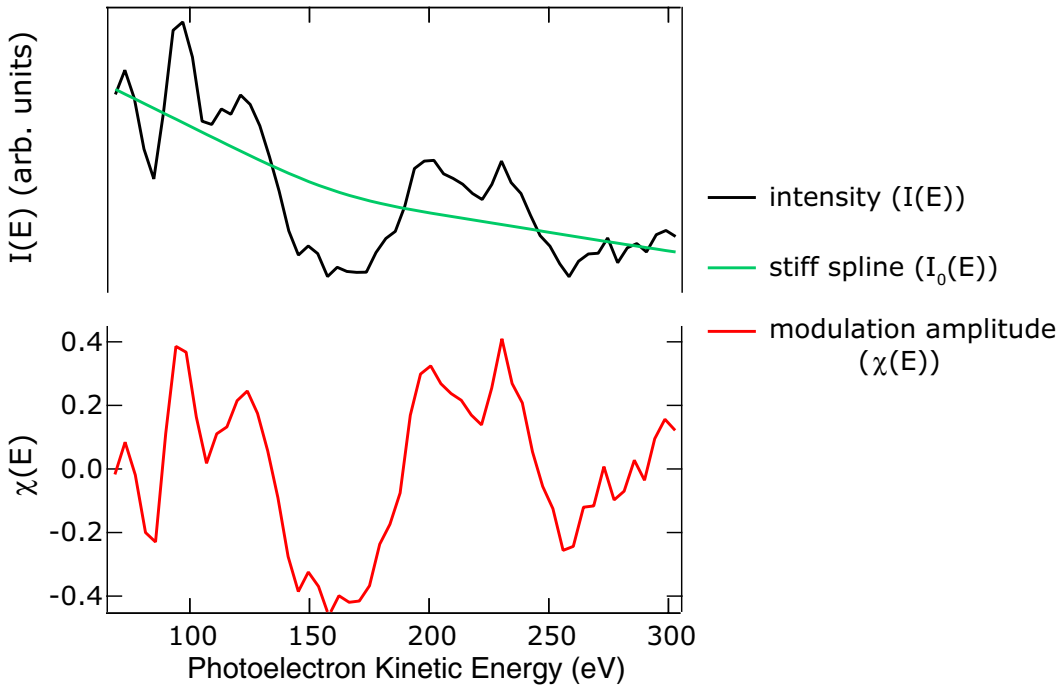

Figure 2.2: Sample peak intensity spectrum (black) reduced from the data shown in Fig 2.1, with a fitted smooth spline (green) and the resulting modulation amplitudes (red) as calculated by equation 2.1.

As PhD is a core electron technique, it provides structural information that is not only elementally sensitive, but is also chemically sensitive. Specifically if an adsorbed species has multiple atoms of the same element that are in chemically different environments [i.e. bonded to atoms of differing electronegativity, species in different bonding enviroments (e.g. double bonding instead of just single bonding)], then there will be a so called "chemical shift" in the EDC / XP spectrum. If this shift is large enough (typically $>\sim 1eV$) then it is generally possible to separate the photoelectron diffraction modulations, as shown in Fig 2.3.

In order to gain quantitative information from the PhD technique it is necessary to simulate theoretically the modulations, but it is possible to gain some qualitative information from inspection of the experimental data. In particular, if a measurement is made in an emission direction such that there is a strongly-scattering nearest neighbour in a 180° backscattering geometry with respect to the emitter and the detector (see Fig. 2.4), then the PhD spectra are normally dominated by a strong long period modulation. Similarly if the emitter atom lies in a high symmetry site (atop, hollow or, to a lesser degree, bridging) then the resultant modulations are expected to be significantly stronger ($\sim>$ 30%) than those originating from a low symmetry site ($\sim<$ 20%).

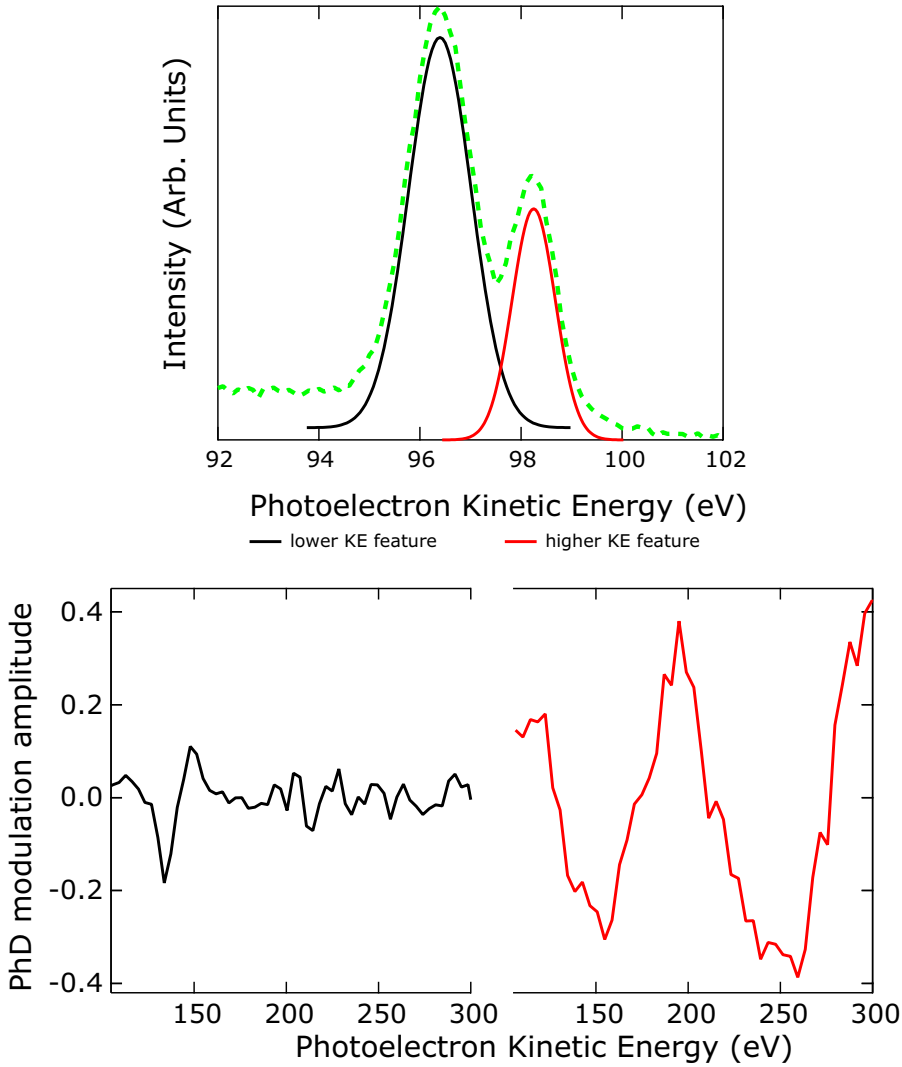

Figure 2.3: Example of a chemical shift in PhD. The top figure is the N 1s XP spectrum from uracil on Cu(110) taken in the normal emission direction (green dashed lines). It has lower (black solid line) and upper (red solid line) kinetic energy features relating to two different nitrogen species in different chemical environments; in other words the spectrum is displaying a chemical shift. The bottom figure shows the two PhD spectra (in the same measurement geometry) that arise from the two separate nitrogen components indicating that the two species are clearly in different local geometries.

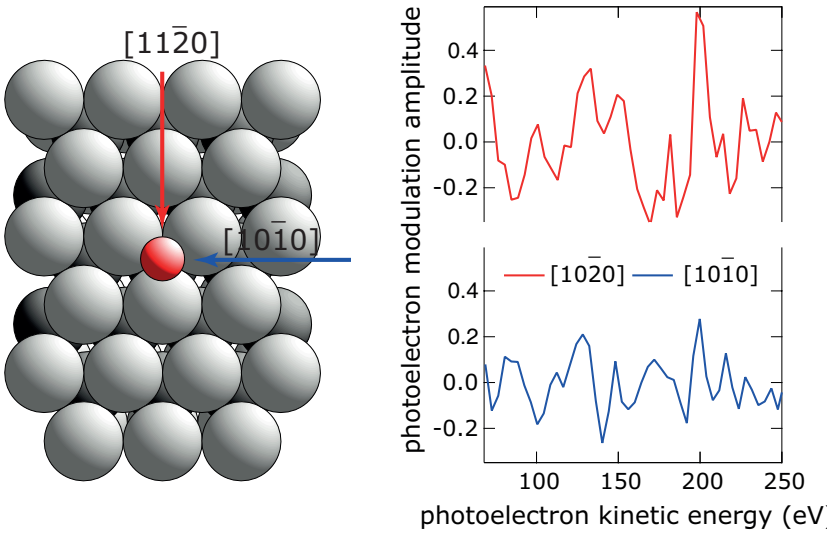

Figure 2.4: Example PhD spectra measured in the two different azimuths of the same surface. On the left is the schematic of the determined adsorption site of O/Ru(0001) (§6.3.2) with an annotation of the two main crystallographic directions, [10$\bar{1}$0] and [10$\bar{2}$0]. On the right are the experimental O1s PhD spectra measured in those two main crystallographic azimuths at an emission angle of 30° with respect to the surface normal. In the direction where there is a direct 180° backscatterer, strong long period modulations are observed. In the direction where there is no such backscatterer no (or at best weak) modulations are observed.

2.4 Multiple scattering theory

As mentioned in section 2.2, to gain quantitative structural information from PhD, it is necessary to calculate theoretically predicted PhD modulations using trial models. The computer codes used within this thesis were developed by Fritzsche[14–20] and this section describes this code and its approximations. The intensity of the electrons, at the detector, $(I(E)_{the})$ is modulus squared of the photoemitted electron wavefunction $(\Psi(E,r))$,

$$I(E)_{the} = |\Psi(E,r)|^2, \tag{2.2}$$

$$\Psi(E,r) = \int \mathrm{d}^3 r'\, G\,(r,r',E)\,\mathbf{E}\cdot p\,\Psi_0(r'), \tag{2.3}$$

where E is the photoelectron energy inside the crystal, $\mathbf{E}$ is the vector potential of the photon field, p is the momentum operator, r is the position of the detector, $\Psi_0(r')$ is the wave-function of the excited core level energy state and $G\,(r,r',E)$ is the Green's function of the total system [18]. The Green's function can be expanded into a summation over all scattering pathways, such that the total wave function becomes

a sum of partial wave-functions, ψ_j,

$$\Psi(E,r) = \sum_j \psi(E,r)_j, \tag{2.4}$$

The zeroth term of equation 2.4 is generally taken to be the directly emitted component of the wavefield ($\psi(E,r)_0$). The wave function of this component is a sum over all possible initial to final state combinations of the photoelectron. This component is specifically dependent on the azimuthal angular momentum (l) and magnetic quantum number (m) of the initial state - note there is no dependency on the principal or spin quantum number. The number of allowed transitions is limited by the dipole selection rules for the final state (l_f and m_f),

$$l_f = l \pm 1, \tag{2.5}$$

$$m_f = m, m \pm 1. \tag{2.6}$$

By space quantisation, for any given value of l there are $2l+1$ degenerate m states. Using the above selection rules, for any initial state l there are $6l+3$ and $6l-3$ possible transitions corresponding to $l_f = l+1$ and $l_f = l-1$ respectively (note, $l = 0$ - the s-energy level - is the exception to this rule as there are no possible $l-1$ states).

Therefore $\psi(E,r)_0$, using propagating spherical waves[16], becomes[21],

$$\psi_0(E,r) = 4\pi i^l A \sum_{m_f} \sqrt{2l_f - 1}\, C_{(l,ml,l_f,m_f)} \cdot D^{\theta_E,\Theta_{azi}}_{(1,m_f,l_f)}, \tag{2.7}$$

$$A = \frac{\exp\left(\sqrt{\frac{\sqrt{((E_{ana}+V_0)^2+V_i^2)}}{a_{Ryd}}} \cdot \sin\left[\frac{1}{2}\tan^{-1}\left(\frac{V_i}{E_{ana}+V_0}\right)\right] \cdot (Z_e - Z_{OF})\right)}{\cos(\theta_E)}, \tag{2.8}$$

$$\cos(\theta_E) = \sqrt{1 - \frac{E_{ana}}{B^2 a_{rydb}} \sin^2(\theta_{polar})} \tag{2.9}$$

$$B = \sqrt{\frac{\sqrt{(E_{ana}+V_0)^2 + V_i^2}}{a_{rydb}}} \cos\left[\tan^{-1}\left(\frac{1}{2}\frac{V_i}{E_{ana}+V_0}\right)\right] \tag{2.10}$$

$$C_{(l,ml,l_f,ml_f)} = R_{l\to l_f} e^{i\delta_{l_f}} \left(D^{\theta_{polar},\Theta_{azi}}_{(0,m_f,l_f)}\right)^* \int \mathrm{d}\Omega\, Y_{l_\gamma,m_\gamma} Y_{l,m} Y_{l_f,m_f}, \tag{2.11}$$

where E_{ana} is the mean photoelectron kinetic energy as would be measured on detection at the analyser, V_0 and V_i are the real and imaginary part of the optical potential respectively, Z_e and Z_{OF} are the z height above the substrate surface of the emitter atom and the vacuum point where the summation of all the different paths is performed (respectively), a_{Ryd} is the Rydberg unit of energy in eV, $R_{l\to l_f}$ is the radial dipole matrix element for the transition between l and l_f, δ_{l_f} is the scattering phase shift for the emitter, Y_{lm} is the spherical harmonic for the energy state defined by l and m (where l_γ and m_γ are the angular and magnetic moment of the incident radiation), * signifies the complex conjugate, θ_{polar}, and Θ_{azi} are the polar and azimuthal angles (respectively) between the surface normal and the detector, and the orientation of the simulated cluster and the photon polarisation vector (respectively) and the D matrix contains the coefficients that describe the free electron propagator in a two-centre angular momentum expansion[16]. The integrand of equation 2.11 is computed using the Gaunt coefficients[22, 23]. The formulae for numerically calculating the D matrix and the Gaunt coefficients are shown in appendices B and C respectively.

The subsequent terms of equation 2.4 that refer to scattering pathways with only the single scattering event must be summed over all the possible final excitation states, l_f, m_f, and all possible scattered energy states l_s, m_s. However, the scat-

tering phase shifts, δ_{l_s}, for higher angular momenta tend towards zero. Therefore, using the reduced angular momentum expansion (RAME)[14], the maximum calculated scattering azimuthal angular momentum number, l_{max}, is defined by a suitably small cutoff value in the phase shift, such that any l_s value that has a corresponding scattering phase shift smaller than this value is ignored in the calculation[14]. The maximum magnetic quantum number calculated, m_{max}, can be similarly curtailed. As the scattering Green's function is $\propto \frac{1}{r^{m_s}}$[16] scatterers at a larger distance from the emitter atom require fewer calculated magnetic quantum numbers. In practice magnetic quantum numbers greater than $|m_s| = 2$ are rarely required.

Therefore the single scattered wavefield components become, $\psi_1(E,r)_j$:

$$\psi_1(E,r)_j = \sum_{l_s=0}^{l_{max}} A \cdot e^{ir_aB} \cdot i^{-l_s+1} \cdot \sqrt{2l_s+1} \cdot T(l_s) \cdot C_{1(l_s,l,m_\gamma)}, \tag{2.12}$$

$$C_{1(l_s,l,m_\gamma)} = \sum_{m_s=-m_{max}}^{m_{max}} D^{\theta_B,\theta_A}_{(0,l_s,m_s)} \cdot \sum_{m=-l}^{l} \sum_{m_\gamma=-1}^{1} C_{LP(m_f,l_f,m_\gamma,l,m)} \cdot D^{\theta_C,\theta_D}_{(m_s,m_f,l_f)} \cdot G_{l_s,l_f,m_s}, \tag{2.13}$$

$$m_f = m + m_\gamma,$$

$$C_{LP(m_f,l_f,m_\gamma,l,m)} = R_{l\to l_f} \cdot e^{i\delta_l} \left(D^{\theta_{polar},\theta_{azi}}_{(0,l,m)}\right)^* \cdot G_{l_s,l_f,m_s} \int \mathrm{d}\Omega \, Y_{l_\gamma,m_\gamma} Y_{l,ml} Y_{l_f,ml_f}, \tag{2.14}$$

where $\theta_{A,B}$ are (respectively) the polar and azimuthal angle of the angle between the scatterer–detector vector and the z-axis / surface normal, $\theta_{C,D}$ are (respectively) the polar and azimuthal angle between the emitter and the scatterer, A and B are as defined in equations 2.8 and 2.10 (respectively), r_a is the distance between the emitter and the scatterer, $T(l_s)$ is a function of the complex scattering phase shifts of the scattering atom, and takes into account the thermal vibrations and G_{l_s,l_f,m_s} are the scattering Green's function. The formulae for the $T_{(l)}$ matrix and the scattering Green's function are shown in appendices D and E.

For higher order scattering paths, for which the electron path contains two or more scattering events, the calculations are as for single scattering, but with the l_f

and m_f values taking the same range of values as l_s and m_s such that:

$$\psi_n(E,r)_{j,...k} = \sum_{l_s=0}^{l_{max}} A \cdot e^{ir_aB} \cdot i^{-l_s+1} \cdot \sqrt{2l_s+1} \cdot T(l_s) \cdot C_{n(l_s,l_f,m_f)}, \tag{2.15}$$

$$C_{n(l_s,l_f,m_f)} = \sum_{m_s=-m_{max}}^{m_{max}} D^{\theta_B,\theta_A}_{(0,l_s,m_s)} \cdot \sum_{l_f=0}^{l_{max}} \sum_{m_f=-m_{max}}^{m_{max}} C_{n-1(l_s,l_f,m_f)} \cdot D^{\theta_D,\theta_C}_{(m_s,m_f,m_f)} \cdot G_{l_s,l_f,m_s}, \tag{2.16}$$

$$\tag{2.17}$$

where $\psi_n(E,r)_{j,...k}$ is the wavefunction of scattering order n, $(j,...k)$ denote which atoms acted as scatterers and C_{n-1} is the C value calculated for scattering order $n-1$, A and B are as defined in equations 2.8 and 2.10 (respectively), $\theta_{A,B}$ are (respectively) the polar and azimuthal angle between the current- (nth-) scatterer–next- ($n+1$th-) scatterer vector and the z-axis / surface normal, and $\theta_{C,D}$ are (respectively) the polar and azimuthal angles between the current- (nth-) scatterer–previous- ($n-1$th) scatterer vector and the z-axis / surface normal. For the exact solution all possible scattering pathways, starting at the atom where the electron is photo-excited and terminating at the vacuum height Z_{OF}, must be considered. In even a single scattering approximation, this would be prohibitively difficult to calculate as the substrate is effectively infinite; when higher ordering scattering is included this problem increases exponentially (in a cluster of 100 atoms there are 10,000 possible double scattering paths and 1,000,000 triple scattering paths). However, the modulating contribution of each scattering pathway has a period that is inversely-proportional to the path length; as such longer path lengths result in higher frequency modulations. Therefore the experimental reality of finite energy and angular resolution will average out the modulations of these long path lengths. Similarly, due to the large inelastic scattering cross-section of electrons, the contributions to the scattered electron intensity will decrease exponentially with distance. Therefore only scattering pathways within a certain distance need to be considered. The finite energy and angular resolution will also smooth the theoretically calculated intensity, as small energy differences due to experimental broadening will cause small incoherent phase differences, such

that[18]:

$$I(E) \propto \sum_{i,j} \psi_j^*(E)\Phi_i(E) \cdot f_{Gauss} \cdot f_{Lorentz}, \tag{2.18}$$

$$f_{Gauss} = \exp\left[-\sqrt{\frac{m}{8\hbar^2 E \ln 2}}\left(E_b(R_i - R_j)\right)^2\right], \tag{2.19}$$

$$f_{Lorentz} = \exp\left[-\sqrt{\frac{m}{2\hbar^2 E}}E_b|R_i - R_j|\right], \tag{2.20}$$

where the summation is over all possible combinations of pathways i and j, E_b is the energy broadening, f_{Gauss} is the Gaussian broadening from the analyser and monochromator and $f_{Lorentz}$ is the Lorentzian broadening from the instrinsic life-time broadening of the orbital. In practice it is considered sufficient to expand equation 2.4 to include the $\sim$ 2000 shortest single, and the $\sim$ 1000 shortest double and triple scattering pathways.

The amplitude of the result of this summation is then used to define a smooth spline in the same manner as the experimental data are treated. This smooth spline is then subtracted from the amplitude and used to normalise it, similar to the treatment of the experimental data in equation 2.1 to get the theoretical χ, $\chi_{theory(E)}$.

Performing these calculations is moderately computationally intensive, with each modulation spectra taking $\sim$90 seconds to calculate - and each structural calculation will involve 10s to 100s of these calculations depending on the number of contributing emitters, symmetrically identical domains, and multiple measurement directions. Further each structure determination will require thousands of structures to be trialled - if these calculations are performed in serial, then months of real time is needed to perform the simulations. However, the modulation spectra from each of these emitters, domains and directions are independent of each other – the result of the calculations for one is not required to calculate the other – therefore the calculation is very parallelisable in that these calculations can be spread over multiple computer processors. Therefore, with enough computational resources available, though the calculation will still take significant computational time, the real time requirement is drastically slashed.

2.5 Goodness and certainty of fit

In order to have a measure of the level of agreement between theoretical calculations to the experimental data, and therefore to enable quantitative structure determination, a goodness of fit parameter is employed. Specifically a reliability, or R-factor, similar

to that developed by Pendry [24] for LEED, is used:

$$R_{fac} = \frac{\sum \left(\chi_{exp(E)} - \chi_{theory(E)}\right)^2}{\sum \left(\chi^2_{exp(E)} + \chi^2_{theory(E)}\right)}. \tag{2.21}$$

This is defined such that an R-factor of 0 corresponds to perfect agreement, 1 corresponds to uncorrelated data and 2 corresponds to anti-correlated data. Using this R-factor provides an objective measure of fits that look qualitatively similar. This then raises the question of how significant a difference in R-factor qualifies as a statistically significant change. To assess this a variance of the R-factor is defined (similar to that defined by Pendry for LEED) based on the amount of experimental information available:

$$\mathrm{var}\left(R_{min}\right) = R_{min}\sqrt{\frac{2}{N}}, \tag{2.22}$$

where R_{min} is the lowest found R-factor and N is the number of independent pieces of information contained in the experimental spectra [25]. Pendry[24] argues that N is the number of discrete peaks which *could* possibly appear in the energy range (δE) of the spectra. Note that N is *not* the number of peaks which do occur within the spectra, as the absence of a peak provides as much structural information as the presence of a peak. Therefore the intrinsic limitation of the number of peaks is the intrinsic width of these peaks. In LEED the intrinsic peak width is determined by the imaginary part of the inner potential (V_i) which defines the inelastic electron scattering damping length. In PhD, the intrinsic peak width is similarly limited by the inelastic scattering mean-free-path, but also by an energy broadening (E_b term like that introduced in equation 2.19 as the broadening due to experimental limitations also limits the smallest resolvable feature. As these two effects are uncorrelated they must be summed in quadrature. Therefore an estimate of N in PhD is given by:

$$N = \frac{\delta E}{4\sqrt{V_i^2 + E_b^2}}. \tag{2.23}$$

Typically V_i and E_b are estimated to have values of 5 eV[25].

Any structure with a R-factor that is within the variance of R_{min} is considered to be within one standard deviation of the best fit structure. Therefore, by varying any structural parameter until the R-factor exceeds $R_{min}+\mathrm{var}\left(R_{min}\right)$, the uncertainty in the structural parameters of the best-fit structure can be defined. Similarly secondary minima, which have R-factors greater than $R_{min} + \mathrm{var}\left(R_{min}\right)$ can be formally excluded.

2.6 Comparison of global search algorithms

Having defined a goodness of fit parameter, the structural optimisation becomes an R-factor minimisation problem. In order to optimise structures that are "mostly" correct, a linear gradient search can be implemented. Specifically a Levenberg - Marquadt algorithm[26] is used within the work presented within this thesis.

However, a gradient search, if trapped within a local minimum, will never find the global minimum. Therefore, identifying the most promising regions of the multidimensional parameter hyperspace, that might contain the global minimum, is a problem that may be addressed by some form of global search algorithm.

So far the only attempt to apply global search algorithms to photoelectron diffraction appears to be that of Viana et al. [27] using a genetic algorithm, with applications to structure determinations for Pd on Au(111) [28], for the termination of the $SrTiO_3$(100) surface [29], and for chromium oxide on Pd(111) [30]. Rather more exploration of such methods has been undertaken in LEED, including applications of genetic algorithms [31] and fast simulated annealing [32], amongst other techniques [31, 33, 34].

As part of our ongoing programme of application of the PhD method a rather different approach has recently been implemented, using particle swarm optimisation (PSO) [35, 36], a more recently-developed heuristic algorithm that has rarely been exploited in the physical sciences. In order to gauge the efficacy of this optimisation routine it was tested against an implementation of two more established global search algorithms, namely the genetic algorithm [27] (GA) and fast simulated annealing (FSA) [32]. The performance of these three algorithms was also compared with that of a purely random sampling of the parameter hyperspace. The results of these tests are presented in this section. The three heuristic algorithms considered here share a common general strategy in that each proposes a structure whose fitness is then calculated, before new structures are generated stochastically. The techniques vary in how the new structures are generated and in the criterion used for accepting a new structure.

Note that while global search methods are designed to provide a means to find regions of parameter space corresponding to the lowest R-factor value (the best fit between theory and experiment), this purely mathematical procedure must be tempered by physical information. For example, it is perfectly possible for the best fit to correspond to physically unreasonable values of the associated parameters, such as interatomic distances that are too short or (if between bonded atoms) too long; previous examples of this effect in photoelectron diffraction are present in the literature (e.g. [37, 38]) and are also discussed in chapter 5. In applying the global search algorithms, therefore, it is important to impose physically reasonable constraints on

the trialled structures.

2.6.1 Stochastic Algorithms

In the implementations of all three algorithms (as well as the random sampling) that were used in this study, there are several parameters that were kept constant. Specifically each algorithm has "individuals" with a set of specific coordinates in the variable hyperspace (X(i)) defining a particular structural model, and each calculation had 40 individuals making up the calculation's "population". In the tests reported in this section each individual performs 20 iterations per calculation, and ten calculations were performed for each algorithm, so 8000 structures were investigated using each algorithm. In the case of the fast simulated annealing and the random sampling, in which no information is shared between individuals, the population is arbitrary, but this constant number was used for each algorithm in order to make the calculations more comparable. The population size will, however, have a significant effect on both the genetic algorithm and particle swarm optimisation presented in this study. Generally, for both techniques, a larger population will provide a better sampling of the variable hyperspace at the cost of longer computational calculating times and a slower convergence on "good" structures. A population of 40 individuals was chosen in order to provide a reasonably large population. In all cases the initial structures for the search were chosen randomly from the variable hyperspace. The random number generator used was the intrinsic FORTRAN command, with the seed chosen by summation of the rank number of each individual (from 0 to 39) and the hour, minute, and second that the calculation was started.

The details of the FSA and GA codes used within this study are described in more detail by Duncan et al [39], however, the PSO is explained in detail here as it was used in several of the structure determinations presented within this thesis.

Particle swarm optimisation is inspired by the search patterns employed by swarming species; the individual members of the swarm share information to guide the collective towards the "best" area. Specifically, in PSO, each individual has memory. It remembers the best fit that it has achieved ($X(i)_l$), and the best fit that it has been informed of ($X(i)_g$). These two sets of information (the best locally found structure, and the best globally found structure) are then used to determine the location in the variable hyperspace that the individual will occupy in the next iteration:

$$V_{X(i)} = c_p \cdot P_p \cdot V_{X(i)} + c_l \cdot P_l \cdot dX(i)_l + c_g \cdot P_g \cdot dX(i)_g, \tag{2.24}$$

$$dX(i)_l = X(i)_l - X(i), \tag{2.25}$$

$$dX(i)_g = X(i)_g - X(i), \tag{2.26}$$

where $V_{X(i)}$ is how much variable i is going to change by in the next iteration (the velocity of the particle), $X(i)$ is the current set of coordinates of the individual, $X(i)_l$ is the set of coordinates of the best structure the individual has found so far, and $X(i)_g$ the set of coordinates of the best structure that the individual has been informed of. The c prefactors are weighting factors which will be discussed below, while the P prefactors take random values between zero and one.

The first term of equation 2.24 can be thought of as the momentum of the individual, and determines the tendency of the individual to continue searching in the region it currently occupies. If the weighting of this term is too high the population will simply diverge and randomly sample the variable hyperspace, but if it is too low the population may prematurely converge on a local minimum. Typically, values of $c_p < 1$ prevent the system from diverging, and a value of 0.7 was used in all PSO calculations presented in this thesis[35].

The second term of equation 2.24 determines the tendency of an individual to return towards the best structure that it has found and is generally given equal weighting to the third term of equation 2.24, which defines the tendency of the individual to move towards the best structure it has been informed of. As the best location that has been found is not necessarily the global minimum, the balancing of these two "best" locations allows a more thorough search of the parameter space around multiple minima. There are two considerations defining appropriate choice of the values of c_l and c_g. One is that it is important to use a value greater than unity, so that there is no preference to explore only the "near side" of the best minima that have been found. However, it is also important that the system does not take steps over the variable hyperspace that are too large, otherwise the search will effectively become completely random. In the studies presented in this thesis, a value of 1.9 was used for both c_l and c_g, allowing a significant overshoot of the best minima that have been found to occur, but no steps were allowed that were greater than $\frac{1}{4}$ of the difference between the maximum and the minimum values allowed for that coordinate [35]. The calculation was also prevented from going beyond preset maximum and minimum values for each coordinate; if the application of equation 2.24 took a coordinate outside these preset limits, the coordinate was instead set to relevant limiting value.

The significant property of the PSO approach, referred to above, is how information passes between individuals after each iteration. Each individual is informed by K other particles of the best minima they have found. Which individuals act as informants is chosen randomly. An informant is not necessarily informed by this in-

formee, so any given individual could act as an informant to less than, or more than, K individuals. A large value of K may cause the PSO to converge prematurely, but if the value of K is too small, the knowledge of the best areas for optimisation will not be spread effectively through the population. In this thesis a value of K=3 was used [35].

2.6.2 Model Systems

Experimental data from three model adsorption systems were used to test the efficacy of the fitting algorithms. The three systems chosen, as outlined below, provide examples of problems having different degrees of complexity and difficulty. From the point of view of the PhD technique, the data from molecular H_2O adsorbed on TiO_2(110) [40] correspond to the simplest situation. The H atoms are such weak electron scatterers that they are effectively invisible to the technique, so the structural problem is only to identify the O atom adsorption site using O 1s PhD data. Moreover, the experimental data show relatively strong ($\pm$40%) modulations in one (normal) emission direction, indicating a high-symmetry (atop) adsorption site. The original published analysis of the data did find the oxygen atom of the water (O_w) to be directly atop the five-fold coordinated surface Ti atoms (Fig 2.5), with a Ti-O_w bond length of 2.21 $\pm$ 0.02Å, but also found four different substrate surface relaxations to be significant, involving displacements perpendicular to the surface (Δz), and parallel to the surface in the $[1\bar{1}0]$ direction (Δx). Specifically, the z coordinate of the five-fold coordinated Ti atom, the x and z coordinates of the first layer planar O atoms, and the z coordinate of the bridging O atom below the five-fold coordinated Ti atom, were all found to differ significantly from those of an ideal bulk-terminated solid. In the present study these five structural parameters, namely the Ti-O_w bondlength and the four significant coordinate changes noted above, were therefore allowed to vary.

The second system tested, adsorption of SO_2 on Ni(111), originally solved by Knight et al. [41], is more complex. In this case PhD data from both S 2p and O 1s emission were recorded, showing modulation amplitudes of $\sim$ 20% or less. However, the molecular adsorption geometry was assumed to retain some of the symmetry of the molecule and the underlying surface, specifically with the molecule and surface sharing a mirror plane. In the original analysis of these data Knight et al. explored two such models, one in which the mirror plane of the molecule coincides with a true $[2\overline{11}]$ mirror plane of the complete (111) substrate, the other in which the molecular mirror plane lies in a $[1\bar{1}0]$ azimuth that corresponds to a mirror plane of the outermost metal layer alone. The former geometry was found to be preferred, with the molecule approximately centred over hollow sites, with equal occupation of the hcp and fcc hollow sites, directly above second and third layer Ni atoms, respectively (Fig 2.5).

In the present test of the global search algorithms only structures consistent with this correspondence of molecule and substrate mirror plane, and co-occupation of the two hollow sites, were investigated. In these searches a total of 10 parameters were allowed to vary, specifically the inner potential, the vibrational amplitude of the adsorbate, the z coordinate of the molecule above the surface, the displacement of the sulphur group along the $[2\overline{11}]$ azimuth, the S-O bondlength, the O-S-O bond angle, the difference in the z coordinates of the S and O atoms and the difference in z coordinates of the molecule above the fcc and hcp hollows.

Data from CN on Cu(111), presented in a study by Polcik et al. [42], provides a particularly challenging test of any structural search procedure. Both C 1s and N 1s PhD modulation spectra were measured, but these all show very weak modulations ($\sim 10\%$), consistent with the CN adsorption geometry completely lacking any of the point-group symmetry elements of the substrate. The original analysis of Polcik et al. led to the conclusion that the CN species adsorbs in an asymmetric off-atop geometry (Fig 2.5). Additional experimental data (notably near-edge X-ray absorption fine structure) shows the adsorbed molecule to be intact with the C-N axis approximately parallel to the surface, while the fact that the PhD spectra from the constituent C and N atoms show similar periodicity and modulation amplitudes indicate that they are likely to be in similar sites. We have therefore constrained the trialled structures to those in which the molecular axis is approximately parallel to the surface, with the distance between the C and N atoms being comparable to that of the gas phase cyanide species. Eleven parameters were allowed to vary; these were the three Cartesian coordinates of the centre of the molecule, the C-N bondlength, the azimuthal and tilt angles of the molecular axis relative to the surface, the relaxation of the first layer of Cu atoms, the inner potential, and the (isotropic) vibrational amplitudes of the C, N and the Cu atom that is nearest the C and N atoms.

2.6.3 Results of simulations

A comparison of the progress of the three fitting algorithms, and the random sampling, in finding structures of lower R-factor in successive iterations, is shown in Fig. 2.6 for each of the three models systems. These results are the average of 10 separate calculations, with the error bars indicating the standard error of the mean for each iteration. The FSA implementation clearly performs very poorly, being substantially inferior to random sampling for all three test systems. The inherent problems with the FSA implementation used in this trial are discussed elsewhere [39].

Of the other two fitting algorithms, the PSO achieves the lowest R-factors for all the model systems, although its advantage over GA is marginal for $TiO_2(110)/H_2O$ and modest for the Cu(111)/CN system. PSO outperforms the random sampling for

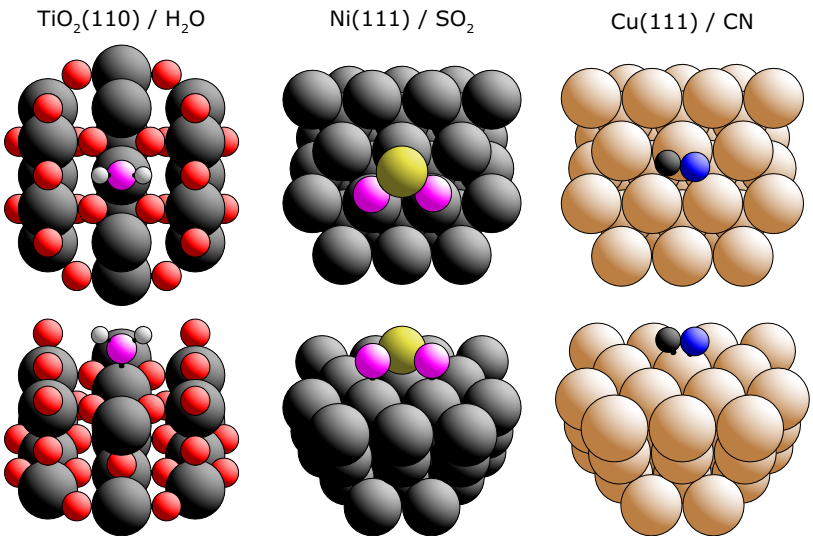

Figure 2.5: Schematic diagrams (in plan and perspective views) of the structures previously determined by PhD of $TiO_2(110)/H_2O$, $Ni(111)/SO_2$, and Cu(111)/CN. Substrate metal atoms are shown as the largest spheres, while the radii chosen to represent other atoms increase with increasing atomic number in individual structures from H to C, N, O and S. Note that in the $TiO_2(110)/H_2O$ structure the O atom of the water is shown in a different colour (shading) from that of the bulk substrate O atoms.

all three model systems, while GA marginally fails to achieve this for the Cu(111)/CN system. The Cu(111)/CN system was identified as the most complex problem to solve, with the largest number of fitting parameters and an expectation that even the best R-factor minimum will be shallow in the variable hyperspace; as such, the limitation of 20 iterations (800 trialled models) used here is unlikely to be sufficient to find the bottom of the global minimum. The fact that both the PSO and GA implementations show a slight downwards gradient at the end of the test supports this view. Indeed, in the applications of the PSO in the following chapters more than 20 iterations were always used to achieve more reliable convergence, but this smaller number of iterations appears sufficient to show the general trends of the different methods.

While the results of Fig. 2.6 provide information as to which algorithm finds the lowest R-factor in the smallest amount of computational time, a further important question is whether the structures corresponding to the lowest R-factor values are the correct structure. Have the searches identified the region of variable parameter hyperspace corresponding to the true global minimum, and have they located the bottom of this global minimum? The first of these two questions is the most important one. A steepest gradient search will locate the true extrema of the minimum far more quickly that any of these algorithms if it is started within the global minimum, but if a gradient search is initiated with a structure corresponding to a local minimum, it will not escape it. The important question is therefore whether the global search

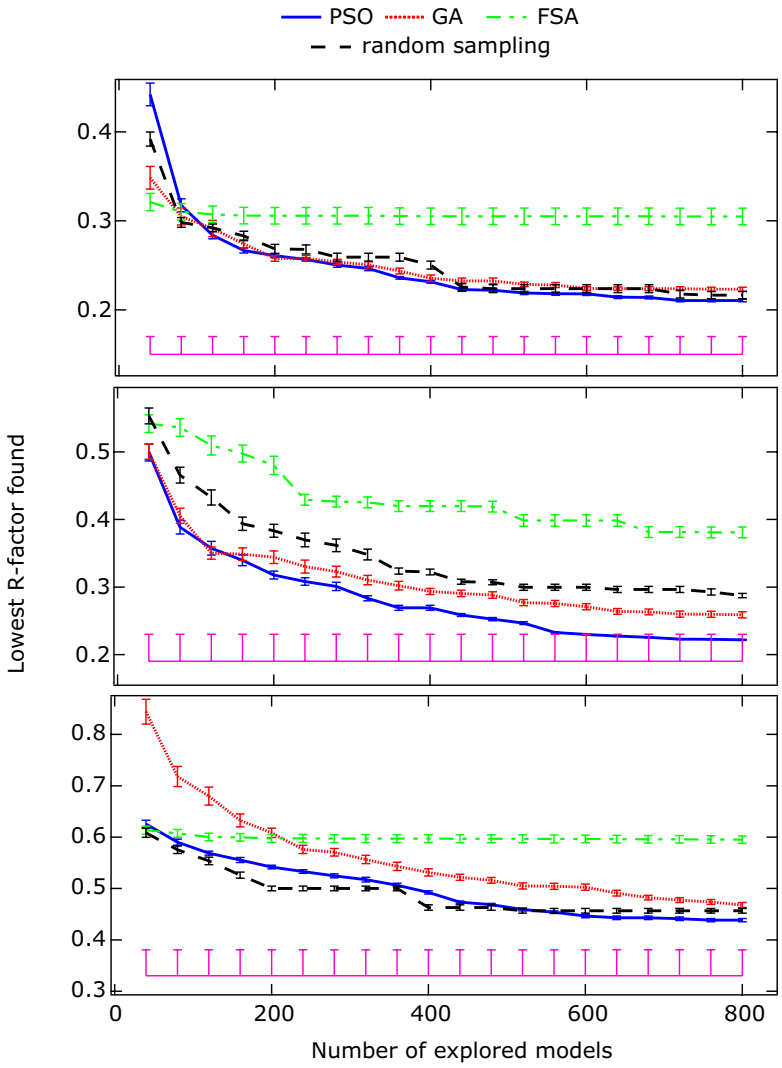

Figure 2.6: Comparison of the dependence of the lowest R-factor found on the number of trialled structural models for the three fitting algorithms and a random sampling of the variable hyperspace, for each of the substrate/adsorbate data sets investigated. Each value represents the average of 10 different repeats of the calculations with different (random) starting structures. The R-factor achieved in the original structure determinations [40–42] is shown by the horizontal (pink) lines at the bottom of each panel, with their variances shown as upper error bars.

algorithms have located the correct region of parameter space corresponding to the global minimum for each system, or have only converged on local minima.

In addition to the R-factor values obtained during the progress of the different search algorithms, Fig. 2.6 also shows, as a horizontal (pink) line, the value of the R-factors obtained in the original structure determination of each of the model systems. It is notable that for all three systems this value is lower than that achieved in any of the search methods, providing further support for the idea that the original analyses (that included structural optimisations using a gradient search algorithm) did identify the true structures. We may therefore ask how similar are the best structures found by the different global search algorithms (after 20 iterations) to these true structures.

To determine how similar the best structures found by the global search algorithms are to the true structures, we can use the difference between the values of the best-found R-factor, and the R-factor for the true structure. This is most appropriately defined relative to the variance in R-factor, by the ratio $\Delta R/\operatorname{var}(R_{min})$. Similarly, we can also compare the size of the deviations of the structural parameters from the true structures with the estimated errors in these parameters, by the ratio $\Delta X/\sigma_X$, where ΔX is the root mean squared difference between the published structural parameter and the best fit structure found by each calculation and σ_X is the estimated error on that parameter. This latter value provides a more direct indication of whether the global search algorithms have located the region of parameter space corresponding to the global minimum (which we infer, from the arguments above, to be at the parameter values of the originally-determined structures). These values are listed in Table 2.1. Note that, even though the implementations of the genetic algorithm and particle swarm optimisation are fairly basic, they both appear to converge in the area of the true structure with a comparable level of accuracy. Though both algorithms could be further optimised to solve these three specific problems, these two generalised and simple implementations provide acceptable results.

As shown in Figure 2.6, and quantified in Table 2.1, for the Ni(111)/SO_2 structure PSO locates a model within the variance ($\Delta R/\operatorname{var}(R_{min}) < 1$) of the correct structure, although the fact that $\Delta X/\sigma_X > 1$ suggests that there may be some parameter coupling in the simulations, such that an increase in R due to a change in one parameter value may be compensated by a reduction due to a change in another. For this system the GA also finds an R-factor value only slightly larger than the variance of the true structure, though the actual parameter values show significantly larger variations. Most of the other values of Table 1 reinforce the information provided by visual inspection of Fig. 2.6. For the Cu(111)/CN system PSO yields a model significantly closer to the correct structure than GA, although only marginally better than the random sampling. For the TiO_2(110)/H_2O system the three methods yield surprisingly similar results, although it is the random sampling that shows the lowest

deviation from the true structure in terms of the structural parameter values.

Table 2.1: Average difference between the previously-determined correct structure of each system, and the structures found using the two algorithms (PSO and GA) and random sampling expressed as normalised differences in the R-factor or the coordinates, as described more fully in the text.

	$TiO_2(110)/H_2O$		$Ni(111)/SO_2$		$Cu(111)/CN$	
	$\frac{\Delta R}{\mathrm{var}(R_{min})}$	$\frac{\Delta x}{\sigma_X}$	$\frac{\Delta R}{\mathrm{var}(R_{min})}$	$\frac{\Delta x}{\sigma_X}$	$\frac{\Delta R}{\mathrm{var}(R_{min})}$	$\frac{\Delta x}{\sigma_X}$
PSO	3.0 ± 0.1	3.7 ± 0.5	0.80 ± 0.02	1.5 ± 0.1	2.2 ± 0.1	2.3 ± 0.2
GA	3.7 ± 0.1	3.2 ± 0.4	1.6 ± 0.1	3.9 ± 0.4	3.0 ± 0.1	3.4 ± 0.3
random	3.3 ± 0.2	2.3 ± 0.3	2.6 ± 0.1	4.1 ± 0.5	2.5 ± 0.1	2.5 ± 0.2

Therefore, both the PSO and GA methods have been found to be applicable to PhD surface structure determination, although the PSO proved better in some cases and worse in none. It is possible that the slightly inferior performance of the GA relative to PSO stems from the discrete nature of this approach. The GA is specifically designed for use in a discrete variable space, hopping between the different values that are present in the population, whereas PSO is designed for a continuous search space, crawling between the values that have already been calculated. The other significant advantage of PSO is its use of memory. The GA, apart from elitism [43], does not actively utilise the shared knowledge of the population, whereas in PSO the best-found structure for each individual of the population is always remembered, as is the best-found structure that each member of the population has been informed of.

Of course, it is dangerous to draw very general conclusions about the relative merits of the different algorithmic approaches on the basis of single implementations for just three model systems. All three techniques use preset parameters, the values of which can have a significant effect on their efficacy. Specifically, in the genetic algorithm, there are the two parameters that define the rate of mutation [39], and in the PSO there are the three parameters (c_p,c_l and c_g) that weight the influence of the three components of Eqn. 2.24. Optimisation of these parameters was not pursued extensively in this study due to limited computational resources. A different set of inputted parameters could make the GA at least as effective as the PSO implementation; however, an important conclusion is that this new PSO approach is at least comparable in efficacy to the better known and more widely applied genetic algorithm.

Moreover, it is clear that at least two of these algorithms (GA and PSO), even in these basic implementations, can be used with good effect to search the variable hyperspace in PhD, and thus contribute in a useful way to the structural solution. Surprisingly an automated random sampling may also be valuable.

Chapter 3

Supporting Techniques and Experimental Methods

3.1 Introduction

This chapter describes the supporting techniques that were used to characterise the adsorption systems in preparation for measurement by the PhD technique. Namely this chapter will provide basic descriptions on the following techniques: LEED (§3.2.1), XPS (§3.2.2), NEXAFS (§3.2.3) and DFT (§3.2.4). This chapter also describes the experimental apparatus employed in the work presented in this thesis, specifically sources of X-ray light (§3.3.1), the UE56/2-PGM2 beam line (§3.3.2) and the experimental end station (§3.3.3).

3.2 Supporting Techniques

3.2.1 Low-energy electron diffraction, LEED

LEED, as described briefly in section 1.1, is one of the oldest and most established techniques within surface science. In its quantitative mode it has been used to determine the surface structures of more systems than any other single technique (eg [44–48]). However it is more widely used, as is the case within this thesis, in a qualitative manner. Specifically, within the work presented here, it was used to determine whether or not the surface (either the clean surface, or a surface with an overlayer) was well ordered. Often it was not employed to characterise the organic overlayers as the incident electron beam can often damage them[49].

In LEED an electron beam, with a well defined kinetic energy (typically in the range of 30-300eV), is incident on a surface. If the surface has regions with a high degree of lateral periodicity, then the elastically back-scattered electrons will

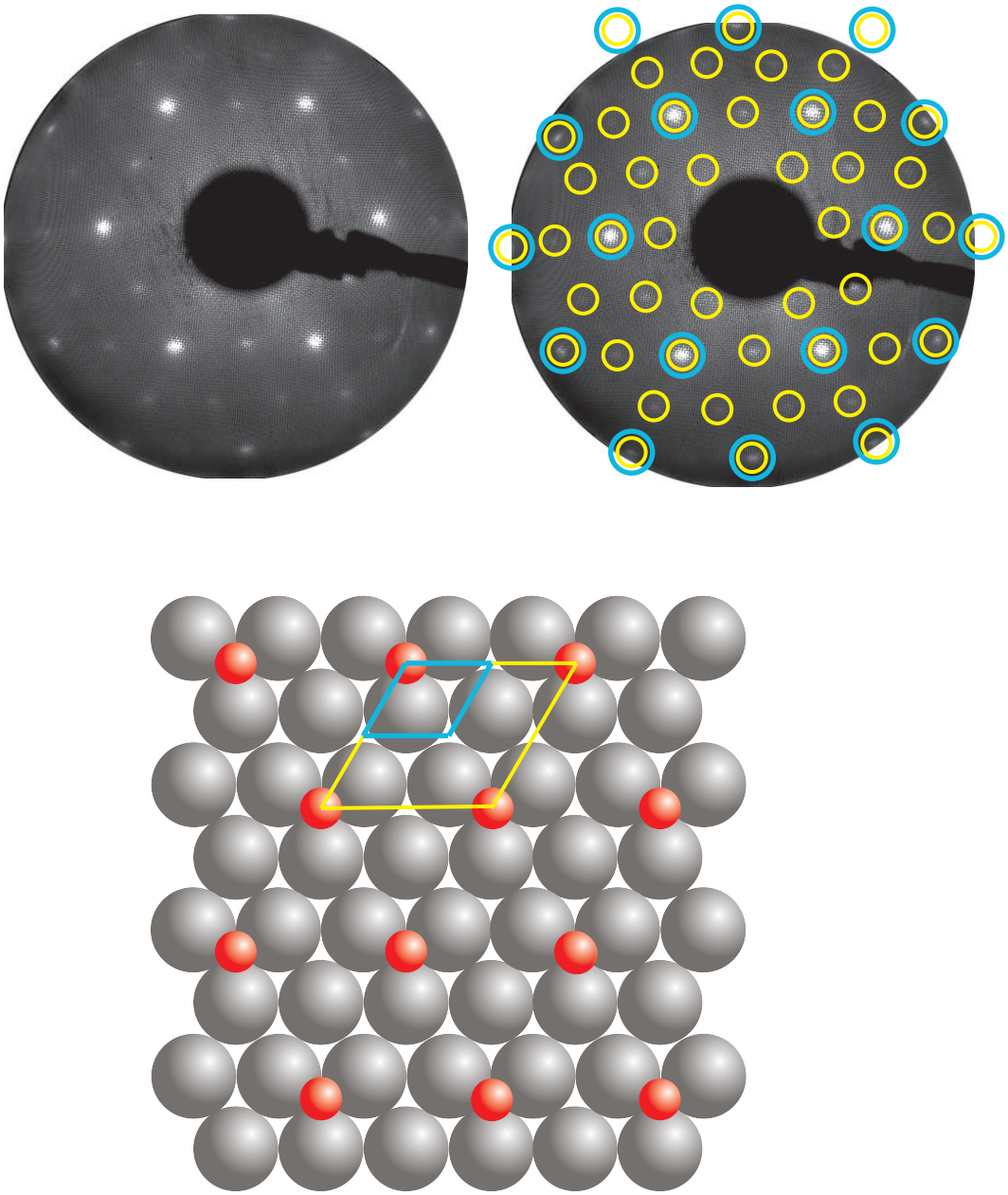

Figure 3.1: (top) Example of a LEED pattern, measured from an Ru(0001)(2x2)-O surface. (top, right) The spots circled cyan are those that would result from a clean Ru(0001)(1x1) surface, the spots circled yellow are those resulting from the (2x2) overlayer periodicity. (bottom) A schematic of the overlayer is shown with the (1x1) [cyan] and (2x2) [yellow] unit mesh indicated. Note that the (2x2) pattern, which has unit mesh vectors twice that of the underlying substrate in real space, results in a reciprocal unit mesh vectors half the length of those from the substrate.

display a pattern that is the projection of the reciprocal net defined by the real space periodicity of the ordered surface regions (see Fig 3.1). Therefore a qualitative examination of the LEED pattern provides information on the lateral periodicity of the surface. The spots that appear in a LEED pattern relate to the Laue conditions being satisfied. If an electron is elastically scattered by a scattering vector $\mathbf{g}$, in order for momentum to be conserved, the magnitude of the incident wave-vector, $\mathbf{k}$, must equal the magnitude of the outgoing wave-vector, $\mathbf{k'}$:

$$\mathbf{k}' = \mathbf{k} + \mathbf{g_{hk}}, \tag{3.1}$$

$$\mathbf{k}'^2 = \mathbf{k}^2. \tag{3.2}$$

These conditions are satisfied by a discrete number of vectors:

$$\mathbf{g_{hk}} = h\mathbf{a}^* + k\mathbf{b}^*, \tag{3.3}$$

where h and k are a set of integers called the Miller indices, and $\mathbf{a}^*$ and $\mathbf{b}^*$ are the primitive reciprocal space net vectors, which are related to the primitive real space net vectors by:

$$\mathbf{a}^* = 2\pi\frac{b \times n}{a \cdot b \times n}, \tag{3.4}$$

$$\mathbf{b}^* = 2\pi\frac{n \times a}{a \cdot b \times n}, \tag{3.5}$$

$$\tag{3.6}$$

where n is a unit vector normal to the surface. Note that there are only two Miller indices / lattice vectors in these formulae as the surface only has periodicity in the two lateral dimensions. The satisfying of equations 3.1 and 3.2 can be represented schematically by an Ewald Sphere (Fig 3.2).

Typically, to measure a LEED pattern experimentally, an electron gun is used to generate the incident electron beam. The beam is focussed by a set (generally 3) of tubes set at different potentials. The backscattered electrons then travel through a field-free region which is created by a grounded hemispherical grid. A negatively biased field is created by a subsequent grid for retarding electrons with a kinetic energy lower than those incident on the surface, effectively suppressing the inelastically scattered electrons. Finally the electrons which have passed the retarding field are

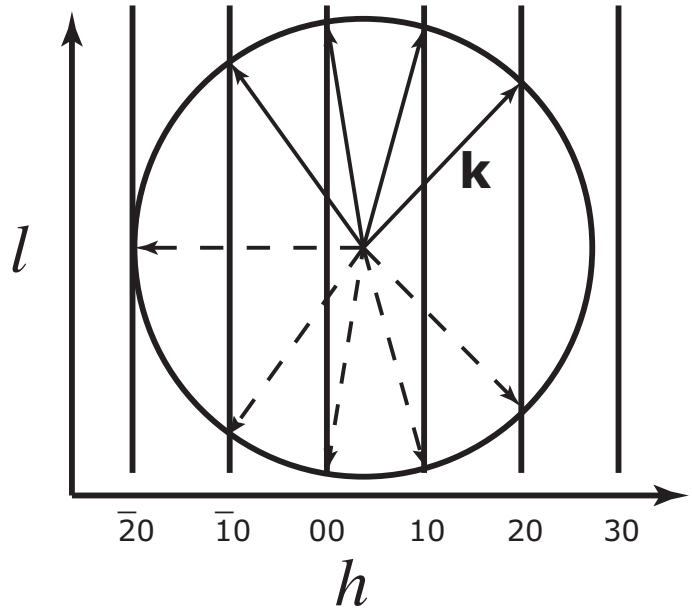

Figure 3.2: Cross-section of the Ewald sphere construction with the Miller index k equal to 0 and varying h and l, where l is the Miller index along the surface normal. The Ewald sphere is plotted in reciprocal space with a radius equal to the wave-vector of the incident electron wave, $\mathbf{k}$. Any line that is bisected by the Ewald sphere will satisfy the Laue condition (Eqn. 3.1), and a diffraction spot will appear in the LEED pattern. Note that the dashed lines represent wave-vectors that are scattered into the substrate and are therefore lost.

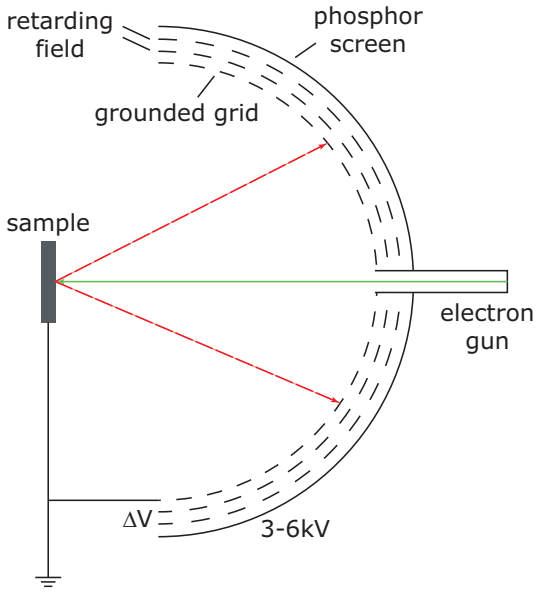

Figure 3.3: Schematic of a LEED optic as described in the text.

accelerated by a high field ($\sim 3-6$ kV) towards a phosphor screen causing fluorescence. A schematic of the LEED optic used in the experiments detailed in this thesis is shown in Fig 3.3. A more in depth explanation of LEED and its applications can be found in various sources (eg [8–10]).

3.2.2 X-ray photoemission spectroscopy, XPS

The photoelectric effect, which is the basis for XPS, was first explained by Einstein [50, 51]. Adsorption of incident light, if it possesses enough energy, will cause an electron to be emitted from its bound state into a vacuum state. The electron will then have a kinetic energy (E_{KE}) of:

$$E_{KE} = h\upsilon - E_b - \varphi_0, \tag{3.7}$$

where E_b is the binding energy of the electron with respect to the Fermi level, and φ_0 is the work function of the material - the energy required to remove an electron from the Fermi level into a vacuum state. Typically the work function is in the order of a few eV [52], which is accessible with light in the UV spectrum. However, in order to probe deeper, core energy levels, whose binding energy is in the order of hundreds to thousands of eV [53], light from the X-ray spectrum is required. Sources of X-ray light are described in section 3.3.1. As energetic levels of different elements will have a different binding energies, measuring photoelectron intensity as a function of kinetic energy can provide a spectral fingerprint of the elemental constituents of the sample surface. If there are multiple chemical species present on the surface, significant shifts in the photoelectron binding energy can also be observed. Therefore XPS can provide not only an elemental spectral fingerprint, but also a chemical spectral fingerprint - hence the early name for this technique ESCA (electron spectroscopy for chemical analysis) [54].

In order to measure photoelectron intensity as a function of energy typically a hemispherical analyser is used. The hemispherical analyser is made of two concentric hemispheres, one concave the other convex. By applying a potential difference between the two hemispheres an electric field will occur between them. The electric field will deflect the incident electrons by a force, F:

$$F = q_e E, \tag{3.8}$$

where E is the strength of the electric field and q_e is the charge of an electron. This force will cause the electron to experience an acceleration, a:

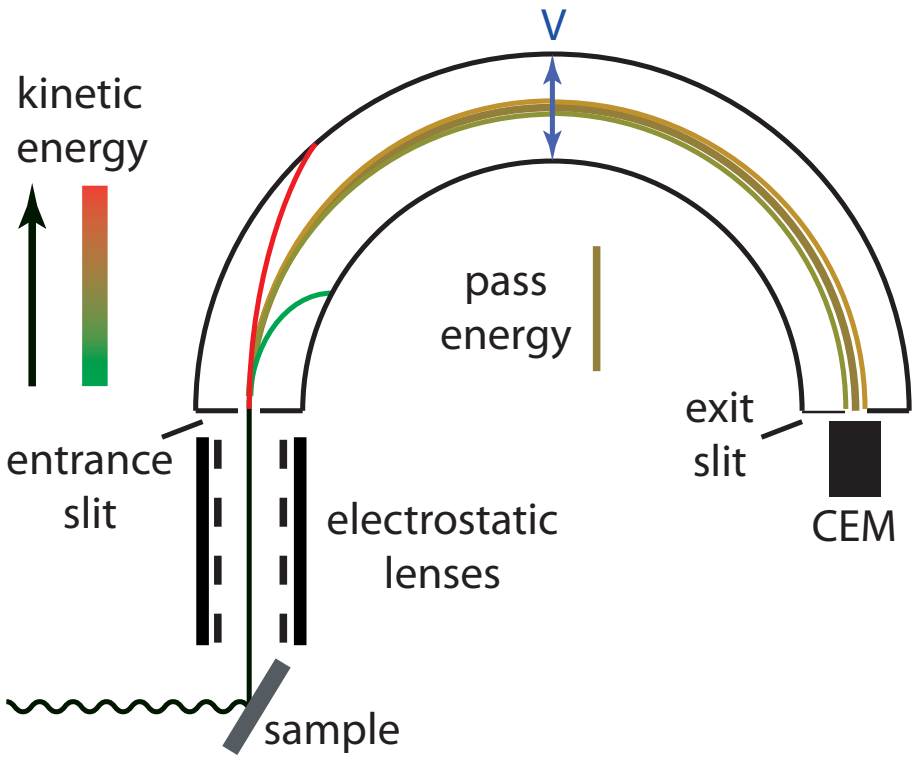

Figure 3.4: Schematic of a hemispherical electron analyser as described in the text.

$$a = \frac{q_e}{m_e} E, \tag{3.9}$$

where m_e is the mass of an electron. Therefore electrons that have too little kinetic energy (and therefore a low velocity) will be pulled into the inner hemisphere wall. Conversely electrons that have too much kinetic energy (and therefore a high velocity) will not be deflected around the analyser and instead collide with the outer hemisphere wall. However there will be a narrow distribution of electron kinetic energies for which electrons pass through the gap between the hemispheres into a detector (typically a channel electron mutliplier, CEM [55]). The mean electron kinetic energy that passes through the analyser is referred to as the "pass energy" (E_{PE}), and the distribution of energies around that mean (ΔE), the energy resolution of the analyser, is related to the radius of the analyser (R), the entrance and exit slit widths (w_{in} and w_{out} respectively) and the pass energy: [56]:

$$\Delta E \propto \frac{S \cdot E_{PE}}{R}, \tag{3.10}$$

$$S = \left(w_{in} + w_{out}\right)/2. \tag{3.11}$$

Therefore, as the pass energy is varied (by varying the potential difference

between the hemispheres) the energy resolution is also varied. By using a retarding field the kinetic energy of the incident electrons can be decreased before they enter the analyser. This allows a lower pass energy to be used, providing a greater energy resolution. Therefore, for measuring electron flux as a function of the kinetic energy of the electron, two operating modes of the analyser are available - one in which the pass energy of the analyser is varied and another in which the retarding field is being varied. By using the latter mode, it is possible to perform this measurement with constant energy resolution. A schematic of a hemispherical analyser, as described here, is shown in Fig 3.4.

Within the work presented here, no attempt was made to make an absolute calibration of the binding energy. The measured XP spectra presented within this thesis were used simply for broad characterisation of the adsorbate system, and the shift in binding energy between chemical species was of far greater importance to the work presented here than having a measure of the absolute binding energy.

3.2.3 Near-edge X-ray absorption fine structure, NEXAFS

There are two phenomena that provide structural information from the scattering of photoelectron wave-fields. One is intensity variations due to the different paths that the electron can take in order to arrive at the detector, such as is the case in PhD (§2). Another possibility is when the photoionisation cross-section is varied in some way. One technique exploiting the latter phenomenon is extended X-ray absorption fine structure (EXAFS). If the photoemitted electron is backscattered onto the original emitter, the incident electron flux will coherently interfere with the outgoing electron wave setting up a standing wave. This incident flux will cause variations in the final state amplitude at the emitter and therefore variations in the photoionisation cross-section. As the photoelectron kinetic energy is varied, the nodes and anti-nodes of the photoelectron standing wave will occur on the emitter. Therefore this effect can provide information about the local environment of the emitter [57].

If the emitter is part of a molecular assembly, such that it takes part in covalent bonding, additional information can be gained originating from intramolecular bonding states. By measuring the intensity of Auger electrons (described elsewhere, eg [8]) as a function of photon energy, sharp resonance features can occur which are associated with transitions from core occupied states into the lowest unoccupied molecular states. These resonances appear at energies near the absorption edge and this phenomenon is generally referred to as near-edge X-ray absorption fine structure (NEXAFS). Typically in NEXAFS there are two main features that are observed. Sharp features that relate to bound unoccupied molecular orbitals (typically π^* orbitals) and broad features that relate to strictly unbound (i.e. above the vacuum level),

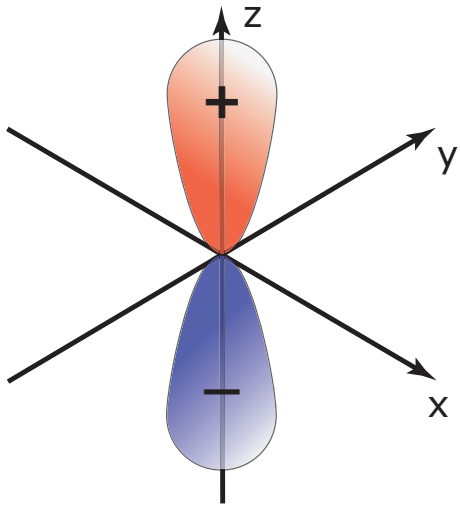

Figure 3.5: Schematic of a $2p_z$ orbital. The direction of this orbital is the vector between the maximum of the positive (red) and negative (blue) components of the orbital - which in this case is along the z-axis.

unoccupied molecular orbitals that are still quasi-bound (typically σ^* orbitals). Assuming the intial excitation was from a 1s state, these features will have a maximum in their intensity when the angle between the electric field vector of the incident photon and the direction of the final state molecular orbital (Fig 3.5) is zero [59]. In the case of π^* orbitals, the orbital direction will be perpendicular to the molecular bond, and in the case of σ^* orbitals, the orbital direction will be parallel to the molecular bond.

Therefore by monitoring the relative amplitudes of the π^* and σ^* features as a function of the incident photon polarisation it is possible to gain clear qualitative information on the adsorption geometry of molecular adsorbates. It is also possible to gain quantitative information on the adsorption geometry as the intensity of these features will vary by:

$$I \propto cos^2(\theta) \tag{3.12}$$

where θ is the angle between the incident photon polarisation vector and the molecular orbital direction - however, fitting NEXAFS spectra [59] is non-trivial. Sample NEXAFS spectra are shown in Fig 3.6 which show π^* and σ^* features with strong angular dependence. The π^* feature is very intense when measured along the [001] azimuth, but has practically vanished when measured along the $[1\bar{1}0]$ azimuth. This feature is also only present in the normal incidence geometry. This implies that the molecular plane is orientated along the close packed $[1\bar{1}0]$ direction and that the molecular plane is perpendicular with respect to the surface.

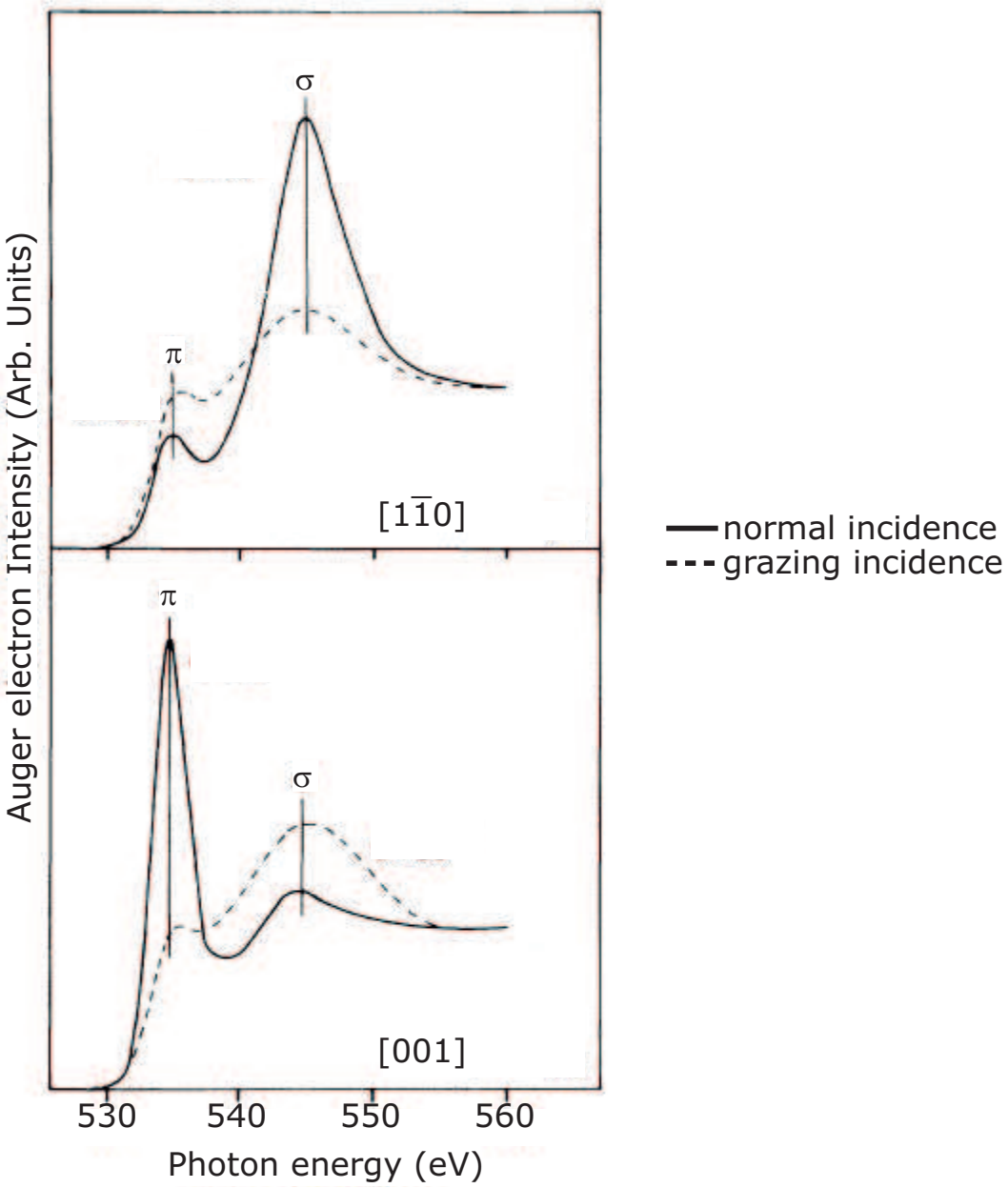

Figure 3.6: Sample NEXAFS spectra reproduced from Puschmann et al [58]. The spectra were measured from a Cu(110) surface dosed with formic acid (HCOOH); upon adsorption formic acid loses the hydrogen atom attached to the oxygen atom and becomes formate (HCOO). Analysis of the spectra is presented in the text.

3.2.4 Density functional theory, DFT

Unlike the other techniques described in this chapter, density functional theory (DFT) is purely theoretical. However, it is often used within the work presented in this thesis to predict possible structural geometries and to test whether proposed structures are physically reasonable. The DFT calculations referenced within this thesis were not performed by the author, however, in several systems these calculations were integral in solving the structure.

The principles of DFT were proposed by Hohenberg, Kohn and Sham [60, 61] and revolve around avoiding the problem of solving the many-body Schrödinger equation, but instead dealing with the total density of electrons ($\rho_{(r)}$). It can be shown [62] that for a given electron density there can only be one specific external potential ($V_{(r)}$), and vice versa. As the external potential determines the electron wavefunction, the wavefunction must also be a unique functional of the electron density ($F\left(\rho_{(r)}\right)$). The other terms in the wavefunction, other than the external potential, are properties of the electron, and are therefore functions of the electron density (e.g. the electron kinetic energy and the electron - electron interaction). Therefore the total energy of the system $E\left(\rho_{(r)}\right)$ is given by:

$$E\left(\rho_{(r)}\right) = F\left(\rho_{(r)}\right) + \int V_{(r)}\rho_{(r)}\,\mathrm{d}r. \tag{3.13}$$

The minimum of this equation will be for the correct density for the given potential. The advantage of considering the total energy in terms of the electron density is that it simplifies the electron kinetic energy to a three dimensional problem instead of a 3n dimensional problem, where n is the number of electrons per unit cell. In order to correct for many bodied effects an exchange-correlation functional is introduced, however, what form this exchange functional should take is still hotly debated in the literature (eg [63, 64]) and the choice of which functional is used has a significant affect on the relative energy of different structures (eg [65–69]). There is also a rather particular similarity between DFT and the main technique of this thesis (PhD) - specifically both techniques are heavily limited by the imagination of the researcher. If the correct structure is not trialled by either PhD or DFT, then it will never be found. Note that this does not mean that if there are small differences in position between the correct structure and the proposed structure that they will not be found, as fitting routines should be able to optimise such differences, but that if the gross structural models are not tested, then they are unlikely to be found by even the best fitting routines. Specifically, systems in which the surface has been heavily reconstructed by an adsorbate species (most famously in the field of alkane-thiols on Au(111) [70]) can suffer from this problem; if the correct reconstruction is not trialled then it will not be found by either DFT theoretical predictions nor PhD experimental

analysis.

3.3 Experimental apparatus

3.3.1 Light sources

In order to exploit photoemitted electrons from core energy levels. light in the X-ray spectrum is required. The traditional method of generating X-ray light is to use a high voltage to accelerate electrons from a hot cathode through a vacuum towards a target anode. If the electrons have enough kinetic energy there is a finite probability that it will cause a core-level electron to be emitted from the target anode. The atom, where this core-level electron originated, will now be in a high energy ionised state, and one of the possible relaxation paths is for an electron from a higher energy level to emit a photon and descend to this core-level. The emitted photon will therefore have an energy that is characteristic of the anode material, and is (broadly) the difference between the binding energy of the core-level that the electron was emitted from and the binding energy of the electron that descended to fill the hole. These characteristic energies are referred to as emission lines. The incident electrons (that are accelerated by the high voltage) that are simply inelastically scattered by interactions with electrons or the ionic potential will emit light in a broad spectrum, referred to as bremsstrahlung radiation.

However, the probability of the incident electrons losing their energy via a pathway that creates light in the X-ray spectrum is very small, with most of the energy being dissipated into heat. As such the available flux is limited by how effectively the anode target can be cooled. The advantage of this system is that it is comparatively cheap and small - as such it can be used as a laboratory source of X-rays. These emission lines are generally satisfactory for XPS measurements (§3.2.2), however, several techniques [e.g. PhD (§2) and NEXAFS (§3.2.3)] require a tunable light source. Though the bremsstrahlung from the X-ray tube does contain a wide spectrum (in energy) of X-ray light, the achievable intensity of the bremsstrahlung in most laboratory sources is very low.

For all the results published within this thesis, the experiments were performed using light from a synchrotron based source. Synchrotron light sources generate large amounts of broad spectrum light, however, instead of using a solid sample to scatter the electrons, a magnetic field is used. Electrons are injected into a ring accelerator, which accelerates the electrons up to near speed of light velocities. These electrons are then injected into a storage ring where the electrons are bent around the ring using strategically placed magnets (bending magnets). Whenever the electrons are "bent", they will emit a high flux of light in a broad spectrum. However, these bending

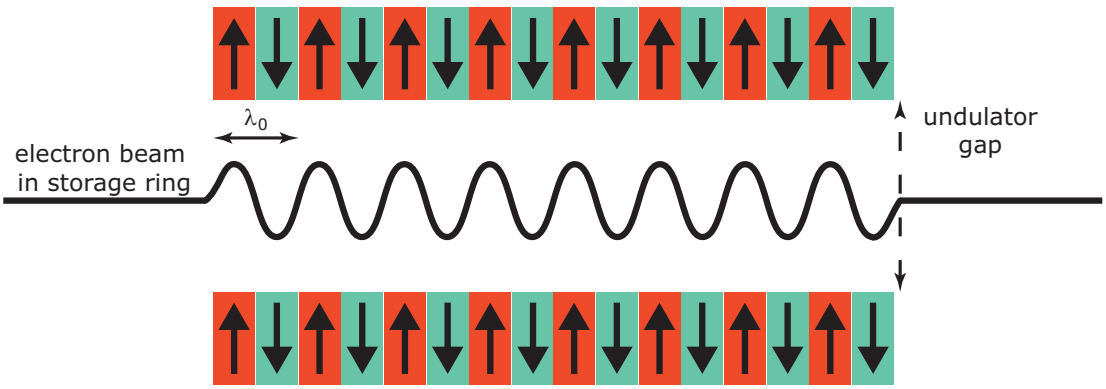

Figure 3.7: Schematic of an insertion device / undulator as described in the text.

magnets are limited, as a light source, due to the structural constraints of having to bend the electron beam around the storage ring. Greater flux can be achieved by inserting a device specifically designed as a light source in a particular energy range. These insertion devices typically contain two parallel rows of several comparatively small magnets ($\sim$ millimeters in length) placed in series with a distinct periodicity and alternating polarity shown schematically in figure 3.7. These two rows of magnets will set up an alternating magnetic field that the electron will oscillate in. These devices still work under the constraint that they must minimise any perturbation of the electron orbit around the storage ring, however, this is a far weaker constraint than that for bending magnets. If large oscillation amplitudes are used then a broad energy spectrum of light will be generated. Small oscillation amplitude causes interference effects that will produce radiation that is concentrated about one primary and several higher order harmonic wavelengths (λ_n):

$$n\lambda_n = \frac{\lambda_0}{2\gamma^2}\left(1 + \frac{K^2}{2} + \gamma^2\theta^2\right), \tag{3.14}$$

$$\gamma = \frac{1}{\sqrt{1 - \nu^2/c^2}}, \tag{3.15}$$

$$K = \frac{q_e B_0 \lambda_0}{2\pi m_e c}, \tag{3.16}$$

where λ_0 is the period of the insertion device, γ is the Lorentz factor, θ is the observer angle (which, for large γ, must be small) and B_0 is the strength of the magnetic field between the two rows of the insertion device. The K-parameter, defined in equation 3.16, is a characteristic parameter for an insertion device. An insertion device with a small oscillation amplitude ($K <\sim 1$) is typically referred to as an undulator and devices with a larger oscillation amplitude ($K <\sim 1$) are typically called a wiggler. Note that, for forward directions with small θ, only odd harmonics ($n = 1, 3, 5, ...$) are present for an undulator.

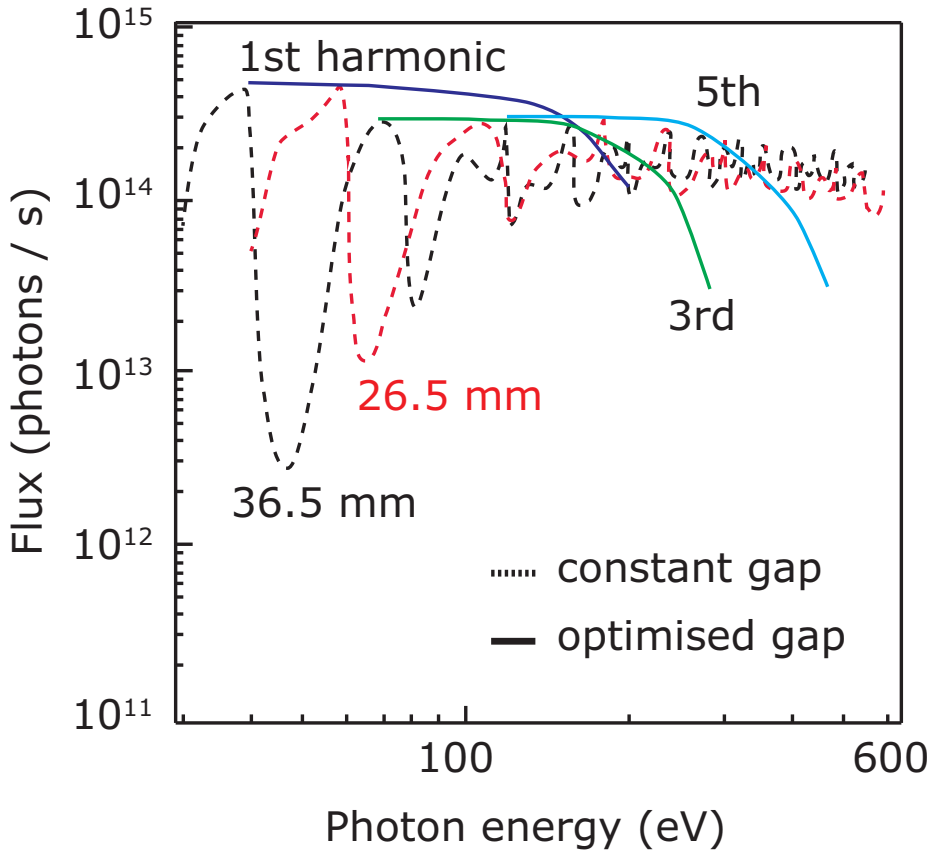

Figure 3.8: Comparison of the photon flux measured from two different gap sizes (36.5 mm and 26.5 mm) and a continuous spectrum measured with an optimised gap size for the first, third and fifth harmonics. Reproduced from BL3.2a beam line at the Siam photon laboratory[71].

The experiments presented here require a tunable photon source, if the parameters of equation 3.14 are varied, then the harmonic wavelengths will also vary. In practice it is not feasible to vary γ, θ or λ_0 as this would require (respectively) varying the velocity of the electrons around the ring, rotating the beam-line or varying the size of the magnets in the insertion device. However, the magnetic field strength, B_0, can be varied by simply changing the size of the gap between the two rows of magnets. Therefore, instead of discrete bands of wavelength, a continuous spectrum is available (as shown in Fig 3.8).

3.3.2 UE56-2-PGM/2 beam line

The beam line that was used in all of the experimental work presented here was the UE56-2-PGM/2 beam line at Berlin Elektronenspeicherring-Gesellschaft für Synchrotronstrahlung (BESSY) II. The light source of this beam line was an undulator (UE56-2) with a λ_0 of 56 mm and 30 repeating periods [73]. The beam line actually contained dual undulators, however, only the one was used during these experiments. The light generated by the undulator was collimated over 16 m before passing through an entrance slit of variable size. A toroidal mirror was then used to further collimate the light onto a plane mirror which reflected the light onto a plane grating monochromator. A cylindrical mirror focussed the beam into an exit slit that removed unwanted higher order diffraction peaks from the monochromator and a conical mirror focussed the light into a sub-mm^2 spot. Such large flux densities were found to cause severe damage to prepared molecular overlayers therefore to mitigate this damage (but yet not lose any incident photon flux) the chamber was mounted a meter behind the focal point of the beam line, such that the spot size had increased to $\sim$ 1 mm^2. The beam line is shown schematically in figure 3.9[72].

The plane grating monochromator (PGM) is used to filter out unwanted photon energies. The PGM and the mirror that reflects the light onto the grating are allowed to rotate independently and the PGM is operated (as with all grating monochromators in this energy range) in a reflection mode. As such the wavelength of light, λ, for a given mirror / PGM geometry is given by [74]:

$$d\,(\sin\theta_i + \sin\theta_d) = n\lambda, \tag{3.17}$$

where d is the spacing between two adjacent grating lines, θ_i and θ_d are (respectively) the incidence and diffraction angles and n is an integer number greater than zero. The grating used in these experiments, discussed in more detail by Follath et al [75], had 1200 lines per millimeter and a resolving power ($\frac{E}{\Delta E}$) of around $10,000$ in the energy range of 100-600eV.

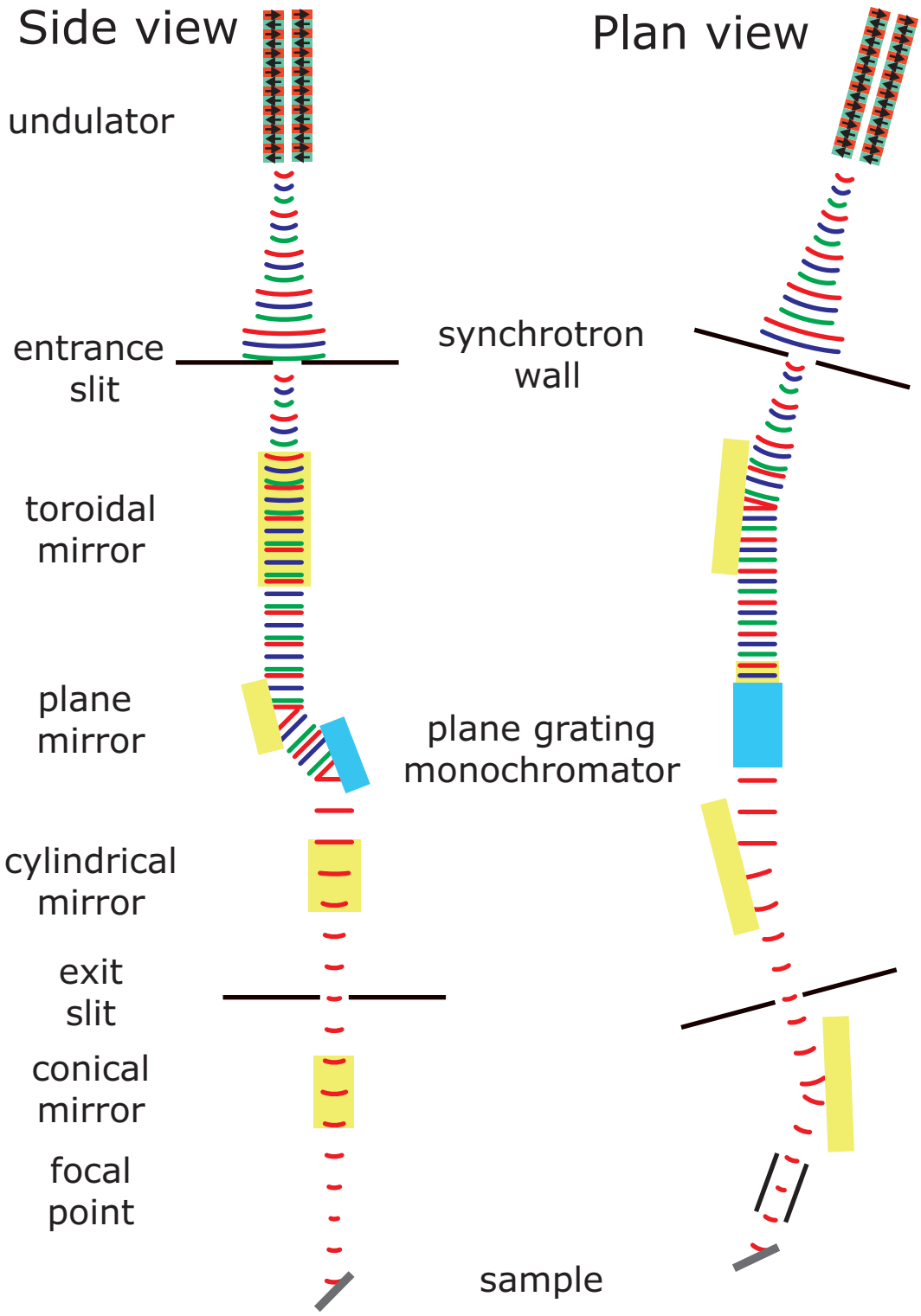

Figure 3.9: Schematic of the UE56-2-PGM/2 beam line[72] as described in the text. Note that the schematic is not to scale.

3.3.3 End station

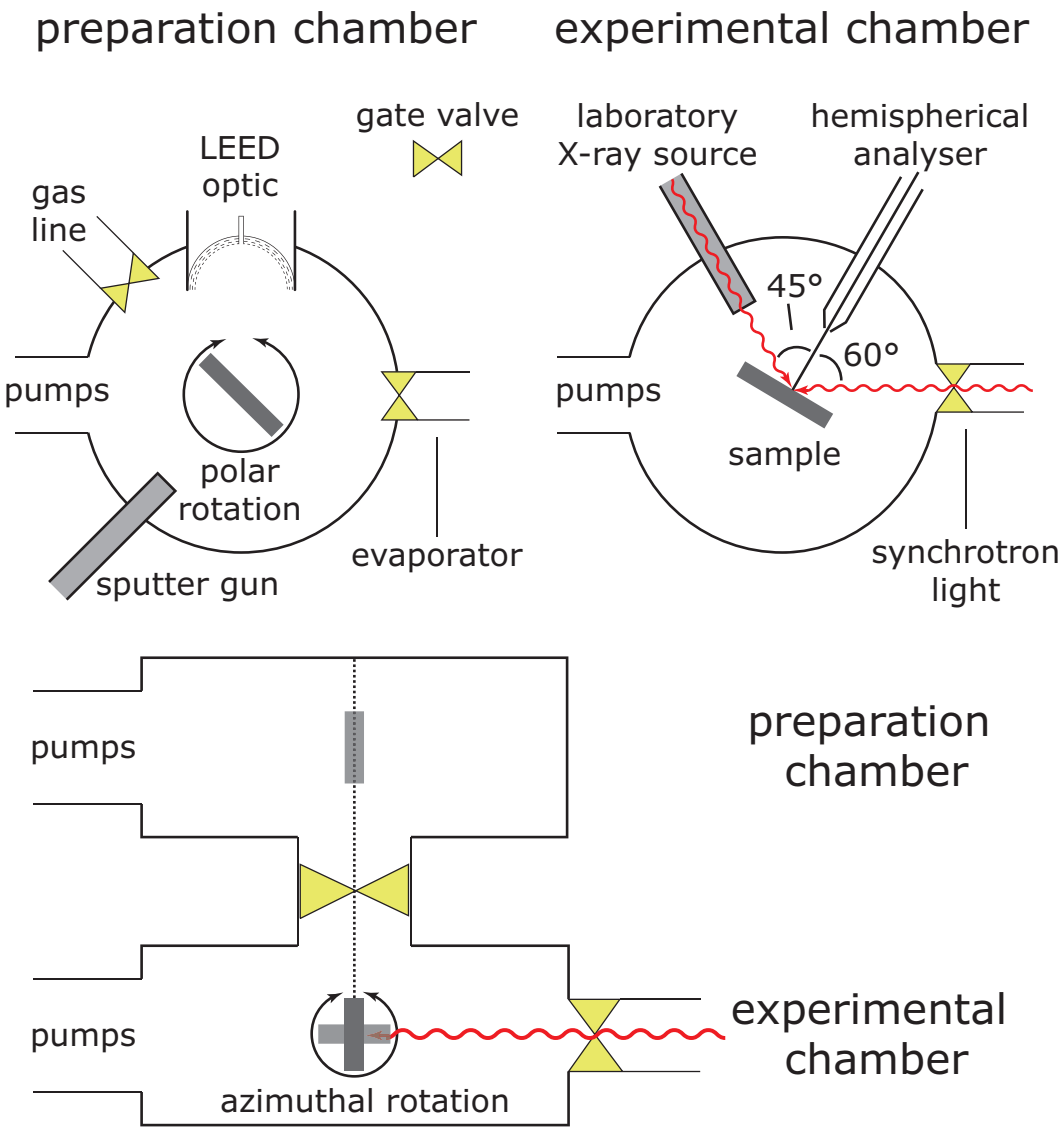

Figure 3.10: Schematic of the end station as described in the text. The top schematics are in a plan perspective, where as the bottom schematic is a side view.

The end station used on the UE56-2-PGM/2 beam line consisted of a preparation chamber and a measurement chamber separated by a gate valve. Both chambers were pumped by turbomolecular and titanium sublimation pumps. Typically the base pressure of both chambers was in the low 10^{-10} mbar range. To move the sample between chambers, it was mounted on a manipulator which allowed 360° rotation along the manipulator's main axis (polar angle) and rotation by $\pm \sim 100°$ around the surface normal (azimuthal angle). The manipulator also contained a filament for direct radiative heating, and the sample plate or the filament could be biased for electron beam heating. The preparation chamber contained a sputter gun for sample cleaning, a gas line for leaking in species with high vapour pressures and a

LEED optics (§3.2.1) for characterising the clean and dosed surfaces. There were additional ports available to which evaporators, mass spectrometers, gas crackers, etc. could be mounted. The experimental chamber contained only an EA–125HR 125 mm mean-radius hemispherical electron energy analyser [55], an X-ray vacuum tube for laboratory based experiment and a port through which the synchrotron radiation passes. The analyser was equipped with seven-channeltron parallel detection. Note that the X-ray vacuum tube (§3.3.1), analyser (§3.2.2) and incident synchrotron radiation (§3.3.1) are all mounted in the same horizontal plane. The geometry of both the upper and lower chambers is shown in figure 3.10.

Chapter 4

Organic overlayers on Cu surfaces

4.1 Introduction

4.1.1 Simple biological molecules

There is a general trend within surface science to look at problems of greater complexity, and one such field that has received a large amount of interest is that of the metal / biological interface [76, 77]. However, most biologically-related molecules of interest are far too complex to understand at an atomic scale, though some attempts – specifically using scanning probe techniques (e.g. scanning tunnelling microscopy (STM), atomic force microscopy (AFM), etc.) – have been made [78]. Most studies, specifically those providing quantitative information, have been into the constituent parts of these molecules, specifically amino acids and nucleobases which form a major fraction of proteins and DNA. Copper has been a popular substrate for these studies as its low reactivity limits dissociation of (but yet is reactive enough for strong adsorption of) organic molecules.

Amino acids have a general formula of $H_2N - CH(-R) - COOH$ (shown in Fig 4.1), where R is a hydrocarbon chain of varying complexity and functionality. The amino acids, when forming proteins, will polymerise by reacting an amine group ($-NH_2$) on one amino acid to the carboxylic acid group ($-COOH$) on another amino acid to form a peptide bond ($-N(H)-C(=O)-$) and a water molecule. This reaction can then be repeated multiple times to create chains of atoms with hundreds to thousands of peptide bonds. This reaction is known as steam polymerisation. The simplest amino acid, glycine (where the R-group is a hydrogen atom) is the only amino acid without a chiral centre (§4.1.2).

Nucleobases have a base unit of either a pyrimidine or a purine ring (shown in Fig 4.1) with various functionalities. These are the molecules that form the base pairs within DNA and RNA (each pyrimidine based nucleobase will only pair with a specific

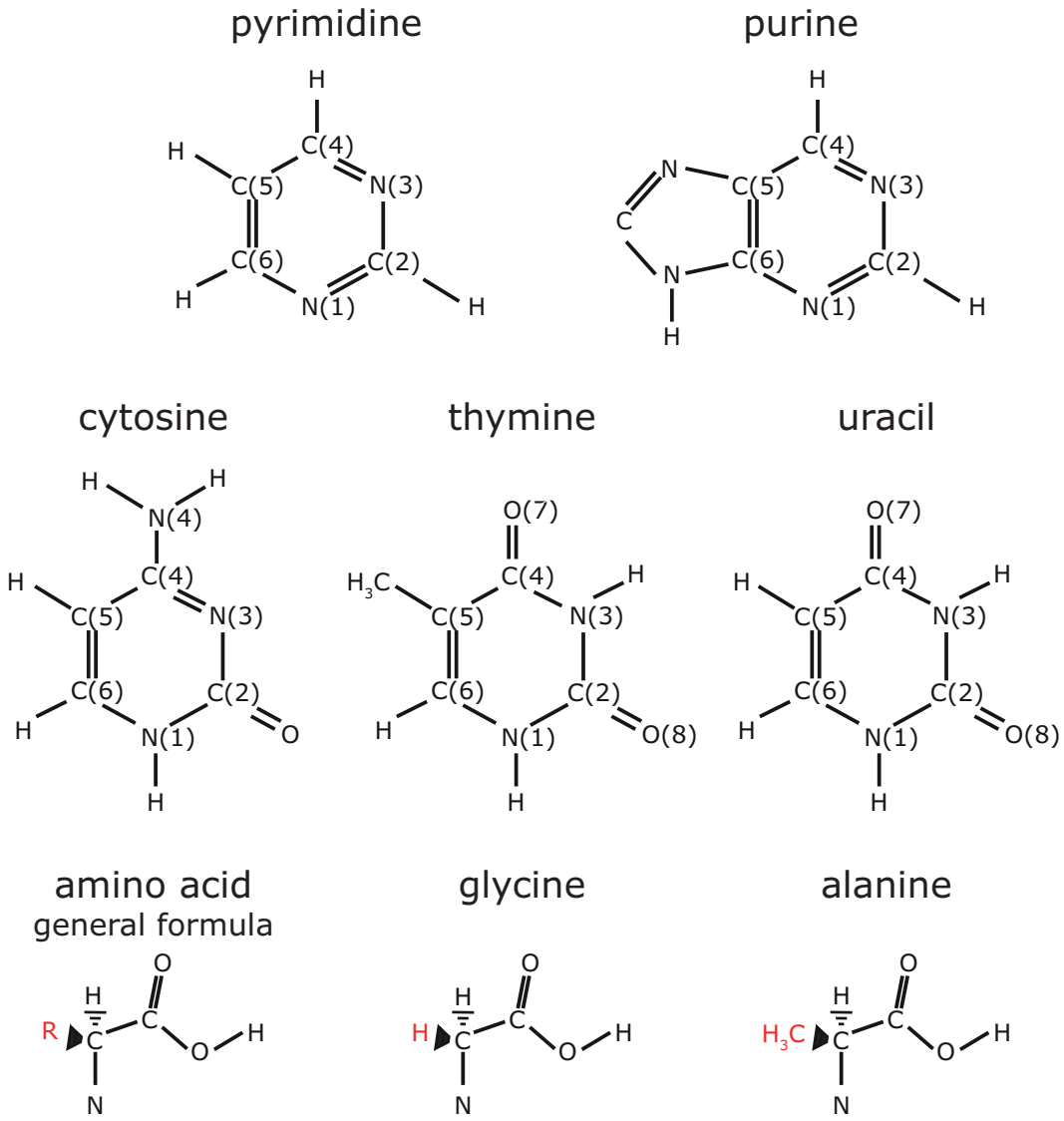

Figure 4.1: (top) Molecular structure of pyrimidine and purine (the base structures of all nucleobases), (middle) the three pyrmidine based nucleobases (cytosine, thymine and uracil) and (bottom) the general molecular structure of amino acids and the two simplest amino acids (glycine and alanine).

purine based nucleobase). The structure of the three pyrimidine based nucleobases are shown in Fig 4.1.

Understanding how these two classes of biological molecules interact with a metal surface, may provide some evidence how more relevant biological molecules could interact with the same surface.

4.1.2 Chirality

A molecule is considered chiral if it lacks a mirror plane (see Fig 4.2). Broadly the two different mirror images (enantiomers) of a chiral molecule are chemically identical - though they have distinct optical and electrical properties [79]. However, in reactions that have a steric (or shape) specificity - as in enzyme activity - the two enantiomers can have radically different effects (as has been tragically observed in the medicinal field [80]). Therefore the ability to produce a single enantiomer is of the utmost importance in the medical industry and can also have more general industrial advantages in order to exploit their distinct optical properties.

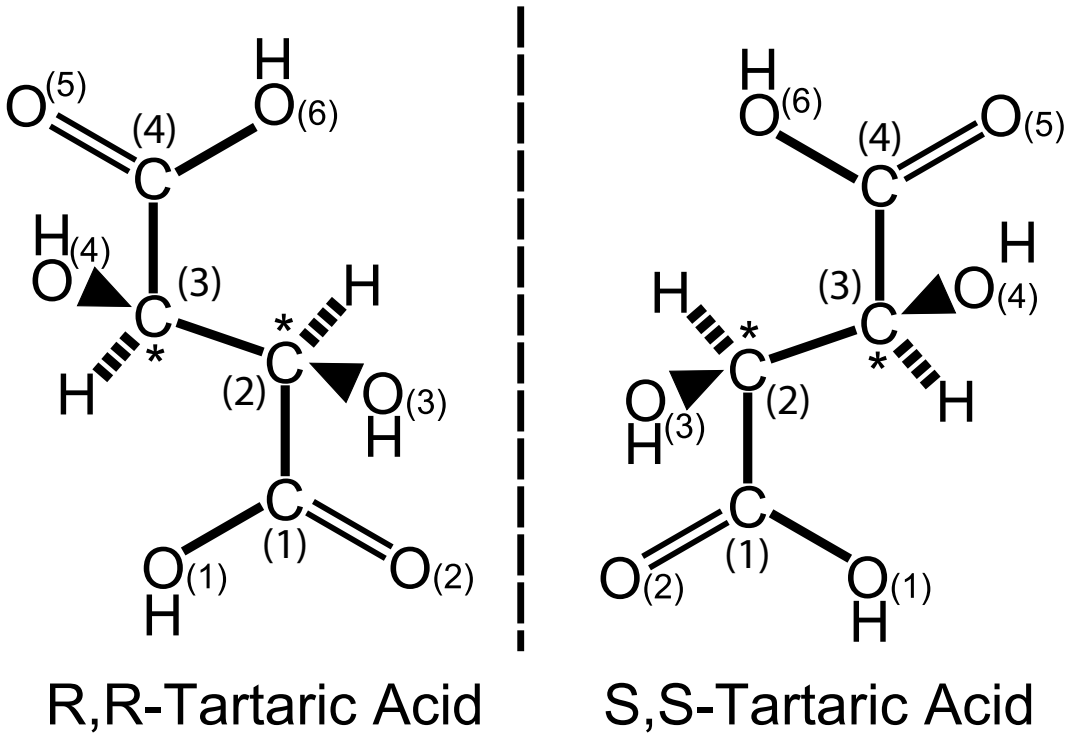

Figure 4.2: Schematic representation of the two chiral forms of tartaric acid with the chiral centres denoted by a *. The molecule on the left is the R,R-enantiomer that was used in the study presented in §4.4 and on the right is the mirror image, the S,S-enantiomer.

The common technique for producing a specific enantiomer has been to use enantioselective catalysis, which preferentially produces one enantiomer over the other. This typically means exploiting the selectivity of homogeneous catalysis, however,

these catalysts tend to be very expensive and difficult to recover[81] – therefore the design of enantioselective heterogeneous catalysts is of great interest. Some success in this field has been found with doping a current, achiral, catalyst with a chiral adsorbate – specifically this has been successfully demonstrated for the hydrogenation reaction of β-ketoesters on a Ni catalyst, which was modified by adsorption of tartaric acid [82–87].

Note that it is also possible for an achiral molecule, like glycine (§4.1.1 & 4.5), to adsorb in a site such that, due to steric constraints, the combination of the adsorbate and adsorption site is chiral. This is typically called a chiral-footprint[88]. However, even if the footprint of the molecule on the surface is chiral, as the adsorbing species is, it self, achiral, there will be an equal (or racemic) mixture of both enantiomers.

4.1.3 Previously determined adsorbate structures

The local adsorption site of the amino acids alanine ($-R$ is $-CH_3$) and glycine have been previously determined on the Cu(110) surface [88–90] via PhD and were observed to adsorb through the two functional groups - the amine (-NH2) and a deprotonated carboxylic acid (or carboxylate) group (-COO) – with the nitrogen and two oxygen atoms in near atop sites forming a chiral footprint the surfaces (note that alanine is in fact chiral). The adsorption site of the nucleobase thymine [91] has also been determined on the surface by PhD and was found to bond via the two carbonyl oxygen atoms ($= O$) and the deprotonated nitrogen atom that lies between them – with all three atoms in near atop sites and a slight twist in the molecular plane (with respect to the close-packed $[1\bar{1}0]$ direction).

4.2 Cytosine on Cu(110)

4.2.1 Introduction

The nucleobase cytosine, which is paired with guanine in DNA and RNA, is shown schematically in Fig 4.1 & 4.4. The adsorbed cytosine species on Cu(110) has been previously characterised by XPS of the O and N 1s photoemission peaks, and O and N K-edge NEXAFS [92] which has provided information on the initial reaction of cytosine with Cu(110) and on the molecular orientation. For the surface species formed at low coverage (~ 0.2 ML) NEXAFS data indicate that the molecular plane is essentially perpendicular to the surface, and aligned in the $\left[1\bar{1}0\right]$ azimuth parallel to the close-packed Cu atomic rows in the surface. The perpendicular orientation of the molecular plane was also inferred from infrared spectroscopy of this system [93]. The XPS data were interpreted as indicating that chemisorption of cytosine

on Cu(110) leads to deprotonation of the N(1) atom (fig. 4.1) within the molecular ring, and it was proposed that the molecule bonds to the surface through this N atom. A second study [94] also concluded, in this case on the basis of high resolution electron energy loss spectroscopy (HREELS), that the vibrational modes observed were consistent only with the molecular plane being perpendicular to the surface. This later investigation also identified two different long-range ordered phases, (6x6)pgg and (6x2)pgg, formed after annealing to $\sim$ 370 K and 480 K respectively, by both LEED and STM (shown in Fig 4.3. Based on this information, and particularly the presence of the two orthogonal glide symmetry lines seen in LEED that identified the space group as pgg, they proposed a structural model for the (6x2)pgg phase based on hydrogen bridge-bonded cytosine dimers, bonded to the surface through the O atoms (fig. 4.4).

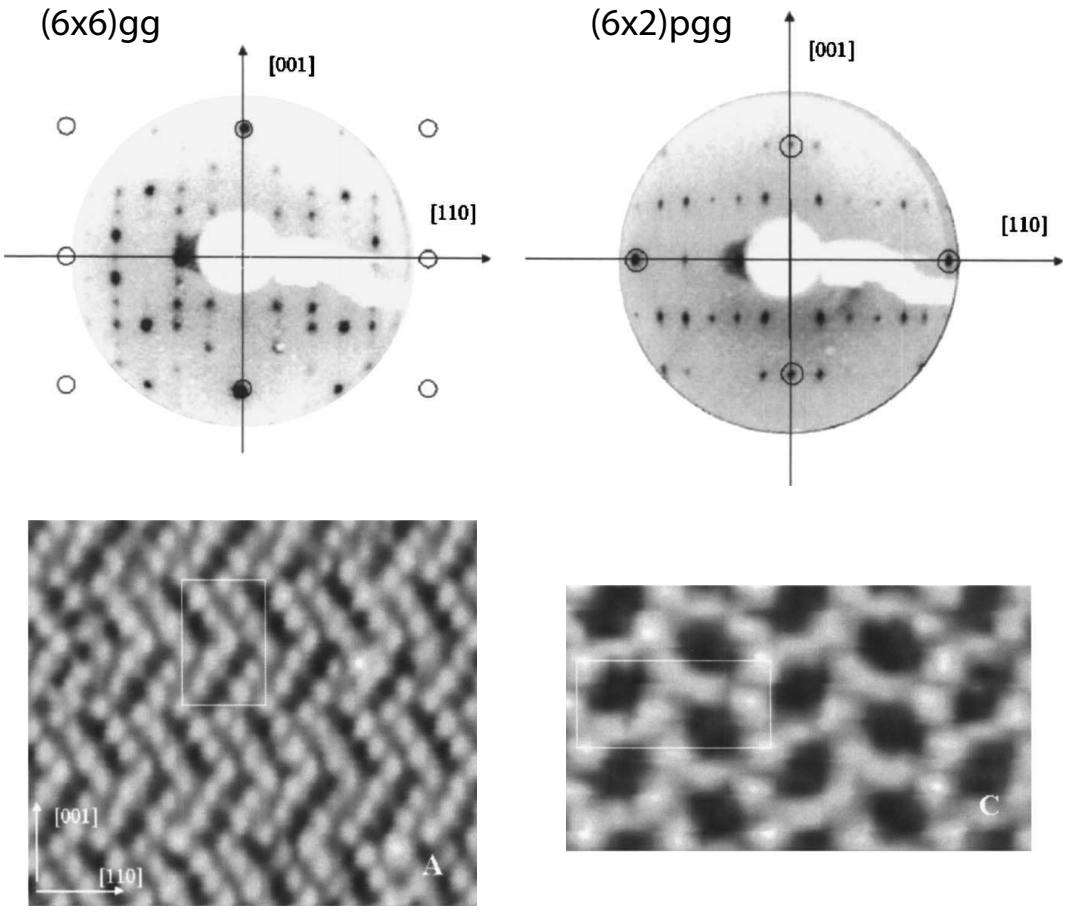

Figure 4.3: (top) LEED and (bottom) STM images from the (left) (6x6)gg and (right) (6x2)pgg overlayers of cytosine on Cu(110), reproduced from Frankel et al. [94].

DFT calculations considering an assembled overlayer found a preference for the molecule to adsorb via the O and N(1) atom in near atop sites (see Fig 4.4) [95]. They also predicted a staggered overlayer with species that are related in the [001] direction offset along the $[1\bar{1}0]$ direction with the molecular plane twisted from the

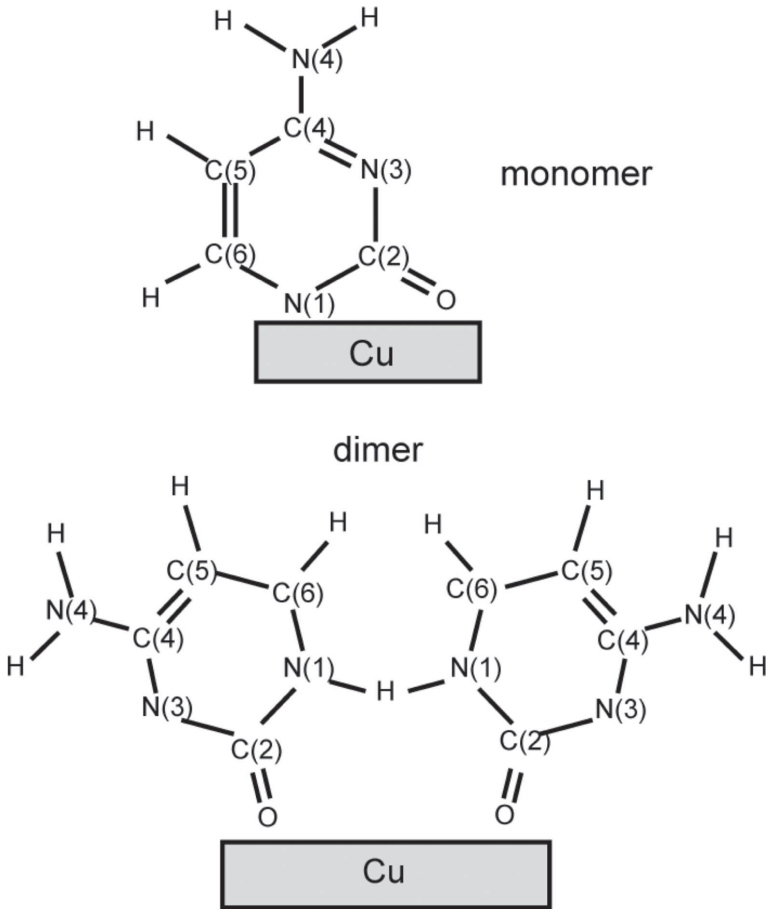

Figure 4.4: Two possible adsorption bonding configurations of cytosine-derived species on Cu(110). The deprotonated monomer is the structural model arising from the DFT study of Jackson et al.[95], and the hydrogen bridge-bonded dimer is the model proposed by Yamada et al [93].

$[1\bar{1}0]$ plane by 4° and tilted off the surface normal by 7°. Here we present the first quantitative experimental determination of the adsorption site using PhD.

4.2.2 Experimental details

Cytosine powder of 99% of purity was obtained from Sigma-Aldrich and loaded into a purpose-built evaporation source. This comprised a glass tube contained within a ceramic cylinder which was heated by passing a current through a copper wire coiled around it. The ceramic tube was used to improve the homogeneity of the heating, and the evaporation rate was controlled by monitoring the temperature of a tantalum end-cap of the source with a thermocouple. The evaporation source was placed in a differentially pumped six-way cross separated from the main chamber by a gate valve, a Cu gasket with a 7 mm diameter hole was placed between the cytosine source and the gate valve in order to collimate the cytosine flux and limit the pressure rise in the experimental chamber during dosing. No sharp overlayer LEED patterns of the type reported by Frankel et al. [94] were observed from any of our surface preparations, although our use of LEED was kept to a minimum to avoid electron-beam damage. Initial deposition led to a loss of order as indicated by LEED, but after annealing to $\sim$ 420 K a pattern showing strongly streaked half-order features did appear. The relative weakness of any possible fractional order diffraction features of the type (0 n/6), and the fact that the streaks indicated the presence of (1/2 m) beams, where m may take a range of fractional values (possibly 1/6th order), might suggest that the surface had a disordered form of the (6x2)pgg phase previously reported by Frankel et al. [94]. However, the recorded temperature to produce this surface is significantly lower than the value of 480 K reported by Frankel et al., and as is shown below, heating to 480 K led to very significant changes in the N 1s XPS data indicative of a different molecular species being present on the surface. On this basis it seems likely that if the streaked LEED pattern was associated with the (6x2)pgg phase, it may arise from small domains of a minority species on the surface.

4.2.3 Results and local structure determination

Spectral characterisation: XPS and NEXAFS

XPS N 1s spectra recorded after an initial deposition of cytosine, and after annealing to $\sim 420K$, are shown in fig. 4.5. These spectra are almost identical to those previously reported by Furakawa et al.[92], although in this earlier study the spectrum equivalent to that from our annealed surface appears to have been obtained by depositing to lower coverage ($\sim$ 0.2 ML) but without annealing. The as-deposited spectrum of fig 4.5 is similar to (but with more-clearly resolved features than) the

N 1s spectrum reported from a $\sim$ 20 nm deposited film of cytosine by Haug et al [96], and thus appears to be characteristic of intact molecular cytosine in a multilayer form, although in our case the film thickness is probably no more than $\sim$ 2 molecular layers.

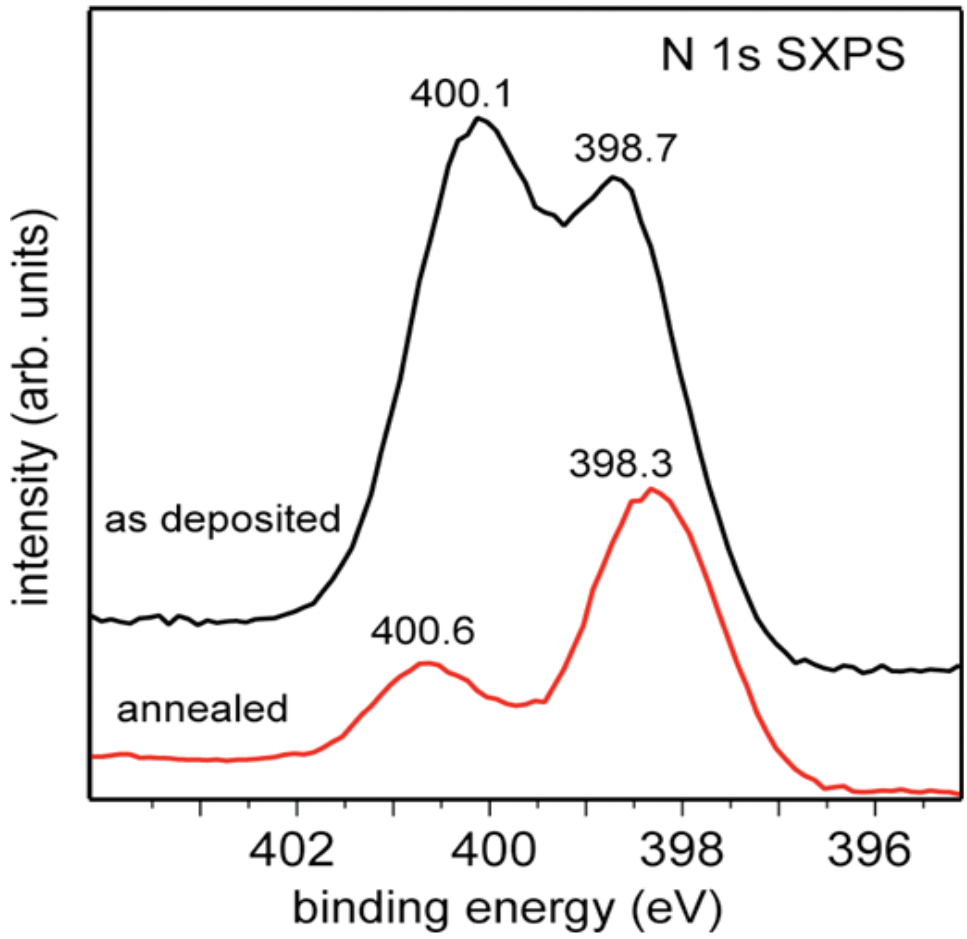

Figure 4.5: X-ray photoelectron spectra in the energy range of the N 1s emission from cytosine deposited on Cu(110) at room temperature, and after annealing to $\sim$ 420 K. The absolute binding energy scale is based on the value assigned to the deepest binding energy state by Furakawa at al [92]. The spectra were recorded at a polar emission angle of 60° using a photon energy of 500 eV.

The lower binding energy peak of the annealed surface is assigned to the two ring N species and the higher binding energy peak to the amino group. This assignment is consistent with the N(1) species (fig 4.1) deprotonating on adsorption.

While all the PhD data presented here were obtained from surfaces leading to N 1s spectra similar to that labelled 'annealed' in Fig. 4.5, we also characterised the effect of further heating or more prolonged annealing. These results are shown in Fig. 4.6. This figure shows a spectrum from a preparation used in the collection of the PhD data reported here in which the sample was briefly annealed after cytosine dosing to 420 K. The remaining spectra show the effect of more extended annealing (a total of $\sim$ 1.5 hours) at 420 K, and then heating more briefly to successively higher

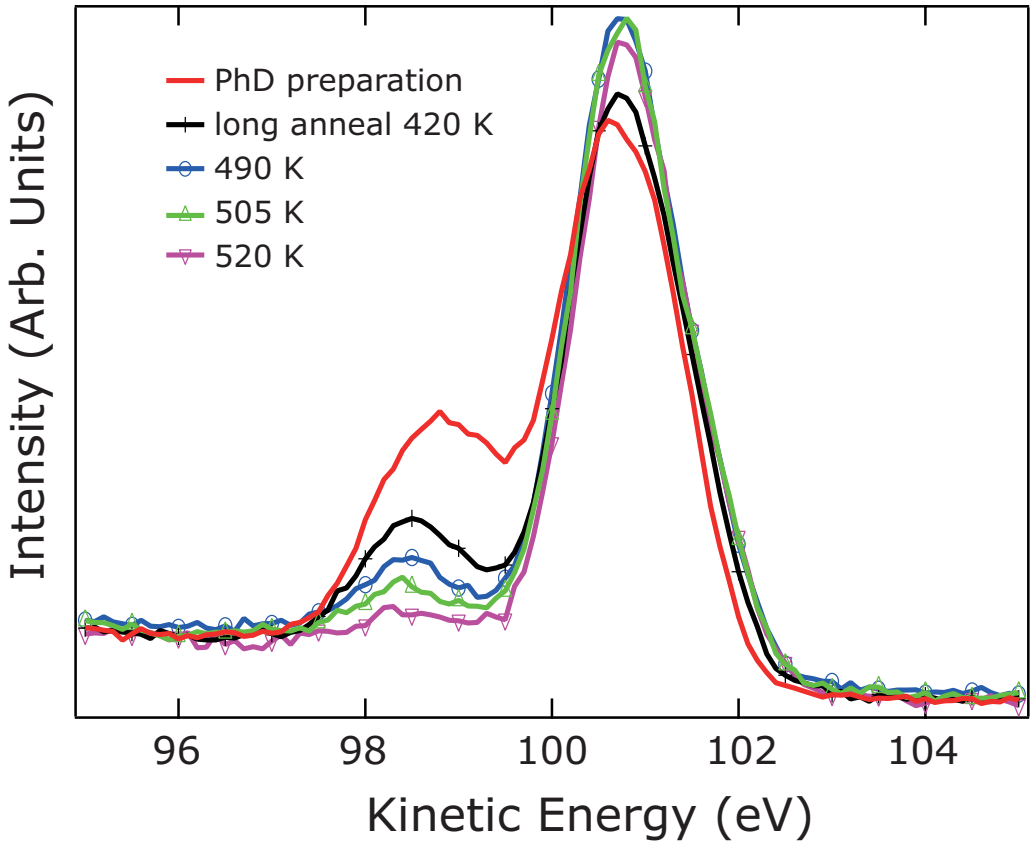

Figure 4.6: X-ray photoelectron spectra in the energy range of the N 1s emission from a preparation of cytosine on Cu(110) used in the PhD study reported here, and from a similar preparation subjected to extended annealing at 420 K and then to annealing to successively higher temperatures. The absolute binding energy scale is as in figure 4.5. The spectra were recorded at a polar emission angle of 40° using a photon energy of 500 eV.

temperatures. Clearly the higher binding energy N 1s peak, attributed to the amino N(4) atom, decreases in intensity, and finally almost vanishes, through this extended heating cycle to 520 K. There is an associated increase in the lower binging energy peak intensity. The clear implication is there is some significant chemical change at the N(4) amino site, most probably some degree of deprotonation. The O 1s XPS data show no change in this temperature range, and it is only on further heating to $\sim 550K$ that major decomposition and desorption occurs with only small residual peaks of C 1s, N 1s and O 1s. While it is difficult to compare temperature measurements in different sample holders, and the heating cycles used by Frankel et al. may also differ from ours, the fact that they report the (6x6) phase after heating to 370 K and the (6x2) phase after heating to 480 K may indicate that these two structural phases are associated with two distinct molecular species on the surface, with and without modified amino N(4) atoms.

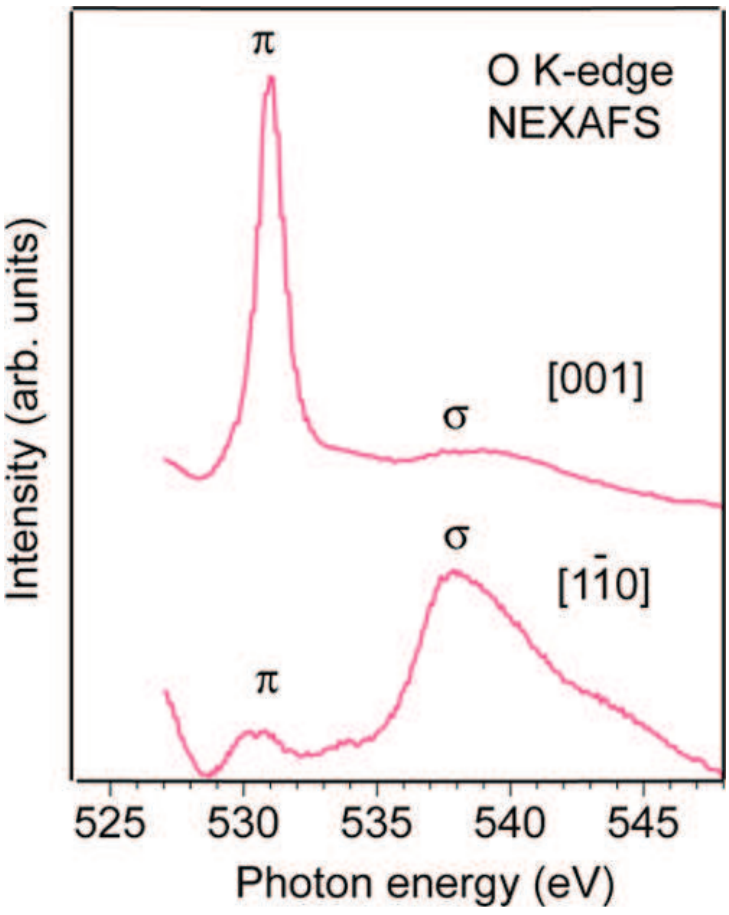

Figure 4.7: O K-edge NEXAFS data from cytosine deposited onto Cu(110) at room temperature and annealed to $\sim$ 400 K. Spectra were recorded at normal incidence with the polarisation vector in the two principal azimuths as shown.

As remarked in the introduction, Furakawa et al. [92] have already reported not only XPS data, but also both N and O K-edge NEXAFS from chemisorbed cytosine (without extended heating) on Cu(110). Our XPS data (Fig. 4.5) are almost identical

to theirs, so we may infer that our different surface preparations have led to similar adsorbed layers, but as a further check we also recorded a few NEXAFS spectra, notably O K-edge NEXAFS at normal incidence with the polarisation vector **E** in the two principle azimuths ([001] and $[1\bar{1}0]$). The resulting spectra are shown in Fig. 4.7. Two main peaks are observed and identified (as labelled) as corresponding to excitations into O-C π^* and σ^* shape resonances. Clearly the intensity of the π^* peak is at its maximum with incidence in the [001] azimuth, while the σ^* peak is largest with incidence in the $[1\bar{1}0]$ azimuth. The spectra are very similar to those reported by Furakawa et al., but while in their spectra the π^* resonance completely vanishes with the polarisation vector **E** along $[1\bar{1}0]$, and the σ^* similarly vanishes with E along [001], in our spectra the polarisation angle dependence is slightly less strong. Furakawa et al. concluded that their data showed the molecular plane to lie perpendicular to the surface and in the $[1\bar{1}0]$ azimuth. At first glance our own data suggest that there may be a small twist of the molecular plane out of this surface direction. However, the degree of polarisation of the incident radiation on the beamline we used in these experiments has been determined to be only 90% [72], and this alone can account for the small residual intensities of the resonances in the forbidden geometries. For comparison, however, it is worth noting that if the degree of polarisation was 100%, the azimuthal twist angle of the molecule required to achieve these residual features, based on the relative amplitude changes of the two resonance peaks measured in the two incidence directions, is approximately 15°. Our results thus indicate that any such twist, if present, must be (significantly) smaller than this.

PhD data: qualitative evaluation

A subset of the PhD modulation spectra, specifically those recorded in the $[1\bar{1}0]$ azimuth in the polar angle range from 0° to 40°, are shown in fig. 4.8. Data collected in the [001] azimuth are qualitatively similar. The striking feature of the data shown in fig. 4.7 is that the normal emission spectra recorded from both the O 1s peak and the low BE N 1s peak do show a single dominant long-period modulation characteristic of a backscattering direction, and that the energetic location and period for these two emitters is essentially the same. Moreover, the amplitude of modulations for these two emitter atoms falls off rather sharply as the detection angle is moved significantly away from normal emission. The clear implication is that both the O atom, and one of the N atoms that contributes to the low BE N 1s peak, are in near-atop bonding sites on the Cu surface, and have similar O-Cu and N-Cu bondlengths. Clearly, if the molecule bonds to the surface through both the O atom and a N atom, the bonding N atom must be either the N(1) or N(3) atom, both of which are adjacent to the O atom. As the XPS data indicates that the N(1) atom is deprotonated by interaction

with the surface, this atom is the more likely bonding atom. We may also note that steric effects probably preclude an adsorption geometry in which the molecule bonds through the O and N(3) atom, as the amino group would be too close to the surface. As we have identified the high BE N 1s peak as deriving from the amino N atom, the observation that this peak shows no strong PhD modulations over the full energy range measured (in any emission direction) is not surprising. If this N emitter atom is not bonded to the surface, scattering from the more distant Cu atoms will be weak, and intramolecular scattering from low atomic number atoms is only expected to contribute to the PhD modulations at the lowest energies.

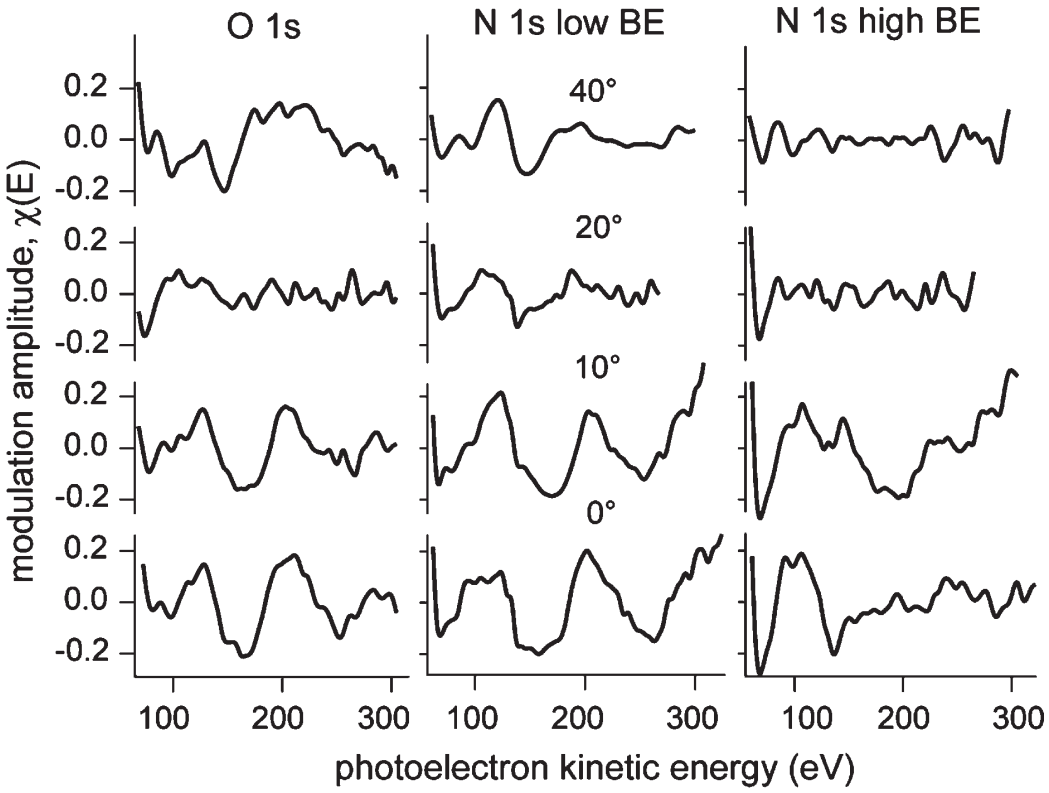

Figure 4.8: Summary of the experimental O 1s and N 1s PhD modulation spectra obtained in the [1$\bar{1}$0] azimuth at polar emission angles from 0° to 40°.

PhD data: quantitative modelling and structure determination

Calculations focussed on the more strongly-modulated PhD spectra arising from the O 1s, and the low-BE N 1s emission, assuming that the modulations of this N 1s emission can be represented by an incoherent sum of the emission from the N(1) and N(3) atoms. Because the N(3) atom is believed to not be involved in bonding to the Cu surface, and is therefore more distant from the surface, the scattering contribution from Cu atoms is weaker, and intramolecular scattering may be expected to dominate the PhD from this emitter. All calculations were therefore conducted

Table 4.1: Optimised values of the structural parameters obtained from the PhD analysis for chemisorbed cytosine on Cu(110) and from some of the DFT calculations by Jackson et al. [95]. Δxy values are the lateral offset parameters from atop site. Δz_1 values are the outward relaxation of the outermost Cu layer atoms, the O and N suffices relating to the Cu atoms directly below the O and N(1) bonding atoms of the cytosine.

Parameter	PhD exp.	DFT isolated	DFT overlayer
z_N (Å)	1.92 ± 0.03	1.98	1.99
d_{Cu-N} (Å)	$1.94(+0.07/-0.03)$	1.98	1.99
$z_{O(8)}$ (Å)	1.90 ± 0.03	1.94	1.93
$d_{Cu-O(8)}$ (Å)	$1.94(+0.06/-0.04)$	1.96	1.94
Θ (°)	$12(+7/-12)$	1.4	6.6
Φ (°)	$10(+20/-10)$	0.0	4.0
Δz_{Cu} (Å)	$-0.16(+0.06/-0.08)$	-0.13	-0.2
$\Delta z_{Cu(O(8))}$ (Å)	-0.04 ± 0.08	0.03	0.01
$\Delta z_{Cu(N)}$ (Å)	0.0 ± 0.1	0.01	0.06
Δxy_N (Å)	0.35 ± 0.50	0.09	0.15
Δxy_O (Å)	$0.4 \pm (+0.2/-0.6)$	0.23	0.21

using the complete molecule (but omitting the very weakly-scattering H atoms), using the known structure in crystalline cytosine [97].

Based on the NEXAFS results (Fig. 4.7), the molecule was initially assumed to have its molecular plane perpendicular to the surface and in the $[1\bar{1}0]$ azimuth, however, during the fit the molecular plane was allowed to tilt with respect to the surface normal (Θ) and twist around the surface normal with respect to the $[1\bar{1}0]$ (Φ).

In addition to these rotations, the relative lateral position of the molecule on the surface in the $[1\bar{1}0]$ (x) and [001] (y) directions, as well as perpendicular to the surface in the [110] (z) direction, was explored. In view of the fact that the experimental PhD spectra showed extremely weak modulations of doubtful reliability at the larger polar emission angles, the multiple-scattering simulations and structural optimisation were performed using a subset of seven such spectra, four O 1s and three low-BE N 1s, recorded at normal emission and 10° polar angle, as shown in fig. 4.9. No attempt was made to exploit the high BE N 1s PhD spectra in view of the absence of any clear and reliable modulations in the experimental spectra. Also shown in fig. 4.9 are the best-fit simulated spectra for the structure shown in Fig. 4.10. The parameter values associated with this structure are listed in Table 4.1. The associated R-factor is 0.20, a value that corresponds to a generally good fit that is well within the range of acceptable structural solutions by PhD. In the structure shown in Fig. 4.10 the bonding N and O atoms of the molecule, with an O-N distance shorter that the corresponding Cu-Cu distance of the substrate, are located approximately symmetrically between these two bonding Cu atoms in good agreement with the DFT

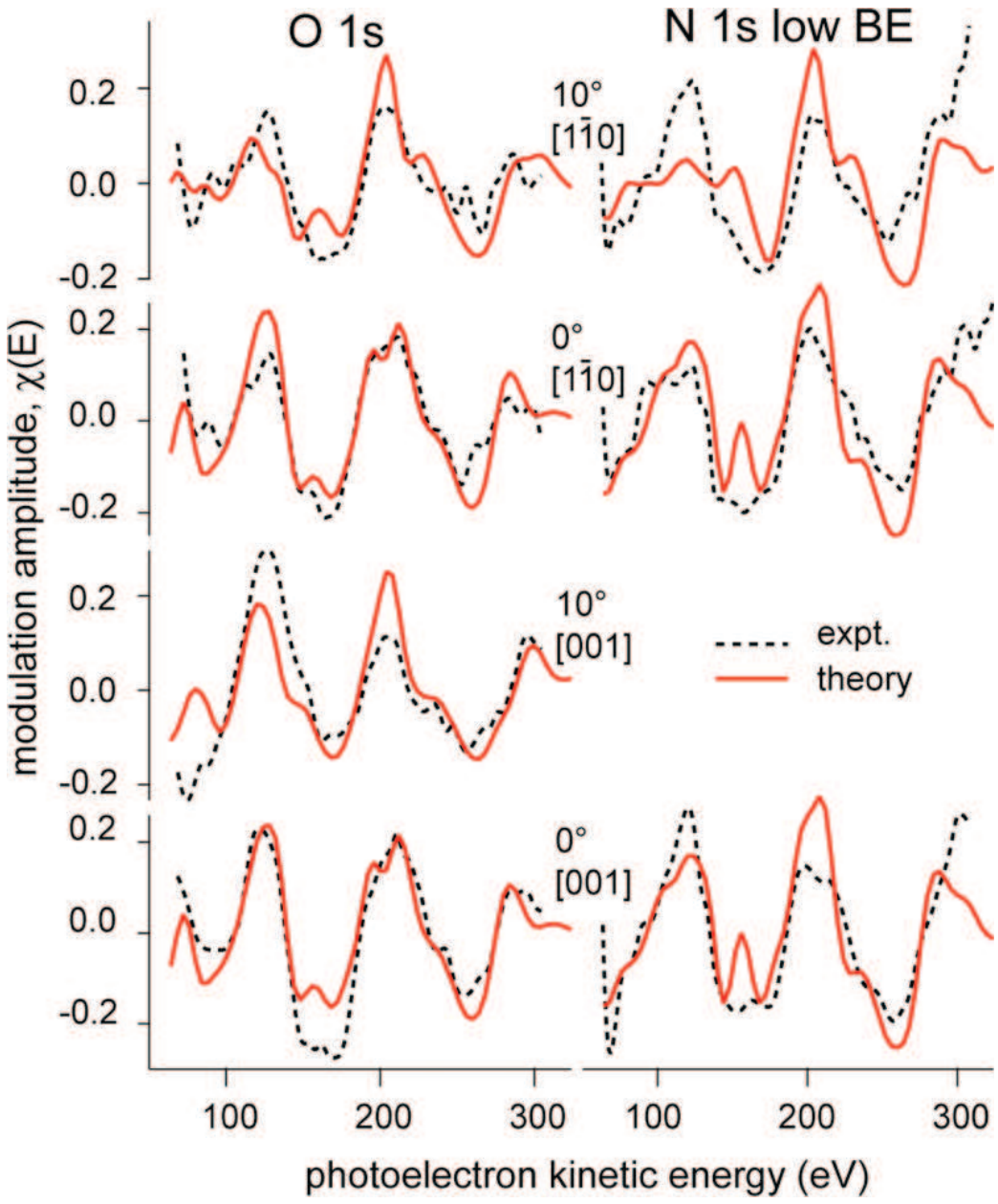

Figure 4.9: Experiment – theory comparison of the O 1s and N1s PhD modulation spectra for the best fit structure for cytosine on Cu(110). The parameters for the structure are shown in table 4.1 and the structure is shown schematically in Fig. 4.10.

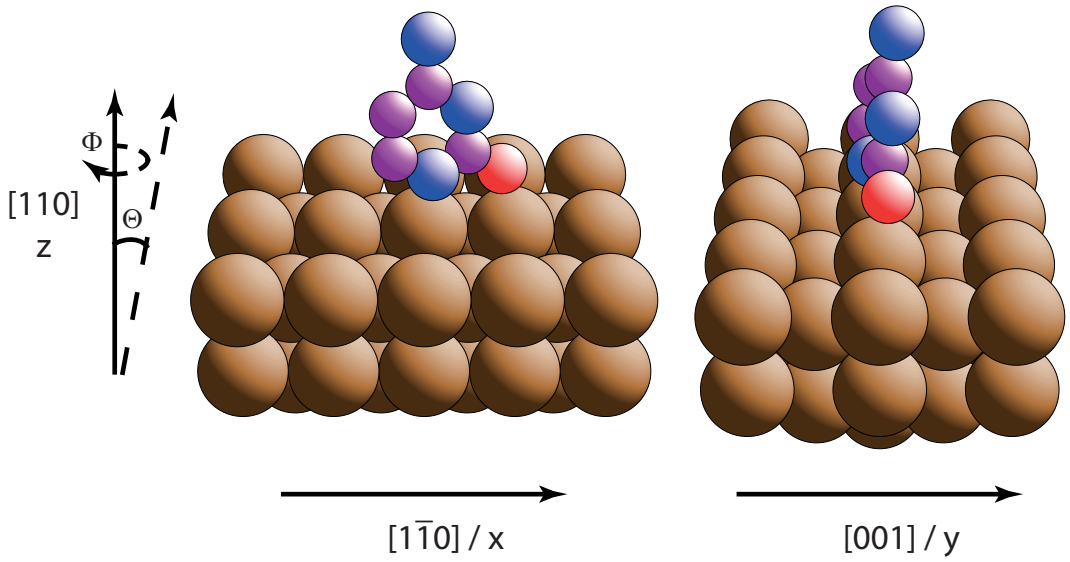

Figure 4.10: Schematic diagram of the optimised local structure of adsorbed cytosine on Cu(110). Note that the H atoms are omitted from this figure as the results presented here provide no direct information on the location of these atoms. Carbon atoms are represented by purple spheres, oxygen atoms by the red and nitrogen by the blue.

calculations of Jackson et al. [95].

However, this solution does have rather large vibrational amplitudes for intramolecular scattering (0.5±0.2 Å), a result also found in the earlier study of thymine adsorption [91]. The physical origin of this effect is unclear, but it influences only the final quality of the experiment/theory fit, and not the optimised structural parameters. We also note that in a search of the tilt angle Θ, a second R-factor minimum was found for values of $+30°$ and $-30°$. These values are clearly incompatible with the NEXAFS data. Although PhD from adsorbate species is relatively insensitive to relaxations of the underlying surface, Table 4.1 does reveal an interesting trend in the values of the relaxations, perpendicular to the surface, of the outermost Cu atom layer. In particular, Δz_1, the relaxation of the atoms in the first layer, that are not bonded to the molecule, show a significant inwards shift, characteristic of the clean Cu(110) surface, the Cu atoms directly below the O and N(1) bonding atoms of the cytosine adopt an outermost layer spacing that is much closer to the ideally-terminated bulk. This same effect is seen in the results of the DFT calculations [95].

4.2.4 General discussion

O 1s and N 1s PhD results, in combination with N 1s XPS and O K-edge NEXAFS, provide a detailed description of the local adsorption geometry of chemisorbed cytosine Cu(110). In particular, the molecule bonds to the surface through the O

atom and the adjacent deprotonated N atom that both occupy off-atop sites along the close-packed $[1\bar{1}0]$ direction. The molecular plane is essentially perpendicular to the surface and lies in, or very close to, the $[1\bar{1}0]$ azimuth. The associated Cu-N and Cu-O bondlengths are $1.94(+0.07/-0.03)$ Å and $1.94(+0.06/-0.04)$ Å, respectively, in excellent agreement with the DFT calculations of Jackson et al.[95].

Our conclusions regarding the bonding and structure are very significantly different from those of Frankel et al. [94], who proposed that cytosine in the (6x2)pgg phase is adsorbed as a hydrogen-bonded dimer with substrate bonding through the O atoms alone. However, our XPS results lead us to suggest that the higher-temperature annealing (to ~ 480 K) used by Frankel et al. to obtain the (6x2)pgg phase may mean that the surface species leading to this phase is distinctly different from that present at the lower annealing temperatures used in our PhD structural study. What is evident from our XPS and PhD data is that neither the low or high temperature phases produced by cytosine adsorption on Cu(110) can correspond to cytosine dimers as shown in Fig. 4.4; our XPS (and that of Furakawa et al. [92]) clearly shows N(1) dehydrogenation at the lowest temperatures. Moreover, at higher temperatures our XPS results can only be interpreted in terms of significant modification - presumably partial dehydrogenation - of the amino N(4) atom. What is possible, of course, is that this species itself forms dimers, with hydrogen bonding through the partially deprotonated amino groups, that then form a (6x2)pgg structure in a similar way to that proposed by Frannkel et al. for cytosine dimers.

4.3 Uracil on Cu(110)

4.3.1 Introduction

The nucleobase uracil, which is paired with adenine in RNA and is replaced by thymine in DNA, is shown schematically in Fig 4.1 & 4.11. There have been rather few studies of uracil adsorption on surfaces at the solid-vacuum interface although the gold / uracil system has attracted significant interest in model electrochemical studies of nucleobase/metal surface interactions. At different applied potentials both physisorbed and chemisorbed species have been proposed, but while there have been several investigations using in situ STM (scanning tunnelling microscopy), no significant information regarding the adsorption geometry at the interface has emerged from most of these studies. Much of this work has been reviewed by Li et al. [98], and through a combination of STM and infrared spectroscopy, they did identify a chemisorbed phase in which they concluded that uracil bonds through the N(3) atom (Fig 4.1) and the two adjacent O atoms with its molecular plane perpendicular to the surface. This geometry is similar to the Cu(110)/thymine structure [91] and is also

consistent with our findings for Cu(110)/uracil reported here. The exact location of the chemisorbed uracil on the Au(111) surface was not, however, identified.

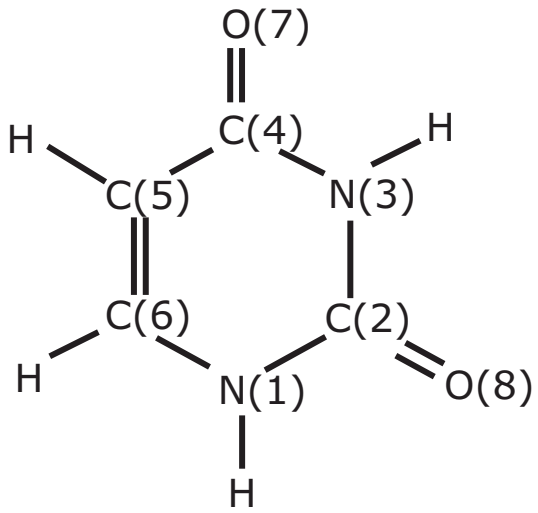

Figure 4.11: Schematic diagram of the uracil molecule.

At the solid-vacuum interface there have been a few studies of uracil adsorption on Cu(110), but little resulting structural information. A brief report of a STM investigation of this system remarks only on the adsorbate-induced surface faceting that occurs at elevated temperatures [99]. Some limited structural information is provided by ARUPS (angle-resolved ultraviolet photoemission spectroscopy) data, which indicate that the molecular plane lies perpendicular to the surface, orientated along one of the substrate mirror symmetry planes[100]. A density functional theory (DFT) calculation of Cu-uracil complexes finds Cu–O bonding to be preferred over Cu–N bonding, with Cu–N and Cu–O bondlengths in the ranges 1.98–2.16 Å and 1.88–2.07 Å, respectively, depending on the ionisation state of the complex [101]. Here, we show that application of the PhD technique to this adsorption system provides a rather complete picture of the local adsorption geometry.

4.3.2 Experimental details

Uracil powder of 99+% purity was obtained from Alfa Aesar. During sample dosing the uracil powder was heated to 575 K, while the substrate was kept at room temperature. No ordered overlayer was observed by LEED. Based on a comparison of the O 1s and Cu 2p photoemission intensity ratio obtained from a Cu(110)(2x1)-O surface the uracil coverage of the surface studied was estimated to be ~ 0.25 ML.

4.3.3 Results

Characterisation by XPS and NEXAFS

Fig. 4.12 shows XP spectra recorded around the O 1s, N 1s and C 1s core level photoemission peaks from uracil on Cu(110), immediately after deposition at room temperature, and after annealing to 500 K. Initial dosing with the surface at 500 K led to spectra identical to those obtained by annealing the lower-temperature deposited layers. While the room-temperature deposited layer exhibits two chemically-distinct N 1s components, annealing to 500 K leads to an almost complete loss of one component and increase of the other, accompanied by a small energy shift. The O 1s spectra, on the other hand, show only a single peak under both conditions, although in this case too, there is a shift in the peak energy following annealing. This behaviour is essentially identical to that seen for thymine on Cu(110) by both Furukawa et al. [92] and Allegretti et al. [91]. Note that as we are primarily interested in relative peak energies and chemical shifts, no experimental absolute calibration of the binding energies was undertaken, but because of the close similarity of these uracil and thymine data our measured values (nominal photon energy minus measured kinetic energy) were adjusted to align the main peaks of the N 1s and O 1s spectra to those previously reported for adsorbed thymine. A similar interpolated energy shift has been applied to the C 1s spectra. The interpretation of the N 1s spectra proposed in the thymine studies was that one of the N atoms in the molecule is dehydrogenated upon adsorption, while heating to 500 K leads to dehydrogenation of the other N atom. For thymine on Cu(110) this second dehydrogenation step is supported by the results of temperature programmed desorption measurements that show H_2 desorption occurs at 463 K [102, 103]. It is therefore infered that similar dehydrogenation steps occur at similar temperatures for uracil on Cu(110). Notice that the higher binding energy component of the N 1s spectrum from the as-dosed surface at 300K seems to be significantly more intense than that of the lower binding energy (deprotonated) component, perhaps indicating some fractional coverage of intact uracil on the surface. In this regard, too, the data from thymine on Cu(110) show exactly the same effect[91]. The observation of only a single O 1s peak is taken to imply that both oxygen atoms in the molecule inhabit similar (if not identical) bonding environments.

The O K-edge NEXAFS spectra are shown in Fig. 4.13 for polar incidence angles of normal incidence and 60° off normal incidence, corresponding to values of the angle θ_p between the principal polarisation vector **E** and the surface normal of 90° and 30°; these spectra were recorded in each of the two principal azimuths from uracil on Cu(110), after dosing at room temperature. In this case, too, the uracil data are closely similar to those reported for thymine on Cu(110) by Allegretti et al. [91] and Furukawa et al. [92], indicating that the orientation of the uracil and thymine

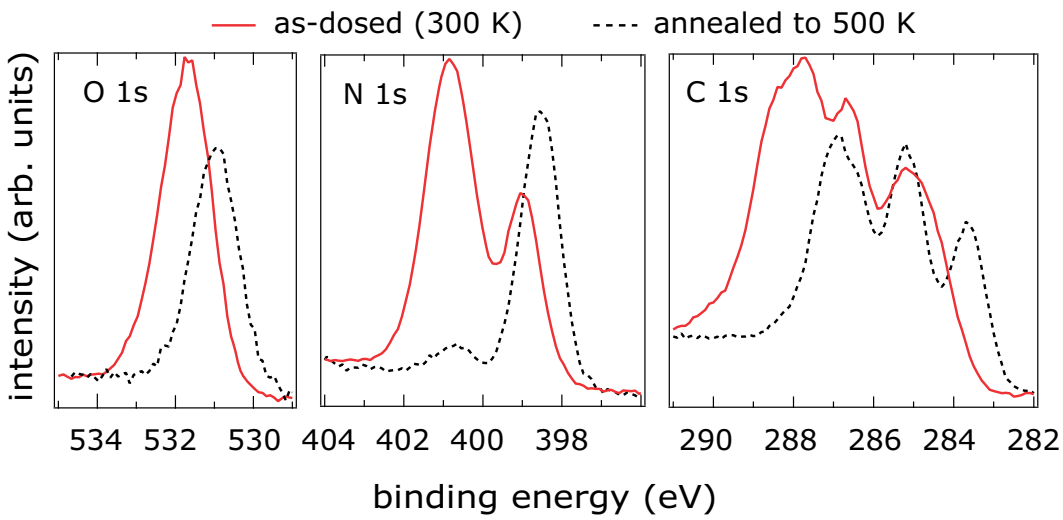

Figure 4.12: Comparison of the XPS in the energy range of the (from left to right) O 1s, N 1s and C 1s emission peaks from uracil deposited on Cu(110) at room temperature, and after annealing to $\sim$ 500 K. The spectra were recorded at normal emission with photon energies of 650 eV, 500 eV and 400 eV for the O 1s, N 1s and C 1s regions, respectively. Absolute binding energies have been adjusted as described in the text.

molecules on Cu(110) are similar. The spectra are dominated by two features, namely a sharp doublet π^* feature at the absorption edge, and a broader σ^* feature at higher energy. That the π^* feature is strongest for normal incidence (**E**-vector parallel to the surface) with the **E**-vector lying along [001] indicates that the molecular plane is approximately perpendicular to the surface and lies within the $[1\bar{1}0]$ azimuth. The angular dependence of the σ^* resonance is consistent with this interpretation. Notice, though, that the fact that the π^* resonance peak does not vanish at normal incidence with the **E**-vector lying along $[1\bar{1}0]$, and that the σ^* resonance does not vanish at normal incidence with the **E**-vector lying along [001] may indicate that there is some twist and tilt of the molecule relative to this ideal high-symmetry orientation. These residual features, however, may also be attributed to the fact that the incident radiation is not 100% linearly polarised.

A more quantitative estimate of the molecular orientation was obtained by fitting the four NEXAFS spectra shown in Fig. 4.13 with the sum of a sloping background, a step function, and five Gaussian peaks. Two identical Gaussian functions were used to fit the sharp π^* doublet feature, and three different Gaussian functions were fitted to the broad σ^* features. Fitting the σ-resonance region of NEXAFS spectra by multiple peaks is of questionable physical significance, but provides a convenient means to achieve more meaningful fits to the much sharper π-resonance peaks; it is the polarisation-angle dependence of only these sharper peaks that we use to extract the molecular orientation. The ratios of the intensities of the doublet features for the four spectra, normalised by the height of the step function, were then used

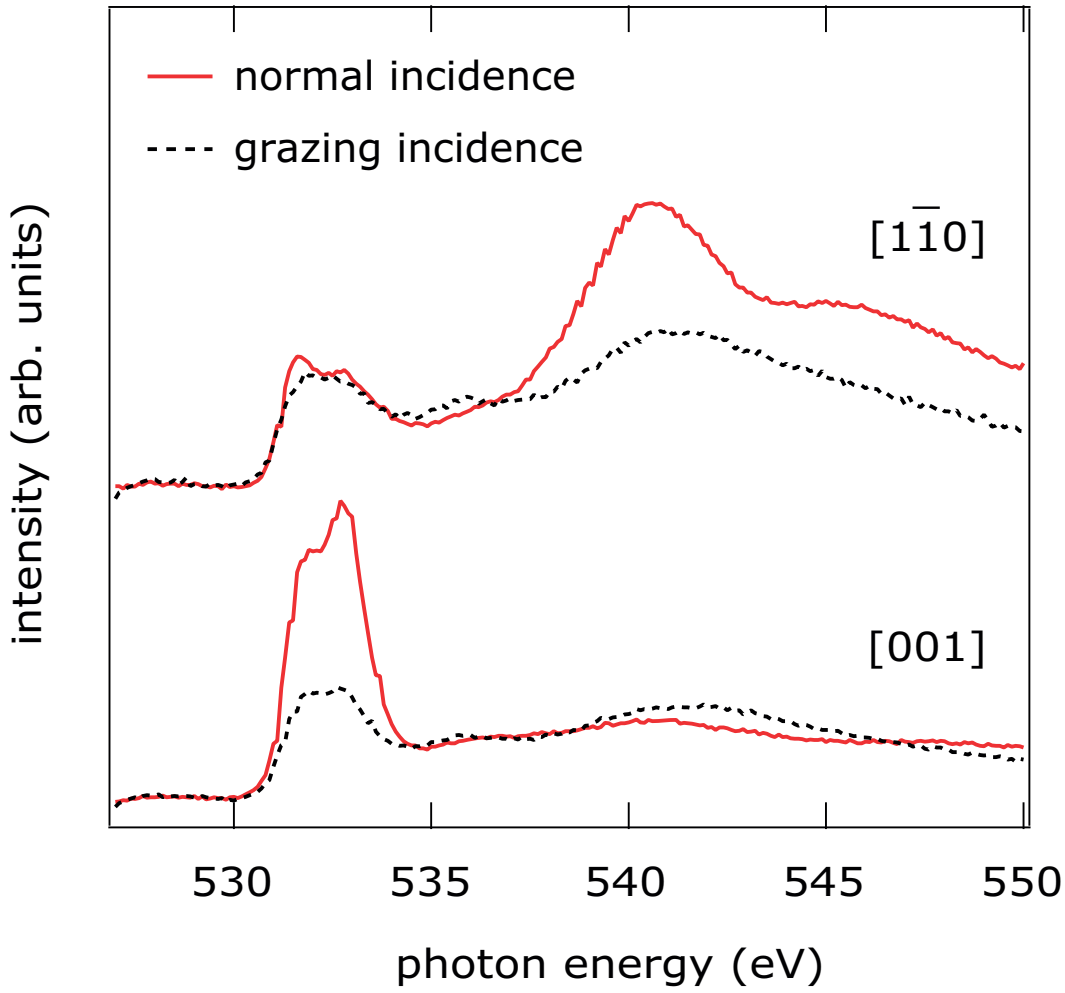

Figure 4.13: O K-edge NEXAFS data from uracil deposited onto Cu(110) at room temperature. Spectra are shown for two polar incidence angles (normal incidence and a grazing incidence, 60° off normal incidence), in each of the two azimuthal angles. The spectra are normalised to the intensity of the adsorption edge step.

to determine the tilt of the molecule with respect to the surface normal (Θ) and the twist of the molecule with respect to the $[1\bar{1}0]$ direction of the surface (Φ). The two angles were determined to be $10 \pm 15°$ and $15 \pm 15°$ respectively. Note that for these calculations the degree of polarisation was assumed to be 90%, as reported for this beamline [72].

The doublet character of the π^* resonance seen here is also a feature of the NEXAFS spectra of thymine. It has been seen for thymine adsorbed on Cu(110) in a partially deprotonated form [91, 92], but also in deposited thin films of both thymine and uracil [104]. The doublet has been interpreted as indicative of the inequivalence of the two carbonyl species, resulting from the different environment within the molecular ring occupied by the C(2) and C(4) atoms; as such it is believed to be a feature of the localised NEXAFS final state. This interpretation is consistent with the fact that there is no evidence in any of these studies of a similar spectral splitting in the O 1s XPS data for which the final state is delocalised in the continuum. Fuji et al. [104] actually assign the lower and higher energy π-resonances to the O(7) and O(8) atoms, respectively, but do not explain this assignment and we do not make any such assignment here. Why the relative intensities of the two components of the doublet should appear to be weakly dependent on the polarisation direction of the incident radiation is unclear, but exactly the same effect is seen in the data recorded from thymine on Cu(110)[91, 92].

Qualitative analysis of the PhD data

Figure 4.14 shows a comparison of the PhD spectra from both the lower and higher binding energy N 1s peaks seen in Fig. 4.12 in the seven emission directions showing the largest modulation amplitudes, together with the four O 1s PhD spectra showing the strongest modulations. These data were collected from surfaces prepared by deposition of uracil with the Cu(110) substrate at room temperature, with no subsequent annealing. As remarked above, the XPS from such a preparation shown in Fig. 4.12 may indicate the presence of some weakly coadsorbed intact uracil. A coadsorbed component of this type is not expected to form strong (short) bonds to the Cu surface, so emission from this species is unlikely to contribute significantly to the observed PhD modulations and will not, of course, have any influence on the PhD spectra from the lower binding energy (deprotonated) N 1s component; it is therefore not considered further in our analysis. The presence of a weakly-coadsorbed species of this type was deemed to be preferable to a fractional coadsorbate coverage of the fully deprotonated species that is produced by partial annealing.

The PhD spectra of Fig. 4.14 from the lower binding energy N 1s peak show significantly stronger modulations than those from the higher binding energy peak,

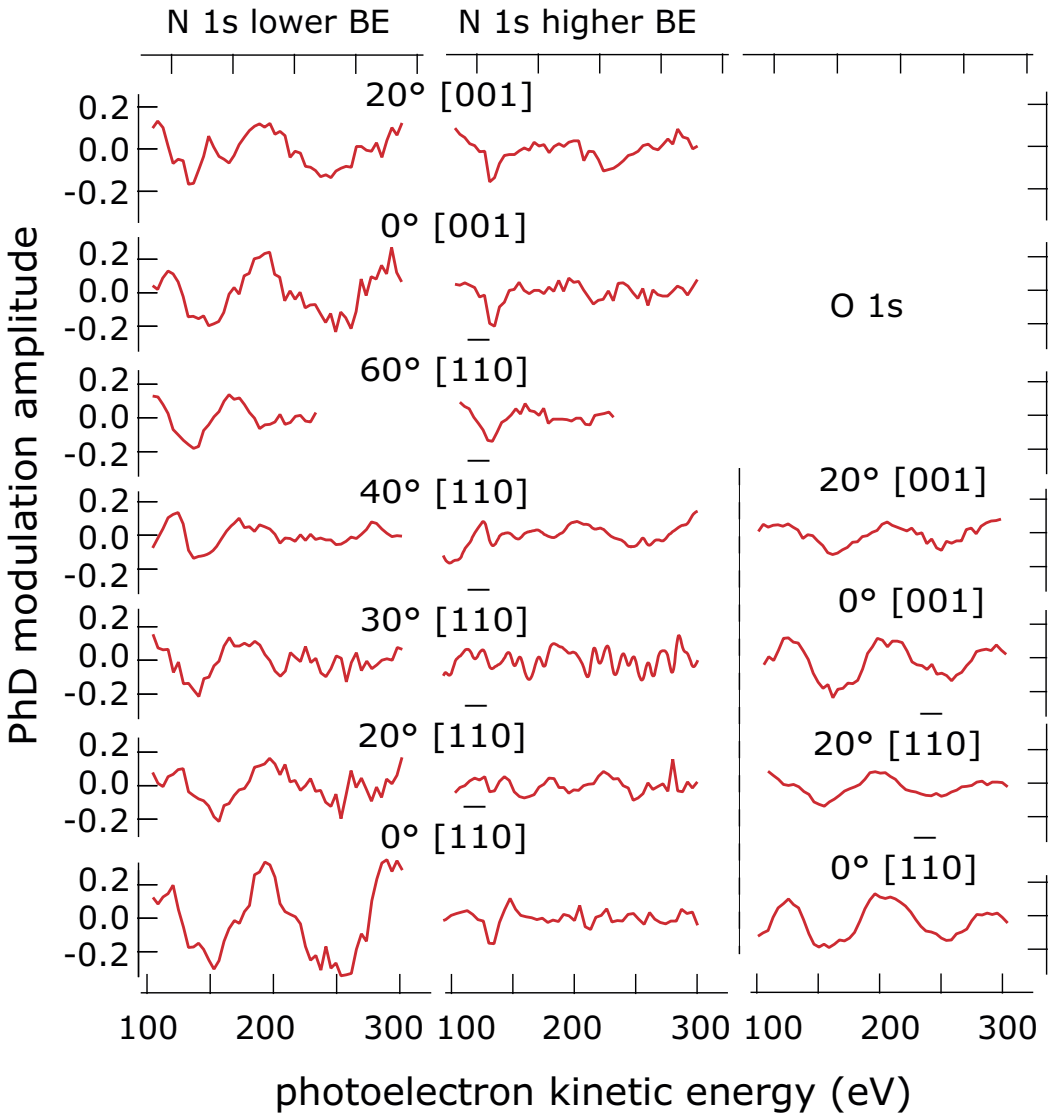

Figure 4.14: O 1s and N 1s PhD spectra from uracil deposited onto Cu(110) at room temperature. Shown are the seven N 1s spectra from the higher and lower binding energy peaks seen in Fig 4.12, and from the four O 1s spectra that show the largest modulations.

while the strongest modulations for both this N 1s component, and O 1s peak, occur at angles close to normal emission. These dominant long period modulations strongly suggest that both the nitrogen emitter atom with the lower 1s binding energy (attributed on the basis of the XPS to a deprotonated N in the uracil ring), and at least one of the two oxygen emitter atoms, are sufficiently close to the substrate to be involved in the molecule/surface bonding. Furthermore, we may infer that all these bonding atoms are in atop or near-atop sites. The close similarity of the energies of the main maxima in the normal emission O 1s and (bonding) N 1s PhD spectra also indicates that the Cu-O and Cu-N bondlengths must be quite similar. The fact that the O 1s modulation amplitudes are significantly weaker than those of the N 1s emission could be indicative of either one of two alternative scenarios. One is that only one of the oxygen atoms is bonding to the surface while the other is much further from the surface and thus contributes very little to the PhD modulations due to the weak scattering of the more distant Cu atoms. Alternatively, both oxygen atoms may bond to the surface but either occupy slightly different sites such that their PhD modulations are slightly out of phase, or occupy similar sites that are further displaced from the most symmetric atop sites than those occupied by the bonding nitrogen atom.

The fact that the XPS shows only a single O 1s peak strongly suggests that the two O atoms have similar bonding environments, favouring a structure in which the uracil bonds to the surface through both O atoms and the (deprotonated) N(3) atom that lies between them. This would also be consistent with the structure found for thymine on Cu(110). On the basis of the preliminary evaluation of our data, however, we cannot formally exclude the possibility that uracil bonds to the surface through only one (O(8)) oxygen atom and the (deprotonated) N(1) atom. Nevertheless, both basic structural models of the uracil/Cu bonding have been explored in our quantitative evaluation of the PhD spectra, as described below.

4.3.4 Quantitative analysis of the PhD data

Simulations were performed for the complete set of O 1s and low-binding-energy N 1s PhD spectra (seven N 1s spectra, and four O 1s spectra) shown in Fig. 4.14, and the global R-factor for these eleven spectra was the parameter minimised in the fitting procedure.

For both the basic models (substrate bonding through the N(1) and O(8) atoms, or bonding through the N(3) and both O atoms) calculations were performed with the adsorbed molecule constrained to retain the intra-molecular bondlengths and bond angles similar to those found in crystalline solid uracil [105], although small relative displacements of the O and N atoms bonding to the surface were allowed. The

Table 4.2: Comparison of the structural fitting parameters for thymine on Cu(110) [91], cytosine on Cu(110) [95], and the N(1)/O(8) and O(7)/N(3)/O(8) bonding models for uracil on Cu(110). It is important to note that, although O(7) and O(8) have been assigned below, it has not been possible to differentiate which O atom is further away from the surface in the O(7)/N(3)/O(8) bonding model of uracil. The four values for the relaxation of the Cu surface atoms perpendicular to the surface, Δz, are with respect to an ideal bulk-terminated structure. The z values are distances perpendicular to the surface, xy values parallel to the surface, and d values are interatomic distances.

Parameter	Uracil $N_{(1)}/O_{(8)}$ bonding	Uracil $O_{(7)}/N_{(3)}/O_{(8)}$ bonding	Thymine	Cytosine
z_N (Å)	1.95 ± 0.03	1.94 ± 0.03	1.96 ± 0.02	1.92 ± 0.03
d_{Cu-N} (Å)	1.96 ± 0.04	1.96 ± 0.04	1.96 ± 0.02	$1.94(+0.07/-0.03)$
$z_{O(7)}$ (Å)	–	1.90 ± 0.04	2.00 ± 0.03	–
$d_{Cu-O(7)}$ (Å)	–	1.96 ± 0.04	2.03 ± 0.03	–
$z_{O(8)}$ (Å)	1.89 ± 0.02	1.83 ± 0.04	1.87 ± 0.03	1.90 ± 0.03
$d_{Cu-O(8)}$ (Å)	1.94 ± 0.02	1.93 ± 0.04	1.91 ± 0.03	$1.94(+0.06/-0.04)$
ϕ (°)	6 ± 7	11 ± 5	2 ± 5	$12(+7/-12)$
Θ (°)	$45(+20/-10)$	5 ± 20	24 ± 10	$10(+20/-10)$
Δz_{Cu} (Å)	-0.05 ± 0.05	-0.04 ± 0.05	–	$-0.16(+0.06/-0.08)$
$\Delta z_{Cu(O(7))}$ (Å)	–	-0.1 ± 0.1	0.05 ± 0.10	–
$\Delta z_{Cu(O(8))}$ (Å)	-0.05 ± 0.03	0.0 ± 0.1	0.05 ± 0.10	-0.04 ± 0.08
$\Delta z_{Cu(N)}$ (Å)	-0.21 ± 0.07	-0.17 ± 0.05	-0.08 ± 0.10	0.0 ± 0.1
Δxy_N (Å)	0.15 ± 0.15	$0.25(+0.20/-0.10)$	–	0.35 ± 0.50
Δxy_O (Å)	$0.4(+0.2/-0.4)$	$O_{(7)}0.5(+0.4/-0.6)$ $O_{(8)}0.6(+0.2/-0.6)$	–	$0.4 \pm (+0.2/-0.6)$
d_{N-O} (Å)	2.3 ± 0.2	$2.3(+0.1/-0.2)$	2.3 ± 0.2	2.3 ± 0.3

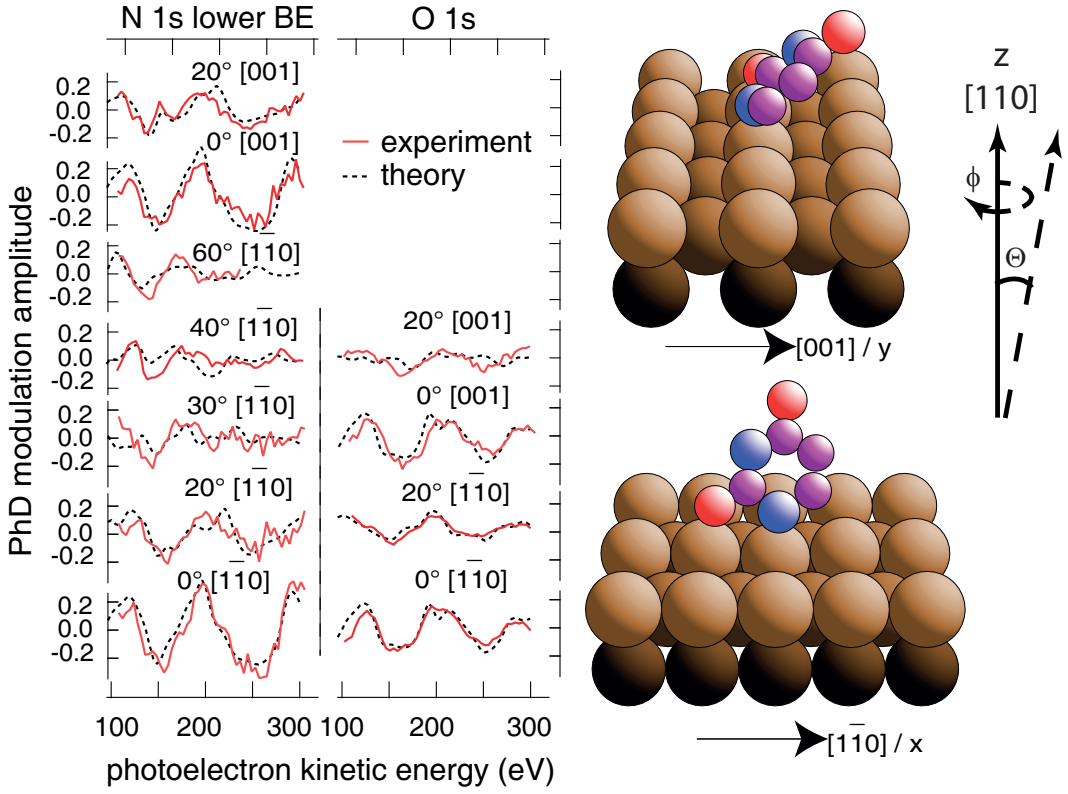

Figure 4.15: Comparison of the experimental and theoretical PhD spectra, and schematic representation of the structure, for the best-fit parameters of the N(1)/O(8) model (as listed in Table 4.2). H atoms are omitted from this figure as the results presented here provide no direct information on the location of these atoms. Carbon atoms are represented by the purple spheres, oxygens atoms by the red and nitrogen by the blue.

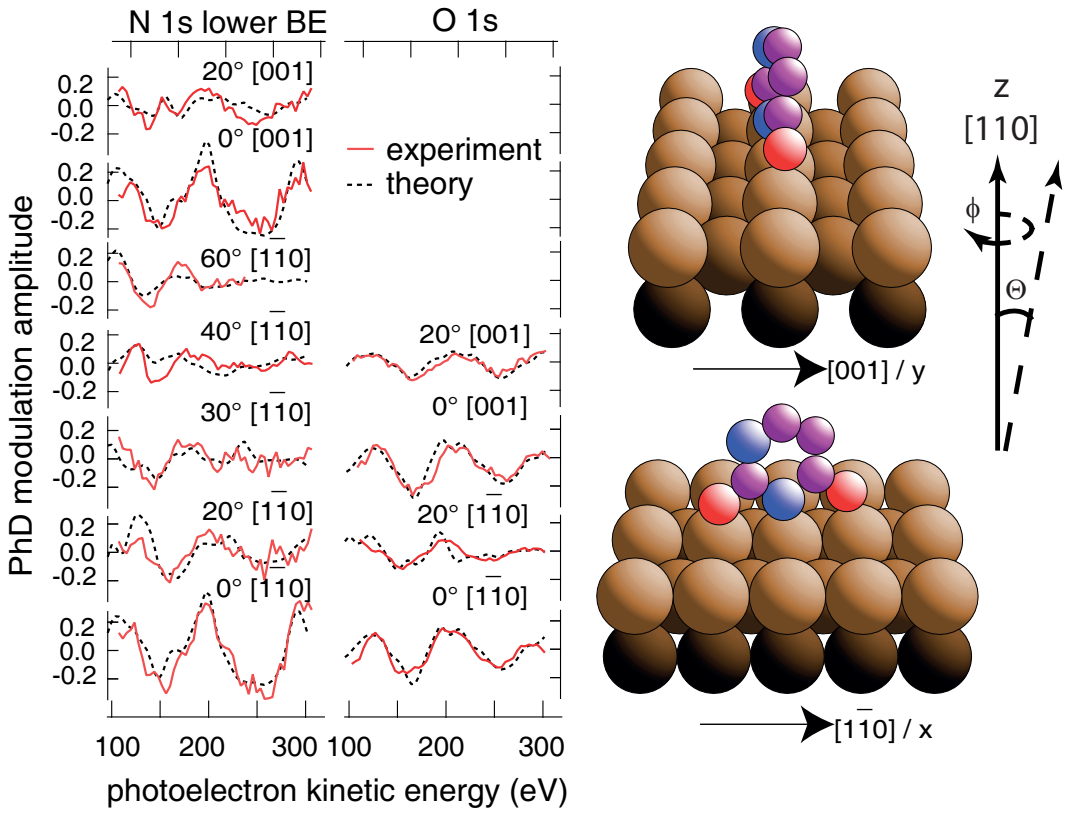

Figure 4.16: Comparison of the experimental and theoretical PhD spectra, and schematic representation of the structure, for the best-fit parameters of the N(3)/O(7)/O(8) model (as listed in Table 4.2). H atoms are omitted from this figure as the results presented here provide no direct information on the location of these atoms. Carbon atoms are represented by the purple spheres, oxygens atoms by the red and nitrogen by the blue.

(rigid) molecular plane was allowed to tilt by an angle, Θ, from the surface normal, and to twist by an angle, ϕ, with respect to the $[1\bar{1}0]$ azimuth. Both rotations were centred on the bonding N atom which was allowed to vary in height above the surface (z_N) and to move to off the ideal atop site by an amount (Δxy_N). In order to establish the primary influence of these rotations on the intramolecular scattering, and avoid confusion with the (much greater) influence of changes in the height of the O emitter atoms above the substrate, the bonding oxygen atom(s) was (were) excluded from the Θ rotation. The height of the bonding oxygen atom or atoms above the surface ($z_{O(7)}$ and $z_{O(8)}$) were allowed to vary (independently), as was the distance between the bonding oxygen atom or atoms and the bonding N atom (r_{N-O}); for the O(7)/N(3)/O(8) bonding model these two distances were assumed to be the same. Cu atoms in the outermost substrate layer were allowed to relax perpendicular to the surface, with different values for the Cu atoms that are nearest-neighbours to the bonding atoms of the uracil, ($\Delta z_{Cu(O7)}$, $\Delta z_{Cu(O8)}$, $\Delta z_{Cu(N)}$), and for the remainder of these surface Cu atoms (Δz_{Cu}). The R-factor values for the best-fit structure for the alternative models involving bonding through the N(1) or the N(3) nitrogen atoms were 0.19 and 0.20, respectively. The Cu-N bondlength in both structures was determined to be 1.96 ± 0.03 Å. For the model involving bonding through the N(1) and O(8) atoms the Cu-O bondlength was determined to be 1.94 ± 0.05 Å while – for the model involving substrate bonding through the N(3) atom and both O atoms – Cu-O bondlengths of 1.93 ± 0.04 and 1.96 ± 0.04 Å were found. As these are the structural parameters to which the PhD technique is most sensitive, it is reassuring, but also unsurprising, that the two models return very similar bondlengths. The other structural parameter values found for these two alternative models are shown in table 4.2, together with the comparable values for adsorbed thymine and cytosine on Cu(110). Comparisons of the theoretical and experimental PhD modulations spectra for these two structures, together with schematic representations showing the adsorption geometry, are presented in Figs. 4.15 and 4.16.

The difference between these two R-factors (0.01) is significantly smaller than the variance in the lowest value (0.03), so on the basis of this PhD analysis alone, it is not possible to formally exclude either model. However, one further significant difference in the two best-fit structures of table 4.2 is the optimum value of the tilt of the molecular plane away from surface normal, Θ. This parameter has a value of $45(+20/-10)^\circ$ for the O(8)/N(1) bonding model, and $5 \pm 20^\circ$ for the model involving bonding through the N(3) atom and both O atoms. Only the second of these molecular orientations is consistent with the value obtained from the NEXAFS data of $15 \pm 15^\circ$. The combination of NEXAFS and PhD results therefore lead us to conclude that the O(8)/N(1) bonding model can be excluded, supporting the assumption made from inspection of the XPS data. Note that two other structures corresponding to

local minima in the R-factor structure could also be excluded. Specifically, for the N(1)/O(8) bonding model an alternative solution was found with a tilt of $15(+10/-5)^\circ$, but its R-factor of 0.26 falls outside the variance of the best-fit N(3) bonding model. Similarly, a second modification of the N(3) bonding model was found with a R-factor of 0.23, just at the limits of the variance, but combined with a significantly larger associated tilt ($35 \pm 20^\circ$) this solution may also be excluded.

4.3.5 General discussion

The combination of O 1s and N 1s PhD data, O K-edge NEXAFS, and O 1s and N 1s XP spectra have provided a clear picture of the structure of uracil chemisorbed on Cu(110), with bonding via both of its oxygen atoms and the N(3) nitrogen atom between them, all three of these atoms occupy singly-coordinated off-atop sites relative to nearest-neighbour surface Cu atoms. Perhaps unsurprisingly, this bonding geometry is essentially identical to that of the closely-related thymine species on the same surface. Table 4.2 shows that the adsorption geometry and chemisorption bondlengths are almost all equivalent to within the precision limits. The one exception is that one of the Cu-O bondlengths is slightly longer for thymine than for uracil, though it is possible this difference stems from slightly different constraints in atom movements allowed in the final refinement of the two structures.

In many other studies of approximately planar molecules on surfaces the role of intermolecular bonding, particularly through hydrogen bonding, is thought to play an important role in the ordering, and indeed this is the basis of a sub-field based on two-dimensional supramolecular self-assembly. In general, however, these effects for uracil have been associated with systems in which the molecules "lie down" on the surface, with the molecular plane approximately parallel to the surface. Indeed, a STM study (without sub-molecular resolution) of uracil on Cu(111) at low temperature (70 K) (Ref. [106] appeared to identify ordering of molecular trimers that was attributed to this effect). In the present case, however, with the molecular plane perpendicular to the surface, such interactions may be expected to be less important, although in the absence of any evidence of long-range or short-range order in the overlayer, it is not possible to address this issue further. Nevertheless, intermolecular interactions are likely to have far more influence on the ordering of the molecules on the surface (the "self-assembly") than on the local adsorbate-substrate registry, so it is particularly unlikely in the present case that any such interactions have significant impact on the local geometry determined here.

It is interesting to note that the nature of a solid surface imposes quite different constraints on the bonding and chemistry of a molecule like uracil relative to its behaviour in gas or solution phases. When forming its nucleoside, uridine, and in most

other N-alkylation reactions, uracil will either react through the N(1) atom, or both the N(1) and N(3) atoms [107–112]. Moreover, to obtain N(3) regioselectivity it is generally necessary to have a protecting group on the N(1) atom [107, 111, 113, 114]. It has also been shown that in the gas phase the enthalpy of dehydrogenation of these two N atoms differs by 0.4 eV, though in polar environments the difference is significantly smaller[115]. At the Cu(110) surface it is evidently the interaction with the N(3) atom that proves to be preferred, but for steric reasons this necessarily also involve interaction of the surface with both O atoms.

4.4 Tartaric Acid on Cu(110)

4.4.1 Introduction

As opposed to the other systems within this chapter, tartaric acid is neither an amino acid nor a nucleobase, and does not, in fact, occur in animals - instead it is an organic acid that occurs within many fruits. However, it does have a special place within organic chemistry as it was the first molecule to display properties now associated with chirality [116]. Tartaric acid has two chiral centres and as such has three different enantiomers: *R*,*R*; *S*,*S*; and *S*,*R*. A molecular schematic of the *R*,*R* and *S*,*S* conformations is shown in fig 4.2.

Its adsorption on the Cu(110) surface has been used as a model system for extensive investigation by a range of experimental techniques including LEED, STM, fourier transform-RAIRS (FT-RAIRS) [117, 118], and also by DFT calculations [119–121]. The FT-RAIRS results, in particular, have identified two different surface species that can be formed through the interaction of tartaric acid with Cu(110) under different conditions, namely monotartrate and bitartrate, depending on whether only one or both carboxylic acid groups are deprotonated to create carboxylate (-COO) groups that can form chemisorption bonds to the surface through the two constituent O atoms. The long-range ordering of these molecules has been of especial interest because of the potential significance of the fact that all the ordered phases are globally chiral, leading to exposed Cu surface regions or gaps in the overlayers that are potential sites for enantiospecific surface chemistry. Several different long-range ordered phases of the monotartrate species have been identified at different coverages and temperatures. At room temperature, a sub-saturation $\begin{pmatrix} 4 & 0 \\ 2 & 3 \end{pmatrix}$ ordered overlayer is formed, which transforms to a $\begin{pmatrix} 4 & 1 \\ 2 & 3 \end{pmatrix}$ phase at higher coverage. Annealing of this high coverage phase to $\sim$ 400 K leads to the formation of a $\begin{pmatrix} 4 & 1 \\ 2 & 5 \end{pmatrix}$ monotar-

trate phase, but similar annealing of the lower-coverage monotartrate phase leads to a $\begin{pmatrix} 9 & 0 \\ 1 & 2 \end{pmatrix}$ bitartrate phase (The LEED images from all four preparations, plus STM images of the $\begin{pmatrix} 4 & 1 \\ 2 & 3 \end{pmatrix}$ and $\begin{pmatrix} 9 & 0 \\ 1 & 2 \end{pmatrix}$ phases are shown in Fig. 4.17) . A recent DFT study [121] concluded that the potential barrier for initial deprotonation, to form the monotartrate species on the Cu(110) surface, is below 0.1 eV, whereas the barrier to form the bitartrate species is more than 1 eV, qualitatively consistent with the need for increased temperatures to create the bitartrate. The fact that this conversion only occurs at lower monotartrate coverages is also consistent with the larger 'footprint' of the bitartrate species on the surface, and thus the need for vacant Cu surface sites. STM images of the $\begin{pmatrix} 4 & 1 \\ 2 & 3 \end{pmatrix}$ and $\begin{pmatrix} 9 & 0 \\ 1 & 2 \end{pmatrix}$ phases each show three adsorbate features per unit cell that are proposed to each correspond to a single tartrate species; this implies that the coverages of these phases are 0.25 ML and 0.17 ML respectively [117].

While these previous studies of the Cu(110)/tartaric acid system provide considerable insight into the surface reaction and molecular ordering, none of the experiments provide information on the local adsorption geometry. It has been generally assumed that the deprotonated species bond to the surface in a fashion locally identical to that of the simple carboxylate species formate (HCOO) [5, 122, 123], acetate (CH_3COO) [124], and benzoate (C_6H_5COO) [125] on this surface, with the two O atoms of each carboxylate species occupying near-atop sites relative to two nearest-neighbour Cu surface atoms along the close-packed [$1\bar{1}0$] rows. This geometry is consistent with the results of the DFT calculations [119]. Of course, in the bitartrate phase, bonding of the molecule through both sets of carboxylate O atoms means that the mismatch of the unstrained surface and molecular geometry imposes constraints on the exact local bonding sites. A similar effect is seen in the simple amino acids, glycine (NH_2CH_2COOH) [88] and alanine ($NH_2CH(CH_3)COOH$) [90], which bond through both the deprotonated carboxylate O atoms and the amino N atom, and this three-point bonding on Cu(110) does force one of the O atoms to adopt a site that is substantially displaced from a local atop geometry. The impact of the four-point bonding of the bitartrate phase is thus an issue of some interest.

Here we present the first direct experimental quantitative determination of the local adsorption site of tartaric acid on Cu(110) for both the monotartrate and bitartrate conformers using PhD.

4.4.2 Experimental details

R,R-tartaric acid (shown schematically in Figs. 4.2 & 4.18) dosing of the sample was achieved by heating the powder (99% purity, Sigma Aldrich) to 400 K. Dosing with

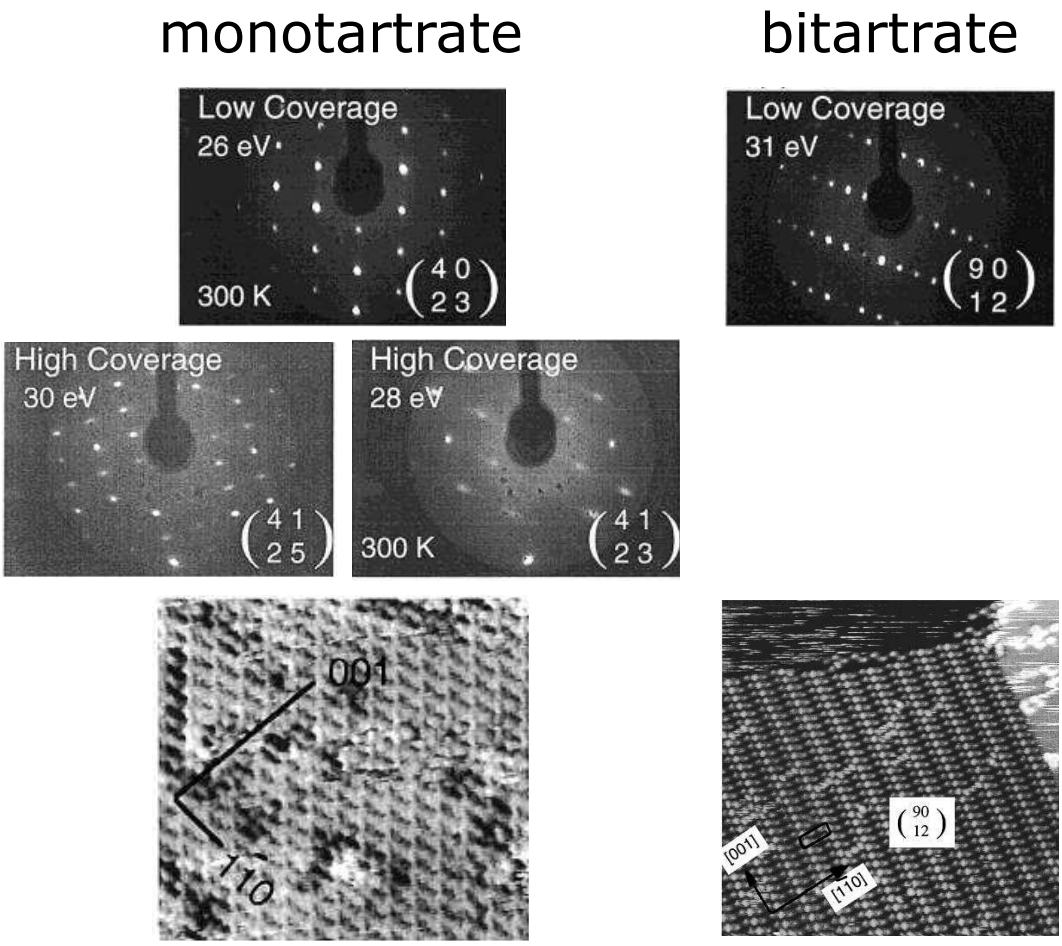

Figure 4.17: (top) LEED and (bottom) STM images from the (left) monotartrate and (right) bitartrate overlayers of tartaric acid on Cu(110), reproduced from Ortega Lorenzo et al. [118]. Note that the STM image of the monotartrate species is from the $\begin{pmatrix} 4 & 1 \\ 2 & 3 \end{pmatrix}$ phase.

the sample held at 400 K yielded a clear $\begin{pmatrix} 9 & 0 \\ 1 & 2 \end{pmatrix}$ LEED pattern, consistent with that expected for the bitartrate phase. Dosing with the sample at room temperature, the conditions known to produce monotartrate layers, yielded a different LEED pattern of poor quality; it was not possible to determine whether the pattern corresponded to the $\begin{pmatrix} 4 & 0 \\ 2 & 3 \end{pmatrix}$, $\begin{pmatrix} 4 & 1 \\ 2 & 3 \end{pmatrix}$, or $\begin{pmatrix} 4 & 1 \\ 2 & 5 \end{pmatrix}$ phase

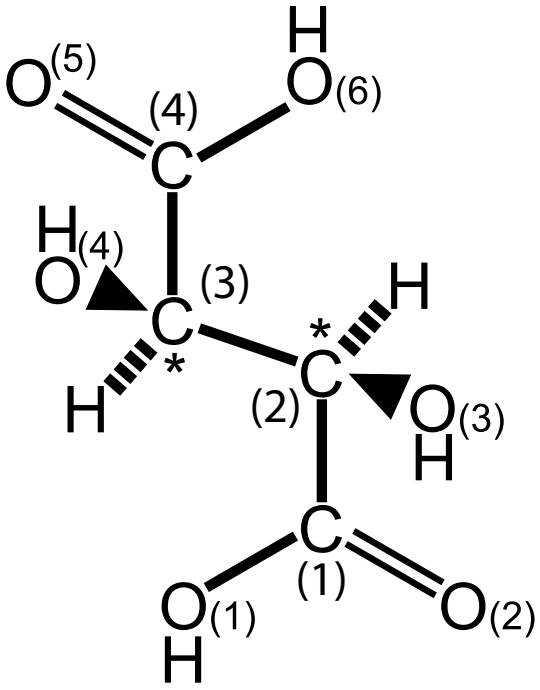

Figure 4.18: Schematic diagram of the R,R-tartaric acid molecule.

4.4.3 Results

XPS Characterisation

The O 1s and C 1s XP spectra from the prepared monotartrate and bitartrate phases are shown in Fig 4.19. These XP spectra clearly show that the coverage in the monotartrate phase measured here is significantly larger than that of the bitartrate phase. Comparison of the O 1s and Cu 3s photoemission intensity ratio obtained from a Cu(110)(2x1)-O surface (O coverage 0.5 ML), with those from the tartrate-covered surfaces provides coverage estimates of 0.3 and 0.2 ML for the monotartrate and bitartrate phases (respectively). The spectra of Fig 4.19 show (at least) two clearly-resolved chemically-shifted components in both the O 1s and C 1s photoemission, with a very significant difference in the relative intensities of the two O 1s components between the monotartrate and bitartrate species. The fact that there is such a change is consistent with the different number of deprotonated carboxylic groups in these two

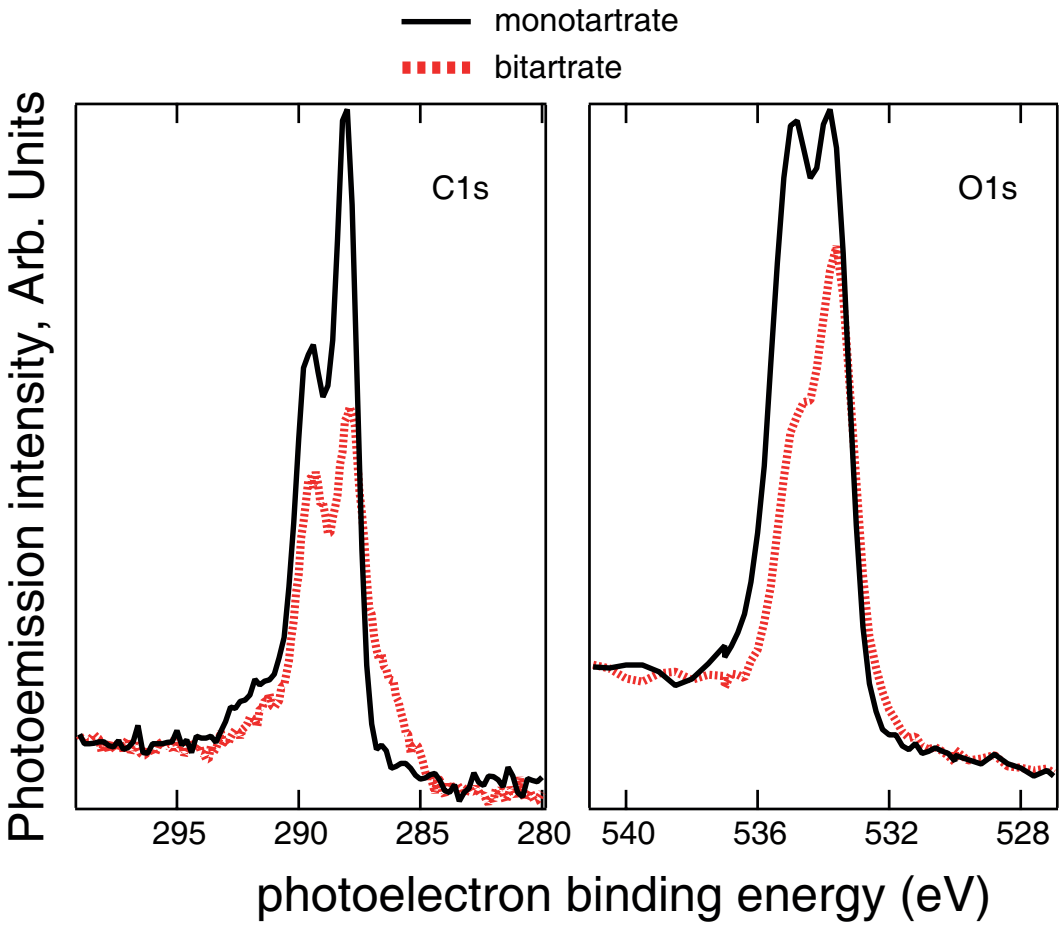

Figure 4.19: O 1s (left) and C 1s (right) XP spectra of monotartrate and bitartrate phases. The C 1s spectra for the bitartrate phase shows a small shoulder at low binding energy, this is attributed to atomic carbon resulting from partial decomposition of tartaric acid. The absolute binding energies are uncalibrated. The O 1s XP spectra were measured at an excitation energy of 624 eV; the C 1s XP spectra were measured with an excitation energy of 400 eV. All spectra were measured in the normal emission direction

species, as identified in the previous FT-RAIRS study.

The assignment of the two peaks in the C 1s XP spectra is relatively straightforward by comparison with spectra from other molecules containing both a carboxylic acid / carboxylate species together with tetrahedrally-coordinated C atoms. The lower binding energy peak may be attributed to the middle carbon atoms, C(2) and C(3) (Fig. 4.2), which are bonded to the alcohol groups, while the higher binding energy peak is associated with the outer carbon atoms, C(1) and C(4), that are part of the carboxylate groups One surprising feature of the C 1s spectra is that the peak at higher binding energy appears to be consistently weaker than the peak at lower binding energy, although according to this assignment, both peaks arise from 2 C atoms in the tartrate species. This effect has been observed in C 1s spectra in multiple carboxylic acid containing species - notable glycinate on Cu(111) [69] / §4.5 and Pd(111) [126], serinate on Cu(110) [127], and alaninate on Cu(110) [128], and must be attributed to loss of intensity in one of the peaks to shake-up satellites; the shoulder visible in the spectra at higher binding energy is consistent with this interpretation.

The assignment of the O 1s XP spectral peaks in the bitartrate species is also clear. In this species there are four O atoms in carboxylate groups (O(1), O(2), O(5) and O(6)), and two O atoms on the OH groups (O(3) and O(4)); this would lead us to expect two peaks with an intensity ratio of 2:1, consistent with the spectrum in Fig. 4.19. We can therefore assign the lower binding energy peak to carboxylate O atoms and the higher binding energy peak to OH species. However, in the case of the monotartrate O1s XP spectrum (Fig 4.19a) there are two peaks with approximately the same area, but the molecule has six O atoms in four different bonding states. As the monotartrate retains two O atoms in OH species (O(3) and O(4)), and two O atoms in the carboxylate group (O(1) and O(2)), these four O atoms may be expected to lead to peaks at the same energies as the two peaks in the bitartrate spectrum. The implication is therefore that the two O atoms in the remaining carboxylic acid group, namely the C=O and C-OH species, must have O 1s chemical shifts similar to the carboxylate and OH species of the bitatrate. It seems most reasonable to assign them to these two components in this order although, as we shall see, for the purposes of our PhD structure investigation, the ordering of these assignments proves to be unimportant.

PhD results: qualitative evaluations

As the PhD data from the adsorbate atoms that are bonded to the surface are the primary source of structural information, and in the present case these are expected to be the O atoms of the deprotonated carboxylate groups, the analysis is focussed on the PhD modulation spectra from the lower binding energy component of the O

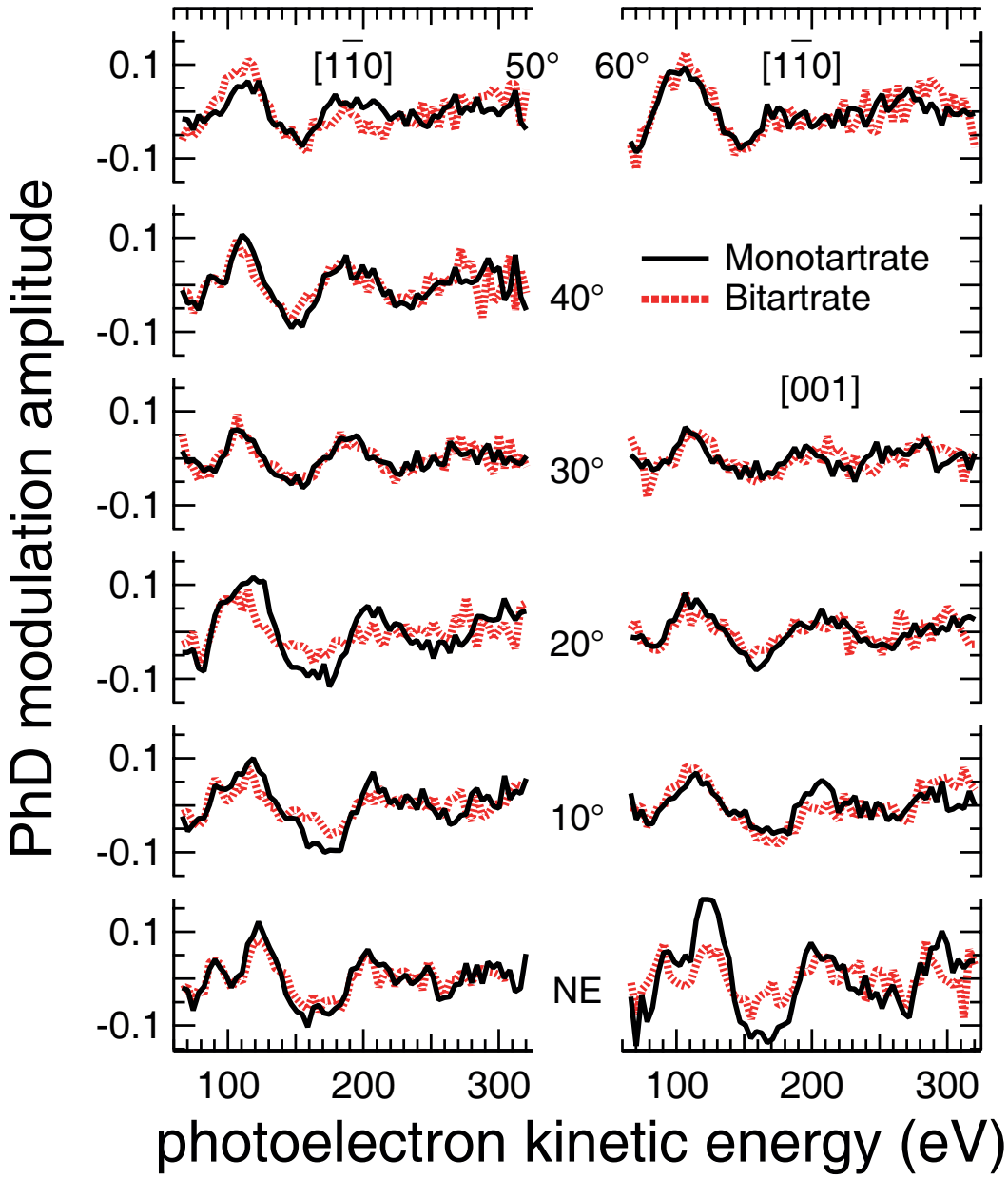

Figure 4.20: Comparison of the PhD spectra from the mono- and bi-tartrate phases for several polar and azimuthal emission directions. Only the 11 spectra with the strongest modulations are shown.

1s emission spectra.

The experimental PhD spectra associated with the lower binding energy O 1s peak recorded from both the monotartrate and bitartrate species are shown in Fig 4.20. The PhD spectra from the O 1s peak at higher binding energy were devoid of any obvious modulations, consistent with our expectation that this emission is from O atoms that are relatively far from the surface and lack any near-neighbour Cu scatterer atoms. A striking feature of the data of Fig. 4.20 is the remarkable similarity of the spectra from the two different species. One might infer from this that the two structures are identical, yet our SXP spectra and the associated coverage estimates, as well as the previously published FT-RAIRS results using similar preparation methods [117], clearly indicate that the two surface species are different, while the FT-RAIRS data and STM images further indicate that the two molecular orientations differ. It is therefore difficult to see how the two adsorption geometries can be equivalent. The different LEED patterns observed in the present work also reinforce the view that we are studying different surface phases, but LEED tends to be dominated by the diffraction pattern of those regions of the surface that show the best long-range order, which may be a minority phase on the surface. SXPS, on the other hand, averages over the whole surface, so the clear difference in these spectra recorded from the two different methods of surface preparation are indicative of the surfaces being predominantly covered by different species.

In fact a strong similarity in PhD data from the two species is to be expected. We have already noted that all the bonding carboxylate O atoms (two in the monotartrate, four in the bitartrate) are likely to adopt near-atop sites. The different constraints of the anticipated two-point and four-point bonding geometries, involving some mismatch between interatomic distances on the surface and within the undeformed molecule, would lead us to expect some subtle differences in the O bonding sites, but after averaging over the sites of the inequivalent atoms in the molecules, these differences may have only a modest effect on the resulting PhD data.

One further qualitative observation is that the dominant long range periodicity of the modulations seen in data recorded at and near normal emission is quite similar to that seen from simple deprotonated carboxylates on Cu(110) [5, 124, 125]. This strongly suggests that the emitter O atoms are in similar near-atop sites and at similar Cu-O bondlengths of $\sim$ 1.90-1.95 Å.

PhD results: quantitative structure determination

In both structure determinations the molecule was assumed to adsorb intact with similar intramolecular bond length and bond angles as in the crystal structure [129]. The x, y and z axes are defined as, respectively, the $[1\bar{1}0]$ direction, the [001] direction

and the surface normal pointing away from the surface.

Monotartrate on Cu(110)

Table 4.3: Structural parameter values for the best-fit monotartrate model and the three best-fit bitartrate models. d values are bondlengths, x, y and z are coordinates of O emitter atoms relative to the nearest-neighbour Cu atom, and of these surface Cu atoms relative to their positions in an ideal bulk-termination, along, respectively, $[1\bar{1}0]$, [001] and the outward surface normal, [110]. $\theta_{(COO)}$ and $\phi_{(COO)}$ are the tilt and twist angles of the COO plane relative to, respectively, the surface normal and the $[1\bar{1}0]$ direction. $\phi_{tartaric}$ is the rotation of the molecule relative to the surface normal around its centre. The special case of $\phi_{tartaric}$ and $\phi_{(COO)}$ equal to 0° has the vector between the O atoms of the carboxylic acid group parallel to the $[1\bar{1}0]$ direction.

Parameter	monotartrate	bitartrate "upright"	bitartrate "flat"	bitartrate "staggered"
$R-factor$	0.32	0.45	0.43	0.43
$d_{Cu_O(1)}$ (Å)	1.92 ± 0.08	1.94 ± 0.06	1.93 ± 0.08	1.94 ± 0.07
$d_{Cu_O(2)}$ (Å)	1.93 ± 0.06	1.95 ± 0.09	1.95 ± 0.08	1.97 ± 0.09
$z_{Cu_O(1)}$ (Å)	1.84 ± 0.06	1.89 ± 0.08	1.78 ± 0.08	1.86 ± 0.08
$z_{Cu_O(2)}$ (Å)	1.89 ± 0.06	1.86 ± 0.08	1.85 ± 0.08	1.77 ± 0.08
$x_{Cu_O(1)}$ (Å)	$0.1(+0.3/-0.1)$	0.2 ± 0.2	0.6 ± 0.1	-0.4 ± 0.1
$y_{Cu_O(1)}$ (Å)	$-0.6(+0.6/-0.4)$	0.4 ± 0.2	-0.4 ± 0.2	$-0.4(+0.2/-0.3)$
$x_{Cu_O(2)}$ (Å)	-0.4 ± 0.4	-0.3 ± 0.1	0.3 ± 0.1	-0.8 ± 0.1
$y_{Cu_O(2)}$ (Å)	$0.2(+0.2/-0.3)$	-0.5 ± 0.2	-0.5 ± 0.3	$-0.4(+0.6/-0.2)$
$\theta_{COO-surface}$ (Å)	17 ± 6	38 ± 6	70 ± 10	70 ± 10
$\phi_{OO-[1\bar{1}0]}$ (Å)	20 ± 10	2 ± 4	-1 ± 3	$-2(+42)$
$\phi_{tartaric}$ (Å)	–	23 ± 4	5 ± 5	0 ± 3
d_{O-O} (Å)	2.2 ± 0.1	2.2 ± 0.1	2.2 ± 0.1	2.2 ± 0.1
$\Delta z_{Cu_O(1)}$ (Å)	0.0 ± 0.1	-0.1 ± 0.1	-0.1 ± 0.2	-0.1 ± 0.1
$\Delta z_{Cu_O(2)}$ (Å)	0.0 ± 0.1	0.1 ± 0.1	0.0 ± 0.1	0.0 ± 0.1
$\Delta y_{Cu_O(1)}$ (Å)	–	0.0 ± 0.4	0.1 ± 0.3	0.1 ± 0.4
$\Delta y_{Cu_O(2)}$ (Å)	–	0.0 ± 0.3	0.0 ± 0.3	0 ± 1

In the PhD simulations of the monotartrate species on Cu(110) three O atoms were considered to emit electrons with a lower photoelectron binding energy and thus to contribute to the measured PhD modulations, namely the two O atoms of the carboxylate graoup, and one of the two O atoms of the carboxylic acid group (-COOH). The exact location of this third O atom proves to have very little influence on the PhD spectra, being located significantly further from the surface than the bonding carboxylate O atoms, so it is unimportant whether this emitter atom is at the C=O or C-O-H location in the molecule. Because the molecule is chiral, the two O atoms in the carboxylate group are not symmetrically identical, with only one of these being adjacent to the neighbouring alcohol group; all three emitter O atoms

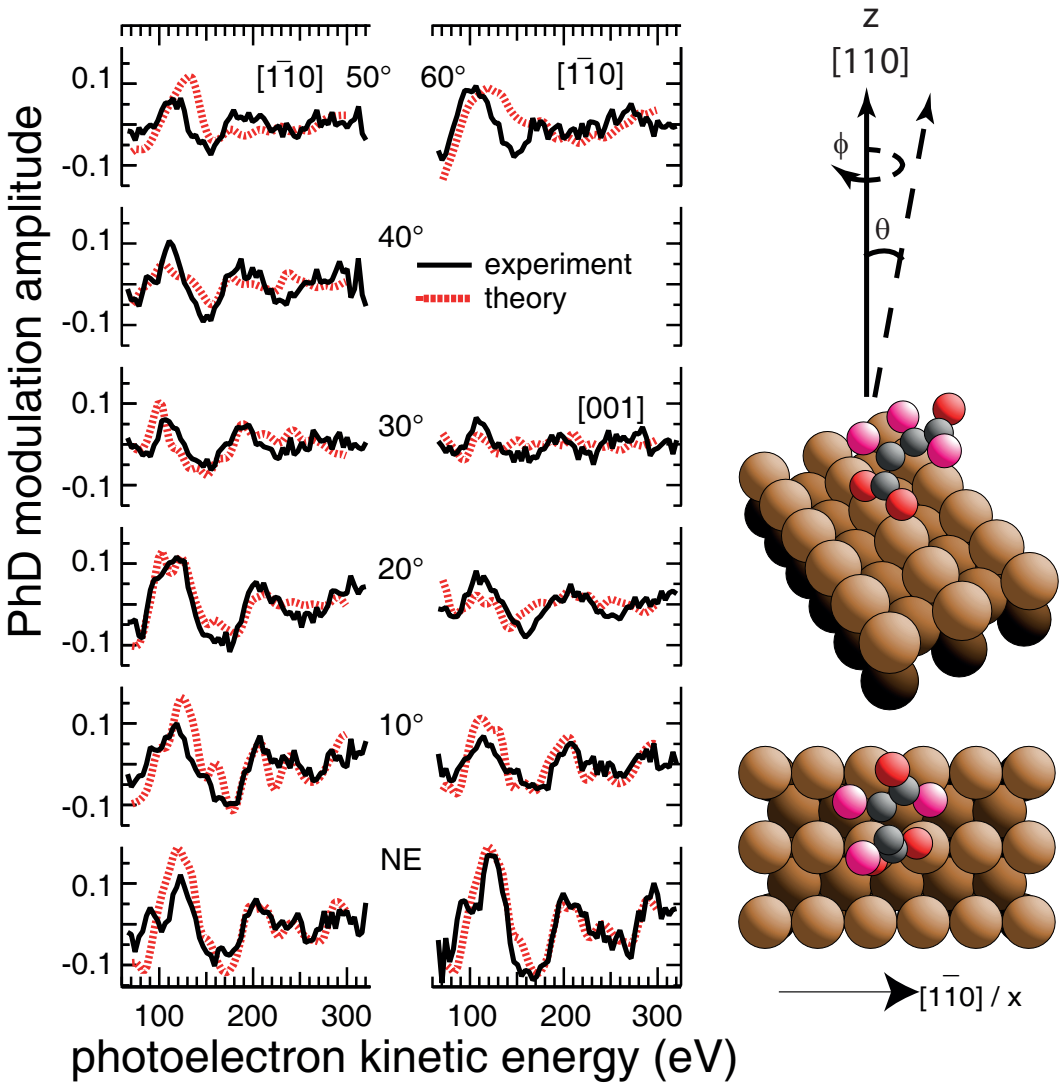

Figure 4.21: Left: Comparison of the experimental PhD spectra from the lower binding energy O 1s peak (Fig 4.19) and the results of the simulations for the best fit model structure (R = 0.32) for the monotartrate species on Cu(110). Right: schematic representation of the adsorption geometry. The C atoms are shown in black, while the O emitter atoms, contributing to the low binding energy O 1s peak, are shaded red. The other O atoms are shaded pink. The (weakly-scattering) hydrogen atoms are not shown, as they were not included in the multiple scattering calculations.

were therefore allowed to occupy inequivalent sites.

In order to explore the multidimensional parameter hyperspace the molecule was allowed to be displaced independently in the x, y and z directions, and the orientation of the plane of the carboxylate group was allowed to tilt with respect to, and rotate about, the surface normal. The PhD technique is generally rather insensitive to the position of intramolecular (low mass number) scatterers, so the sensitivity to variations in the x, y and z position of the whole molecule, and to the rotation ($\phi_{(COO)}$ relative to the $[1\bar{1}0]$ direction) and tilt ($\theta_{(COO)}$ relative to the surface normal) of the plane of the carboxylate group, arises primarily from their effect in changing the vector between the O atoms of the carboxylate group and their nearest Cu atoms; there is also a much weaker dependence on the location of these O atoms relative to the nearest-neighbour carboxylate C atom. The position of the third (carboxylic acid) emitting O atom is effectively varied by the rotation of the three C-C bonds, but the calculations were found to have no sensitivity to the position of this emitter atom as long as it was a significant distance from the substrate. In addition, the nearest-neighbour Cu atoms to the carboxylate O atoms were allowed to relax in z independently relative to the underlying crystal, as was the whole first layer of Cu atoms.

The best fit structure that was found is shown schematically in Fig. 4.21, together with a comparison of the simulated and experimental PhD spectra. The corresponding R-factor value for the full set of spectra measured in 11 different directions is 0.32. Note that several of the experimental spectra show quite weak modulations and thus a poor signal-to-noise ratio. If these spectra are omitted from the theory-experiment comparison, and the R-factor is calculated only for the 5 spectra showing the strongest modulations, the R-factor drops to a value of 0.23. The Cu-O bondlengths in this structural solution are 1.92±0.08 Å and 1.93±0.06 Å for the two carboxylate O atoms (the error estimates being based on the full set of 11 spectra). The values of all the structural parameters in this model are shown in table 4.3.

Bitartrate on Cu(110)

For the multiple scattering PhD simulations of the bitartrate species, it was assumed that the four carboxylate O atoms are the emitters that contribute to the PhD spectra. In this case too, the chirality of the molecule means that the two O atoms in a single carboxylate group need not occupy locally equivalent sites. However, as the molecule does have 2-fold rotational symmetry, the diagonally-related O atoms (O(1)/O(6) and O(2)/O(5) of Fig 4.2) may be expected to occupy equivalent adsorption sites. Strictly, this is only true if the 2-fold rotation axis of the molecule coincides with one of the 2-fold rotation axes of the underlying surface, but we do make this assumption.

The molecule is assumed to bridge two adjacent close-packed [1$\bar{1}$0] Cu rows on the surface.

These two constraints have two implications in the geometry of the molecule. Firstly, the C(2)-C(3) bond in the middle of the molecule must be parallel to the surface. Secondly, the molecule must be centred over a hollow site (directly atop a second-layer Cu atom) or over a long-bridge site (midway between two adjacent Cu atoms along [001], as these are the two positions having 2-fold rotational symmetry that lie between the close-packed [1$\bar{1}$0] Cu rows. Note that the assumption that the intramolecular bond angles remain the same as in the intact molecule also implies that the COO plane must be tilted relative to the surface normal by more than 19°. A global structural search was first conducted using a simplified model that contained only the C and O atoms of the two carboxylate groups. The plane of the carboxylate group was allowed to rotate around the surface normal and to tilt away from the surface normal, while the centre of the group was allowed to move in the x, y and z directions, the z parameter of the two O atoms also varying independently. The results of these calculations showed that models involving a tilt angle of the carboxylate planes of less than 40° relative to the surface normal were unacceptable. This sensitivity to intramolecular scattering is relatively unusual in PhD (although not unique [130, 131]), and seems to arise in this case from the modulations in the spectra recorded at the higher polar angles ($> 30°$); this effect is illustrated in the comparisons between theoretical and experimental PhD spectra, recorded at polar emission angle of 50° and 0°, for extreme tilt angles of 0° and 90° (Fig. 4.22).

A global search including the missing C and O atoms was then pursued (all calculations neglect the extremely weak scattering from H atoms). The two symmetry-constrained models with the molecule centred over hollow and long-bridge sites (as seen in Fig 4.24 and Fig 4.25 respectively), were explored independently. The centre of the molecule was allowed to vary in z, while the carboxylate groups were allowed to rotate around the adjacent C-C (C(1)-C(2) and C(4)-C(3)) axes ($\phi_{(COO)}$), and to tilt with respect to the surface normal ($\theta_{(COO)}$); the whole molecule was also allowed to rotate relative to the surface normal about its centre ($\phi_{tartaric}$). The Cu atoms closest to the emitting O atoms were also allowed to relax by small amounts in the y and z directions, while the emitting O atoms were allowed to vary independently in x by a small amount. Three competing models with comparably-favourable R-factors were found through this search. Two of the models are centred over the hollow site while the third has the molecule centred on the long-bridge site. Of the two hollow-site models, one is found to have a tilt angle of the COO plane of only 38±6° relative to the surface normal (a value slightly less than the minimum value found in the calculations that included only the carboxylate scattering atoms), and we refer to this as the "upright" model. The associated Cu-O bondlengths are 1.94±0.06Å and

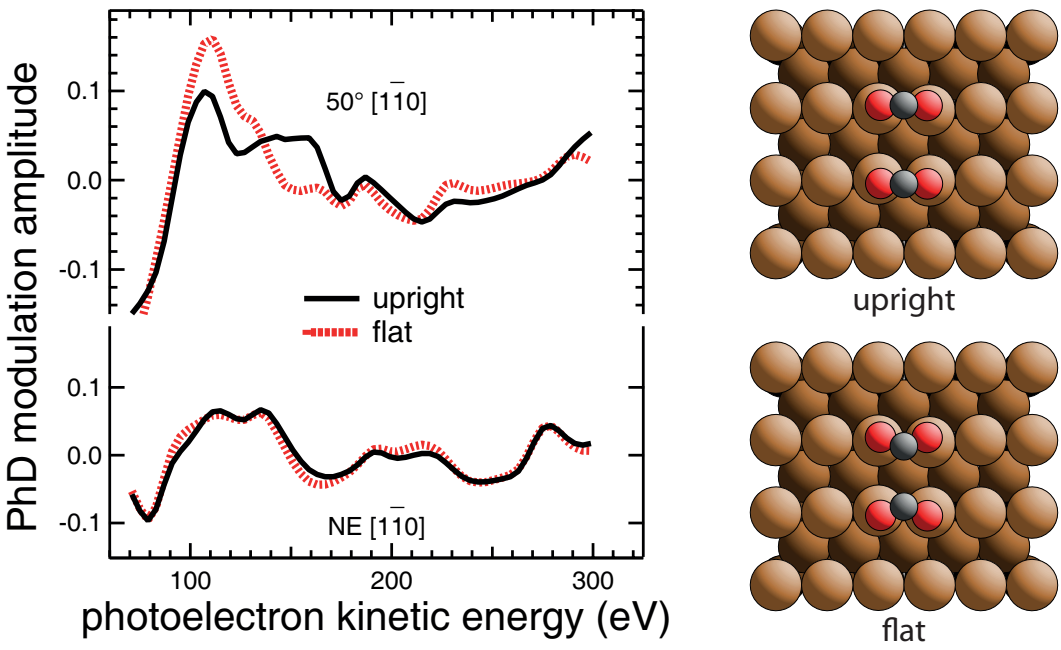

Figure 4.22: (left) comparison of theoretical multiple scattering calculations of an "upright" and "flat" carboxylate species on the Cu(110) surface, shown schematically (right). At near normal emission (NE) directions the difference is negligible (as seen in the NE, [1$\bar{1}$0] direction), at higher emission angles (as seen in the 50° off NE, [1$\bar{1}$0] direction) there is a more pronounced difference.

1.95±0.09 Å , and the R-factor value is 0.45, the highest of the three preferred models. This structure is shown schematically in Fig. 4.23, together with a comparison of the experimental and simulated PhD spectra. The other two models, one with the molecule in the hollow site, the other in the bridge site, are shown in Figs 4.24 and 4.25, together with the associated comparisons of the theoretical and experimental PhD spectra. Despite the differences in the lateral position of the molecule as a whole, the local positions of the bonding O atoms with respect to the substrate Cu atoms are essentially identical, thus leading to closely similar PhD spectra. The Cu-O bondlengths in the two models are 1.93±0.08 Å/1.95±0.08 Å and 1.94±0.07 Å/1.97±0.09 Å; both models give an R-factor of 0.43. These two models have the COO planes comparatively flat on the surface, with a tilt of 70±10° relative to the surface normal.

The comparatively high R-factors found in these bitartrate structures can be attributed to the relatively poor signal-to-noise ration of the PhD spectra that arise, at least in part, from the lower molecular coverage (by a factor of ~ 2), and the thus weaker photoemission signal, than that of the monotartrate phase.

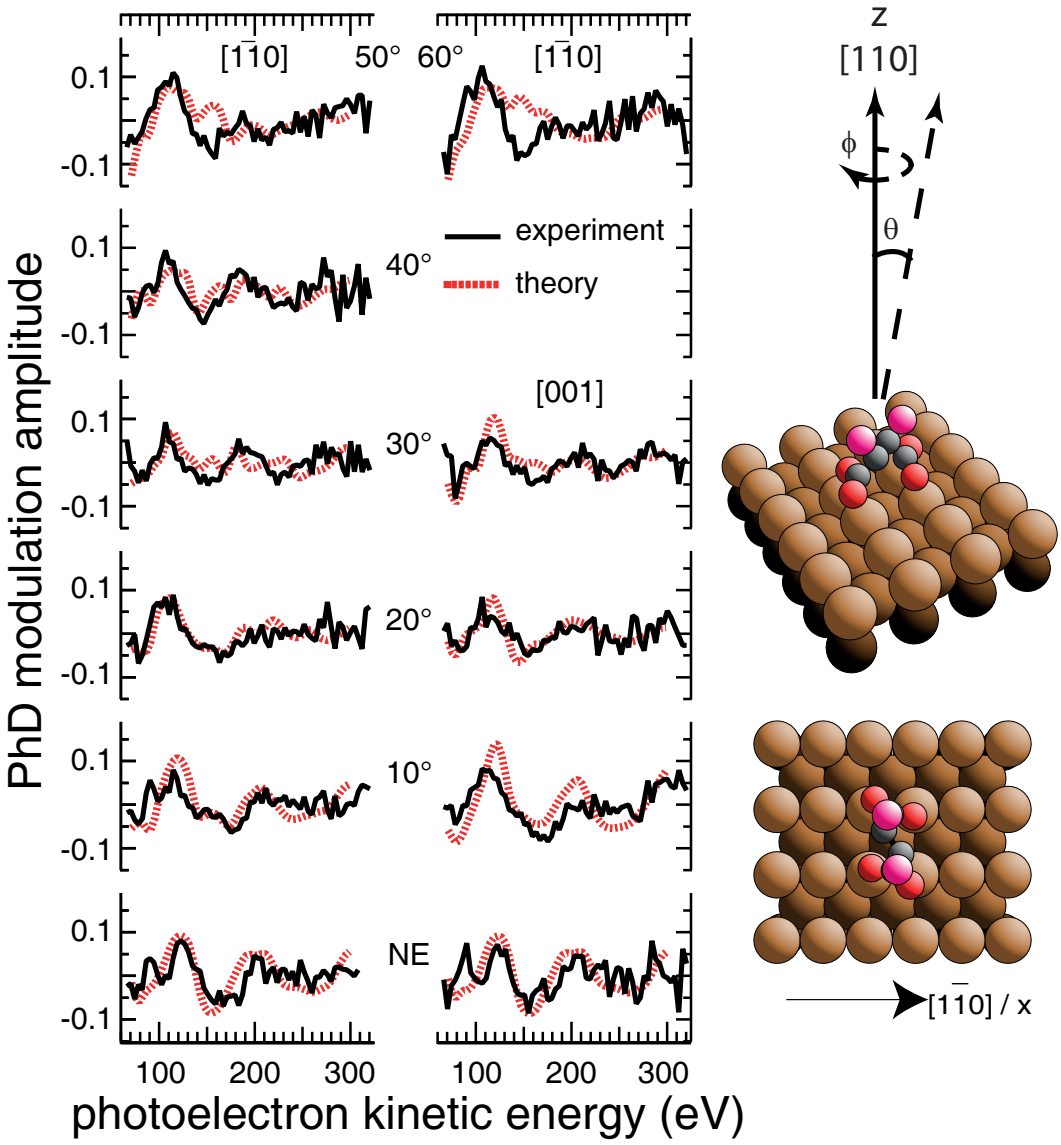

Figure 4.23: Left: Comparison of the experimental PhD spectra from the lower binding energy O 1s peak (Fig. 4.19) and the results of the simulations for the best-fit 'upright' hollow structure (R = 0.45) for the bitartrate species on Cu(110). Right: schematic representation of the adsorption geometry. The C atoms are shown in black, while the O emitter atoms contributing to the lower binding energy O 1s peak are shaded red. The other O atoms are shaded pink. The (weakly-scattering) hydrogen atoms are not shown, as they were not included in the multiple scattering calculations.

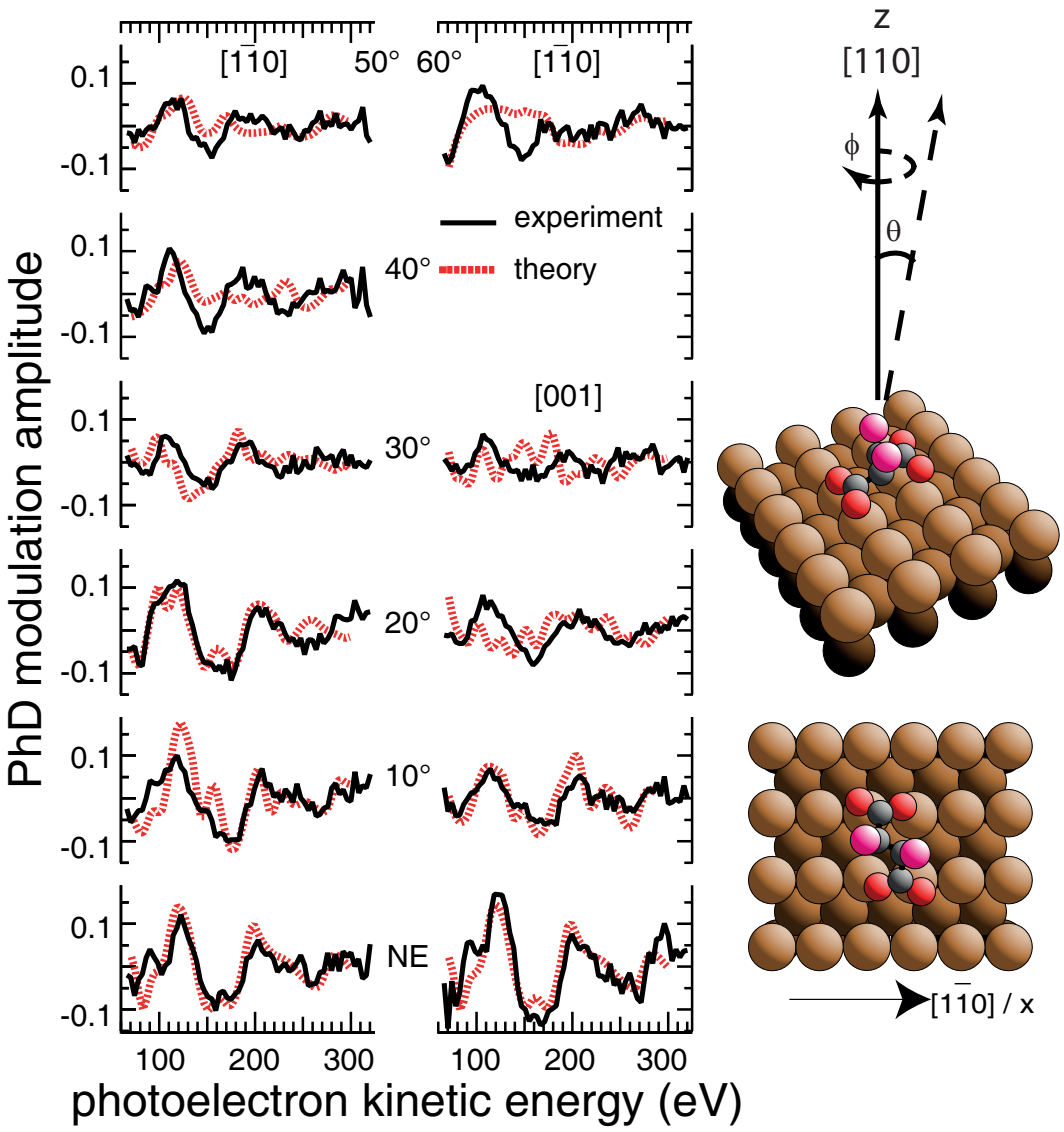

Figure 4.24: Left: Comparison of the experimental PhD spectra from the lower binding energy O 1s peak (Fig. 4.19) and the results of the simulations for the best-fit 'flat' hollow structure (R = 0.43) for the bitartrate species on Cu(110). Right: schematic representation of the adsorption geometry. The C atoms are shown in black, while the O emitter atoms contributing to the low binding energy O 1s peak are shaded red. The other O atoms are shaded pink. The (weakly-scattering) hydrogen atoms are not shown, as they were not included in the multiple scattering calculations.

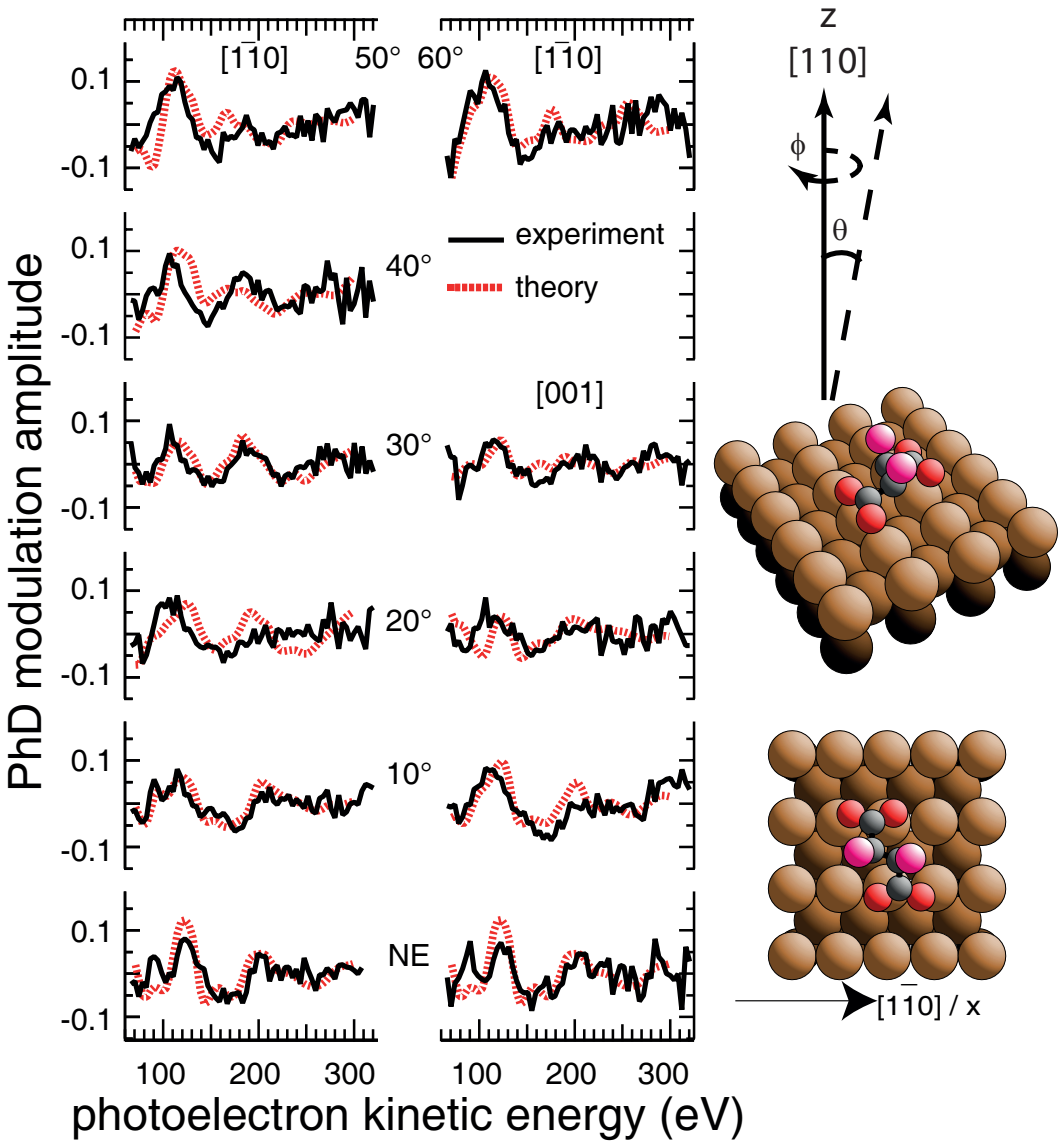

Figure 4.25: Left: Comparison of the experimental PhD spectra from the lower binding energy O 1s peak (Fig. 4.19) and the results of the simulations for the best-fit bridge structure (R = 0.43) for the bitartrate species on Cu(110). Right: schematic representation of the adsorption geometry. The C atoms are shown in black, while the O emitter atoms contributing to the low binding energy O 1s peak are shaded red. The other O atoms are shaded pink. The (weakly-scattering) hydrogen atoms are not shown, as they were not included in the multiple scattering calculations.

4.4.4 General discussion

Here we have presented the results of the first direct structural information for the local adsorption site of tartaric acid on Cu(110). As expected, the bonding carboxylate O atoms in the monotartrate and bitartrate phase were found to occupy similar near-atop sites, with no significant differences in Cu-O bondlengths (1.92±0.08/1.93±0.06 Å and 1.93-1.97±0.06-0.09Å, respectively). These values are comparable to those found in DFT calculations for the bitartrate species (1.96-1.98 [119] and 1.92-2.01 Å[121]).

Based on the PhD data analysis alone we are unable to distinguish between the three competing bitartrate models. We note, however, that the published DFT calculations [119, 121] show the bitartrate centred on the hollow site which would exclude our bridge site solution (Fig. 4.25), although it is not clear that the bridging model was explicitly tested in these calculations. Although none of the DFT investigations report specific values for the orientation of the COO plane in the bitartrate calculations, the schematic diagrams presented in these papers indicate the tilt angles from the surface normal are small, suggesting that the upright hollow geometry of Fig. 4.23 is the one closest to the preferred geometry found in these theoretical calculations. Further, forward scattering photoelectron diffraction measurements by Fasel *et al.* [132] which provides far stronger support for the 'upright' hollow geometry, with its best fitting structure having a tilt of ~ 30 °. Note that the model predicted by Fasel *et al.* does have the hydroxyl O atoms in a different site than that of the 'upright' hollow geometry shown here, however the data presented here have no sensitivity to the position of these atoms, and their position is intead inferred from the tilt of carboxylate plane and the rotation of the molecule around the surface normal. Therefore, the 'upright' hollow geometry is clearly the favoured structure.

4.5 Glycine on Cu(111)

4.5.1 Introduction

As mentioned in §4.1.1, part of the motivation of this work is to try and shed some light on the organic / biological interface in order to gain insight into how more biologically-related molecules may interact in a similar environment. Glycine (shown schematically in Fig. 4.1 & 4.26) may, immediately, seem as a poor choice with this objective in mind, as its two functional groups (–COOH and $–NH_2$) will be unavailable in biologically functional molecules as they will be used in forming peptide bonds. However, other, more complex, amino acids will contain these functional groups and understanding how steric effects influence the interaction of these functional groups

with the metal surface could provide an indication of how far more sterically constrained systems (eg proteins, DNA) might interact.

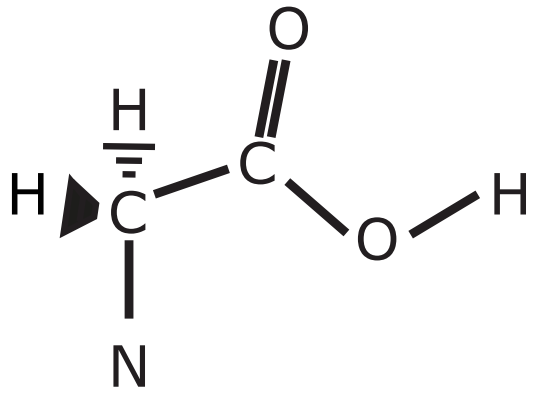

Figure 4.26: Schematic diagram of the glycine molecule.

An early LEED study of the Cu(111)/glycine systems showed that, after deposition at room temperature, an (8x8) diffraction pattern is observed [133]. Later STM experiments showed that this (8x8) pattern may be attributed to the coexistence of three equivalent domains of an (8x4) structure[134] (see Fig. 4.27). The STM images also indicate that the (8x4) unit mesh contains two quite similar (4x4) components. Each (4x4) area was assumed to contain several glycinate species. The STM study also revealed the formation of a $(2\sqrt{13} \times 2\sqrt{13})$ phase on annealing the surface to 400 K for 10 minutes. reflection absorption infrared spectroscopy (RAIRS) measurements [135] provided strong evidence that, as on Cu(100) and (110), the glycine is deprotonated upon adsorption onto Cu(111) in both of these structural phases. Structural models have been proposed on the basis of the STM images, but these are largely speculative and the images obtained contain no information on the adsorbate-substrate registry. We note, however, that the structural models suggested for the (8x4) phase involve only glycinate species lying down on the surface with tridentate bonding to the surface through both O atoms and the N atom, although symmetry considerations require that at least two different local geometries are involved. By contrast, in the $(2\sqrt{13}\times 2\sqrt{13})$ phase it has been suggested that some of the glycinate species adopt an O-O-bidentate configuration, bonding to the surface only through the two O atoms. This suggested behaviour is opposite to that seen on the (100) and (110) surface, with annealing on these surfaces apparently causing conversion of a mixed O-O-bidentate + tridentate layer to a pure tridentate phase. However, the RAIRS study on Cu(111) [135] did identify other conditions leading to the formation of the $(2\sqrt{13} \times 2\sqrt{13})$ phase, and the associated spectra lend some support for this suggested partial orientation change, though recent higher resolution STM measurements imply similar molecular orientations in both phases (see Fig. 4.28, [136]) DFT calculations using different functionals (GGA-RPBE[137], GGA-PW91[138] and

LDA) were performed on this system looking at both an isolated and an assembled system [69]. The different functionals predicted different molecular orientations as being favourable, with the RPBE functional heavily supporting an upright structure with only the oxygen atoms interacting with the surface and the LDA functional strongly supporting adsorption via both the oxygen atoms and the nitrogen atom. The predicted structures are shown in Fig 4.29.

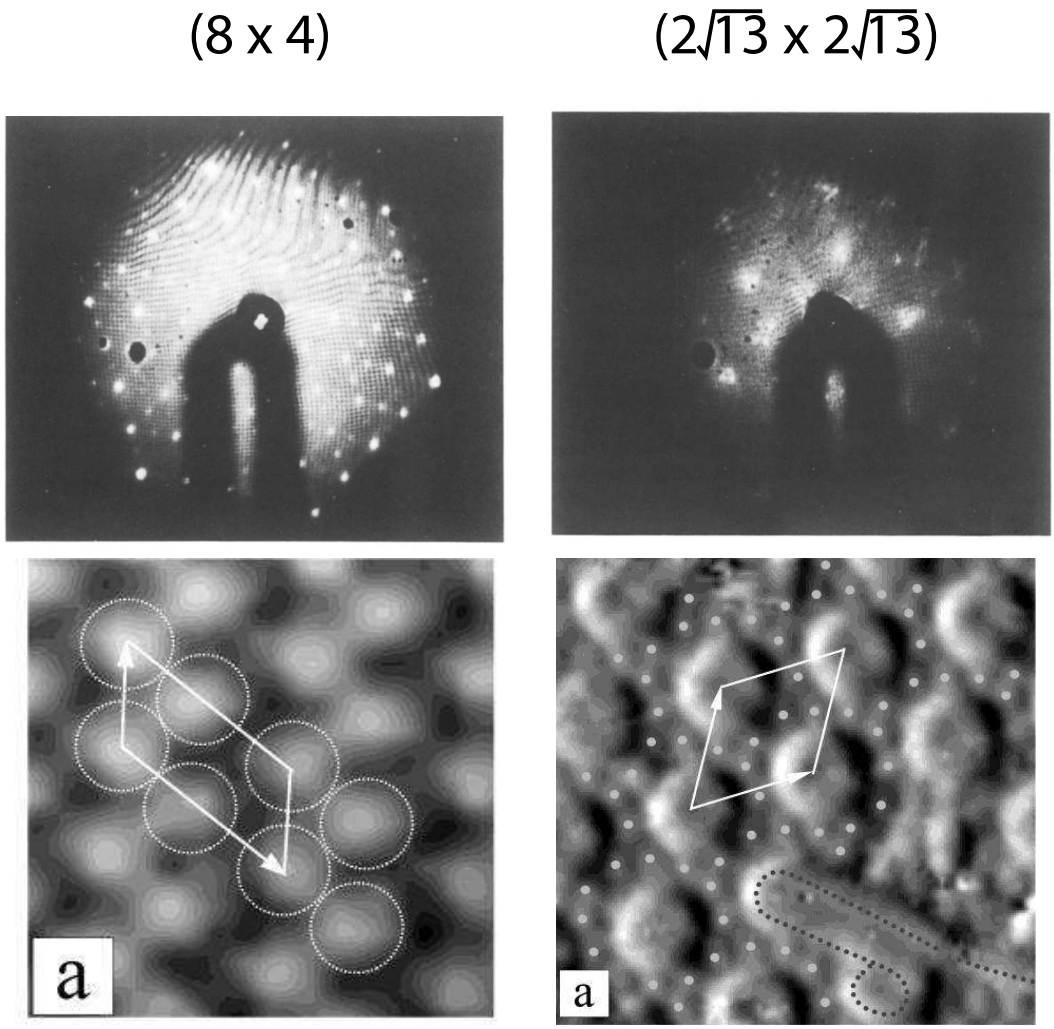

Figure 4.27: (top) LEED and (bottom) STM images of the (left) (8×8) and (right) $(2\sqrt{13} \times 2\sqrt{(13)})$ phases of glycine on Cu(111). The LEED images are reproduced from work by Atanasoska *et al.* [133], the STM images are reproduced from work by Zhao *et al.* [134].

However, no study, to date, has produced direct structural information on the local adsorption site of glycine on Cu(111); here we present the results of such an experimental investigation using N 1s and O 1s PhD.

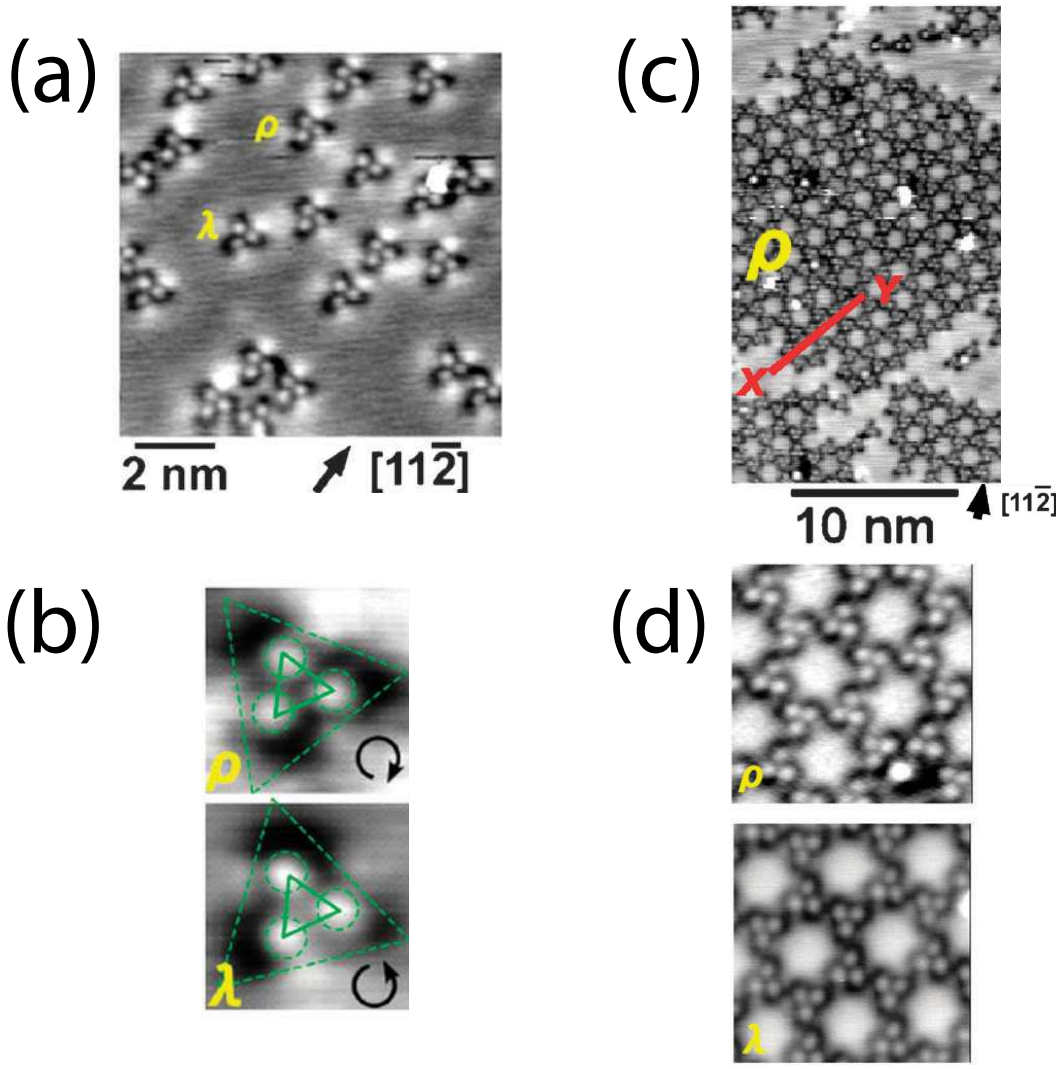

Figure 4.28: High resolution STM images of a glycine on Cu(111) overlayer prepared using conditions to form the $(2\sqrt{13} \times 2\sqrt{13})$ overlayer. (a) Isolated glycine units, presumably trimers, (b) a magnification of the two enantiomers units, (c) and (d) the fully assembled $(2\sqrt{13} \times 2\sqrt{13})$ overlayer. Reproduced from work by Kanazawa *et al.* [136]. These higher resolution images imply that, in the $(2\sqrt{13} \times 2\sqrt{13})$ all of the glycine atoms are in a similar site (i.e. they are not in a mixture of 'upright' and 'lying-down' orientations), and the observed trimer shapes may well be related to the features observed in the (8x8) phase.

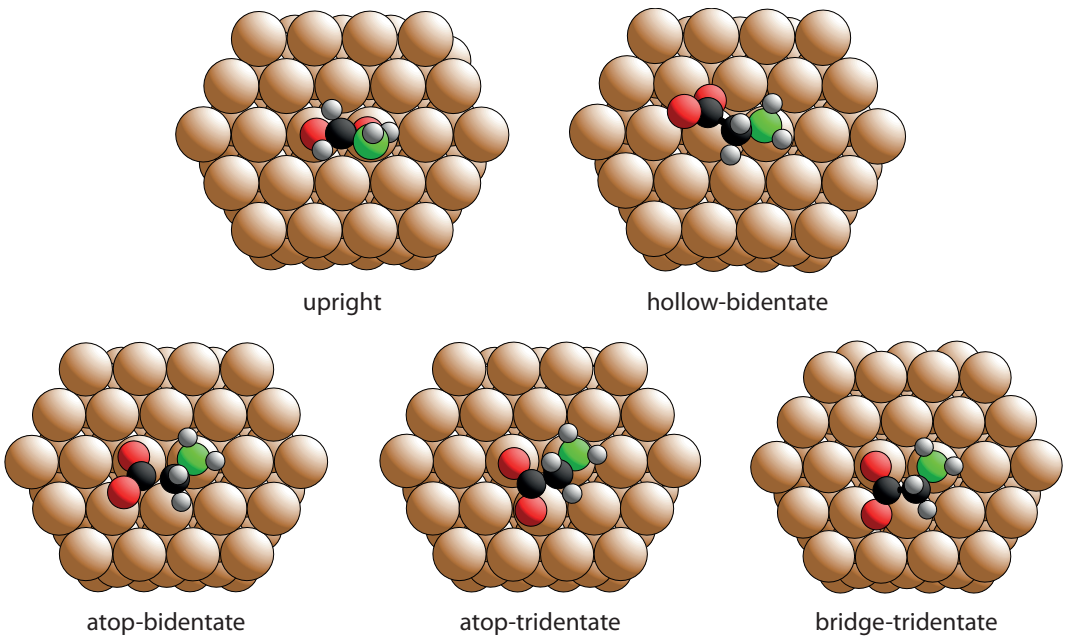

Figure 4.29: Schematic diagrams of the minimum energy Cu(111) / glycinate models as presented by Duncan et al [69]. The largest (copper coloured) atoms are the substrate copper atoms, with the other atoms scaled in size with their atomic number. Specifically the O atoms are red, N atoms are green, C atoms are black and H atoms are white.

4.5.2 Experimental details

Sample dosing was achieved by heating glycine powder (Sigma-Aldrich $>$ 99% purity) in a simple glass tube evaporator to 400K while the sample was held at room temperature, followed by brief annealing to 400 K. An ordered (8x8) pattern was observed by LEED in initial characterisation experiments, but this quickly faded with continued exposure to the electron beam. In view of this evidence of electron-beam damage, subsequent preparations for the PhD measurements used the same doing method but the surface order was not checked by LEED. The surface coverage as judged by XPS was essentially independent of whether or not the initial deposition produced a multilayer film of glycine as the brief annealing to 400 K consistently produced a saturation sub-monolayer coverage.

4.5.3 Results

Characterisation by SXPS and Qualitative analysis of PhD data

The SXP spectra from the prepared Cu(111)/glycinate surface are shown in Fig 4.30. In the absence of a relaible aboslute energy calibration in these experiments the nominal binding energies (the difference between the monochromator energy and the measured kinetic energy) have been displaced by a constant amount such as to yield

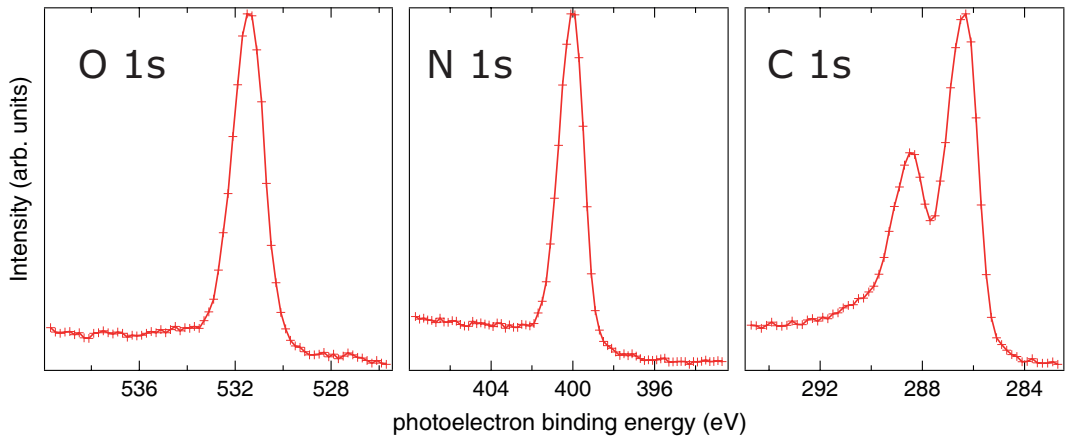

Figure 4.30: XP spectra for the prepared Cu(111) / glycinate surface. Nominal calibration of the absolute binding energies was performed as described in the main text. The O 1s, N 1s and C1s spectra were measured at 650, 500 and 400 eV (respectively) in the normal emission direction.

the same O 1s and C 1s binding energies as those reported by Hasselstöm et al. [139] for glycine on Cu(110). The C1s spectra contains two peaks, with the higher binding energy peak corresponding to the carboxylate carbon and the lower binding energy peak arising from the carbon bonded to the amine species. The origin of the very significant difference in the intensity of the two components is discussed elsewhere in this chapter (§4.4). Both the N1s and O1s SXP spectra show only a single peak. A single O 1s peak clearly indicates that the molecule is deprotonated to produce the glycinate species, but also indicating that the two O atoms in each molecule are in chemically similar sites on the surface. The single N 1s peak is consistent with the fact that there is only one N atom in each molecule, but we may also infer that if the adsorbed glycinate molecule does occupy more than one local geometry, the associated N and O sites are chemically very similar.

Figure 4.31 shows the 7 strongest N1s and 5 strongest O1s experimental PhD spectra. The strongest modulations from both the nitrogen and oxygen emitter atoms arise at or near normal emission, and have similar long range periodicity. This may be taken to imply that both the N and O atoms occupy atop or near atop sites, relative to an underlying Cu backscattering atom. However, it is also notable that the modulations in the O 1s PhD spectra are significantly weaker than those measured from N 1s. This leads to the suggestion that at least one O atom is likely to be significantly more laterally displaced from an exact atop site that the single N emitter atom, or indeed that one O atom occupies a distinctly different (probably low symmetry) site. Interestingly, a similar qualitative effect in the normal emission PhD modulation amplitudes for N 1s and O 1s was seen in the measurements of glycine on Cu(100), with the O 1s modulations about a factor of 2 weaker [88], but in the present case of glycine on Cu(111) the effect is much larger with a difference of a

factor of ~ 5. Less surprisingly, perhaps, the O 1s PhD modulations from glycine on Cu(111) are a factor of ~ 3 weaker than those seen for formate, HCOO, on the same surface [5], as this simpler species bonds to the surface *only* through the two carboxylate O atoms. Nevertheless, these comparisons highlight not only the effect of the constraints imposed on the carboxylate-Cu bonding by the presence of an additional N-Cu bonding in glycinate, but also the effect of the difference in these constraints on the (100) and (111) surfaces.

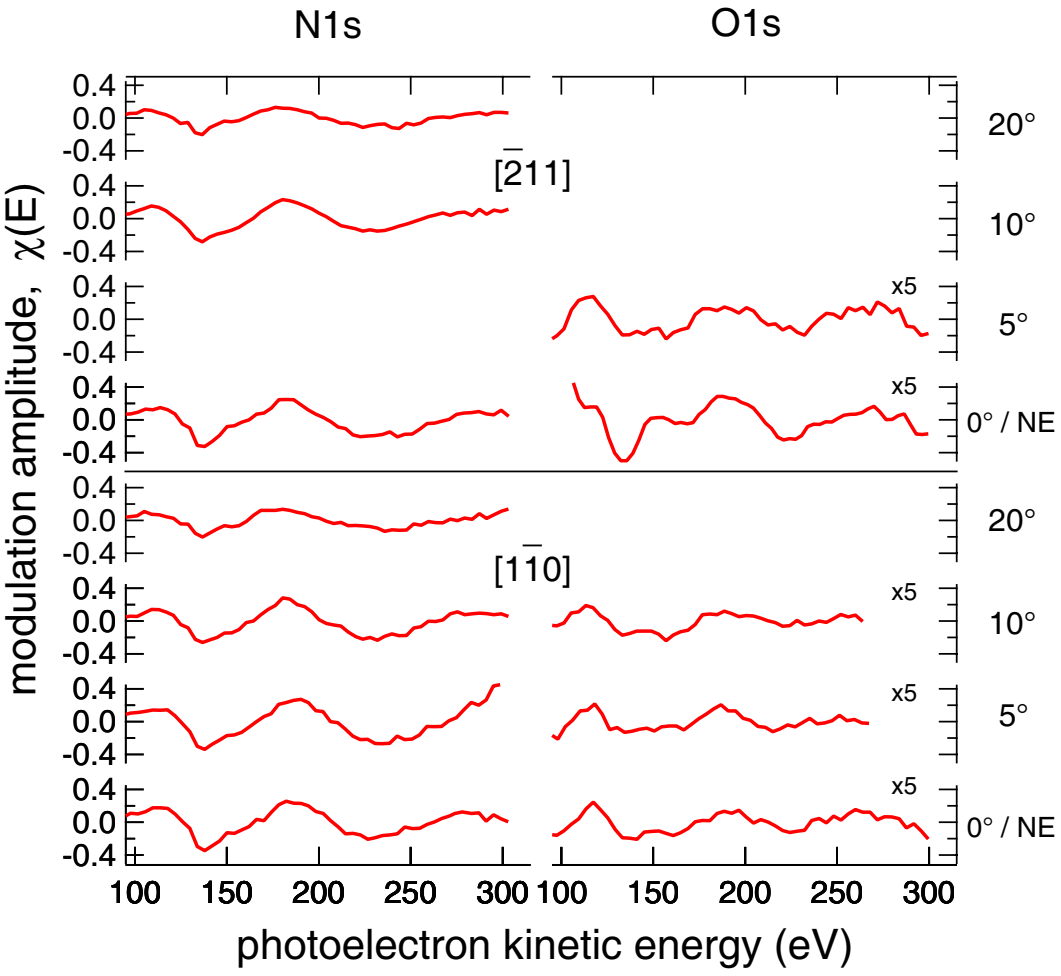

Figure 4.31: Experimental N 1s and O 1s PhD spectra from the Cu(111) / glycinate surface. Note that the modulation amplitudes of the O 1s spectra have been scaled up by a factor of 5.

Note that the strong long period modulations for the N 1s PhD data are in stark contrast to the upright structure (Fig 4.29) predicted by DFT calculations by Duncan et al. [69] using the GGA-RPBE functional.

4.5.4 Quantitative analysis of PhD data

In view of the reasonably strong modulations seen in the N 1s PhD spectra, initial calculations focussed on the determination of the adsorption site of the N atom (within

Table 4.4: Structural parameter values obtained from the three models giving the lowest R-factors in simulations of O 1s and N 1s PhD spectra, compared with the values obtained in the GGA-PW91 DFT calculations for a (4x4) phase presented by Duncan et al. [69] d values are interatomic distances, z values are interlayer spacings and xy values are lateral offset values from atop a surface Cu atom. In structures in which an oxygen atom is close to a bridge site, the two Cu-O nearest-neighbour parameter values are given. O1 is the oxygen atom that is closer to the N atom. Values in parentheses are the error estimates in the last digit(s) of the parameter value.

	atop-bidentate		atop-tridentate		bridge-tridentate	
Parameter	DFT	PhD	DFT	PhD	DFT	PhD
d_{Cu-N} (Å)	2.10	2.02 ± 0.03	2.19	2.02 ± 0.03	2.13	2.02 ± 0.03
z_{Cu-N} (Å)	2.09	1.96 ± 0.02	2.11	1.96 ± 0.02	2.12	1.96 ± 0.02
xy_{Cu-N} (Å)	0.21	0.5 ± 0.1	0.58	0.5 ± 0.1	0.17	0.5 ± 0.1
d_{Cu-O1} (Å)	1.95	2.00 ± 0.03	2.19	2.00 ± 0.07	2.10	2.02 ± 0.04
z_{Cu-O1} (Å)	1.92	1.98 ± 0.03	2.12	1.98 ± 0.07	2.08	2.02 ± 0.04
xy_{Cu-O1} (Å)	0.37	0.2 ± 0.2	0.54	0.3 ± 0.4	0.24	0.1 ± 0.4
d_{Cu-O2} (Å)	–	–	2.10	2.01 ± 0.07	2.33	2.5 ± 0.1
					2.57	3.0 ± 0.1
z_{Cu-O2} (Å)	3.42	3.45 ± 0.07	2.07	2.00 ± 0.04	1.98	2.31 ± 0.07
					2.14	2.55 ± 0.07
xy_{Cu-O2} (Å)	–	–	0.37	0.2 ± 0.3	1.22	1.0 ± 0.3
					1.42	1.6 ± 0.3

the molecule) on the surface. Bearing in mind the qualitative assessment in §4.5.3 above, suggesting that the N species is in a near atop site, this initial determination of the N adsorption site was pursued by a grid search of the parameter space for an isolated N atom place on the surface close to an atop site. The position of the N atom was defined in spherical coordinates with the nearest-neighbour Cu atom as the origin, the three defining parameters being the bondlength between the N and Cu atom (d_{Cu-N}), the tilt of the Cu-O bond away from the surface normal, and the azimuthal orientation of the bond around the surface normal.

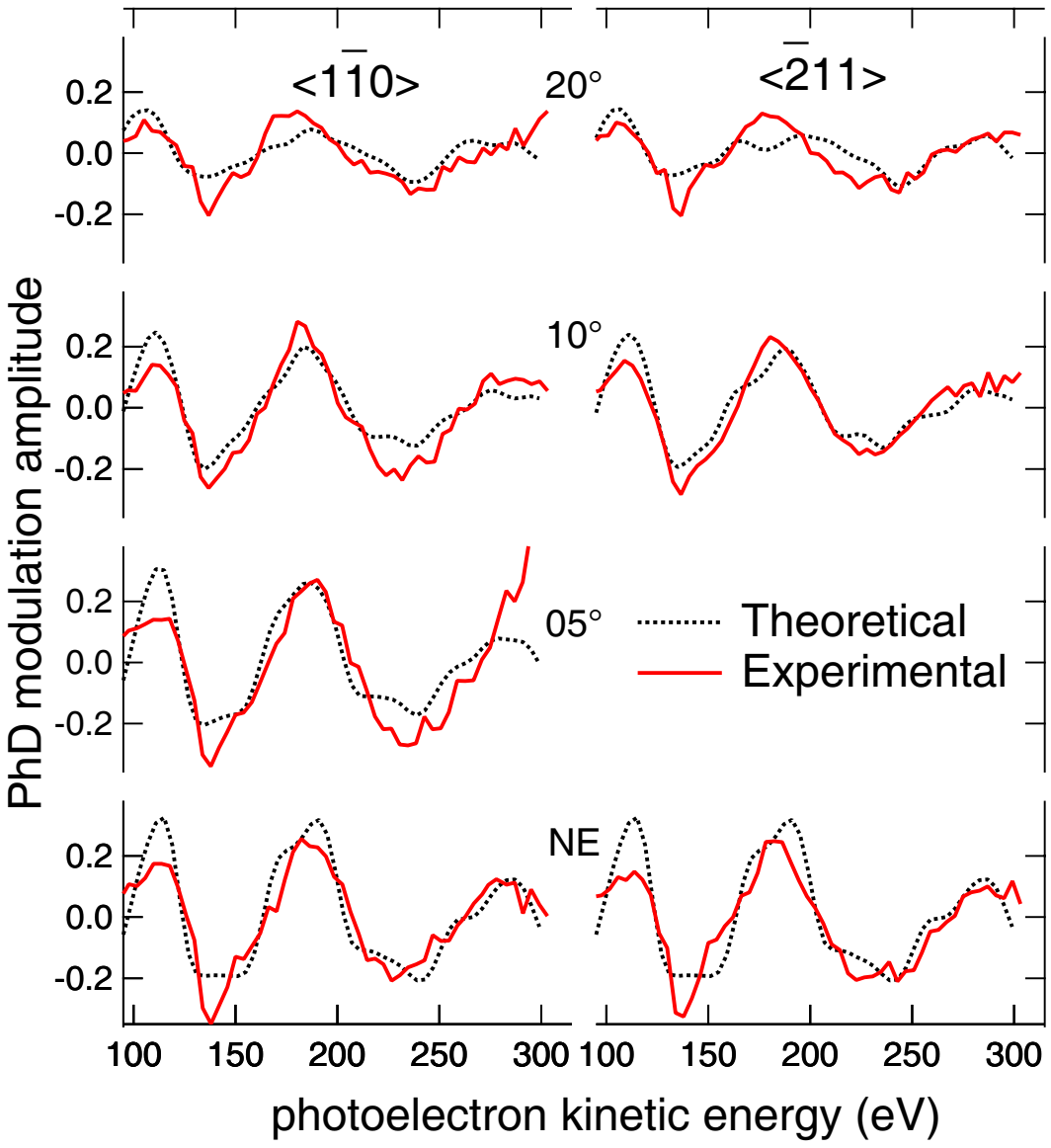

Figure 4.32: Comparison of the experimental N 1s PhD modulation spectra of Fig 4.31 with the results of the theoretical simulations for the best-fit local site of the N emitter atom, including its nearest neigbour C atom scatterer.

The results showed no significant sensitivity of the calculated PhD spectra to the azimuthal rotation, but there was a strong dependence on both the d_{Cu-N} and

polar angle. The best fit, with an R-factor of 0.17, was found with values for d_{Cu-N} and the polar angle of 2.02±0.02 Å and 12±5°, respectively. This combination of parameters means that the N atom is laterally displaced by 0.42±0.18 Å from an exact atop site. Including the nearest-neighbour C atom within the molecules as an additional scatter in the calculation did not significantly affect the fit. Figure 4.32 shows a comparison of the seven experimental N 1s PhD spectra of Fig. 4.31 with the results of the multiple scattering simulations for this best-fit structure. Notice that this experimental Cu-N bondlength (2.02±0.02 Å) is significantly shorter than that predicted by the DFT calculations using the GGA-RPBE functional (2.15-2.29 Å) reported by Duncan et al. [69], consistent with the expectation of underbinding with this functional. The measured bondlength is actually much closer to the comparable predictions of the calculations using the LDA functional also reported by Duncan et al..

The much weaker PhD modulations in the O 1s PhD spectra are clearly indicative of multiple sites and / or low-symmetry sites on the surface, although the similarity of the periodicity of the O 1s and N 1s spectra at normal emission also indicate that at least one O atom is in the vicinity of an atop site. Initial searches of possible tridentate structures proved rather inconclusive.

Further calculations based on the stable structures predicted by the DFT calculations of Duncan et al. [69] were therefore performed. Note that, in these calculations, it was assumed that the glycinate layer on the Cu(111) surface was racemic; calculations were therefore averaged over the local structures shown in Fig. 4.29, and their mirror images. Because PhD is intrinsically a local structural probe, it cannot distinguish between an intrinsically heterochiral structure (which would be created if the (8x4) ordering was due to adjacent (4x4) units of opposite chirality), and the alternative situation of homochiral domains of the two enantiomers. Of course, we may anticipate that the exact structural paramters found in the DFT calculations may not be correct, so the parameter space around these computed minimum-energy structures was explored to optimise the agreement between the PhD experimental data and the resulting multiple scattering simulations. To achieve this the PSO algorithm (§2.6,[39]) was used, constraining the Cartesian coordinates of the two O atoms to lie within 0.2 Å in the x, y and z directions of the theoretically predicted structures shown in Fig. 4.29. Initially the calculations were performed with only the two O atoms on the surface (acting as both emitters and scatterers), but the final refinement was performed including scattering from both C atoms of the glycinate molecule. Only the nearest-neighbour (carboxylate) C atom influenced the simulated spectra, so the more distant N atom was not included. Although the presence of the carboxylate C atom did have a significant effect on the simulated spectra, they were very insensitive to its exact location. No acceptable structure starting from

the hollow-O-N-bidentate model was found in these structural optimisations, but three acceptable fits were found for structures orginating from the bridge-tridentate, atop-O-N-bidentate and atop-tridentate models, with R values of 0.24, 0.24 and 0.23, respectively.

Figure 4.33 shows a comparison of the five experimental O 1s PhD spectra of Fig 4.31 compared with the results of the multiple scattering simulations for these three best-fit structures. Note that all three models are consistent with the adsorption site determined for the N atom. The associated experimentally-determined structural parameter values for these three models are shown in table 4.4 and are compared with the values obtained from the DFT calculations using the GGA-PW91 functional (which are generally intermediate between the values obtained from the GGA-RPBE and LDA calculations) by Duncan et al. [69]. Based on the PhD data analysis alone, all of these structures are equally acceptable, but additional information may provide a basis for further discrimination

One such piece of information is the results of the previous (RAIRS) vibrational spectroscopic study of this system [135]. An important difference between the three models is that in the O-N-bidentate bonding model the O-C-O plane of the carboxylate species is tilted far out of the surface plane, while the two O atoms are clearly in quite distinct local bonding environments. In this configuration one would expect the asymmetric C-O stretching mode to appear very strong in the RAIR spectra as this mode becomes strongly dipole active, or indeed the two C-O stretches could become uncoupled. The RAIRS spectra, however, show an asymmetric C-O stretching mode with a frequency and relative intensity that is very similar to that seen on Cu(100) on which glycinate adopts a tridentate bonding. It therefore seems unlikely that this O-N-bidentate bonding is present on the Cu(111) surface.

The remaining question is therefore whether there is any basis on which to distinguish the two tridentate bonding models in which the key difference is the location of the O atoms on the surface. In this regard, the data of Table 4.4 are relevant. The structures found in the PhD analysis were based on a re-optimisation of the detailed structural parameters of models found to correspond to stable and reasonably low-energy structures in the DFT calculations of Duncan et al.[69]. It is therefore instructive to compare the resulting parameter values of the PhD and DFT solutions; while we may certainly anticipate bondlength differences of as much as 0.1-0.2 Å, much larger differences in several parameters might indicate a more fundamental inconsistency. In this regard, two aspects of the parameters for the bridge-tridentate model are questionable. One is the distance of the bridging O atom from the nearest-neighbour Cu atom which in the PhD analysis is 2.5±0.1 Å; this distance is clearly too long to correspond to a chemisorption bond with the surface and is actually significantly longer than the value found in the DFT analysis.

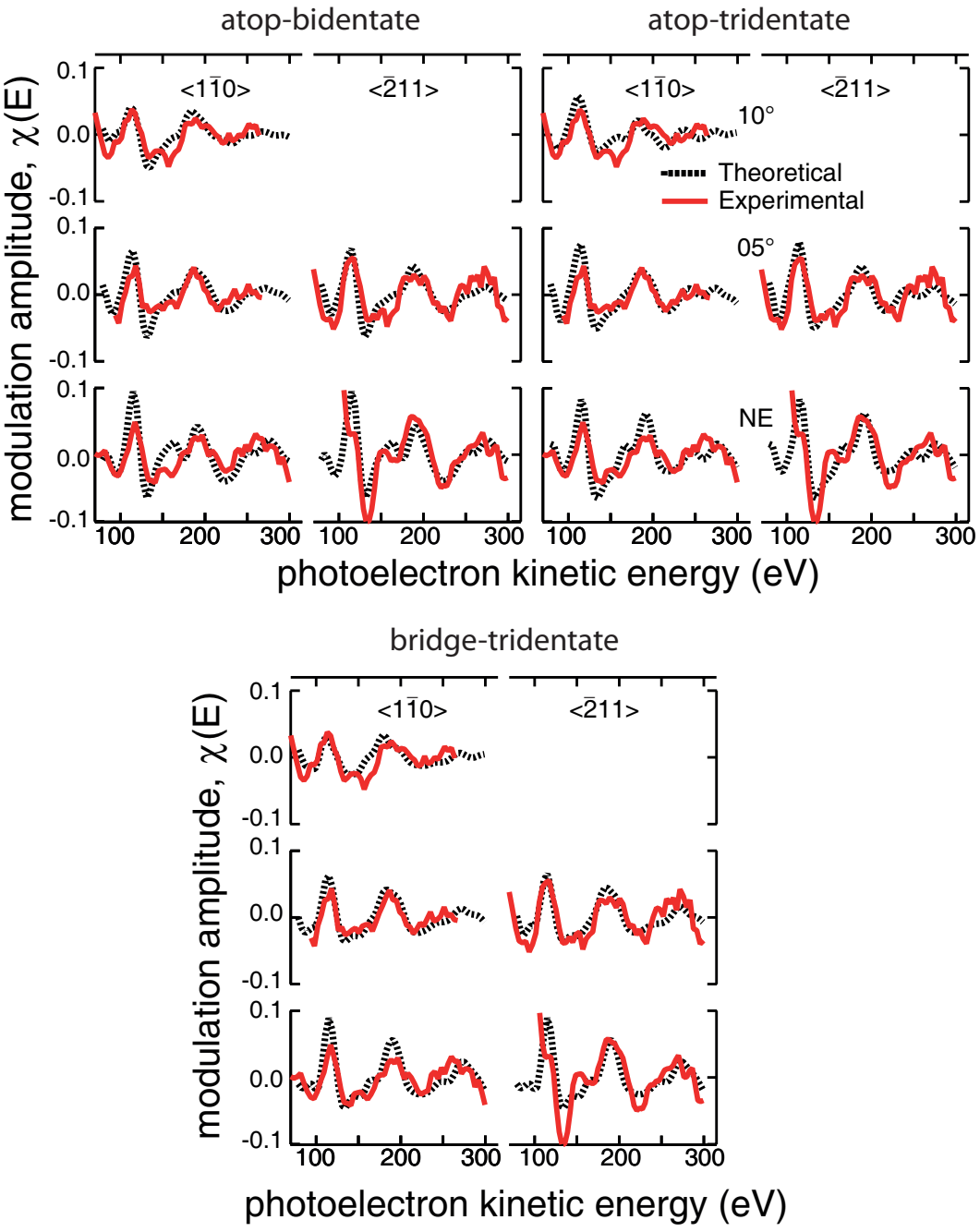

Figure 4.33: Comparison of the experimental O 1s PhD modulation spectra of Fig 4.31 with the results of the theoretical simulations for the three alternative models giving the lowest R-factors. Note that all three structures are compatible with the local site of the N atom giving rise to the best fit N 1s PhD data (Fig 4.32).

This contrasts with the fact that the DFT calculations appear to consistently yield chemisorption bondlengths that are too long. Indeed, the near-atop O atom in this structure is found in the PhD analysis to have an associated Cu-O bondlength of 2.02±0.04 Å, consistent with chemisorption, and quite close to the value found in the GGA-PW91 calculations of Duncan et al.. In effect, therefore, the nominal bridge-tridentate structure found to be compatible with the PhD data is not tridentate in its bonding, and is a fundamentally different structure from that identified in the DFT calculations. One further significant difference between the values of a parameter in the PhD and DFT analysis is the lateral offset of the N atoms from an atop site, xy_{Cu-N}. An excellent theoretical fit to the N 1s PhD data was obtained, with a value for this parameter of 0.42±0.18 Å. This value is in good agreement only with that found in the DFT calculations for the atop-tridentate model, providing a further basis for regarding this solution as the most probable one.

4.5.5 General discussion

Using energy-scanned photoelectron diffraction we have clearly identified the N adsorption site of the glycinate species on the Cu(111) to be close to atop, and while on the basis of this technique alone there is some ambiguity over the exact bonding sites of the O atoms, it is clear that glycinate bonds to the surface through both the N and O atoms. DFT calculations by Duncan et al. [69] identified several stable adsorption geometries of glycinate on this surface, and it has been shown here that three of those possible models are potentially consistent with the PhD data. In particular structures based off the atop-O-N-bidentate, atop-tridentate and bridge-tridentate models (Fig. 4.29) were found to fit the PhD data comparably well. The former model seems to be inconsistent with the results of previously-published RAIRS experiments and in the latter model there is a striking difference between the predicted structure from Duncan et al.'s DFT calculations and the best fitting structure found conforming to this model. We therefore conclude that the most probable local adsorption geometry is the atop-tridentate model.

While the results of this work appear to identify one specific preferred adsorption geometry, we should recall that the observed (8x4) periodicity of the ordered phase of glycinate on Cu(111) probably implies that at least two different geometries are occupied. One possibility is that the two geometries simply correspond to the two different enantiomers of a tridentate-bonded glycinate species; this possibility is already included in our PhD simulations. However, it is also possible that two or more distinct sites are occupied. In this regard we should note that the best-fit PhD simulations for the three structures of Table 4.4 were all performed with root-mean-squared vibrational amplitudes for the O atoms of 0.13±0.02 Å, significantly

larger than those of bulk Cu atoms at room temperature (0.08 Å). The associated Debye-Waller factor does not, of course, distinguish between dynamic and static displacements of the atoms, so this apparent vibrational enhancement may be a result of static displacements, either of different specific sites, or due to local disorder. On the other hand, the DFT calculations indicate that the corrugation of the surface potential across the surface experienced by tridentate-bonded glycinate is rather weak, so those molecules that are not locked in the ordered phase may have quite a high surface mobility.

4.6 Conclusions

The adsorption sites of four different biologically-related molecules on copper surfaces have been determined using O 1s and N 1s PhD spectra. In all four cases the oxygen atoms were found to (at least partially) occupy near atop sites, with clear single coordination to a surface atom. In all cases the bonding nitrogen atoms were also found in near atop sites with bond lengths that are comparable to those already published in the literature (Table 4.5).

In three of the systems presented within this chapter, the bonding (at least partially) is via a carboxylate group (-COO). For the two phases of tartaric acid on Cu(110) (§4.4), mono- and bi-tartrate, the carboxylate species adsorb with the individual O atoms in near atop sites, and the centre of the carboxylate bond in a near-bridge site. This is qualitatively similar to that of formate (the simplest molecule containing a carboxylate group, HCOOH) on the same surface. On the Cu(110) surface formate adsorbs with its two O atoms in near atop sites, and the carboxylate bond is centred over the bridge site. The Cu-O bond lengths found for these similar sites are also not significantly different (Table 4.5). In the case of glycinate on the same surface [88, 89], while the bonding geometry is qualitatively similar (O atoms in near atop sites, etc.) the bond length found is significantly longer (Table 4.5); in fact the bond length is more comparable to that of formate on Cu(111) [5]. It could be argued that the glycine molecule must accomodate 3 different points of contact with the surface (the two O atoms in the carboxylate group and the N atom in the amine group) - however, bitartrate must accomodate 4 different points of contact - so the steric / shape hinderence could be greater for bitartrate species than glycine; though it is likely that the bitartrate molecule is more flexible, relieving some of the steric hinderance. The source of this descrepancy could also be attributed to intramolecular interactions. The glycine-glycine interaction is predicted to have relatively strong (attractive) hydrogen bonding component between the amine group and the carboxylate group [69], perhaps drawing the molecule out of the surface, and the bitartrate-bitartrate interaction has been predicted to have no

Table 4.5: Comparison of the determined Cu-O and Cu-N bond lengths presented in this thesis to those present in the literature

System	d_{Cu-O} (Å)	d_{Cu-N} (Å)
formate Cu(110) [5]	1.90 ± 0.03	–
formate Cu(111) [5]	1.99 ± 0.04	–
acetate Cu(110) [124]	1.91 ± 0.04	–
benzoate Cu(110) [125]	1.91 ± 0.02	–
monotartrate Cu(110) (§4.4)	1.92 ± 0.08 / 1.93 ± 0.06	–
bitartrate Cu(110) (§4.4)		
hollow - 'upright'	1.94 ± 0.06 / 1.95 ± 0.09	–
hollow - 'flat'	1.93 ± 0.08 / 1.95 ± 0.08	–
bridge	1.94 ± 0.07 / 1.97 ± 0.09	–
glycine Cu(111) (§4.5)		
atop-bidentate	2.00 ± 0.03	2.02 ± 0.03
atop-tridentate	2.00 ± 0.07 / 2.01 ± 0.07	2.02 ± 0.03
bridge-tridentate	2.02 ± 0.04 / 2.5 ± 0.1	2.02 ± 0.03
glycine Cu(110) [88, 89]	2.02 ± 0.04 / 2.00 ± 0.04	2.04 ± 0.02
glycine Cu(100) [88]	2.05 ± 0.02	2.04 ± 0.02
alanine Cu(110) [90]	1.98 ± 0.03	2.02 ± 0.03
uracil Cu(110) (§4.3)	1.96 ± 0.04 / 1.93 ± 0.04	1.96 ± 0.04
cytosine Cu(110) (§4.2)	$1.94(+0.06/-0.04)$	$1.94(+0.07/-0.03)$
thymine Cu(110) [91]	2.03 ± 0.03 / 1.91 ± 0.03	1.96 ± 0.02
ammonia Cu(110) [25]	–	2.00 ± 0.04
ammonia Cu(111) [140]	–	2.09 ± 0.03
pyridine Cu(110) [141]	–	2.00 ± 0.02
2-methyl-pyridine [142]	–	2.04 ± 0.02

hydrogen bonding component, with the ordering resulting from repulsive rather than attractive interactions [119]. The Cu-O and Cu-N bond length for glycine on the three high index Cu face - (100), (110) and (111) - does not change significantly (Table 4.5). However, the simple molecules containing similar functional groups, formate (carboxylate group) and ammonia (amine group), show a significant difference in bond length between the (110) and (111) face [5, 25, 140] - implying that whatever is causing the longer bond length for glycine (with respect to formate / bitartrate) is overwhelming the effect of the different surface terminations. The implication of the observed difference in bond length resulting from the (110) and (111) face is discussed by Kreikemeyer et al. [5].

The other two systems within this chapter, cytosine on Cu(110) (§4.2) and uracil on Cu(110) (§4.3), the molecules are observed to interact with the surface through O and N atoms adsorbed in near atop sites (see Figs 4.9 and 4.16 respectively). The associated bond lengths (Table 4.5) are quantitatively similar to those of formate and ammonia, as well as the other pyrimidine based nucleobase, thymine [91], on the Cu(110) surface . As the distance between the bonding species ($\sim$ 2.3 Å) and the nearest neighbour Cu atoms (2.56 Å) is quite similar for both of these molecules, there is only a limited steric hinderance in accomodating the bonding atoms. The cytosine intramolecular interactions are attractive [95], however, this does **not** produce a longer O-Cu bond length than uracil on the same surface (which does not form ordered overlayers on the Cu(110) surface - implying no strong intramolecular interactions). The intramolecular hydrogen bonding between cytosine molecules is most likely mediated by the amine group (N(4), Fig 4.1), which is not coordinated to the surface.

Chapter 5

Hydrocarbon remnant of furan decomposition on Pd(111)

5.1 Introduction

Furan, C_4H_4O, is the simplest oxygen-containing aromatic hydrocarbon, and is sometimes used as a model in hydrodeoxygenation studies of such compounds that need to be removed from crude petroleum and liquids derived from coal and biomass [143]. It therefore provides a convenient model for detailed surface science investigations of this process on well-characterised single crystal surfaces, yet rather few such studies have been conducted. On the clean coinage metal surfaces, Cu(100) [144] and Ag(110) [145], the molecule has been found to adsorb and desorb intact. On Pd(111) furan adsorbs intact at low temperatures, but around room temperature deoxygenation occurs, believed to lead to the presence of coadsorbed CO, atomic H and a C_3H_3 species on the surface [146–149] (Fig. 5.1):

$$C_4H_4O \longrightarrow CO + C_3H_3 + H. \tag{5.1}$$

There is clear spectroscopic evidence for the dissociation of the furan, adsorbed at low temperature, to create surface CO together with a second C-containing species when heated to $\sim 230 - 270$ K, from XPS, ultraviolet photoemission spectroscopy (UPS) and HREELS [146]. Temperature-programmed desorption (TPD) shows CO desorption occurs only at a higher temperature of ~ 500 K. Also seen in TPD is H_2 desorption at a peak temperature of 350-360 K [146, 147]; this temperature is similar to that of associative desorption of molecular hydrogen from Pd(111) following adsorption of atomic H, so this H_2 TPD peak is believed to be desorption - rather than dissociation - limited. The implication is thus that atomic H is lost from the furan in the deoxygenation reaction at the lower temperature of ~ 270 K, at which there

is spectroscopic evidence of dissociation. Thus, if there is a single C_3H_x hydrocarbon fragment resulting from the reaction, it seems that $x < 4$ is most likely. The strongest evidence to suggest that the hydrocarbon fragment resulting from this deoxygenation is C_3H_3 comes from laser-induced thermal desorption (LITD), which shows small amounts of benzene desorption in the surface temperature range $\sim 330-430$ K [148]. Surface C_6H_6 is believed to arise from a C_3H_3 coupling reaction, but its presence is not detected in conventional TPD, because benzene dissociates on Pd(111) before it desorbs in a heating cycle. STM studies of the surface at ~ 200 K (a temperature too high to image the mobile CO species at low coverage), following this heat treatment, have identified a molecular species on the surface was attributed to C_3H_3 [150].

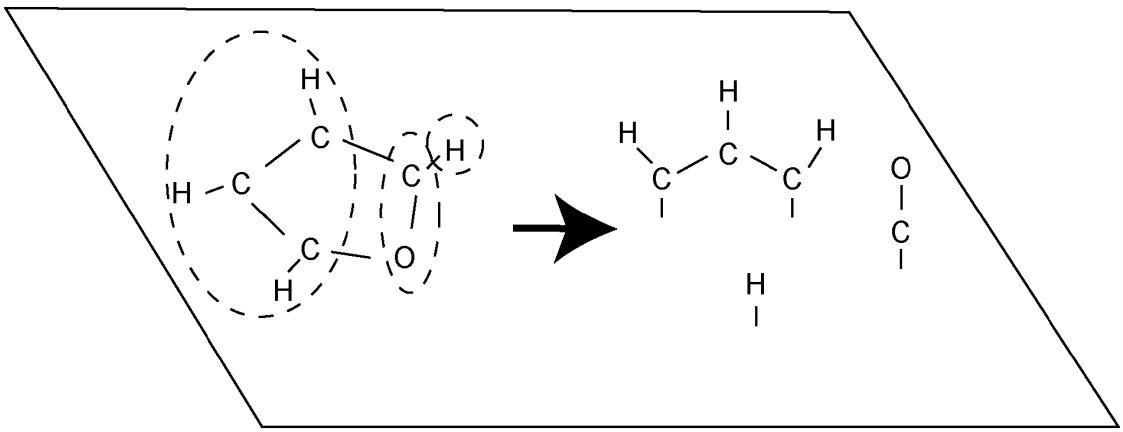

Figure 5.1: Schematic diagram of the furan dissociation reaction on Pd(111), showing the C_3H_3 fragment in the half-benzene conformer.

More recently, an investigation of this surface has been conducted by PhD using C 1s XPS [38]. In the PhD study of the furan dissociation products on Pd(111), two C 1s components (previously observed by Ormerod et al.[146]) were clearly resolved by XPS. The higher binding energy state, previously identified with adsorbed CO, yielded PhD data corresponding to occupation by the associated C atom of three-fold coordinated fcc hollow sites (directly above third-layer Pd atoms); this is one of the two hollow adsorption sites known to be occupied by CO on this surface in the absence of coadsorbates. The lower binding energy component was assigned to the C_3H_3 species, and an extensive search was conducted of possible adsorption sites consistent with the PhD data from this component. These PhD data were recorded after dosing the surface with furan at low temperature ($\sim$ 160 K), slowly heating to 340 K, and re-cooling before collecting the data. On the basis of the previously-published TPD data, the surface studied is expected to retain the CO and C_3H_3 co-adsorbates, but most of the atomic H produced in the initial dissociation reaction is likely to have been desorbed.

Determining the local adsorption geometry of C_3H_3 species on Pd(111) is a

challenging problem for the PhD technique, because the constituent C atoms must occupy at least two, and possibly three, different local adsorption sites, but any binding energy differences for these C atoms were too small to be resolved. The measured PhD modulations from the hydrocarbon C 1s component therefore arise from an incoherent sum of the modulations of these distinct emitter sites. In view of this, it is not surprising that the observed modulations were extremely weak (typically $\pm 10\%$). In order to render the structural search viable, certain symmetry constraints were therefore applied. Specifically, the C_3H_3 species was assumed to adopt a half-benzene (CH-CH-CH) configuration (as had been previously suggested schematically [148], and as reproduced in Fig. 5.1), with the outer two C atoms in symmetrically equivalent locations with respect to the outermost Pd atomic layer, such that the molecule shares the mirror planes of this substrate layer. While a generally good fit to the PhD data could be achieved for two alternative but closely similar model structures of this type (Fig. 5.2), the surprising conclusion was that the molecular plane was found to lie almost parallel to the surface. By contrast, in an analogue organometallic carbonyl cluster compound, in which a fully methylated C_3R_3 species (i.e. $(CCH_3)_3$ rather than $(CH)_3$)) is bonded to a triangular group of three Ru atoms [151], the C_3 plane is tilted by $\sim 63^\circ$ out of the Ru_3 plane (Fig. 5.2).

The symmetry constraints of this PhD analysis were applied in the interests of expediency, to allow a preferred structural model to be identified, rather than because there was prior evidence that such symmetry was a necessary requirement for C_3H_3 adsorption. Recently, total energy calculations using density functional theory (DFT), performed by Bradley et al. [37] found the planar configuration proposed by Knight el al. [38] (shown schematically in Fig 5.2) to be unfavourable - predicting a tilt of 58°, similar to that found for the $Ru_3(CCH_3)_3$ cluster. The DFT calculations also showed a significant decrease in energy by moving to a site that did not conserve the symmetry of the surface. The DFT calculations by Bradley et al. also predicted several other possible stable conformations, which are shown with their respective energies in Fig 5.3. Note that a lower energy corresponds to a more tightly bound adsorbate species.

Armed with a series of lowest-energy structures obtained by DFT calculations for the different C_3H_3 conformers [37], we have a new opportunity to utilise the experimental PhD data. Specifically, we can ask if PhD simulations based on any of the DFT-derived structures provide a good description of the experimental data, and whether the conformer found to have the lowest energy is the one that provides the best description of the PhD data.

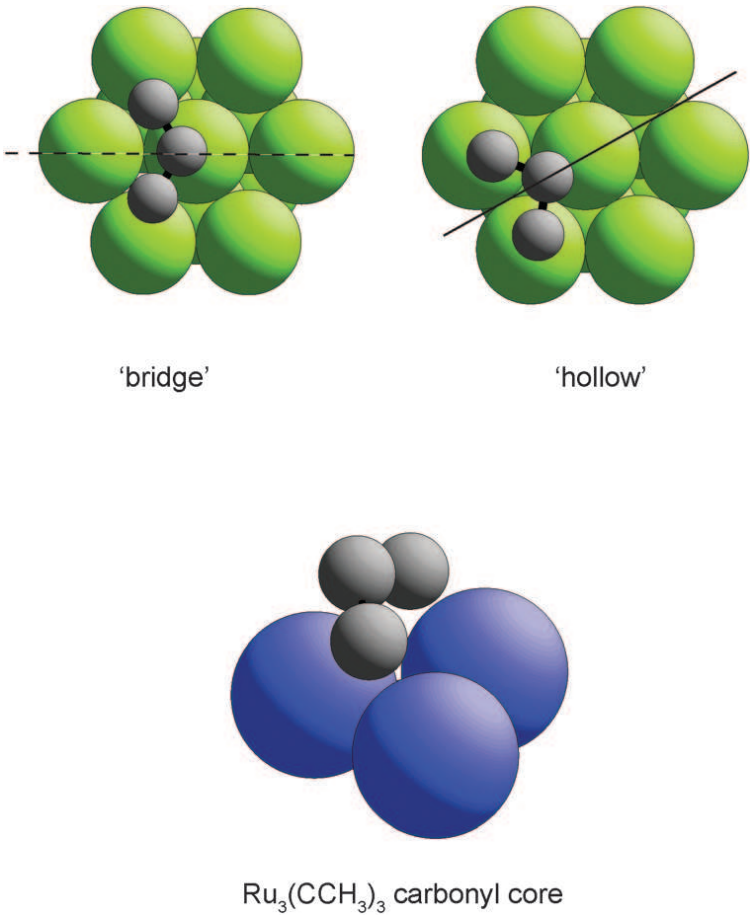

Figure 5.2: (top) Plan views of the two alternative adsorption geometries of the half-benzene conformer of C_3H_3 on Pd(111) derived from the original analysis of the PhD data [38]. Only the C atoms are shown, as the PhD technique is insensitive to their position. The full line shows a mirror plane of the substrate, the dashed line a mirror plane of the first layer of substrate only. (bottom) relative locations of three Ru atoms (large blue spheres) and the three C atoms of the CCH_3 ligands in the organometallic complex (μ -H)$Ru_3(\mu_3 - \eta^3$-CMeCMeCMe)$(CO)_9$[151].

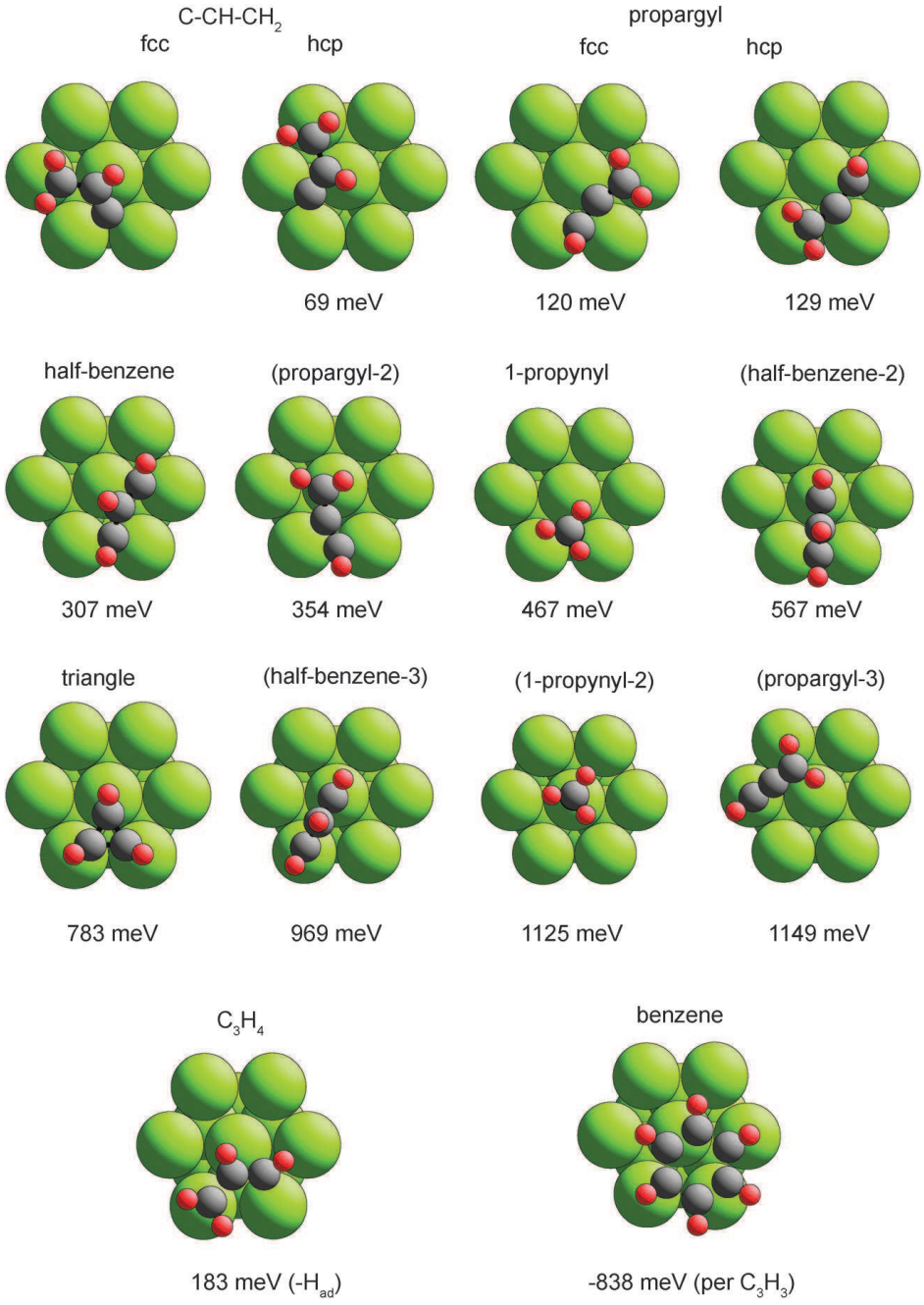

Figure 5.3: Plan view of the Pd(111) surface showing the different optimised molecular configurations and adsorption geometries predicted by DFT calculations [37] for C_3H_3, together with those of a C_3H_4 and benzene species. All energies are shown with respect to the lowest energy structure (C-CH-CH_2). The structures with the bracketed names correspond to local energy minima of other models.

5.2 Results of PhD simulations

The obvious strategy, to compare the geometries predicted by DFT to the experimental data, is to run PhD simulations using the exact atomic positions found to give the lowest total energy in the DFT calculations, but past experience shows that this is unlikely to be successful. Firstly, the DFT calculations are performed on a Pd slab substrate in which the lateral periodicity is set to the value corresponding to the lowest-energy bulk structure; this differs from the true value by $\sim 1.5\%$, so some rescaling of all bond lengths must be applied to ensure that the substrate, at least, is correctly described in the diffraction simulations. Secondly, particularly for molecular adsorbates, experimentally determined adsorption bond lengths, mainly obtained using the PhD technique, can differ by up to ~ 0.1 Å from the values obtained in DFT calculations (e.g. [90]), and a bond length change of this magnitude can have a very significant effect on simulated PhD spectra. It is therefore essential to allow some structural optimisation in the PhD simulations, aimed at improving the agreement between experiment and simulations. There are, however, some limitations in the PhD structural optimisation. In a DFT total energy calculation, the coordinates of all the substrate atoms in the outermost several layers, as well as those of all the atoms within the adsorbed molecules, are optimised; small variations in the positions of substrate atoms from their bulk-termination positions are found routinely, particularly for the outermost one or two atomic layers. Optimising such a large number of parameters in PhD is unrealistic, in part because the size of the experimental dataset is too small, in part because PhD spectra are insensitive to small movements of subsurface atoms that are distant from the emitter atom. The main sensitivity is to the emitter-substrate near-neighbour distances, and particularly the components of these distances perpendicular to the surface.

In order to ensure that the optimised structures of the PhD calculations corresponded to essentially the same conformer and adsorption geometry as in the initial DFT structures, constraints were placed on the optimisation; specifically, none of the Cartesian coordinates of the C atoms positions was allowed to move by more than 0.1 Å from their original positions.

The numerical results of these PhD simulations are summarised in Table 5.1 for the DFT structures that correspond to the lowest-energy solution for each of the conformers investigated; a comparison of the experimental PhD spectra with the results of the theoretical simulations for the three lowest-energy structures is shown in Fig. 5.4. The table shows the R-factor values obtained, and provides a comparison of the C-Pd nearest neighbour bonding distances in the original DFT solution and the modified structure found to give improved agreement with the PhD data. The R-factor values of these PhD-optimised structures fall in the range 0.32 to 0.76. Two

Table 5.1: Summary of the results of the simulations of the PhD modulation spectra for the minimum-energy structures identified in the DFT calculations (Fig. 5.3). For each structure the table shows the C-Pd nearest-neighbour distances in the exact DFT structure, and in the re-optimised structure obtained from the PhD simulations, including the value of the R-factor that provides a measure of the level of agreement between the PhD experimental data and these simulations

Structure	DFT C-Pd nn distances (Å)	PhD C-Pd nn distances (Å)	PhD R-factor
C-CH-CH_2	2.14 (CH_2) 2.27, 2.95 (CH) 1.96, 1.97 2.05 (C)	2.13 2.19, 2.98 1.97,1.98,2.02	0.52
propargyl	2.13 (CH_2) 2.02, 2.26 (C) 2.04, 2.15 (CH)	2.14 1.94, 2.29 2.04, 2.16	0.32
half-benzene	2.01, 2.14 2.32, 2.89, 3.09 2.00, 2.12	2.03, 2.10 2.13, 2.82, 3.05 1.95, 1.96	0.43
1-propynyl	2.10	2.10	0.76
triangle	2.05	2.12	0.59
C_3H_4	2.11 (CH_2) 2.36, 2.76 (CH) 2.01, 2.12 2.71 (CH)	2.12 2.43, 2.68 2.08, 2.08, 2.66	0.23
benzene	2.23 2.23 2.20	2.14 2.11 2.15	0.47

of the C_3H_3 conformer structures yield potentially acceptable R-factor values, namely propargyl and half-benzene. The C–CH–CH_2 conformer that corresponds to the lowest energy structure in the DFT calculations, yields a significantly higher R-factor value of 0.52, strongly suggesting that this is not the structure that occurs in practice. In assessing the compatibility of the DFT and PhD results, it is also important to compare the C-Pd bondlengths, because the PhD optimisation we have conducted allows these to change significantly from the DFT values, and large changes could mean that we are not really comparing the same conformers. In this context we should recall that PhD is insensitive to the location of the very weakly-scattering H atoms, so while PhD identifies the preferred position of the C atoms, it does not distinguish C atoms in C, CH, CH_2, and CH_3 species. In fact Table 5.1 indicates that the C-Pd bond lengths of the DFT and PhD structures for each conformer are very similar. Perhaps most notable is the C-Pd nearest-neighbour distance of the middle C atom in the half-benzene conformer, with DFT and PhD values of 2.32 Å, and 2.13 Å, respectively. This results in rather different tilt angles of the C-C-C plane relative to the surface normal, namely 32° and 41°, respectively.

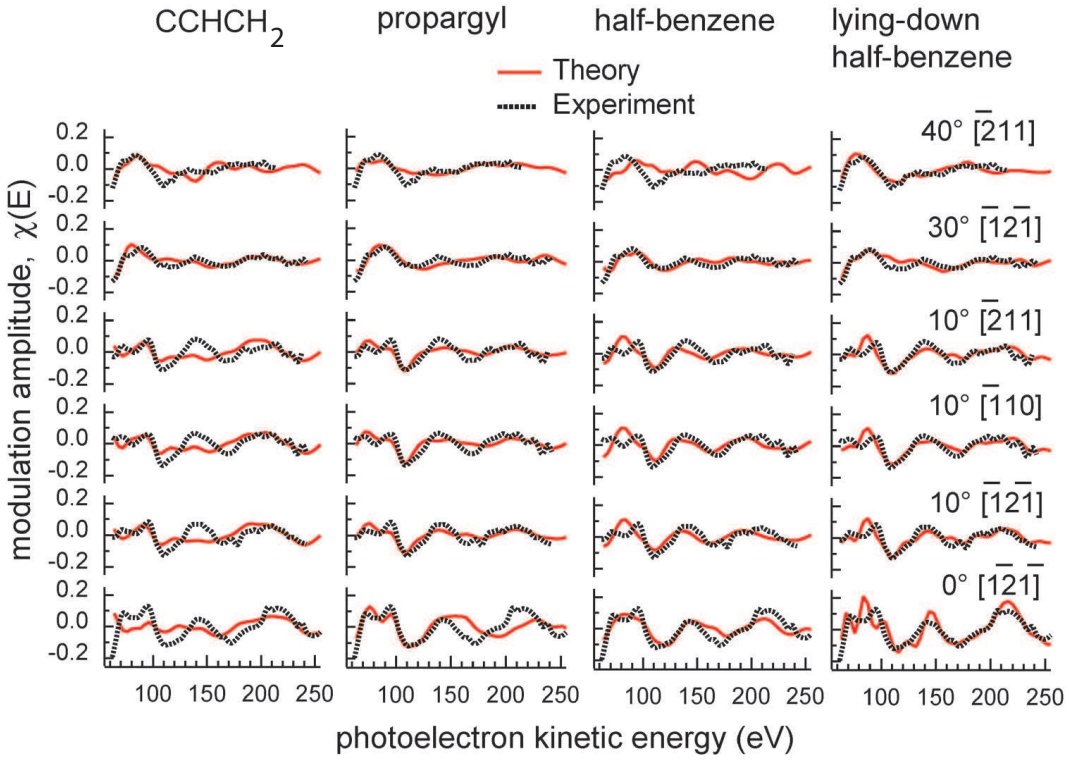

Figure 5.4: Comparison of the experimental C 1s PhD modulations spectra, recorded from the hydrocarbon fragment resulting from furan decomposition on Pd(111) [38], with the results of theoretical simulations for several different structures. On the left are shown the results for the three lowest energy conformers, according to the DFT calculations. On the right, are the results of calculations for the lying-down half-benzene hollow structure shown in Fig. 5.2.

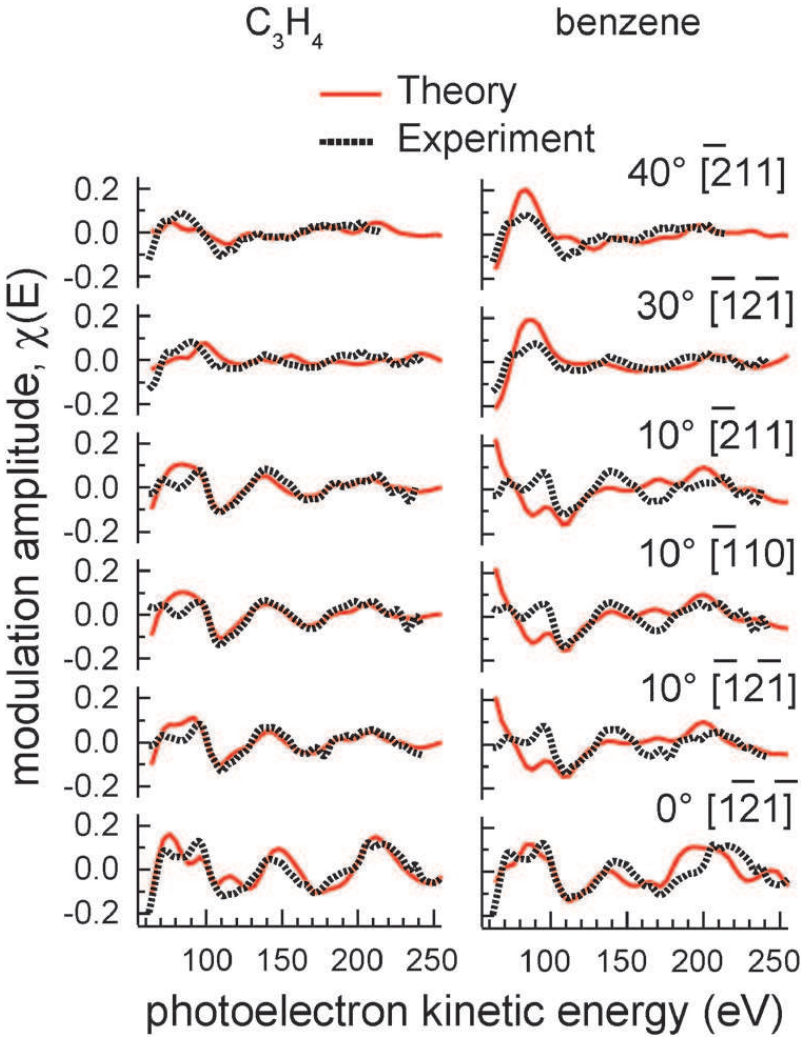

Figure 5.5: Comparison of the experimental C 1s PhD modulations spectra, recorded from the hydrocarbon fragment resulting from furan decomposition on Pd(111) [38], with the results of theoretical simulations for adsorbed C_3H_4 and for benzene, in the structures shown in Fig. 5.3.

Note that the values of the R-factors for the re-optimised DFT C_3H_3 structures listed in Table 5.1 are all significantly larger than the value of 0.23 found in the original PhD analysis for the lying-down half-benzene structures shown in Fig. 5.2 (the comparison of experimental and simulated PhD spectra for one of these structures is included in Fig. 5.4). The results of our DFT calculations, however, indicate that these structures do not correspond to stable molecule-surface bonding states, despite having reasonable values of the C-C and C-Pd bondlengths. This highlights the fact that, particularly for a complex problem with multiple emitter sites, such as in the present case, it is possible to find structural solutions that give a good description of the PhD data, but do not correspond to physically reasonable solutions. This proved also to be a feature of a wider, less-constrained, search of possible structures that are compatible with the PhD data using the PSO search algorithm [39]. Structures yielding R-factor values as low as 0.1 could be found, but these had entirely unreasonable associated bond lengths. This is, of course, a timely reminder that, with sufficient free parameters, any data can be fitted. However, physical constraints are an important ingredient of meaningful solutions. Nevertheless, through a series of calculations involving more reasonable constraints, one plausible structural model was identified that did not correspond to any of the DFT solutions. Consideration of the coordination of the three C atoms to the surface Pd atoms led to the conclusion that this model could be rationalised in terms of a C_3H_4 conformer. DFT calculations for such a species confirmed this conclusion, and yielded a structure quite similar to the model first identified though the PSO PhD structure search. The results for this structure are included in Table 5.1, together with the outcome of a similar procedure for the lowest-energy configuration of the benzene molecule on Pd(111) obtained from DFT calculations. Comparisons of the experimental PhD spectra with the results of the simulations for these two models are shown in Fig. 5.5. Clearly this C_3H_4 model does yield an R-factor that is lower than any of the C_3H_3 conformers; whether it is reasonable to believe that the hydrocarbon fragment resulting from the furan dissociation could be C_3H_4, rather than C_3H_3, is discussed in the following section.

5.3 General Discussion and Conclusions

Our objective in undertaking this study (and the objective of the earlier PhD study) was to try to identify the structure of the C_3H_3 species formed on the Pd(111) surface as a result of the partial dissociation of furan. The original studies that characterised the associated surface chemistry led to the suggestion that C_3H_3 may retain the CH-CH-CH half-benzene conformation that arises if one simply removes O-CH from the furan ring. Fig. 5.1 shows this simple idea schematically, although we note that even this simple scheme requires three bonds within the furan molecule to be broken (as

illustrated by the dashed elipses). Such a process is likely to involve transient intermediates, rather than a single concerted action, but whatever the detailed pathway, the energy released as a result of the fragmentation could allow rearrangement of the C_3H_3 fragments. The fact that there is evidence for some (but probably only a small amount of) benzene formation on the surface, in the temperature range $\sim 330 - 430$ K, does suggest that a stable half-benzene conformer may result from the dissociation, because coupling of this conformer to produce benzene seems likely to be more easily effected than for any of the alternative C_3H_3 conformers. On the other hand, the DFT calculations [37] show that there are significant energetic advantages associated with the adsorbed species being in the C–CH–CH_2 or CH–C–CH_2 (propargyle) conformations. Of course, these calculations provide no information on the energy barriers associated with the required relocation of the H atoms, although a shift of one H atom from the central C atom to one end seems less challenging than a shift of a H atom from one end to the other. However, if the H atom is transiently adsorbed on the surface, both mechanisms seem plausible.

The results of the PhD simulations presented in the previous section provide rather strong evidence that the lowest-energy structure for a C_3H_3 species adsorbed on Pd(111), as predicted by DFT calculations, namely C–CH–CH_2, is not present in significant amounts on the surface following dissociation. The most likely reason for this is that, when the C_3H_3 fragment is created by the partial dissociation of furan, there is too large an energy barrier for the fragment to reconfigure to form this C–CH–CH_2 conformer. Based on a combination of the DFT energies, and R-factors found in the PhD simulations, the most likely surface species is the propargyl conformer, although at least some fractional coverage of the half-benzene configuration cannot be excluded.

While this discussion has focussed on the possible conformations and bonding sites of a surface C_3H_3 species, there are two alternative surface species that may be considered, namely C_3H_4 and benzene. Removing CO from furan leaves 3 C atoms and 4 H atoms, so from the point of view of stoichiometry a C_3H_4 species is clearly reasonable. The local structure of the C_3H_4 species found in the DFT calculations evidently leads to a particularly favourable set of PhD modulation spectra, and the adsorption energy is only slightly larger than that of the propargyl C_3H_3 species coadsorbed with atomic H. The alternative possibility of benzene on the surface due to coupling of two C_3H_3 species is, on the basis of the equilibrium total energy alone, strongly favoured. On the other hand, the energy barrier to its formation by C_3H_3 coupling is not known, and the quality of agreement of the PhD simulations for this structure with the experimental data is rather marginal.

Key data relevant to the plausibility of the hydrocarbon intermediate in furan dissociation being C_3H_4, rather than C_3H_3, are the previously-published thermal

desorption spectra. Molecular hydrogen is desorbed from the surface in a TPD experiment at a peak temperature of 350-360 K, so above this temperature it is clear that the average stoichiometry of the residual C_3H_x fragment after CO extraction from furan must have a value of $x < 4$. This does not exclude the possibility that some partial coverage of C_3H_4 is present on the surface even above this temperature range, but if only a single hydrocarbon fragment remains it must have x=3. The PhD experiments were performed on samples that had been heated to 340 K, but as the time at, or close to, this temperature would have been several minutes, one may expect that essentially all the available hydrogen would be desorbed. Some error in the exact sample temperature cannot be excluded, so it is possible that the PhD data were taken under conditions which did not lead to hydrogen desorption. However, the fact that hydrogen desorption temperature is the same as, or very close to, that seen for hydrogen desorption from a Pd(111) surface that has only adsorbed atomic hydrogen, has been taken to imply that the rate limiting step in hydrogen desorption following furan decomposition is associative desorption of adsorbed atomic hydrogen, and not molecular dissociation. If this is the case, the initial furan dissociation at the lower temperature of $\sim 230 - 270$ K (as seen in spectroscopic data) must lead to coadsorption of atomic H and a C_3H_x fragment with a value of $x < 4$. On the other hand, if we regard the close similarity of the H_2 desorption temperature of the hydrogen-dosed and furan-dosed samples as coincidence, it is then possible that its origin in the case of furan decomposition is loss of hydrogen from a C_3H_4 species to C_3H_x with $x = 3$. However, in view of the need for both a fortuitous coincidence in these temperatures, and a significant mis-calibration of the thermocouple in the PhD study, it seems rather unlikely that the surface species studied was C_3H_4.

Rather different arguments lead us to conclude that it also unlikely that the surface species investigated in the PhD study was benzene. The one piece of evidence that surface benzene may result from furan decomposition on Pd(111) is the LITD experiments, which showed small amounts of benzene desorption from the surface during heating in the temperature range $\sim 330-430$ K. The desorbed yield of benzene in these experiments was very low, suggesting that surface benzene that is formed in this temperature range is a minority species, although the report of this work does suggest that the LITD cross-section for benzene desorption may be low. It is notable, though, that ultra-violet photoemission spectra recorded in this temperature range [146] do not show peaks at the characteristic energies of the molecular orbitals of adsorbed benzene (e.g. [152]). Also absent in this temperature range are the γ_{CH} vibrational bands of the benzene ring in HREELS around $800cm^{-1}$ [146], that are dominant in spectra recorded from benzene adsorbed on Pd(111) [153]. This seems to be a clear basis for excluding adsorbed benzene as a major surface species in the PhD experiments.

We therefore conclude that, on the basis of the DFT energies and the PhD R-factors, the most probable structural outcome of furan decomposition on Pd(111) is coadsorbed CO (in hollow sites, as previously established by PhD [38]), atomic H (predicted by DFT to occupy hollow sites [37]) and C_3H_3 in the propargyl conformation, straggling a bridging site as shown in Fig. 5.3. On the same basis, the next most probable form of C_3H_3 is the half-benzene conformer, with the two end C atoms in local bridging sites (Fig. 5.3) with the molecular plane tilted by $\sim 35°$ from the surface normal. The fact that this conformer leads to significantly poorer agreement between theory and experiment for the PhD data, as well as being energetically disfavoured by ~ 180 meV per molecule, does suggest that this is not the sole or dominant conformer on the surface, but partial co-occupation of this species could help to account for the partial production of surface benzene indicated by the LTID data.

Further experiments and theoretical studies could provide a more complete resolution of this problem. Experimentally, new higher-resolution vibrational spectroscopy could provide a clearer spectroscopic fingerprint of the adsorbed species, though the clearest such information would come from single-molecule vibrational spectroscopy using an STM tip. Theoretically, a better understanding could be achieved through calculations of the pathways and energy barriers to the formation of the different C_3H_3 conformers on the Pd(111) surface following furan decomposition.

Chapter 6

Methanol on Ru(0001)

6.1 Introduction

Interest in the interaction of methanol with ruthenium has been motivated in part by the use of Ru as part of a Ru/Pt alloy, in the direct methanol fuel cell [154, 155]. It is well-established that methanol is reduced to carbon monoxide on the Ru(0001) surface, and it has generally been believed that dehydrogenation leads to the production of a surface methoxy species, CH_3O, even at low temperatures $\sim$ 85 K. This was the conclusion of Hrbek et al., using HREELS [156], which was subsequently supported by Brito de Barros et al. [157] using RAIRS who reported increased production of the surface methoxy species through the use of preadsorbed oxygen. Pulsed field desorption mass spectrometry data [158] were also interpreted in terms of a stable surface methoxy species on this surface. More recently, however, this interpretation has been called into question. In particular, a detailed FT-RAIRS study by Gazdzicki, Uvdal and Jakob [159] has concluded that no dissociation of methanol occurs on Ru(0001) at temperatures below 80 K, with isolated methanol molecules or dimers being present at low coverage and temperature, while at higher coverages and temperatures clusters of molecular methanol are formed. A subsequent study by Gazdzicki and Jakob [160], extending the investigation to higher temperatures, concluded that a surface methoxy species is formed, but only in a narrow temperature range from $\sim$ 180-220 K; moreover, dissociation to produce coadsorbed CO already occurs at 220 K.

Here is presented the results of an investigation, using XPS and PhD, of the interaction of methanol with Ru(0001) at $\sim$ 150 K. Our original objective for this work (initiated prior to the most recent report of the FT-RAIRS study at higher temperature) was to try to establish the nature of the adsorbed species produced by this interaction, in part through a determination of its local adsorption site. In particular, DFT calculations of methoxy adsorption indicate that it should bind strongly in either (or both) the hcp or fcc three-fold coordinated hollow sites (directly above

a second layer Ru atom, or in the hollow site which has no Ru atoms below), the two sites being almost energetically equivalent [161]. By contrast, the low-temperature FT-RAIRS experiments indicate that under the conditions of our experiment we may expect to find only methanol clustering, with no well-defined local site for the individual molecules.

In the present case of methoxy or methanol adsorption, O 1s PhD data should provide a clear way of distinguishing between the two alternative adsorbate species and their associated local geometries. A methoxy species in either or both of the high-symmetry hollow sites should give strong O 1s PhD modulations that can be modelled with multiple scattering calculations to determine the exact adsorption site. By contrast, if clustered methanol is present, with no well-defined bonding site for the constituent O atoms relative to the underlying Ru(0001) surface, we expect to see little or no PhD modulations. A further internal check on the consistency of our approach can be obtained by measurement of O 1s PhD data for the atomic oxygen chemisorption phase on Ru(0001) for which the local geometry, involving occupation of the high-symmetry hcp hollow site alone, is well-established [46, 47, 162, 163].

6.2 Experimental details

A clean, well-ordered Ru(0001) surface was prepared from an oriented and polished crystal slice by the usual combination of Ar ion bombardment and brief annealing to $\sim$ 1100 K, to give a sharp (1 $\times$ 1) LEED pattern and a XP spectrum devoid of impurities. Methanol, contained in a glass ampoule attached to the gas-handling line, was purified by multiple freeze-thaw pumping cycles prior to introduction of the vapour into the sample chamber through a leak valve to a partial pressure in the 10^{-8} mbar range. Oxygen and carbon monoxide dosing was effected in a similar fashion by introducing molecular oxygen gas to a similar partial pressure through the leak valve.

6.3 Results

6.3.1 XPS characterisation

Figure 6.1 shows the XP spectra in the energy range of the O 1s emission from the Ru(0001) surface after exposure at $\sim$ 150 K to molecular oxygen, CO and methanol. The oxygen exposure used (40×10^{-6} mbar.s) corresponds to nominal saturation at low pressures and gave rise to a (2x2) LEED pattern which, on the basis of previous work, is attributed to a 0.5 ML (2x1) phase of atomic oxygen. A true 0.25 ML (2x2) phase of atomic oxygen also exists at lower exposures, while a 1.0 ML (1x1) phase

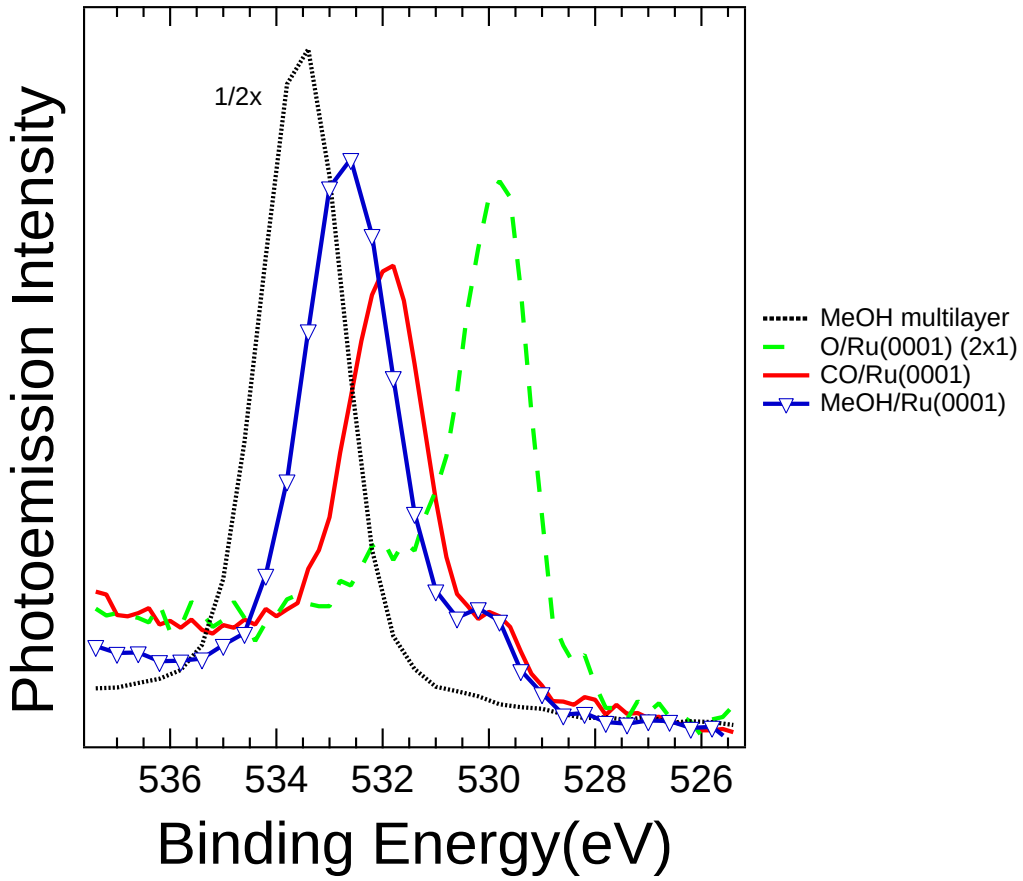

Figure 6.1: XP spectra in the energy range of the O 1s emission peaks from different surface preparations of methanol, oxygen and CO on Ru(0001). All spectra were recorded at normal incidence (emission at a polar angle of 60°) using a photo energy of 650 eV. Absolute binding energies are referenced to the value reported Fuggle et al. [164] for a Ru(0001)/O surface.

can also be produced, but only through high pressure or NO2 exposure [46, 47, 163]. The CO exposure (also 2×10^{-6} mbar.s) produced a $(\sqrt{3}\text{x}\sqrt{3})R30°$ LEED pattern. The results of the two different methanol exposures (2×10^{-6} mbar.s and $\sim 15 \times 10^{-6}$ mbar.s) produced sub-monolayer and multilayer coverages estimated, on the basis of the O 1s intensity relative to that from the (2x1)-O phase to be ~ 0.5 ML and ~ 1.5 ML (the latter value probably corresponding to at least two molecular layers). The multilayer is assumed to contain mostly intact methanol, even if some dissociation to produce a methoxy species occurs at the molecule/metal interface. The absolute experimental binding energy scale was uncalibrated, and the scale shown in Fig. 6.1 was established using a value for the O 1s binding energy for the chemisorbed O species as 529.8 eV reported by Fuggle et al. [164]. Note that the difference in chemical shift of the O 1s peak between the atomic oxygen and CO adsorbed on the surface seen in Fig. 6.1 is also consistent with the value reported by Fuggle et al. of 1.9 eV. These spectra show clearly that the layers produced by exposure to methanol do not contain either adsorbed CO or atomic oxygen. On the basis of these spectra alone, however, it is unclear as to whether the lower-coverage molecular species is methanol or methoxy. Note that we would expect a submonolayer coverage of methanol to show a lower binding energy that the multilayer, so the shift relative to the multilayer need not imply a change in species.

6.3.2 Photoelectron diffraction

While the XPS data provide a valuable spectral fingerprint of the surface species produced by the interaction of methanol with Ru(0001), clear assignment of the peaks to specific species is not possible, and they contain no structural information. Photoelectron diffraction offers a means to obtain this structural information and, by comparison with the conclusions of previous studies by other methods, to infer the probable associated species. In particular, DFT calculations have predicted that if a surface methoxy species is present this should occupy a three-fold coordinated hollow site on the surface, a geometry expected to lead to strong PhD modulations. By contrast, if the surface species is intact methanol that is clustered, as indicated by the FT-RAIRS results, no such strong modulations are to be expected. Of course, it is always more difficult to rely on a negative result than a positive one: if no strong modulations are observed, is this simple qualitative argument sufficient to resolve the issue convincingly? With this in mind measurements of O 1s PhD spectra from the chemisorbed O overlayer on Ru(0001) is first reported. The structure of this system is well-established and, indeed, the O atoms are also known to occupy three-fold coordinated hollow sites. If the PhD data from this species match our (quantitative) expectations, this may be regarded as strengthening the significance of a negative

result from the methanol-derived molecular species.

Ru(0001)(2x1)-O

As reported above, there are two simple chemisorption phases of oxygen on Ru(0001) that can be obtained by exposure to molecular oxygen under UHV conditions, namely the (2x1) and (2x2) phases, with coverages of atomic oxygen of 0.5 ML and 0.25 ML, respectively. Due to the effects of coexistent rotational domains on the three-fold symmetric surface, both phases lead to a (2x2) diffraction pattern, so while it is generally accepted that a nominal saturation exposure of molecular oxygen should lead to a pure (2x1) surface, it is difficult to be certain, on the basis of the LEED pattern alone, that there may not be some co-occupation of both phases. Fortunately, the PhD technique is sensitive only to the local structural environment of the (O) emitter atoms, and as previous work has shown that the oxygen atoms occupy the same local site in both phases (with only minor differences in substrate relaxation) [46, 47, 162], some coexistence of a true (2x2) phase has no significant impact on the results we report here.

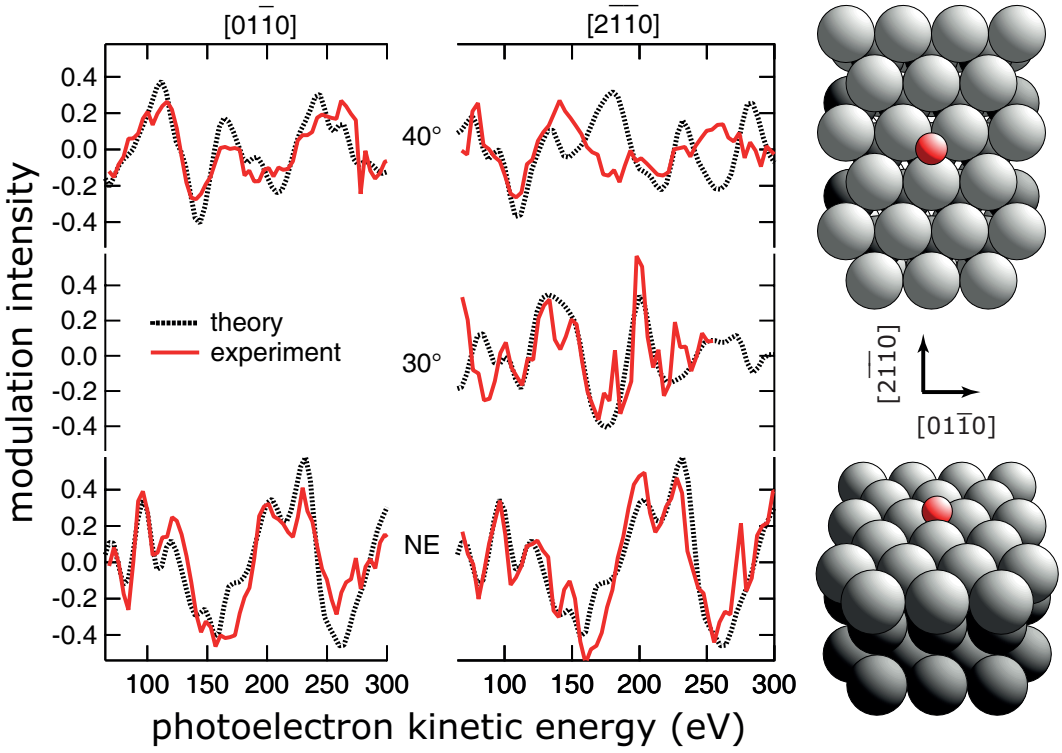

Figure 6.2: O 1s PhD experimental data recorded from the Ru(0001)(2x1)-O surface compared with theoretical simulations for the best-fit geometry as reported in the main text. On the right are shown schematic plan and projection views of this local structure, with O atoms in 'hcp' hollow sites.

Fig. 6.2 shows 5 O 1s experimental PhD modulation spectra recorded from the

Ru(0001)(2x1)-O surface in different emission directions. Also shown in this figure are the results of multiple scattering simulations for an optimised model structure in which the O emitter atoms are located in hcp hollow sites with an O-Ru bondlength of 2.01 ± 0.02 Å. Clearly the level of agreement is good (as reflected in a value for the associated R-factor of 0.25). This bondlength may be compared to values previously reported from the (2x1) and (2x2) phases using the quantitative LEED technique, and for the (2x1) phase using medium energy ion scattering, of 2.02 ± 0.06 Å, 2.03 ± 0.06 Å, and 2.02 ± 0.05 Å, respectively [46, 47, 162]. In our PhD data analysis no Ru relaxations were found to be significant, relative to the bulk termination, to within the limited precision on the method (±0.1 Å); the previous studies had found such relaxations to be within these limits. We conclude, therefore, that the PhD analysis of the structure of the Ru(0001)(2x1)-O structure is fully consistent with previous determinations of this structure by other methods. Moreover, as the methoxy species has been predicted to occupy similar sites on Ru(0001), albeit with somewhat longer bondlengths, we may anticipate that if methoxy does occupy these sites O 1s PhD data from this system should show similarly strong modulations to those seen for atomic oxygen in Fig. 6.2.

Ru(0001)($\sqrt{3} \times \sqrt{3}$)$R30°$-CO

As a further consistency check on the application of PhD to adsorbates on this Ru(0001) surface, the normal emission O 1s PhD modulation spectrum from the adsorbed CO was compared with the results of multiple scattering for the known adsorption site. In particular, previous quantitative LEED studies [48, 165] have shown the molecule to occupy an atop site with a Ru-O interlayer spacing of 3.03 ± 0.06 Å; the optimised PhD fit yields a value of 3.06 ± 0.04 Å. Figure 6.3 shows this comparison of experimental and simulated spectra. The single experimental spectrum is rather noisy, and a single spectrum is certainly inadequate to form the basis of a serious quantitative surface structure determination for this structure, but nevertheless it is clear that the simulation reproduces well all the main features of the experimental spectrum (as reflected by an R-factor value of 0.17).

Ru(0001)/methanol-methoxy

Fig. 6.4 shows O 1s PhD modulation spectra recorded in six different emission directions the peak recorded at a binding energy of $\sim$ 532.6 eV following methanol exposure at $\sim$ 150 K (Fig. 6.1). The spectra appear to be dominated by noise with little evidence of any meaningful modulations. However, to provide a more quantitative assessment of these data, also included in Fig. 6.4 are the results of multiple scattering calculations for the adsorption geometry expected for an adsorbed methoxy

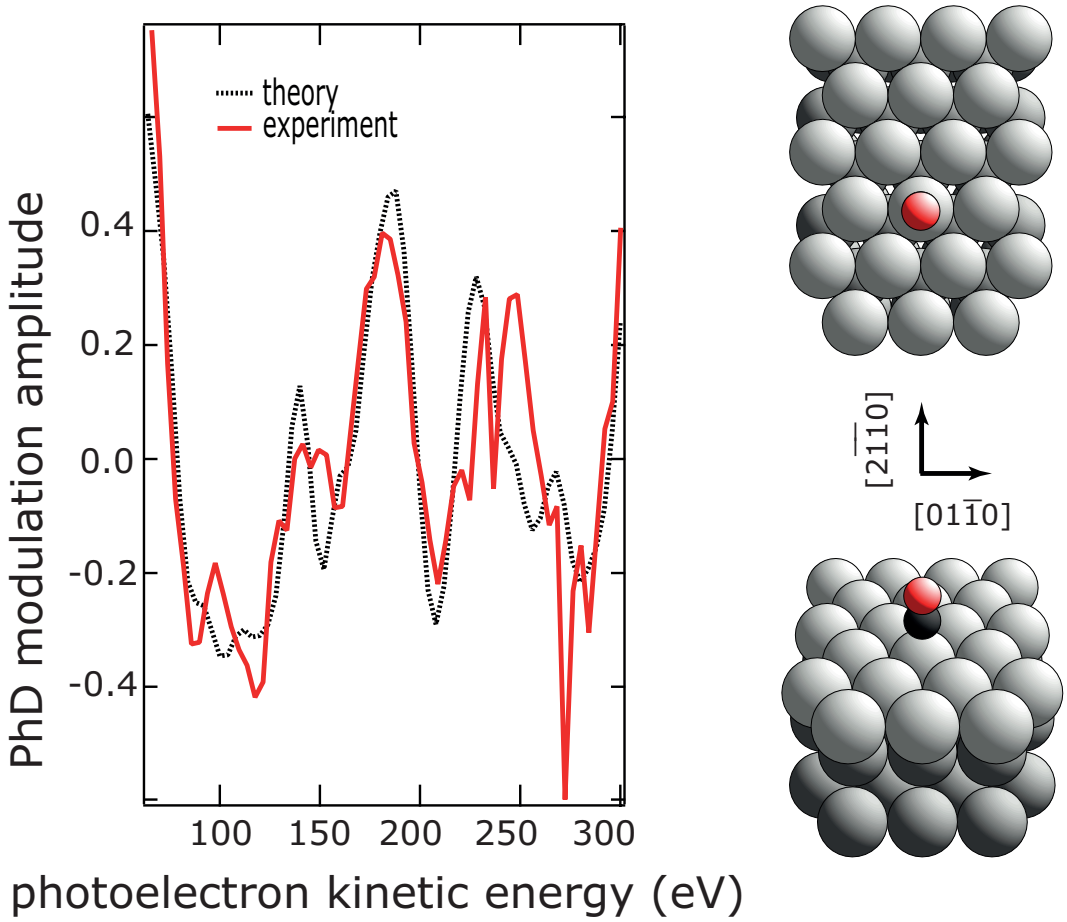

Figure 6.3: O 1s PhD experimental normal emission modulation spectrum recorded from the Ru(0001)-CO surface compared with theoretical simulations for the best-fit geometry as reported in the main text. On the right are shown schematic plan and projection views of this local structure, with CO molecules in atop sites.

species on the basis the published results of DFT calculations [161]. The DFT results concluded that the methoxy species should occupy three-fold coordinated hollow sites at a Ru-O bondlength of 2.21 Å, but the adsorption energy at the two inequivalent (hcp and fcc) hollow sites was found to be essentially the same. The PhD simulations presented in Fig. 6.4 are therefore based on the assumption that these two sites are co-occupied with equal probability. In view of the rather long Ru-O bondlength associated with this proposed structure, and the fact that molecular chemisorption bondlengths obtained in DFT often differ from experimental values by up to 0.1 Å or more, Fig. 6.4 also shows the results of the PhD simulations at both larger and smaller values of the Ru-O interlayer spacing in increments of 0.1 Å. Clear trends in the energetic location of the main modulation peaks allow one to establish that none of the experimental spectra show modulations with either the correct period or amplitude to match any simulated spectra. This shows that any modulations in the experimental spectra are dominated by noise, and have an amplitude that is much too small to be attributable to emitters in well-defined hollow sites. Simulations for occupation of only the hcp or fcc hollow sites lead to the same conclusions; near normal emission, in particular, the spectra are rather weakly dependent on which hollow site is occupied, but the single-site modulations do have a slightly larger amplitude due to the small differences that do exist in the spectra from the two sites.

6.4 General discussion and conclusions

The recent evidence presented by Gazdzicki, Uvdal and Jakob [159] that methanol does not deprotonate to form a surface methoxy species on Ru(0001) at low temperatures challenged conventional wisdom regarding this system, but the results presented here appear to provide significant further support for this conclusion. Based only on the O 1s photoelectron binding energies measured in XPS, it is not possible to reliably identify, with any confidence, whether the submonolayer adsorbate formed at 150 K is methanol or a methoxy species. However, PhD measurements from this species fail to show the clear modulations that would be expected from a methoxy species, chemisorbed through the O atoms to a high-symmetry site on the surface, and specifically does not show those to be expected for hollow-site adsorption as predicted from DFT calculations. By contrast, atomic oxygen on this surface does show the expected PhD modulations, and indeed a quantitative analysis of the experimental PhD spectra from this species yields a structure essentially identical to that previous identified by LEED and ion scattering. Indeed, O 1s PhD data from adosprbed CO on this surface are also consistent with the known atop geometry of this species.

In PhD very weak modulations occur when the emitter atoms occupy multiple (often low-symmetry) sites, a situation which occurs if adsorbate-adsorbate interac-

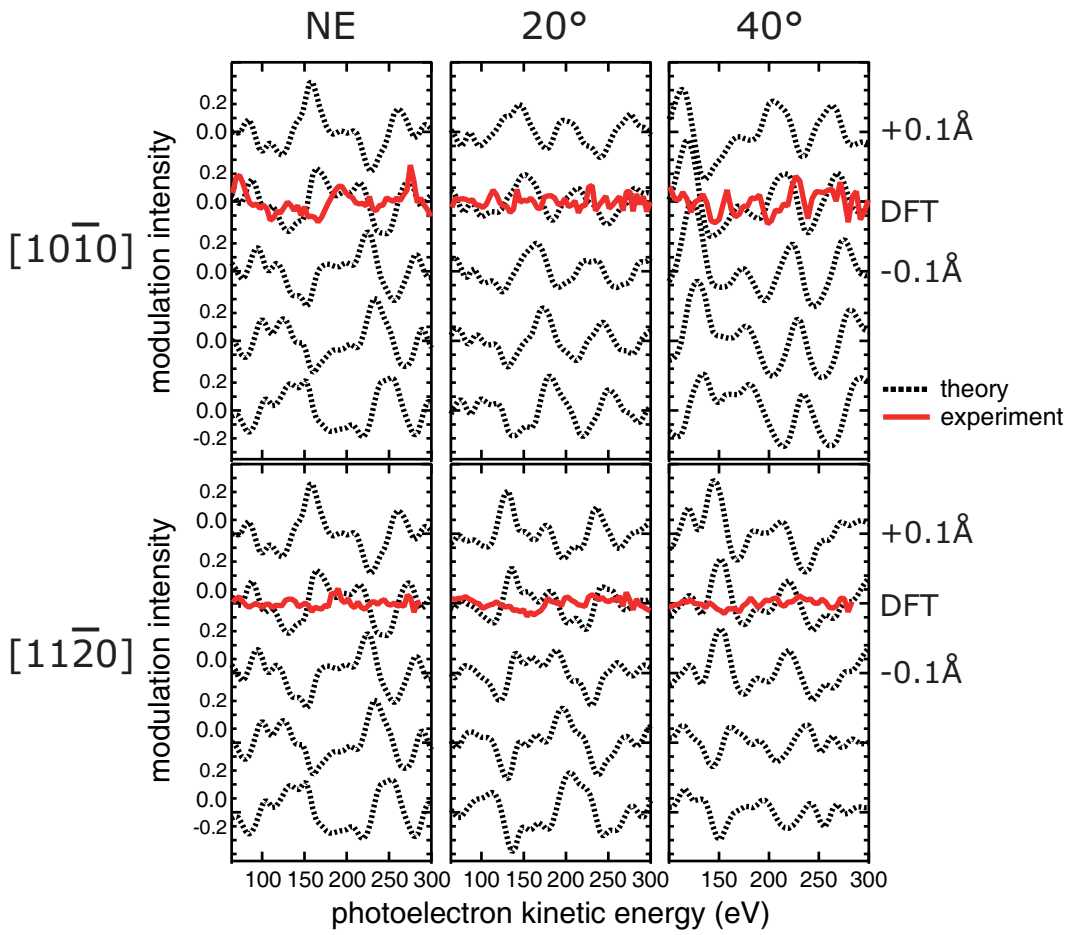

Figure 6.4: O 1s PhD data for a sub-monolayer exposure of methanol on Ru(0001) at $\sim$ 150 K, compared with theoretical simulations for mixed hcp / fcc site occupation of a methoxy species at the O-Ru layer spacing determined by the previous DFT calculations [161], and some variations of this layer spacing.

tions are much stronger than the corrugation of the adsorbate-substrate potential. Molecular clustering is just such a situation, so the absence of significant PhD modulations from the low-temperature molecular adsorbate species is not only inconsistent with the behaviour expected for methoxy, but is qualitatively consistent with that expected for the methanol clustering found by Gazdzicki, Uvdal and Jakob.

Chapter 7

Water decomposition on TiO_2(110)

7.1 Introduction

The (110) surface of the rutile phase of TiO_2 is the most-studied of all oxide surfaces [3, 166, 167], not least because of the technological importance of titania as a heterogeneous catalyst, and particularly the discovery some 30 years ago of the photochemical production of hydrogen from water over titania [168]. However, despite the importance of this TiO_2/H_2O interaction, aspects of the interaction of water with TiO_2(110) have remained controversial. In particular, many theoretical studies, mainly based on DFT, predict that dissociation of H_2O on a perfectly-ordered stoichiometric surface should be facile, at least at some coverages, while experiments have generally found this not to be the case. Debate over the appropriate computational methods to tackle this problem correctly have continued even relatively recently [169–172]. By contrast, it is widely agreed that water dissociation does occur at the surface oxygen vacancy sites of a defected surface; bridging oxygen atom vacancies are replaced by an OH species with the remaining H atoms from the water bonding to adjacent bridging oxygen atoms, leading a healing of the vacancy and the creation of two bridging hydroxyl (OH_br) species (Fig. 7.1). This process has been predicted in a number of DFT studies and has been observed rather directly by STM [173, 174]. On the undefected surface, the same STM experiments show that molecular water is located atop the undercoordinated surface Ti atoms, while PhD studies shows the associated Ti-O bondlength to be 2.21 Å[40, 175]. Recent DFT calculations have stressed that on the perfect TiO_2(110) surface, the predicted dissociated state may only be pseudo-dissociated in that the resulting surface species, a hydroxyl species atop a surface Ti atom (OH_t) and an adjacent hydroxylated bridging O atom producing an OH_{br} (Fig. 7.1), may be unable to separate on the surface, and indeed that the detached H atom from the (atop) molecular water may switch rapidly between the OH_t species and the two adjacent bridging O atoms on either side, making it difficult

or impossible to identify this process in STM.

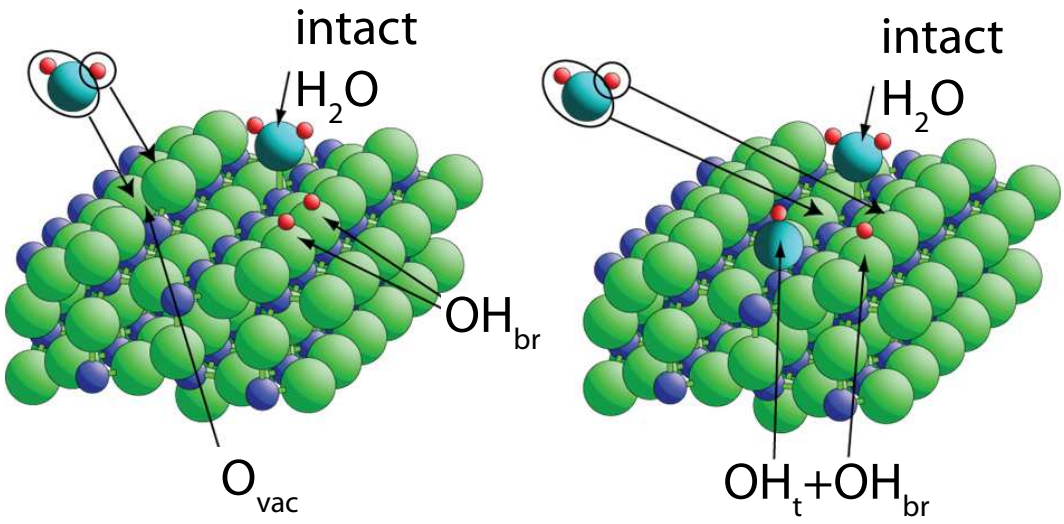

Figure 7.1: Schematic diagram of the interaction of molecular H_2O with TiO_2(110) on (lefT) a surface containing bridging oxygen vacancies, O_{vac}, to produce two bridging hydroxyl species, OH_{br} and (right) on a perfect surface to produce atop and bridging hydroxyl species, OH_t and OH_{br}. At low temperatures coadsorbed intact molecular water also occupies Ti-atop sites.

Here we show that using the PhD technique we can not only demonstrate the presence of these coadsorbed OH_{br} and OH_t species as a result of water dissociation, but can also determine the local Ti-O bondlengths of these two species. We find these values to be in excellent agreement with the published DFT results. As such, we provide the missing link to finally reconcile experiment and theory in the TiO_2/water dissociation problem.

A key result that underpins this study comes from the work of Walle et al. [176], who investigated the temperature dependence of O 1s XPS data from the TiO_2(110)/water surface. It is well-established that at low temperatures ($<\sim$ 250 K) this spectrum comprises three components, a main peak from the oxide substrate, a second component shifted by $\sim$ 1.3 eV to higher binding energy associated with surface OH species, and a third peak at a larger chemical shift ($\sim$ 3.5 eV) associated with molecular water. What Walle et al. were able to show is that the OH component corresponds not only to a state that is stable above room temperature, and has previously been assigned to the OH_{br} species associated with dissociation at defect sites, but also to a second state that desorbs below room temperature and which has a substantial coverage even on an almost perfect starting surface. This implies that there is water dissociation on the perfect surface but that recombination of the dissociated components leads to desorption at room temperature. The implication is that the additional OH detected at low temperature is the combined OH_{br} + OH_t pseudo-dissociated state predicted by theory. The experimental data on which

this analysis is based were obtained by Allegretti et al. [40, 175] in their structure determination of the adsorbed intact water species, and details of the methods used are reported in these earlier publications.

7.2 Results

The structure yielding the lowest R-factor value (0.31) for a set of spectra recorded in five different directions (Fig. 7.2) was found to correspond to a OH_t:OH_{br} co-ocupation ratio of 30:70. The OH_t species has a Ti-O bondlength of 1.85±0.08 Å, while for the OH_{br} species this bondlength is 1.94±0.07 Å. This latter value is in excellent agreement with the value of 1.97±0.05 Å found using the same PhD technique to study a surface hydroxylated by exposure to atomic hydrogen and thus containing only OH_{br} species by Unterberger et al [177]. These bond lengths are fully consistent with strong chemisorption and are much shorter than the value associated with molecular water in the Ti-atop site on this surface (2.21±0.02 Å) [40, 175]. Rather few of the many published DFT calculations on this system quote values for the calculated bondlengths; for example, one recent study gives perfect agreement with experiment for the Ti-O_{water} bondlength [178] but provides no details of the dissociated state. Menetrey et al. [179] find a slightly longer value for Ti-O_{water} of 2.28 Å, but also report the Ti-OH_t bondlength to be 1.85 Å. These authors do not quote the Ti-OH_{br} bondlength on the perfect surface, but on the initially-defected surface they give a value of 2.09 Å; this is quite similar to the value of 2.04 Å obtained recently in similar calculations for 0.5 ML of OH_{br} on the surface [177]. Only two earlier studies report values for the Ti-OH_t and Ti-OH_{br} bond lengths coexisting in the dissociated state on the perfect surface; these are 1.87 Å and 2.06 Å[179], and 1.63 Å and 1.87 Å[180], respectively. While the latter pair of values include at least one that seems unreasonably short, the former are fully consistent with the other more fragmentary results and are clearly consistent with our experimental finding that the Ti-OH_t distance is significantly shorter than that of the Ti-OH_{br} bond, with particularly good quantitative agreement for the Ti-O_t bond length.

A further key parameter in our experimental results is the fractional coverage of OH_t species. For water adsorption on a perfect TiO_2(110) surface, we expect an equal number of OH_t and OH_{br} species, but it is now well-established that even well-prepared surfaces contain a significant number (typically $\leq\sim$ 10%) of O_{vac} defects, each of which will lead to two OH_{br} species following exposure to water.

A 30% occupation of OH_t species, as found in our experiments, implies that a further 30% of the OH species are OH_{br} arising from dissociation at perfect areas of the surface, with the remaining 40% coming from defect-site dissociation. This implies that the initial concentration of O_{vac} defects corresponds to 20% of the surface that

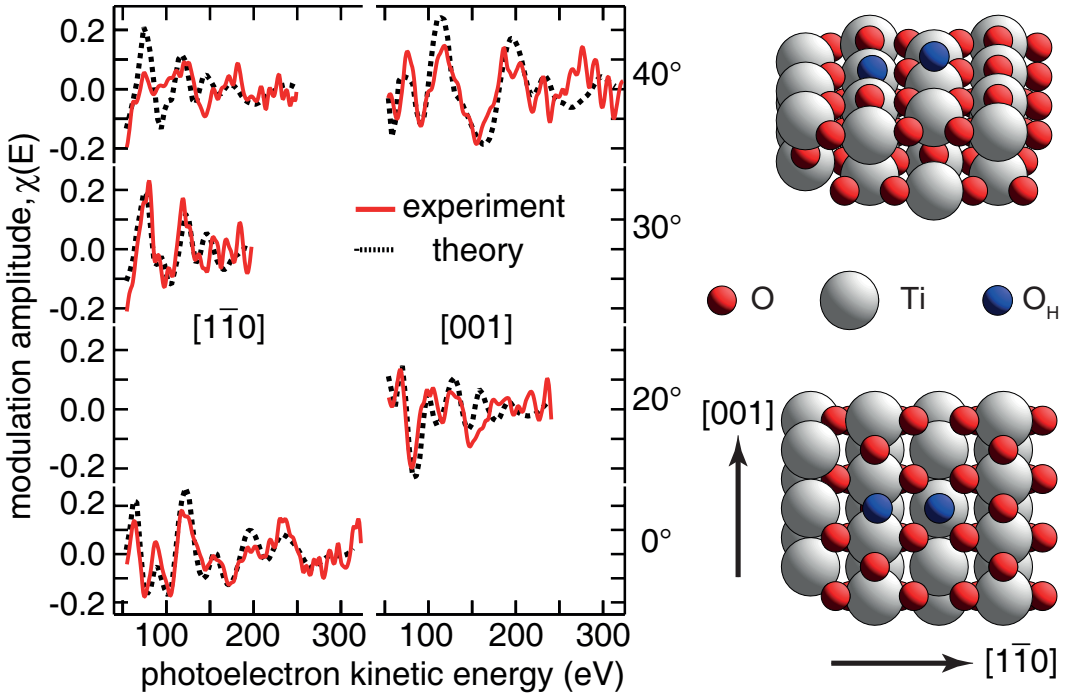

Figure 7.2: Comparison of the experimental O 1s (OH) PhD spectra with theoretical simulations for the best fit structure discussed in the text.

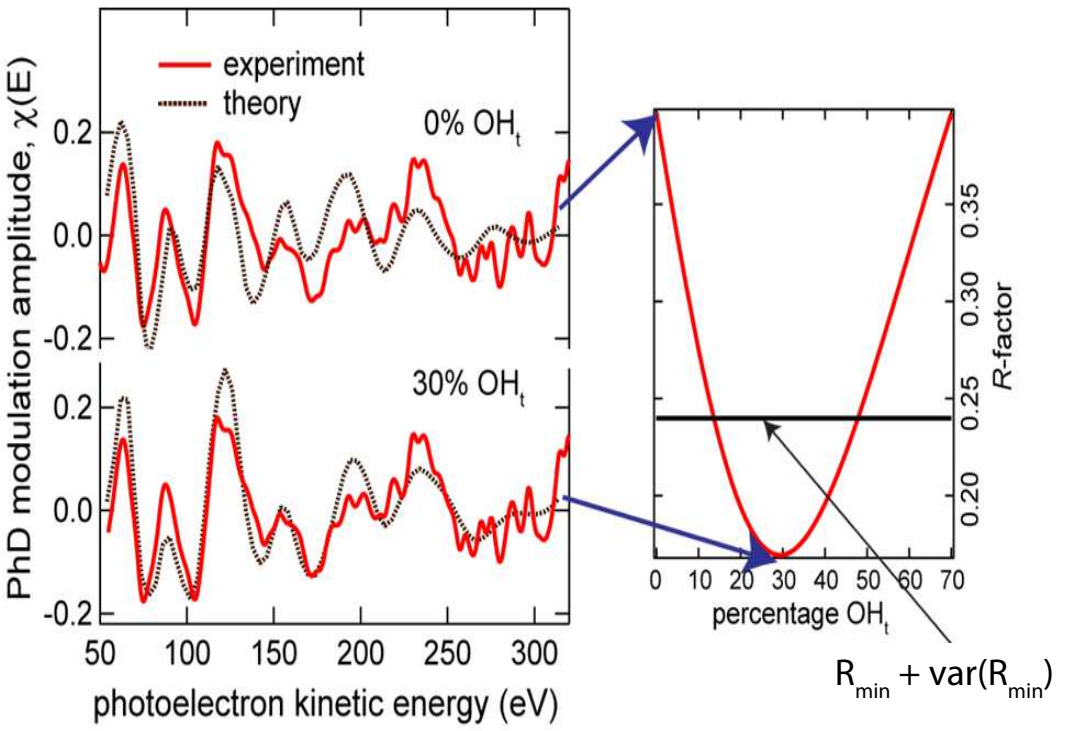

Figure 7.3: Dependence of the level of agreement between experiment and theory for the normal emission PhD spectrum as a function of the fractional occupation of OH_t species. On the left are shown theory/experiment comparisons for 0% and 30% OH_t occupation, on the right is shown the dependence of the R-factor on this parameter.

is covered by OH. We note, however, that these OH species are coadsorbed with molecular water with a coverage previously estimated to be in the range 0.5-1.0 ML [40]. Analysis of the different components of the O 1s spectra indicates that the OH coverage is $\sim 50-80\%$ that of H_2O, so if we take the *total* coverage of both species to be 1ML (almost certainly an upper limit), the OH coverage is ∼0.33-0.44 ML, so the O_{vac} concentration on the whole surface is $\sim$ 7-9%; this upper limit is entirely consistent with the expected value. Using the full set of PhD spectra shown in Fig. 7.2 we obtain a precision for the fractional occupation of OH_t sites of ±30%, but this poor precision results from the use of several PhD spectra in directions that are very insensitive to the presence of the atop species. The modulations in the off-normal emission spectra, particularly in the [001] azimuth will be dominated by the backscattering from the (majority) bridging species. By contrast, the normal emission spectrum is expected to have modulations that are far more strongly influenced by scattering from the atop species. This is confirmed by our calculations which show that, despite the much-reduced data set, the use of this one spectrum alone yields a factional occupation value for the OH_t species of 30(-15/+18)%, clearly excluding the possibility that only OH_{br} species are present. This is illustrated in Fig. 7.3 which shows comparisons of the experimental PhD spectrum at normal emission with simulations for 0% and 30% OH_t species, together with a plot of the variation of the associated *R*-factor as a function of the fractional occupation value (the horizontal line corresponding to $R = R_{min} + var(R_{min})$).

7.3 General discussion and conclusions

Utilising the chemical-state specificity of the PhD technique has allowed us to demonstrate that at temperatures of ∼190-200 K water adsorption on TiO_2(110) leads to the formation of both OH_t and OH_{br} species, whereas it is known that only OH_{br} species are formed by reaction of water with O_{vac} defects on the surface. This qualitative result is fully consistent with predictions of many theoretical calculations that show water can dissociate on a perfect surface to produce dissociation to form an OH_t + OH_{br} pair of species that may be unable to move apart. Moreover, the Ti-OH bond lengths found for these two species, 1.85±0.08 Å (OH_t), and 1.94±0.07 Å (OH_{br}) are also consistent with theoretical calculations, the qualitative difference being reconciled with their one-fold and two-fold coordination to surface Ti atoms. This finally resolves a long-standing controversy concerning the consistency of experimental and theoretical studies of the dissociation of water on TiO_2(110).

Chapter 8

Vanadyl Phtalocyanine on Au(111)

sectionIntroduction The metallophthalocyanines, MPc, have attracted considerable interest in recent years, as an important class of organic semiconductors with a range of valuable electronic and optical properties and resultant potential applications [181, 182]. For example, vanadyl phthalocyanine (VOPc), investigated here, possesses a large third-order nonlinear optical susceptibility, ultra-fast optical response, and good stability against visible light irradiation.(e.g. [183–186]). Most associated structural investigations are concerned with the properties of deposited thin films of these materials (e.g. [187, 188]), but there have also been a number of investigations of the earliest stages of such growth and the properties of the first molecular layer and its interaction with the substrate. Typically, MPcs are near-planar molecules that appear to lie flat on the surface at the substrate interface, although there are very few detailed structural studies of these adsorbed layers. Most MPcs contain a single metal atom at the centre of the molecule, but in VOPc the V-O axis lies perpendicular to the plane of the molecule, leading the vanadyl oxygen atom to stick out of the overall molecular plane. A model of the structure of this molecule, as determined in its crystalline form [189], is shown in Fig. 8.1; note that while the O atom lies 1.58Å above the V atom in this structure, the V atoms also lies some 0.56Å above the nearest neighbour N atoms, and even higher relative to the C atoms that are not strictly planar in configuration.

A STM study of VOPc deposited onto Au(111) yielded images that show ordering and symmetry consistent with an overall flat-lying orientation of the molecular plane (see Fig 8.2), but raised the interesting question of whether the V=O bond is directed into or out of the surface [190]. Based on considerations of the electronic structure of the adsorbed molecule and its impact on the appearance of the STM images, it was concluded that the V=O points out of the surface, as might have been anticipated to be more physically reasonable. However, a simple structural study, such as that presented here, offers a far more direct route to establishing this molec-

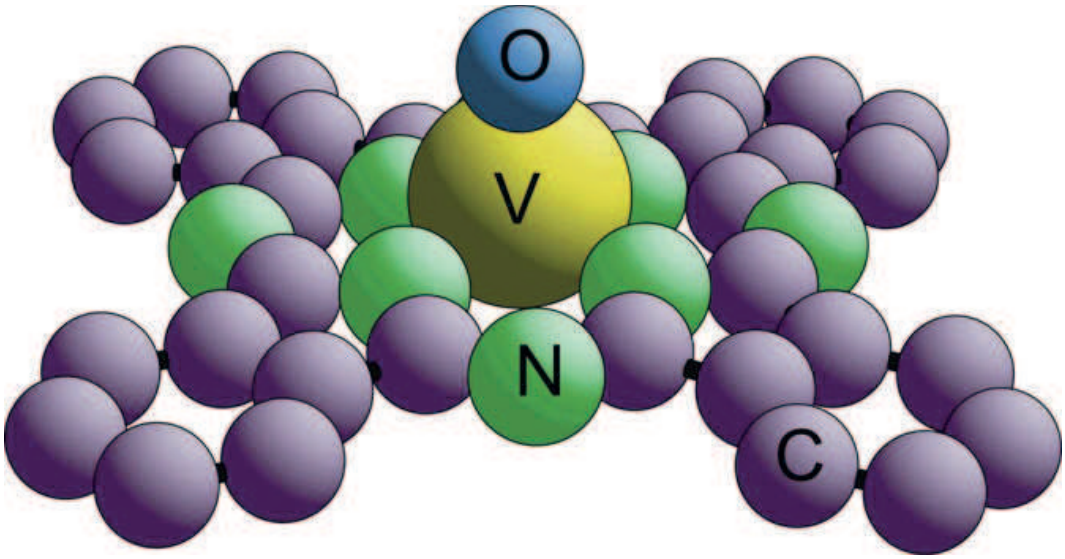

Figure 8.1: Model of the VOPc molecule.

ular orientation. We may also note that a structural study of SnPc on Ag(111) [191] by normal incidence X-ray standing waves (NIXSW) [192] concludes that under most conditions the Sn atom, which is significantly out of the plane defined by the surrounding atoms, does lie closer to the surface; i.e. in this system the central atom points down to the substrate. The question of the molecular orientation is therefore not necessarily trivial, although the situations of a central metal atom and a central V=O species are clearly different. Our study allows us to clearly establish that the V=O bond of VOPc does, indeed, point outwards from the surface in a monolayer film on Au(111), but also provides some quantitative information on the internal structure of the adsorbed molecule.

While the structure of VOPc on Au(111) is of intrinsic interest, our study was also motivated by a rather different issue related to the chemical properties of surface vanadyl species at vanadium oxide surfaces. Our particular interest has been in the (0001) face of vanadium sesquioxide, V_2O_3, with a bulk structure comprising alternate buckled V_2 layers and planar O_3 layers, $-O_3VVO_3VV$- etc. It is generally believed that when this surface is prepared in a low partial pressure of oxygen in an ultra-high vacuum system, it has a half-metal termination but with additional oxygen atoms bonded atop these surface metal atoms to form local vanadyl species (i.e. to produce a termination, $-O_3VVO_3V = O$). Moreover, it has generally been assumed that hydroxylation of this surface would lead to H attachment to these vanadyl O atoms (i.e. - $-O_3VVO_3V-OH$) which would retain their V-atop sites. Our structural study of these surfaces using the PhD technique, however, failed to provide clear support for these ideas and, in particular, seems to show rather clearly that the hydroxyl O atoms are not in these atop sites [193, 194]; specifically, the rather clear 'spectral signature' that we would expect to see in PhD from a hydroxyated vanadyl species

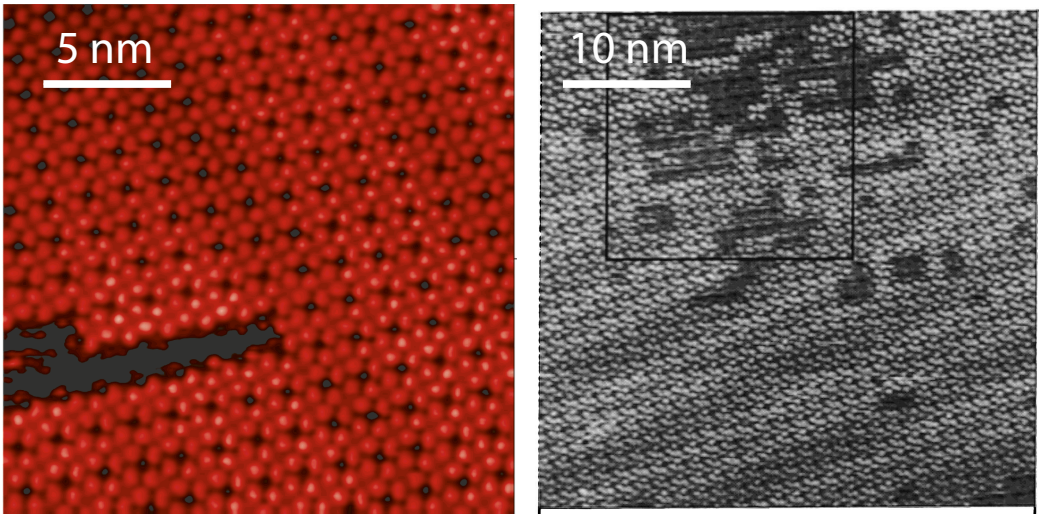

Figure 8.2: STM image of VOPc on Au(111). (right) The herringbone reconstruction of the Au(111) surface can still be seen under the VOPc overlayer, implying a weak interaction between the Au surface and the adsorbate. Reproduced from the work of Barlow and Hipps [190].

was not observed.

The O 1s PhD data does show the expected modulation behaviour described above, providing a clear measurement of the V=O bondlength within the adsorbed molecule as well as identifying the molecular orientation. A more complete analysis of both O 1s and V 2p PhD measurements in normal emission, however, also yields some information on the adsorption-induced modification of the molecular conformation.

8.1 Experimental Details

The Au(111) crystal was cleaned in situ by several cycles of 500 eV Ar ion bombardment followed by brief annealing to $\sim 600°C$; typically the LEED showed a nominal (1x1) pattern, but with the weak splitting of the integral order beams characteristic of the herring-bone reconstruction of the clean surface. XPS showed no evidence of surface contamination. The VOPc, obtained from Alfa Aesar, was evaporated from an indirectly-heated horizontal glass tube with line-of sight of the sample. The source temperature during deposition, as measured by a thermocouple in contact with the outside of this tube, was $575-625$ K, while the sample temperature during deposition was generally ~ 425 K. An estimate of the coverage was obtained by comparing the intensity of the N 1 s and C 1s signals with that of the Au 4d emission at a photon energy of 900 eV, using the relative photoionisation cross-sections calculated by Yeh and Lindau [195] and the attenuation length of the Au 4d photoelectrons given by the NIST database [196]. This led to an estimated coverage of 0.015 ML. For comparison, we note that the published STM images of the ordered layer of VOPc formed on

Au(111) (Fig. 8.2, [190]) indicate that the area occupied by each VOPc molecule is approximately 200 Å^2, implying a molecular coverage for this single complete molecular layer of ~ 0.035 ML. Our coverage is thus $\sim 50\%$ of the saturation coverage of this first molecular layer.

Three separate sets of scanned-energy photoelectron diffraction data were recorded at normal emission from the O 1s signal from different surface preparations, by recording a sequence of photoelectron EDCs around this photoemission peak at equal steps in photon energy in the photoelectron kinetic energy range of $\sim 60-300$ eV at normal emission. In addition, two such sets of V 2p emission PhD data were collected in a similar manner in the kinetic energy range from $\sim 60-250$ eV.

8.2 Results and data modelling

Figure 8.3 shows the normal emission O 1s and V 2p PhD modulation spectra, clearly the main modulation features are reproducible despite the relatively high noise level to be expected in view of the very low adsorbate coverage; with only one V and one O atom per adsorbed molecule, the coverage of these emitter atoms is at least an order of magnitude less than that associated with most PhD structural studies of small molecules at saturation coverage on surfaces [11, 12]. In view of the consistency of the repeated measurements, the structural analysis that follows was conducted using averages of these multiple measurements (also shown in fig. 8.3) in order to achieve some reduction of the noise. The O 1s PhD spectra show a single dominant modulation that appears to be approximately periodic in photoelectron wavevector (proportional to the square root of the energy); this would be consistent with there being a single dominant backscattering pathway. The V 2p PhD spectra, on the other hand, seem to show only a single significant valley and peak at low energy. This behaviour is qualitatively in agreement with our expectation that the molecule lies flat on the surface with the V=O bond pointing outwards along the surface normal; we may then expect 180° backscattering from the V atom to dominate the PhD modulations for the O 1s spectra at normal emission, while the V 2p PhD spectrum should show no similar periodic modulations due to backscattering.

As the molecule is expected to be a significant distance from and incommensurate to the metal surface [190], only intermolecular scattering was considered.

As remarked above, the O 1s PhD spectrum appears, on inspection, to be consistent with an adsorption geometry in which the V=O bonds points outwards from the surface, and in this case it is this modulation spectrum that is expected to provide the most information on the internal conformation of the adsorbed VOPc molecule as the O 1s emitter atom is ideally located for backscattering from the V atoms and its near-neighbour N and C atoms. However, if the orientation of the adsorbed molecule

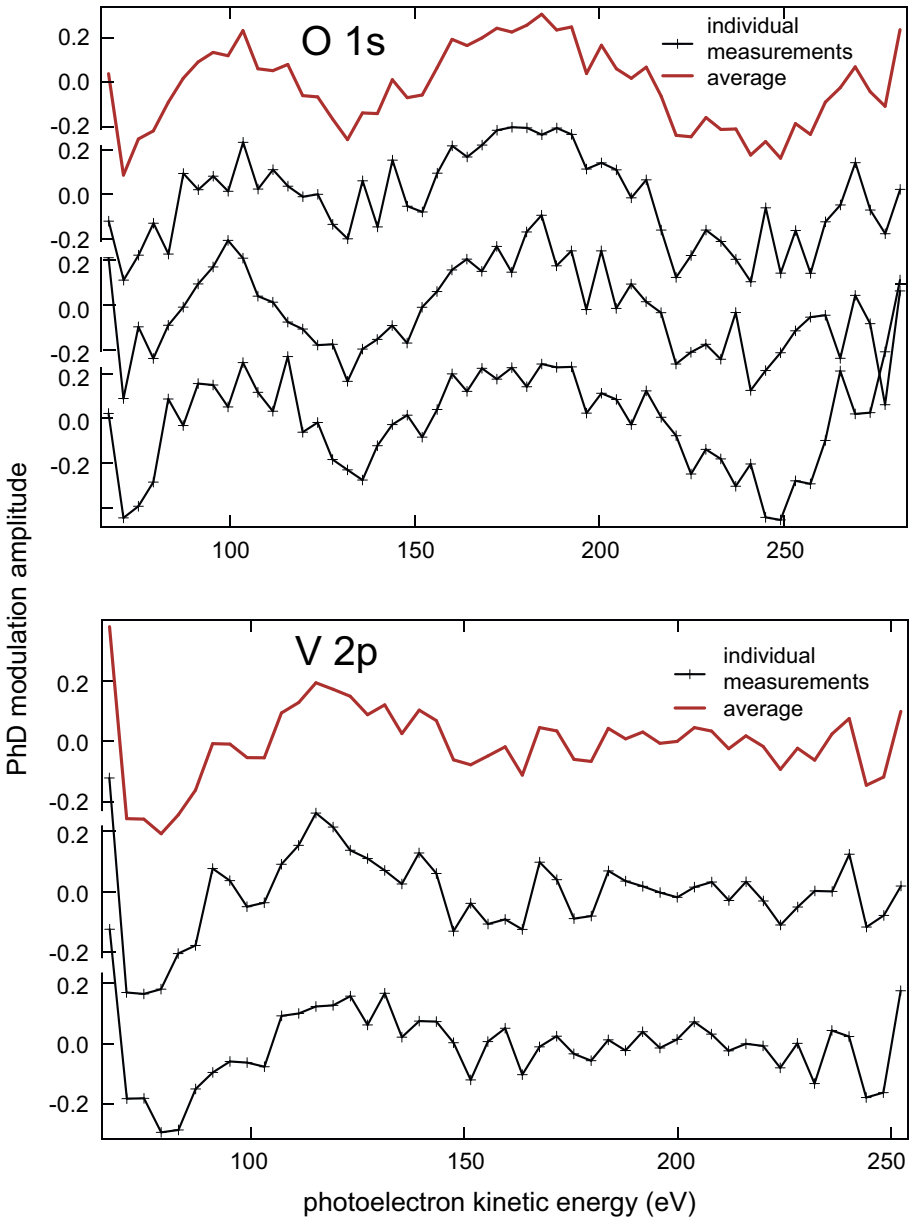

Figure 8.3: Comparison of the three separate experimental measurements of the O 1s PhD spectra and two separate measurements of the V 2p PhD spectra from VOPc on Au(1 1 1) at normal emission. Also shown are the average spectra, used in the structure determination, that are obtained from these individual measurements.

is inverted, with the V=O bond pointing down towards the substrate, it is the V 2p PhD spectrum that may be expected to provide more structural information, at least of the V=O bondlength, through 180° backscattering from the O atom. A consistent procedure was adopted in which we have optimised the fits to both of these spectra simultaneously for both of the possible molecular orientations.

Fig. 8.4 shows the results of a calculation for the best-fit structure (as determined by the combined R-factor for both the O 1s and V 2p PhD spectra) in which scattering from all the N and C atoms, as well as the V and O atoms, have been included. In view of the small data set, the large number of (weakly-scattering) N and C atoms, and indeed the neglect of Au scattering effects, it is clearly unrealistic to expect to obtain meaningful and precise optimised positions of all the scattering atoms in an unconstrained fashion. In order to achieve this optimised fit to the experimental data we have therefore first conducted a series of calculations on unconstrained models including scattering from only sub-sets of the N and C atoms within the molecule in order to explore the importance of their different scattering contributions. These calculations showed that the most important scattering contributions (beyond those from the V and O atoms) arise from the ring of four N atoms that are closest to the V atom, while a significant influence is also seen from the eight C atoms that are closest to the V atom. This is not particularly surprising; this relative ordering of importance corresponds to the most important contributions arising from the shortest scattering paths from the two emitter atoms and, for the O emitter, from the atoms closest to the favoured 180° backscattering geometry. The fact that the innermost N atoms, in particular, but also the next shell of C atoms, do have a significant influence on the PhD spectra, means that their location relative to the O and V emitter atoms can be optimised to achieve the lowest R-factor. Nevertheless, the variation of the R-factor with the structural parameters determining the position of these atoms shows multiple minima, so to locate the physically meaningful solutions constraints were applied to the local interatomic bondlengths. Specifically, the V-N and N-C nearest-neighbour distances were initially constrained to lie within 0.1Å of their values in crystalline VOPc [189]) while the C-C bonds were fixed to within ~ 0.03Å of these crystalline values. In addition the outer phenyl rings were assumed to have only a minimum tilt relative to the molecular plane, consistent with the optimised positions of the inner N and C atoms found with the smaller clusters.

The length of the V=O bond in this calculation is 1.60 ± 0.04 Å, which is in good agreement with the value in crystalline VOPc (1.580 ± 0.003 Å)[189]. Fig. 8.5 shows a side view of the VOPc molecule, comparing its conformation in its bulk crystalline solid with that determined here when adsorbed on Au(111). Adsorption appears to make the molecule significantly more nearly planar; the near-neighbour N and C atoms have almost the same height above the surface and are significantly more

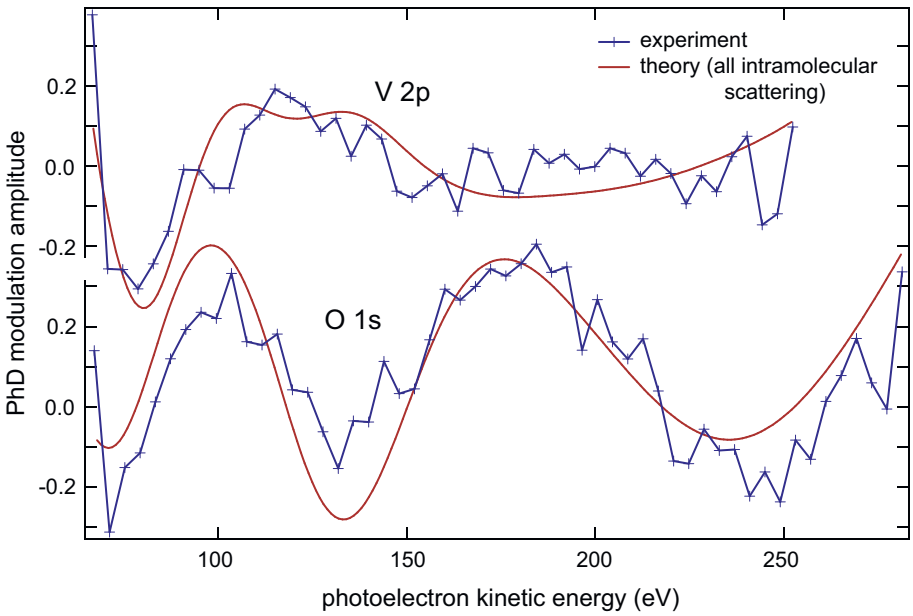

Figure 8.4: Comparison of the averaged experimental O 1s PhD and V 2p spectra from VOPc on Au(1 1 1) (Fig. 8.3) with the results of multiple-scattering simulations of a structurally-optimised model (with the V=O bond pointing out from the surface) including scattering from all atoms within the molecule. The overall R-factor is 0.29.

coplanar with respect to the V atom. The location of the C atoms in the outer phenyl rings cannot be determined with any meaningful precision from the PhD simulations, but the planarity of the inner atoms suggests this must also be the case for these outer atoms if reasonable constraints are applied to all the relevant bondlengths.

The distance of the O atom to the inner shell of four nearest-neighbour N atoms, $O-N_{nn}$ is found to be $2.50(+0.14/-0.07)$ Å, to be compared with a value of 2.90 Å in crystalline VOPc. Similarly, the distance from the O atom to the inner shell nearest-neighbour C atoms, $O-C_{nn}$ is $3.49(+0.24/-0.12)$ Å, compared with 3.72 Å in crystalline VOPc. These comparisons do indicate that the enhanced molecular planarity reflected in the best-fit structure, relative to that in crystalline VOPc, as shown in Fig. 8.5, is, indeed significant. Indeed, calculations of the values and precision of the $V-N_{nn}$ and $V-C_{nn}$ distances projected along the V-O direction are -0.05(+0.14/-0.10) Å and -0.25(+0.28/-0.14) Å. The negative values indicate the N and C atoms are below the V atom and closer to the substrate, and may be compared with values of -0.57 Åand -0.65 Å, respectively, in the crystalline solid. The key difference induced by the adsorption appears to be that the vanadyl species is pulled down into the molecular plane defined by the nearest-neighbour N atoms by $0.52(+0.14/-0.10)$ Å, such that it is only the O atom that is very significantly out of the approximately planar location of the remaining atoms. Notice that the change in the interlayer spacing of the nearest neighbour N and C atoms given by these figures [0.12(+0.31/-0.17) Å] is clearly not formally significant.

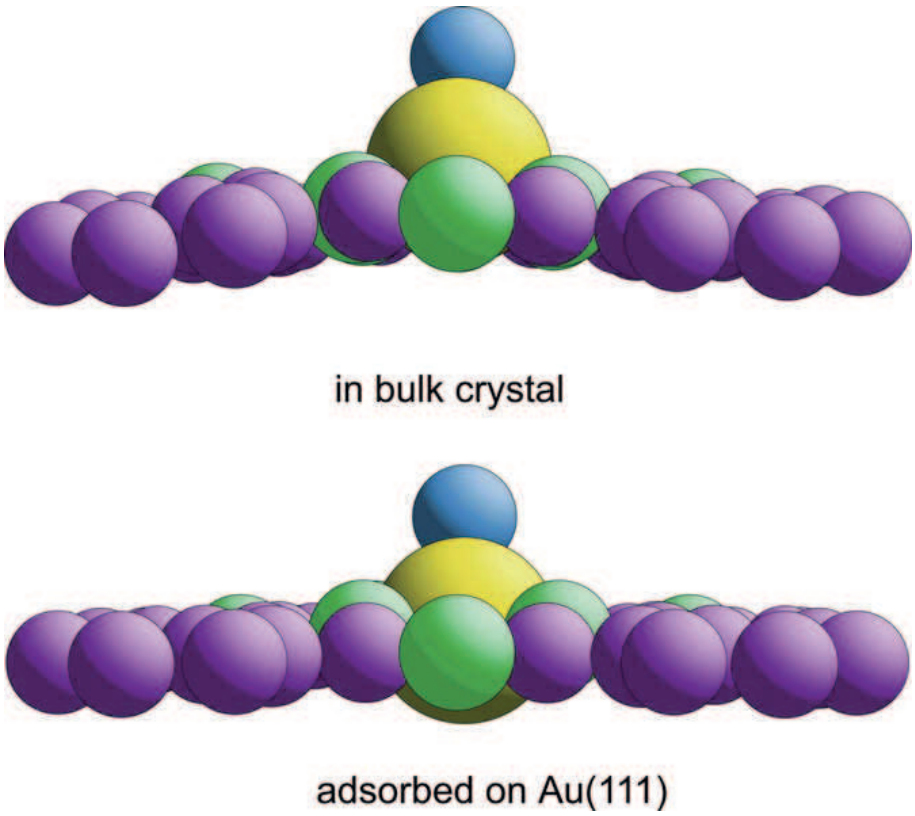

Figure 8.5: Side view of the VOPc molecule in the bulk crystalline solid [189] and as found in this study for the molecule adsorbed on Au(111).

This analysis assumes that the molecule is oriented with the V=O bond pointing outwards from the surface. Could it be that the molecule inverted, with the V=O pointing inwards towards the Au bulk? To investigate this possibility we have investigated a similar structural optimisation of such a model through comparisons of the results of the multiple scattering simulations with the experimental PhD spectra. The structural search failed to identify any structural model with the molecule in this orientation that gave a reasonable fit to both the V 2p and O 1s PhD spectra; the lowest R-factor found for such structures was 0.79. A moderate fit to the V 2p spectrum was possible, but this gave a very poor description of the O 1s spectrum. The only structure identified that provided a reasonable fit to the O 1s spectrum was found to be entirely unphysical, with the V and adjacent N atoms almost coincident in space. To illustrate the problem we show in Fig. 8.6 the results of a calculation for a model in which the best-fit structure of Fig. 8.4 was simply inverted. Clearly the simulated O 1s spectrum is quite unlike that of the experiment, as reflected in an overall R-factor of 0.86. We conclude, therefore, that the PhD data clearly excludes this possible orientation of the adsorbed molecule.

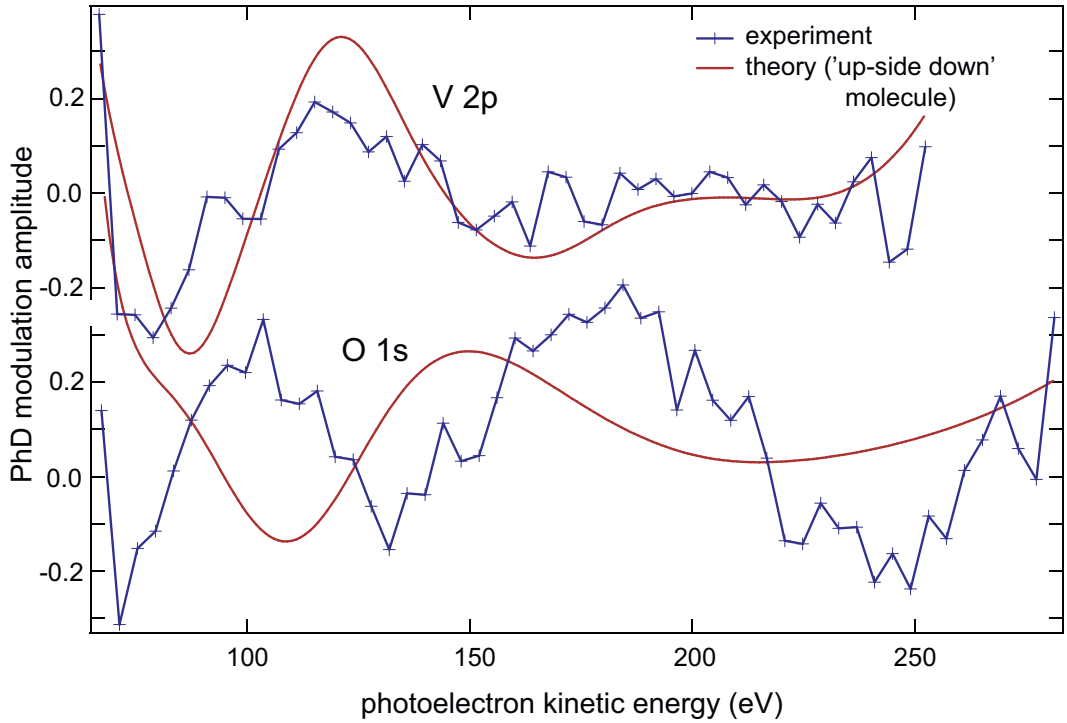

Figure 8.6: Comparison of the averaged experimental O 1s PhD and V 2p spectra from VOPc on Au(1 1 1) (Fig. 8.3) with the results of multiple-scattering simulations for a structural model in which the molecule is inverted such that the V=O bond points towards the Au(111) substrate. The overall R-factor is 0.86.

8.3 General discussion and conclusions

Scanned-energy mode photoelectron diffraction using the O 1s and V 2p emission perpendicular to the surface has been used to investigate the orientation and internal conformation of vanadyl phthalocyanine (VOPc) adsorbed on Au(111). The O 1s PhD spectrum shows a reasonably strong long-period modulation characteristic of backscattering from the V atoms directly below, as to be expected if the V=O vanadyl bond points out of the surface, along the surface normal. The observation of this clear (predicted) modulation function reinforces the conclusions of an earlier PhD study of the surface regarding the influence of surface vanadyl species on the $V_2O_3(0001)$ termination [193, 194]. This observation also indicates that the VOPc molecule adsorbs onto the Au(111) surface with the V=O pointing out of, rather than into, the underlying substrate.

A fully quantitative evaluation of the PhD data using multiple scattering simulations confirms this molecular orientation and shows that the V=O bondlength is 1.60 ± 0.04Å, not significantly different from its value in bulk crystalline VOPc. However, the calculations indicate that the V atom in the adsorbed molecule is almost coplanar with the surrounding N atoms and is thus pulled down into the approximately planar region, defined by the N and C atoms, by $0.52(+0.14/-0.10)$ Å,

relative to its location in the molecule in crystalline VOPc. This change must be attributed to the bonding interaction between the molecule and the underlying metal surface.

In general the PhD technique provides rather reliable quantitative structural information, but in the present case we have used a small data set and made a number of simplifications in the data analysis. Could these influence the precision of the conclusions? One constraint we have applied is to limit the range of variation of the intramolecular bondlengths. With so many potential structural parameters, and a limited data set, such a constraint is necessary to identify a meaningful solution. The more distant C atoms (relative to the O and V emitters) contribute little to the scattering, while interatomic bondlengths are unlikely to change in a molecule of this type by more than a few hundredths of an Ångström unit, so this constraint seems unlikely to influence the results. Potentially more significant is the neglect of Au scattering. For the V=O orientation and bondlength it is clear that the conclusions are very stable. It is more difficult to conclusively exclude the possibility that the Au scattering has no influence the V-N interlayer spacing because a significant change in the PhD spectra below 100 eV, where the Au scattering cross-section is large, could influence the structural optimisation, particularly for the V emitter that is closest to the substrate. On the other hand, the fit to the O 1s PhD spectrum is also very significantly improved by this modification to the molecular conformation, and the O atom is (even with the V=O pulled down into the molecular plane) more than 2 Å above the underlying C atoms and so likely to be almost 5 Å above the outermost Au layer. It is unlikely, therefore, that Au scattering has a significant influence on our numerical conclusions.

There are very few previous structural studies of adsorbed planar or near-planar molecules with which to compare this result. The most relevant is probably the NIXSW study of SnPc on Ag(111) [191] discussed in §8. In addition, NIXSW has also been used to study fully fluorinated phthalocyanine, $F_{16}CuPc$, on Cu(111) and Ag(111) [197]. This investigation showed that adsorption on these two surfaces (with the phthalocyanine plane parallel to the surface) led to different changes in the relative heights of the C and F atoms, but the height of the central Cu metal atom above the surface was not determined. NIXSW has also been used to investigate the adsorption of PTCDA (1,4,5,8-perylene-tetracarboxylicacid-dianhydride) [198] on Ag(111) and was able to show that inequivalent O atoms on the periphery of the nominally planar molecule (four carboxylic O atoms at the corners and two intermediate anhydride O atoms) occupy different heights above the surface, clearly an effect of the nature of the molecule-substrate bonding. Both of these previous studies clearly support the notion that bonding of large near-planar molecules to metal surfaces can lead to some modification of the internal conformation of the molecule. In the present case, the

rather large shift of the V atom down into the near-planar region defined by the C and N atoms would appear to indicate that the V atom itself does have a significant interaction with the underlying Au surface.

Chapter 9

Conclusions

The structures of eight systems, varying from simple molecular adsorbates (§6) to (comparitively) large organic molecules (§8) on noble metal (§4 & 8), platinum group metal (§5 & 6) and metal oxide (§7) surfaces, have been quantitatively determined using energy scanned photoelectron diffraction. In almost every system presented here the structure determination would have been impossible to determine with any certainty if it were not for the results of complementary techniques. In multiple systems (§4.2, 4.5 & 5) theoretical predictions from density functional theory calculations were of fundamental importance in determining the correct geometry. In two systems information on the orientation of the molecular plane from near-edge X-ray adsorption fine structure spectra was pivotal in understanding the adsorption site (§4.2 & 4.3). No single surface science technique stands by itself, especially one which provides quantitative structural information. The use of global search algorithms, like the particle swarm optimisation used within this work (§2.6), and greater access to high performance computing, can provide a more thorough exploration of the variable hyperspace, but without the insight provided by complementary techniques (that generally provide qualitative information) it is easy to be fooled by mathematically good fits that bear no resemblance to physical reality (e.g. §5).

However, with this limitation in mind, PhD is clearly a powerful technique that can be applied in a breadth of applications. When considering the Cu / biological interface it has provided some insight into how these interactions will proceed with increasing complexity. In the specific case of glycine on the different faces of Cu (refs [69, 88, 89] and §4.5) we have seen the molecule interacting as would have probably been expected, by bonding with both the nitrogen atoms and (at least some proportion of) the oxygen atoms in near atop sites, as is observed for the far less sterically hindered molecules (containing similar functional groups) of ammonia [25, 140] and formate / acetate [5, 124]. That the bond length shortening on rougher surfaces that is observed for both ammonia and formate [5, 25, 140] is not reproduced

for glycine on the [110] & [111] faces, indicates that the steric effects or intermolecular interactions are constraining the geometries. However, these forces do not seem to be strongly affecting how these groups coordinate to the surface. If we consider tartaric acid (§4.4) which has, in the bitartrate phase, possibly a stronger steric hindrance, we see a significant displacement of the bonding O atoms off atop ($0.4 - 0.9 \pm 0.2 - 0.3$ Å); however, the oxygen atoms are still clearly coordinating to a single substrate atom. This is in contrast to methoxy on the same surface which adsorbs in a higher coordination site [6, 199–201]. Clearly the functional group (alcohol or carboxylic acid in this case) is what is important, not simply the atom, when considering the interaction with this surface.

The ability to reliably separate the PhD modulation spectra for different chemical species was also integral to studying some of these relatively complex (for quantitative structural analysis) molecules and oxide surfaces. The ability to separate these different chemical species was of the utmost necessity for the study of water dissociation on TiO_2(110). If this technique were not chemically sensitive, then not only would it be impossible to separate the modulations from the hydroxyl species (the result of water decomposition) from the water species – but there would also be an overwhelming effect from the bulk oxide species. Therefore exploiting the core-level binding energy shift due to chemical effects can allow this technique (PhD) to study relatively complext systems in, effectively, a very simple way.

When considering the vanadyl phthalocyanine / Au(111) system, a surprisingly large amount of information was obtained about the geometry of the light elements (specifically carbon and nitrogen atoms) that were nearest neighbours to the vanadyl group. Generally light atoms contribute little to the theoretical fits, as the spectra are dominated by larger scatterers (typically metal atoms). However, in this case the metal atoms (specifically Au atoms) were not only a significant distance from the emitters, but also inhabited a near-random geometry with respect to the emitters. The light elements, in this system, were instead relatively close (< 4Å) and were in high symmetry sites with respect to the emitters. Another surprise from this system is that this information was gained from a relatively low coverage (~ 0.015 ML), an order of magnitude lower than systems typically measured by this technique. This suggests that similar information can be gleamed from systems consisting of light elements that have a high degree of local ordering, and from systems consisting of relatively low coverage systems, for which this technique would not previously have been considered, to be viable.

Appendix A

Publications list

List of articles that have been / will be published during the PhD period:

- D.A. Duncan, W. Unterberger, D.C. Jackson, M.K. Knight, E.A. Kröger, K.A. Hogan, C.L.A. Lamont, T.J. Lerotholi and D.P. Woodruff, "Quantitative structure determination of R,R-tartaric acid on Cu(110): Monotartrate and Bitartrate phases", to be published

- D. A. Duncan, F. Allegretti and D. P. Woodruff *Water does partially dissociate on the perfect TiO_2 surface: a quantitative structure determination*, submitted to Physical Review Letters

- D. A. Duncan, W. Unterberger, D. Kreikemeyer Lorenzo and D. P. Woodruff, *Dose methanol produce a stable methoxy species on Ru(0001)?*, submitted to Surface Science

- D. A. Duncan, M. K. Bradley, W. Unterberger, D. Kreikemeyer Lorenzo, T. J. Lerotholi, J. Robinson and D. P. Woodruff, *Glycine on Cu(111): A quantitative structure determination by energy-scanned photoelectron diffraction.*, submitted to Journal of Physical Chemistry C

- D. A. Duncan, J. I. J. Choi and D. P. Woodruff, *Global search algorithms in surface structure determinations using photoelectron diffraction*, Surface Science, 606 (2012), 278

- W. Unterberger, T. J. Lerotholi, E. A. Kröger, M. J. Knight, D. A. Duncan, D. Kreikemeyer Lorenzo, K. A. Hogan, D. C. Jackson, R. Wlodarczyk, M. Sierka, J. Sauer and D. P. Woodruff, *Local hydroxyl adsorption geometry on TiO_2(110)*, Physical Review B, 84 (2011), 115461

- D. Kreikemeyer Lorenzo, W. Unterberger, D. A. Duncan, M. K. Bradley, T. J. Lerotholi, J. Robinson and D. P. Woodruff, *Face-dependent bond lengths*

in molecular chemisorption: The formate species on Cu(111) and Cu(110), Physical Review Letters, 107 (2011), 046102

- D. A. Duncan, W. Unterberger, D. Kreikemeyer Lorenzo and D. P. Woodruff, *Uracil on Cu(110): A quantitative structure determination by energy-scanned photoelectron diffraction*, Journal of Chemical Physics, 135 (2011), 014704

- M. K. Bradley, D. A. Duncan, J. Robinson and D. P. Woodruff, *The structure of furan reaction products on Pd(111)*, Physical Chemisty Chemical Physics, 13 (2011), 7975

- D. Kreikemeyer Lorenzo, M. K. Bradley, W. Unterberger, D. A. Duncan, T. J. Lerotholi, J. Robinson and D. P. Woodruff, *The structure of methoxy species on Cu(110): A combined photoelectron diffraction and density functional theory determination*, Surface Science, 605 (2011), 193

- D. C. Jackson, D. A. Duncan, W. Unterberger, T. J. Lerotholi, D. Kreikemeyer Lorenzo, M. K. Bradley and D. P. Woodruff, *Structure of cytosine on Cu(110): A scanned-energy mode photoelectron diffraction study*, Journal of Physical Chemistry C, 114 (2010), 15454

- M. K. Bradley, D. Kreikemeyer Lorenzo, W. Unterberger, D. A. Duncan, T. J. Lerotholi, J. Robinson and D. P. Woodruff, *Methoxy species on Cu(110): Understanding the local structure of a key catalytic reaction intermediate*, Physical Review Letters, 105 (2011), 086101

- D. A. Duncan, W. Unterberger, K. A. Hogan, T. J. Lerotholi, C. L. A. Lamont and D. P. Woodruff, *A photoelectron diffraction investigation of vanadyl phthalocyanine on Au(111)*, Surface Science, 604 (2010), 47

Appendix B

Spherical wave propagator

As the distance between scattering events is comparable to the wavelength of the electron, plane-wave approximations are not an acceptable approximation for low and medium energy electron scattering, therefore a spherical wave description is necessary. However a full numerical spherical wave expansion is computationally time consuming. If, for each scattering event, the coordinate system is rotated such that the electron is propagating along the z axis the expansion is significantly simplified[16]. Therefore, for a wave propagating between atom R_1 and R_2:

$$D^{\theta,\Theta}_{(m_2,m_1,l_1)} = E_{(\theta,\Theta)} d_{(m_2,m_1,l_1)} E'_{(\theta,\Theta)}, \tag{B.1}$$

$$\tag{B.2}$$

where $E_{(\theta,\Theta)}$ transform the propagation term, $d_{(m_2,m_1,l_1)}$, into the rotated coordinate system with the wave propagating along the z-axis and $E'_{(\theta,\Theta)}$ transforms the propagation term back into the original basis system, θ and Θ are the spherical polar coordinates of the vector between R_1 and R_2 in the original basis system, m_1 and m_2 are the magnetic quantum numbers of the wave at atom R_1 and R_2, and l_1 is the angular momentum at atom R_1. For $m_1 = m_2 = 0$ and $l_1 = 0, 1$, the propagator, $D^{\theta,\Theta}_{(m_2,m_1,l_1)}$, is calculated numerically as:

$$\begin{aligned} D^{\theta,\Theta}_{(0,0,0)} &= 1, \\ D^{\theta,\Theta}_{(0,0,1)} &= cos(\theta). \end{aligned} \tag{B.3}$$

For the extrema values of the magnetic quantum number, $|m_1| = |m_2| = l_1$, and $l_1 > 0$ the propagator is calculated by:

$$
\begin{aligned}
&D^{\theta,\Theta}_{(m_2=-l_1,m_1=l_1,l_1)} \\
&\quad = D_{(m_2+1,m_1-1,l_1-1)} \frac{1-cos(\theta)}{2} e^{i\Theta}, \\
&D^{\theta,\Theta}_{(m_2=l_1,m_1=-l_1,l_1)} \\
&\quad = D^{*}_{(-m_2,-m_1,l_1)}, \\
&D^{\theta,\Theta}_{(m_2=l_1,m_1=l_1,l_1)} \\
&\quad = D_{(m_2+1,m_1-1,l_1-1)} \frac{1+cos(\theta)}{2} e^{i\Theta}, \\
&D^{\theta,\Theta}_{(m_2=-l_1,m_1=-l_1,l_1)} \\
&\quad = D^{*}_{(-m_2,-m_1,l_1)},
\end{aligned}
\tag{B.4}
$$

and finally for the other possible m_1, m_2 and l_1 values:

$$
\begin{aligned}
&D^{\theta,\Theta}_{(m_2=l_1,-l_1<m_1<l_1,l_1)} \\
&\quad = D_{(m_2-1,m_1,l_1-1)} \frac{1-cos^2(\theta)}{2} \sqrt{\frac{2l_1\left(2l_1-1\right)}{l_1^2-m_1^2}}, \\
&D^{\theta,\Theta}_{(-l_1<m_2<l_1,m_1=l_1,l_1)} \\
&\quad = (-1)^{m_2+m_1} D_{(m_2,m_1-1,l_1-1)} \frac{1-cos^2(\theta)}{2} \sqrt{\frac{2l_1\left(2l_1-1\right)}{l_1^2-m_1^2}} e^{i\Theta}, \\
&D^{\theta,\Theta}_{(-l_1<m_2<l_1,m_1=-l_1,l_1)} \\
&\quad = (-1)^{m_2+m_1} D^{*}_{(-m_2,-m_1,l_1)}, \\
&D^{\theta,\Theta}_{(m_2=-l_1,-l_1<m_1<l_1,l_1)} \\
&\quad = (-1)^{m_2+m_1} D^{*}_{(-m_2,-m_1,l_1)}, \\
&D^{\theta,\Theta}_{(-l_1<m_2<l_1,-l_1<m_1<l_1,l_1>1)} \\
&\quad = \frac{D_A - D_B}{\sqrt{\left(l_1^2-m_1^2\right)\left(l_1^2-m_2^2\right)}}, \\
&D^{\theta,\Theta}_{A} \\
&\quad = D_{(m_2,m_1,l_1-1)} \left[\left(2l_1-1\right) l_1\theta - \frac{\left(2l_l-1\right) m_2 m_1}{l_1-1}\right], \\
&D^{\theta,\Theta}_{B} \\
&\quad = D_{(m_2,m_1,l_1-2)} \sqrt{\left[\left(2l_1-1\right)^2-m_2^2\right]\left[\left(2l_1-1\right)^2-m_1^2\right]} \frac{l_1}{l_1-1}.
\end{aligned}
\tag{B.5}
$$

Appendix C

Gaunt coefficients

The Gaunt coefficients generalise the rules of angular momentum conversion in angular momentum coupling interactions [22] (e.g. photoexcitation of an electron from one state into another). If angular conservation laws are not satisfied, then the Gaunt coefficients will be zero. The non-zero Gaunt coefficients for the interaction of three spherical harmonics, defined by their angular momentum (l) and magnetic quantum numbers (m) $l_1, m_1, l_2, m_2, l_3, m_3$, are calculated by:

$$\int \mathrm{d}\Omega\, Y_{l_1,m_1} Y_{l_2,m_2} Y_{l_3,m_3} = (-1)^{A_1} \cdot A_2 \cdot A_3 \cdot A_4, \tag{C.1}$$

$$A_1 = \frac{l_1 + l_2 + l_3}{2} - l_{2a} - |m_{3a}| + \frac{|m_1| + |m_2| + |m_3|}{2} + m_3,$$

$$A_2 = \sum_{q=0}^{Q} \frac{(-1)^q \,(l_{1a} + |m_{1a}| + q)!(l_{2a} + l_{3a} - |m_{1a}| - q)!}{q!(l_{1a} - |m_{1a}| - q)!(l_{1a} - l_{2a} + |m_{1a}| + q)!(l_{3a} - |m_{3a}|)!}, \tag{C.2}$$

$$Q = min\left[(l_{2a} + l_{3a} - |m_{1a}|)\,, (l_1 - |m_1|)\,, (l_2 - |m_2|)\,, (l_3 - |m_3|)\right]$$

$$A_3 = \frac{(l_{2a} + |m_{2a}|)!(l_{3a} + |m_{3a}|)!(l_{1a} + l_{2a} - l_{3a})!\left(\frac{l_1+l_2+l_3}{2}\right)!}{(l_{2a} - |m_{2a}|)!\left(\frac{l_2+l_3-l_1}{2}\right)!\left(\frac{l_1+l_2-l_3}{2}\right)(l_1 + l_2 + l_3 + 1)!},$$

$$A_4 = \sqrt{\frac{(l_1 - |m_1|)!(l_2 - |m_2|)!(l_3 - |m_3)!}{(l_1 + |m_1|)!(l_2 + |m_2|)!(l_3 + |m_3|)!}\,\frac{(2l_1 + 1)(2l_2 + 1)(2l_3 + 1)}{4\pi}}.$$

where m_{1a} (and l_{1a}) is the larger absolute value of the three magnetic quantum numbers ($|m_1|$,$|m_2|$ and $|m_3|$) (and its corresponding orbital angular momentum number (l_1,l_2 and l_3)), l_{2a} and m_{2a} are the larger of the two remaining orbital angular momentum numbers and its corresponding magnetic quantum number and l_{3a} and m_{3a} are the remaining orbital angular momentum number and its corresponding magnetic quantum number. The conditions that must be satisfied in order to have a non-zero Gaunt coefficient are detailed by Pinchon and Hoggan [22].

Appendix D

T matrix

The T-matrix takes into account the scattering phase shifts (δ_J) and the effect of the thermal vibrations, which are modelled using a Debye-Waller factor. It is calculated numerically in the Fritzsche code by:

$$T(l_s) = \sum_{J=0}^{l_{max}} \sum_{K=|l_s-J|}^{l_s+J+1} t_{l_s,J,K} \tag{D.1}$$

$$t_{l_s+J+K \text{ is odd}} = 0 \tag{D.2}$$

$$t_{l_s+J+K \text{ is even}} = S_{(J)} \cdot e^{-X} \cdot B_{(K)} \cdot \sqrt{4\pi \frac{(2K+1)(2J+1)}{2l_s+1}} \int \mathrm{d}\Omega \, Y_{l_s,0} Y_{K,0} Y_{J,0},$$

where $\int \mathrm{d}\Omega \, Y_{l_s,0} Y_{K,0} Y_{J,0}$ is calculated using Gaunt coefficients (Appendix C), and $S_{(J)}$ and $B_{(K)}$ are the phase shift and the thermal vibration components (respectively), and are numerically calculated by:

$$S_{(J)} = -i \cdot e^{i\delta_J} \cdot sin(\delta_J), \tag{D.3}$$

$$B_{(K)} = \frac{X^K}{\prod_{a=0}^{K} 2a+1} \sum_{b=1}^{\infty} \prod_{c=1}^{b} \frac{X^2}{2b(2(b+K)+1)},$$
$$X = E^2 \cdot \frac{A_{vib}}{a_{Bohr^2}}, \tag{D.4}$$

where A_{vib} is the mean square thermal vibration amplitude and a_{Bohr} is the Bohr radius in Ångströms.

Appendix E

Scattering Green's function

The scattering Green's function, $G_{(l_2,l_1,m_2)}$, is used to describe the scattering of the electron by a potential. The Green's function is summed over all the possible angular momenta it can have at its origin (l_1) and all the possible angular momenta (l_2) and magnetic quanta (m_2) that the electron can have after being scattering by the potential. For the case where either l_2 or l_1, and m_2 is equal to zero, the Green's function is calculated numerically by:

$$\begin{aligned} G_{(0,0,0)} &= e^{-B_G \cdot R_s} \cdot D_{G(0)}, \\ G_{(l_s,0,0)} &= (-1)^{l_s} \sqrt{2l_s+1} e^{-E \cdot R_s} \cdot D_{G(l_s)}, \\ G_{(0,l_f,0)} &= \sqrt{2l_f+1} e^{-E \cdot R_s} \cdot D_{G(l_f)}, \end{aligned} \tag{E.1}$$

where R_s is the distance between the electron's origin and the centre of the scattering potential, B_G is defined similarly to the B parameter in Eqn. 2.10 with the cosine replaced by a sine and $D_{G(l)}$ is calculated by:

$$\begin{aligned} D_{G(0)} &= \frac{-i \cdot e^{-iE \cdot R_s}}{E \cdot R_s}, \\ D_{G(1)} &= \frac{E \cdot R_s e^{iE \cdot R_s} + i e^{iE \cdot R_s}}{(E \cdot R_s)^2}, \\ D_{G(l_s>1)} &= \frac{2l_s - 1}{E \cdot R_s} D_{G(l_s-1)} - D_{G(l_s-2)} \cdot \end{aligned} \tag{E.2}$$

For the extrema values of m_2, $|m_2| = l_2$ or $|m_2| = l_1$, the Green's function is calculated numerically by:

$$G_{(l_s,l_f,m_s=l_s)} = \frac{G_{(l_s-1,l_f,m_s-1)}\sqrt{\left(1+\frac{1}{2m_s}\right)\cdot(l_f+m_s)\cdot(l_f-m_s+1)}}{E\cdot R_s},$$

$$G_{(l_s,l_f,m_s=l_f)} = (-1)^{l_f+l_s}\cdot G_{(l_f,l_s,m_s)}. \tag{E.3}$$

For all other intermediate values of m_2, the Green's function is calculated numerically by:

$$G_{(1,l_f>l_s,m_s)} = \frac{G_1 - G_2}{\sqrt{\frac{(l_s^2-m_s^2)}{\left[4(l_s-1)^2-1\right]}}}, \tag{E.4}$$

$$G_{(l_s>1,l_f>l_s,m_s)} = \frac{G_1 - G_2 + G_3}{\sqrt{\frac{(l_s^2-m_s^2)}{\left[4(l_s-1)^2-1\right]}}},$$

$$G_1 = G_{(l_s-1,l_f-1,m_s)}\cdot\sqrt{\frac{l_f^2-m_s^2}{4l_f^2-1}},$$

$$G_2 = G_{(l_s-1,l_f+1,m_s)}\cdot\sqrt{\frac{(l_f+1)^2-m_s^2}{4(l_f+1)^2-1}},$$

$$G_3 = G_{(l_s-2,l_f,m_s)}\cdot\sqrt{\frac{(l_s+1)^2-m_s^2}{4(l_s+1)^2-1}},$$

$$G_{(l_s>l_f,l_f>0,m_s)} = (-1)^{l_s+l_f}\cdot G_{(l_f,l_s,m_s)}.$$

Bibliography

[1] F. Schreiber *Prog. Surf. Sci.*, vol. 65, p. 151, 2000.

[2] C. M. Niemeyer *Ange. Chem. Int. Ed.*, vol. 40, p. 4128, 2001.

[3] U. Diebold *Surf. Sci. Rep.*, vol. 48, p. 53, 2003.

[4] C. Woell *Prog. Surf. Sci.*, vol. 82, p. 55, 2007.

[5] D. Kreikemeyer-Lorenzo, W. Unterberger, D. A. Duncan, M. K. Bradley, T. J. Lerotholi, J. Robinson, and D. P. Woodruff *Phys Rev Lett*, vol. 107, p. 046102, 2011.

[6] D. Kreikemeyer Lorenzo, M. K. Bradley, W. Unterberger, D. A. Duncan, T. J. Lerotholi, J. Robinson, and D. P. Woodruff *Surf. Sci.*, vol. 605, p. 193, 2011.

[7] D. I. Sayago, J. T. Hoeft, M. Polcik, M. Kittel, R. L. Toomes, J. Robinson, D. P. Woodruff, M. Pascal, C. L. A. Lamont, and G. Nisbet *Phys. Rev. Lett.*, vol. 90, p. 116104, Mar 2003.

[8] D. Woodruff and T. Delchar, *Modern Techniques of Surface Science*. Cambridge University Press, second edition ed., 1994.

[9] J. B. Pendry, *Low Energy Electron Diffraction*. New York: Academic Press, 1974.

[10] M. A. Van Hove, *Low-energy electron diffraction: experiment, theory and surface structure*. Berlin: Springer, 1986.

[11] D. P. Woodruff *Surf. Sci. Rep.*, vol. 62, p. 1, 2007.

[12] D. P. Woodruff and A. M. Bradshaw *Rep. Prog. Phys.*, vol. 57, p. 1029, 1994.

[13] M. K. Knight. PhD thesis, University of Warwick, 2007.

[14] V. Fritzsche and P. Rennert *Phys Stat Sol (b)*, vol. 135, p. 49, 1986.

[15] V. Fritzsche *Surf. Sci.*, vol. 213, p. 648, 1989.

[16] V. Fritzsche *J. Phys: Condens. Matter*, vol. 2, p. 1413, 1990.

[17] V. Fritzsche *J. Phys: Condens. Matter*, vol. 2, p. 9735, 1990.

[18] V. Fritzsche *Surf. Sci.*, vol. 265, p. 187, 1992.

[19] V. Fritzsche and J. B. Pendry *Phys. Rev. B*, vol. 48, pp. 9054–, 1993.

[20] V. Fritzsche, R. Davis, X. M. Hu, D. P. Woodruff, K. U. Weiss, R. Dippel, K. M. Schindler, P. Hofmann, and A. M. Bradshaw *Phys Rev B*, vol. 49, p. 7729, 1994.

[21] V. Fritzsche, "Photoelectron Diffraction Program, DMSUP398," January 1995.

[22] D. Pinchon and P. Hoggan *Int J Quantum Chem*, vol. 107, p. 2186, 2007.

[23] J. A. Gaunt *Phil Trans R Soc A*, vol. 228, p. 151, 1929.

[24] J. B. Pendry *J Phys C: Solid State Phys.*, vol. 13, no. 5, p. 937, 1980.

[25] N. A. Booth, R. Davis, R. Toomes, D. P. Woodruff, C. Hirschmugl, K. M. Schindler, O. Schaff, V. Fernandez, A. Theobald, P. Hofmann, R. Lindsay, T. Giessel, P. Baumgärtel, and A. M. Bradshaw *Surface Science*, vol. 387, p. 152, 1997.

[26] H. William, S. Teukolsky, W. Vetterling, and F. Flannery, *Numerical Recipes in C++*. New York: Cambridge University Press, 2nd ed., 2005.

[27] M. L. Viana, R. Diez Muiño, E. A. Soares, M. A. van Hove, and V. E. de Carvalho *J. Phys. Condens. Mat.*, vol. 19, p. 446002, 2007.

[28] A. Pancotti, P. A. P. Nascente, A. de Siervo, R. Landers, M. F. Carazzolle, D. A. Tallarico, and G. G. Kleiman *Top Catal*, vol. 54, p. 70, 2011.

[29] A. Pancotti, N. Barrett, L. F. Zagonel, and G. M. Vanacore *J. App. Phys.*, vol. 106, p. 034104, 2009.

[30] A. Pancotti, A. de Siervo, M. F. Carazzolle, R. Landers, and G. G. Kleiman *Top. Catal.*, vol. 54, p. 90, 2011.

[31] R. Döll and M. A. Van Hove *Surf. Sci.*, vol. 355, p. L393, 1996.

[32] V. B. Nascimento, V. E. de Carvalho, C. M. C. de Castilho, B. V. Costa, and E. A. Soares *Surf Sci*, vol. 487, p. 15, 2001.

[33] M. Kottcke and K. Heinz *Surf. Sci.*, vol. 376, p. 352, 1997.

[34] Z. Zhao, J. C. Meza, and M. A. Van Hove *J. Phys.: Condens. Matter*, vol. 18, p. 8693, 2006.

[35] M. Clerc, *Particle Swarm Optimisation*. ISTE Ltd, 2006.

[36] J. Kennedy and R. Eberhart *IEEE Neural Networks Proceedings*, vol. 4, p. 1942, 1995.

[37] M. K. Bradley, D. A. Duncan, J. Robinson, and D. P. Woodruff *Phys. Chem. Chem. Phys.*, vol. 13, p. 7975, 2011.

[38] M. J. Knight, F. Allegretti, E. A. Krger, M. Polcik, C. L. A. Lamont, and D. P. Woodruff *Surf. Sci.*, vol. 602, p. 2743, 2008.

[39] D. A. Duncan, J. I. J. Choi, and D. P. Woodruff *Surf. Sci.*, vol. 606, p. 278, 2012.

[40] F. Allegretti, S. O'Brien, M. Polcik, D. I. Sayago, and D. P. Woodruff *Surf. Sci.*, vol. 600, p. 1487, 2006.

[41] M. J. Knight, F. Allegretti, E. A. Krger, K. A. Hogan, D. I. Sayago, T. J. Lerotholi, W. Unterberger, and D. P. Woodruff *Surf. Sci.*, vol. 603, p. 2062, 2009.

[42] M. Polcik, M. Kittel, J. T. Hoeft, R. Terborg, R. L. Toomes, and D. P. Woodruff *Surf Sci*, vol. 563, p. 159, 2004.

[43] M. Affenzeller, S. Winkler, S. Wagner, and A. Beham, *Genetic Algorithms and Genetic Programming*. Boca Rotan, Florida: CRC Press, 2009.

[44] S. R. Puisto, G. Held, V. Ranea, S. J. Jenkins, E. E. Mola, and D. A. King *J Phys Chem B*, vol. 109, p. 22456, 2005.

[45] M. Blanco-Rey, J. Abad, C. Rogero, J. Mendez, M. F. Lopez, J. A. Martin-Gago, and P. L. de Andres *Phys Rev Lett*, vol. 96, p. 055502, 2006.

[46] M. Lindroos, H. Pfnür, G. Held, and D. Menzel *Surf. Sci.*, vol. 222, p. 451, 1989.

[47] H. Pfnür, G. Held, M. Lindroos, and D. Menzel *Surf. Sci.*, vol. 220, p. 43, 1989.

[48] G. Michalk, W. Moritz, H. Pfnür, and D. Menzel *Surf. Sci.*, vol. 129, p. 92, 1983.

[49] S. Driver and D. King *Surf Sci*, vol. 601, p. 510, 2007.

[50] A. Einstein *Annalen der Physik*, vol. 322, p. 132, 1905.

[51] A. B. Arons and M. B. Peppard *Am. J Phys*, vol. 33, p. 367, 1965.

[52] H. L. Skriver and N. M. Rosengaard *Phys Rev B*, vol. 46, p. 7157, 1992.

[53] A. C. Thompson, D. T. Attwood, E. M. Gullikson, M. R. Howells, J. B. Kortright, A. I. Robinson, J. Underwood, K. J. Kim, J. Kirz, I. Lindau, P. Pianetta, H. Winick, G. P. Williams, and J. H. Scofield, *X-ray data booklet*. Lawrence Berkeley National Laboratory, 2001.

[54] K. Siegbahn *Phil. Trans. Roy. Soc. Lond. A.*, vol. 268, p. 33, 1970.

[55] Omicron NanoTechnology, Limburger Strasse 75, 65232 Taunusstein, Germany, *EA 125 Energy Analyser*, 2.1 ed., July 2002.

[56] http://bama.ua.edu/∼surfspec/cha_details.htm.

[57] E. A. Stern *Phys Rev B*, vol. 10, p. 3027, 1974.

[58] A. Puschmann, J. Haase, M. D. Crapper, C. E. Riley, and D. P. Woodruff *Phys Rev Lett*, vol. 54, p. 2250, 1985.

[59] Joachim Stör, *NEXAFS spectroscopy*. Springer, 1996.

[60] P. Hohenberg and W. Kohn *Phys Rev*, vol. 136, p. B864, 1964.

[61] W. Kohn and L. J. Sham *Phys Rev*, vol. 140, p. A1133, 1965.

[62] E. Kaxiras, *Atomic and Electronic Structure of Solids*. New York: Cambridge University Press, 2003.

[63] K. Carling and G. Wahnström *Phys Rev Lett*, vol. 85, p. 3862, 2000.

[64] S. Mehta, G. D. Price, and D. Alfe *J Chem Phys*, vol. 125, p. 194507, 2006.

[65] M. J. Harrison, D. P. Woodruff, and J. Robinson *Surf. Sci.*, vol. 600, p. 340, 2006.

[66] P. J. Feibleman, B. Hammer, J. K. Norskov, F. Wagner, M. Scheffler, R. Stumpf, R. Watwe, and J. Dumesic *J Phys Chem B*, vol. 105, p. 4018, 2001.

[67] B. K. Agrawal, S. Agrawal, S. Singh, and R. Srivastava *J Phys Condens Matter*, vol. 18, p. 4649, 2006.

[68] S. G. Santos, J. V. Santana, F. F. Maia Jr, V. Lemos, V. N. Freire, E. W. S. Caetano, B. S. Cavada, and E. L. Albuquerque *J Phys Chem B*, vol. 112, p. 14267, 2008.

[69] D. A. Duncan, M. K. Bradley, W. Unterberger, D. Kreikemeyer-Lorenzo, T. J. Lerotholi, J. Robinson, and D. P. Woodruff *submitted to J. Phys. Chem. C*.

[70] P. Maksymovych, O. Voznyy, D. B. Dougherty, D. C. Sorescu, and J. T. Yates Jr. *Prog. Surf. Sci.*, vol. 85, p. 206, 2010.

[71] http://www.slri.or.th/en/index.php?option=com_content&view=article &id=298&catid=57:bl32a-pes, 2011.

[72] http://www.bessy.de/bit/upload/ID_05_2.pdf.

[73] http://www.helmholtz-berlin.de/forschung/grossgeraete/undulatoren/ geraete/ue56_en.html.

[74] G. Margaritondo, *Introduction to synchrotron radiation.* New York: Oxford University Press, 1988.

[75] R. Follath, F. Senf, and W. Gudat *J. Syhnchrotron Rad.*, vol. 5, p. 769, 1998.

[76] Y. Gao *Mat. Sci. Eng. R*, vol. 68, p. 39, 2010.

[77] K. J. Hughes and J. R. Engstrom *J. Vac. Sci. Technol. A*, vol. 28, p. 1033, 2010.

[78] D. P. Allison, N. P. Mortensen, C. J. Sullivan, and M. J. Doktycz *WIREs Nanomed Nanobiotechnol*, vol. 2, p. 618, 2010.

[79] G. L. J. A. Rikken *Science*, vol. 331, p. 864, 2011.

[80] W. F. Kean, C. J. L. Lock, and H. E. Howard-Lock *The Lancet*, vol. 338, p. 1565, 1991.

[81] J. I. Garcia, B. Lopez-Sanchez, and J. A. Mayoral *Org. Lett.*, vol. 10, p. 4995, 2008.

[82] J. A. Groenewegen and W. M. H. Sachtler *J. Catal.*, vol. 38, p. 501, 1975.

[83] A. Hoek and W. M. H. Sachtler *J. Catal.*, vol. 58, p. 276, 1979.

[84] Y. Izumi *Adv. Catal.*, vol. 60, p. 215, 1983.

[85] G. Wittmann, G. B. Bartk, M. Bartk, and G. V. Smith *J. Mole. Catal.*, vol. 60, p. 1, 1990.

[86] M. A. Keane and G. Webb *J. Catal.*, vol. 136, p. 1, 1992.

[87] M. A. Keane *Langmuir*, vol. 13, p. 41, 1997.

[88] J. H. Kang, R. L. Toomes, M. Polcik, M. Kittel, J. T. Hoeft, V. Efstathiou, D. P. Woodruff, and A. M. Bradshaw *J. Chem. Phys.*, vol. 118, p. 6059, 2003.

[89] N. A. Booth, D. P. Woodruff, O. Schaff, T. Giessel, R. Lindsay, P. Baumgartel, and A. M. Bradshaw *Surf. Sci.*, vol. 397, p. 258, 1998.

[90] D. I. Sayago, M. Polcik, G. Nisbet, C. L. A. Lamont, and D. P. Woodruff *Surf. Sci.*, vol. 590, p. 76, 2005.

[91] F. Allegretti, M. Polcik, and D. P. Woodruff *Surf. Sci.*, vol. 601, p. 3611, 2007.

[92] M. Furukawa, H. Fujisawa, S. Katano, H. Ogasawara, Y. Kim, T. Komeda, A. Nilsson, and M. Kawai *Surf. Sci.*, vol. 532-535, p. 261, 2003.

[93] T. Yamada, K. Shirasaka, A. Taknao, and M. Kawai *Surf. Sci.*, vol. 561, p. 233, 2004.

[94] D. J. Frankel, Q. Chen, and N. V. Richardson *J. Chem. Phys.*, vol. 124, p. 204704, 2006.

[95] D. C. Jackson, D. A. Duncan, W. Unterberger, T. J. Lerotholi, D. K. Lorenzo, M. K. Bradley, and D. P. Woodruff *J. Phys. Chem. C*, vol. 114, p. 15454, 2010.

[96] A. Haug, S. Schwiezer, F. Latteyer, M. B. Casu, H. Peisert, C. Ochsenfeld, and T. Chasse *Chem Phys Chem*, vol. 9, p. 740, 2008.

[97] D. Barker and M. Marsh *Acta Cryst.*, vol. 17, p. 1581, 1964.

[98] W. H. Li, W. Haiss, S. Floate, and R. J. Nichols *Langmuir*, vol. 15, p. 4875, 1999.

[99] Q. Chen and N. V. Richardson *Prog. Surf. Sci.*, vol. 73, p. 59, 2003.

[100] M. L. M. Rocco, R. Dudde, K. H. Frank, and K. E. E *Chem. Phys. Lett.*, vol. 160, p. 366, 1989.

[101] A. Martinez *J. Chem. Phys.*, vol. 123, p. 024311, 2005.

[102] A. McNutt. PhD thesis, University of Liverpool, 2002.

[103] A. McNutt, S. Haq, and R. Raval *Surf. Sci.*, vol. 502-503, p. 185, 2002.

[104] K. Fujii, K. Akamatsu, and A. Yokoya *J. Phys. Chem. B*, vol. 108, p. 8031, 2004.

[105] R. F. Stewart and L. H. Jensen *Acta Cryst.*, vol. 23, p. 1102, 1967.

[106] T. Nakagawa, H. Tanaka, and T. Kawai *Surf. Sci.*, vol. 370, p. L144, 1997.

[107] S. Boncel, M. Maczka, and K. Z. Walczak *Tetrahedron*, vol. 66, p. 8450, 2010.

[108] A. P. Martinez and W. W. Lee *J. Org. Chem.*, vol. 30, p. 317, 1965.

[109] A. Alahiane, A. Rochdi, M. Taourirte, N. Redwane, S. Sebti, and H. B. Lazrek *Tetra. Lett.*, vol. 42, p. 3579, 2001.

[110] O. D. Gupta, B. Twamley, R. L. Kirchmeier, and J. M. Shreeve *J. Fluorine Chem*, vol. 106, p. 199, 2000.

[111] S. Boncel, D. Osyda, and K. Z. Walczak *Beilstein J. Org. Chem*, vol. 3, p. 40, 2007.

[112] K. Yamauchi and M. Kinoshita *J.C.S. Perkin I*, p. 391, 1973.

[113] J. T. Kusmierek and B. Singer *Nucleic Acids Research*, vol. 3, p. 989, 1976.

[114] A. Gambacorta, M. E. Farah, and D. Tofani *Tetrahedron*, vol. 55, p. 12615, 1999.

[115] M. A. Kurinovich and J. K. Lee *J Am. Chem. Soc.*, vol. 122, p. 6258, 2000.

[116] L. Pasteur *Annal Chim Phys*, vol. 24, p. 442, 1848.

[117] M. Ortega Lorenzo, S. Haq, T. Bertrams, P. Murray, R. Raval, and C. J. Baddeley *J. Phys. Chem. B*, vol. 103, no. 48, p. 10661, 1999.

[118] M. Ortega Lorenzo, C. J. Baddeley, C. Muryn, and R. Raval *Nature*, vol. 404, p. 376, 2000.

[119] L. A. M. M. Barbosa and P. Sautet *J. Am. Chem. Soc.*, vol. 123, p. 6639, 2001.

[120] C. G. M. Hermse, A. P. van Bavel, A. P. J. Jansen, L. A. M. M. Barbosa, P. Sautet, and R. A. van Santen *J. Phys. Chem. B*, vol. 108, p. 11035, 2004.

[121] J. Zhang, T. Lu, C. Jiang, J. Zou, F. Cao, and Y. Chen *J. Chem. Phys.*, vol. 131, p. 144703, 2009.

[122] M. D. Crapper, C. E. Riley, and D. P. Woodruff *Surf. Sci.*, vol. 184, p. 121, 1987.

[123] D. P. Woodruff, C. F. McConville, A. L. D. Kilcoyne, T. Lidner, J. Somers, M. Somers, M. Surman, G. Paolucci, and A. M. Bradshaw *Surf. Sci.*, vol. 201, p. 228, 1988.

[124] K. U. Weiss, R. Dippel, K. M. Schindler, P. Gardner, V. Fritzsche, A. M. Bradshaw, A. L. D. Kilcoyne, and D. P. Woodruff *Phys. Rev. Lett.*, vol. 69, p. 3196, 1992.

[125] M. Pascal, C. L. A. Lamont, M. Kittel, J. T. Hoeft, R. Terborg, M. Polcik, J. H. Kang, R. Toomes, and D. P. Woodruff *Surf Sci*, vol. 492, p. 285, 2001.

[126] F. Gao, Z. Li, Y. Wang, L. Burkholder, and W. T. Tysoe *J. Phys. Chem. C*, vol. 111, p. 9981, 2007.

[127] T. Eralp, A. Shavorskiy, Z. V. Zheleva, G. Held, N. Kalashnyk, Y. X. Ning, and T. R. Lineroth *Langmuir*, vol. 26, p. 18841, 2010.

[128] G. Jones, L. B. Jones, F. Thibault-Starzyk, E. A. Seddon, R. Raval, S. J. Jenkins, and G. Held *Surf. Sci.*, vol. 600, p. 1924, 2006.

[129] F. Stern and C. A. Beevers *Acta Cryst.*, vol. 3, p. 341, 1950.

[130] J. H. Kang, R. L. Toomes, J. Robinson, D. P. Woodruff, O. Schaff, R. Terborg, R. Lindsay, P. Baumgärtel, and A. M. Bradshaw *Surf Sci*, vol. 448, p. 23, 2000.

[131] D. A. Duncan, W. Unterberger, K. A. Hogan, T. J. Lerotholi, C. L. A. Lamont, and D. P. Woodruff *Surf. Sci.*, vol. 604, p. 47, 2010.

[132] R. Fasel, J. Wider, C. Quitmann, K. H. Ernst, and T. Greber *Ange. Chem. Int. Ed.*, vol. 43, p. 2853, 2004.

[133] L. L. Atanasoska, J. C. Buchholz, and G. A. Somorjai *Surf. Sci.*, vol. 72, p. 189, 1978.

[134] X. Zhao, H. Yan, R. G. Zhao, and W. S. Yang *Langmuir*, vol. 19, p. 809, 2003.

[135] V. Efstathiou and D. P. Woodruff *Surf. Sci.*, vol. 531, p. 304, 2003.

[136] K. Kanazawa, A. Taninaka, H. Huang, M. Nishimura, S. Yoshida, O. Takeuchi, and H. Shigekawa *Chem. Commun.*, vol. 47, p. 11312, 2011.

[137] Y. Zhang and W. Yang *Phys Rev Lett*, vol. 80, p. 890, 1998.

[138] J. P. Perdew, K. Burke, and Y. Wang *Phys Rev B*, vol. 54, p. 16533, 1996.

[139] J. Hasselström, O. Karis, M. Weinelt, N. Wassdahl, A. Nilsson, M. Nyberg, L. G. M. Pettersson, M. G. Samant, and J. Stöhr *Surf. Sci.*, vol. 407, p. 221, 1998.

[140] P. Baumgärtel, R. Lindsay, T. Giessel, O. Schaff, A. M. Bradshaw, and D. P. Woodruff *J Phys Chem B*, vol. 104, p. 3044, 2000.

[141] T. Giessel, O. Schaff, R. Lindsay, P. Baumgärtel, M. Polcik, A. M. Bradshaw, A. Koebbel, T. McCabe, M. Bridge, D. R. Lloyd, and D. P. Woodruff *J. Chem Phys*, vol. 110, p. 9666, 1999.

[142] R. Terborg, M. Polcik, J. T. Hoeft, M. Kittel, M. Pascal, J. H. Kang, C. L. A. Lamont, A. M. Bradshaw, and D. P. Woodruff *Surf Sci*, vol. 457, p. 1, 2000.

[143] E. Furimsky *Catal. Rev.*, vol. 25, p. 421, 1983.

[144] B. A. Sexton *Surf Sci*, vol. 163, p. 99, 1985.

[145] J. L. Solomon, R. J. Madix, and Stör *J. Chem. Phys.*, vol. 94, p. 4012, 1991.

[146] R. M. Ormerod, C. J. Baddeley, C. Hardacre, and R. M. Lambert *Surf Sci*, vol. 360, p. 1, 1996.

[147] D. P. Caldwell, T. E. and *J. Phys. Chem. B*, vol. 103, p. 7869, 1999.

[148] T. E. Caldwell and D. P. Land *Polyhedron*, vol. 16, p. 3197, 1997.

[149] T. E. Caldwell and D. P. Land *J Phys Chem B*, vol. 103, p. 7869, 1999.

[150] A. Loui. PhD thesis, University of California at Davis, 2005.

[151] M. R. Churchill, L. A. Buttrey, J. B. Keister, J. W. Ziller, T. S. Janik, and W. Striejewske *Organometallics*, vol. 9, p. 766, 1990.

[152] J. E. Demuth and D. E. Eastman *Phys. Rev. Lett.*, vol. 32, p. 1123, 1974.

[153] G. D. Waddill and L. L. Kesmodel *Phys. Rev. B*, vol. 31, p. 4940, 1985.

[154] H. Hoster, T. Iwasita, H. Baumgärtner, and W. Vielstich *Phys. Chem. Chem. Phys.*, vol. 3, p. 337, 2001.

[155] M. P. Hogarth and G. A. Hards *Platinum Met. Rev.*, vol. 40, no. 4, p. 150, 1996.

[156] J. Hrbek, R. A. DePaola, and F. M. Hoffmann *J Chem Phys*, vol. 81, p. 2818, 1984.

[157] R. Brito de Barros, A. R. Garcia, and L. M. Ilharco *Surf Sci*, vol. 502-503, p. 156, 2002.

[158] N. Kruse, G. K. Chuah, G. Abend, D. L. Cocke, and J. H. Block *Surf Sci*, vol. 189-190, p. 832, 1987.

[159] P. Gazdzicki, P. Uvdal, and P. Jakob *J. Chem. Phys.*, vol. 130, p. 224703, 2009.

[160] P. Gazdzicki, P. Jakob *J. Phys. Chem. C*, vol. 114, p. 2655, 2010.

[161] M. N. D. S. Cordeiro, A. S. S. Pinto, and J. A. N. F. Gomes *Surf. Sci.*, vol. 601, p. 2473, 2007.

[162] P. Quinn, D. Brown, D. P. Woodruff, T. C. Q. Noakes, and P. Bailey *Surf. Sci.*, vol. 491, p. 208, 2001.

[163] C. Stampfl, S. Schwegmann, H. Over, G. Scheffler, and G. Ertl *Phys Rev Lett*, vol. 77, p. 3371, 1996.

[164] J. C. Fuggle, T. E. Madey, M. Steinkilberg, and D. Menzel *Surf. Sci.*, vol. 52, p. 521, 1975.

[165] H. Over, W. Moritz, and G. Ertl *Phys Rev Lett*, vol. 70, p. 315, 1993.

[166] M. A. Henderson *Surf. Sci. Rep.*, vol. 66, p. 185, 2011.

[167] C. L. Pang, R. Lindsay, and G. Thornton *Chem. Soc. Rev.*, vol. 37, p. 2328, 2008.

[168] A. Fujishima and K. Honda *Nature*, vol. 238, p. 37, 1972.

[169] P. J. D. Lindan and C. Zhang *Phys Rev B*, vol. 72, p. 075439, 2005.

[170] L. A. Harris and A. A. Quong *Phys Rev Lett*, vol. 93, p. 086105, 2004.

[171] P. J. D. Lindan and C. Zhang *Phys Rev Lett*, vol. 95, p. 029601, 2005.

[172] L. A. Harris and A. A. Quong *Phys Rev Lett*, vol. 95, p. 029602, 2005.

[173] I. M. Brookes, C. A. Muryn, and G. Thornton *Phys Rev Lett*, vol. 87, p. 266103, 2001.

[174] R. Schaub, P. Thostrup, N. Lopez, E. Laegegaard, J. K. Norskov, and F. Besenbacher *Phys Rev Lett*, vol. 87, p. 266104, 2001.

[175] F. Allegretti, S. O'Brien, M. Polcik, D. I. Sayago, and D. P. Woodruff *Phys Rev Lett*, vol. 95, p. 226104, 2005.

[176] L. E. Walle, A. Borg, P. Uvdal, and A. Sandell *Phys Rev. B*, vol. 80, p. 235436, 2009.

[177] W. Unterberger, T. J. Lerotholi, E. A. Kröger, M. J. Knight, D. A. Duncan, D. Kreikemeyer-Lorenzo, K. A. Hogan, D. C. Jackson, R. Wlodarczyk, M. Sierka, J. Sauer, and D. P. Woodruff *Phys Rev B*, vol. 84, p. 115461, 2011.

[178] B. Hammer, S. Wendt, and F. Besenbacher *Top Catal*, vol. 53, p. 423, 2010.

[179] M. Menetry, A. Markovits, and Minot *Surf Sci*, vol. 524, p. 49, 2003.

[180] J. Goniakowski and M. J. Gillan *Surf. Sci.*, vol. 350, p. 145, 1996.

[181] S. R. Forrest *Chem. Rev.*, vol. 97, p. 1793, 1997.

[182] Y. Shirota *J. Mater. Chem*, vol. 10, p. 1, 2000.

[183] P. Yuan, Z. Xia, Y. H. Zou, L. Qui, J. Shen, Y. Shen, and H. Xu *J. Appl. Phys.*, vol. 75, p. 4648, 1994.

[184] S. Fang, H. Tada, and S. Mashiko *Appl. Phys. Lett.*, vol. 69, p. 767, 1996.

[185] L. Guo, G. Ma, Y. Liu, J. Mi, S. Qian, and L. Qiu *Appl. Phys. B*, vol. 74, p. 253, 2002.

[186] D. Gu, Q. Chen, J. Shu, X. Tang, F. Gan, S. Shen, K. Liu, and H. Xu *Thin Solid Films*, vol. 257, p. 88, 1995.

[187] Y. L. Pan, Y. J. Wu, L. B. Chen, Y. Y. Zhao, Y. H. Shen, F. M. Li, S. Y. Shen, and D. H. Huang *Appl. Phys. A*, vol. 66, p. 569, 1998.

[188] T. Del Cano, V. Parra, M. L. Rodriguez-Mendez, R. F. Aroca, and J. A. De Saja *Appl. Surf. Sci.*, vol. 246, p. 327, 2005.

[189] R. F. Ziolo, C. H. Griffiths, and T. J. M *J.C.S. Dalton*, p. 2300, 1980.

[190] D. E. Barlow and K. W. Hipps *J Phys. Chem. B*, vol. 104, p. 5993, 2000.

[191] C. Stadler, S. Hansen, F. Pollinger, C. Kumpf, E. Umbach, T. L. Lee, and J. Zegenhagen *Phys Rev B*, vol. 74, p. 035404, 2006.

[192] D. P. Woodruff *Rep. Prog. Phys.*, vol. 68, p. 743, 2005.

[193] E. A. Kröger, D. I. Sayago, F. Allegretti, M. J. Knight, M. Polcik, W. Unterberger, T. J. Lerotholi, K. A. Hogan, C. L. A. Lamont, and D. P. Woodruff *Surf. Sci.*, vol. 601, p. 3350, 2007.

[194] E. A. Kröger, D. I. Sayago, F. Allegretti, M. J. Knight, M. Polcik, W. Unterberger, T. J. Lerotholi, K. A. Hogan, C. L. A. Lamont, M. Cavalleri, K. Hermann, and D. P. Woodruff *Surf. Sci.*, vol. 602, p. 1267, 2008.

[195] J. J. Yeh and I. Lindau *At. Data Nucl. Data Tables*, vol. 32, p. 1, 1985.

[196] C. J. Powell and A. Jablonski, *NIST Electron effective-Attenuation-Length Database, V 1.1.* NIST, Gaithersburg, USA: NIST Standard Reference Database 82, 2003.

[197] A. Gerlach, F. Schreiber, S. Sellner, H. Dosch, I. A. Vartanyants, B. C. C. Cowie, T. L. Lee, and J. Zegenhagen *Phys. Rev. B*, vol. 71, p. 205425, 2005.

[198] A. Hauschild, K. Karki, B. C. C. Cowie, M. Rohlfing, F. S. Tautz, and M. Sokolowski *Phys. Rev. Lett.*, vol. 94, p. 036106, 2005.

[199] M. K. Bradley, D. Kreikemeyer Lorenzo, W. Unterberger, D. A. Duncan, T. J. Lerotholi, J. Robinson, and D. P. Woodruff *Phys. Rev. Lett.*, vol. 105, p. 086101, Aug 2010.

[200] P. Hofmann, K. M. Schindler, S. Bao, V. Fritzsche, D. E. Ricken, A. M. Bradshaw, and D. P. Woodruff *Surf. Sci.*, vol. 304, p. 74, 1994.

[201] T. Lindner, J. Somers, A. M. Bradshaw, A. L. D. Kilcoyne, and D. P. Woodruff *Surf. Sci.*, vol. 203, p. 333, 1988.